

Dark matter vistas in the light of 21cm cosmology and some aspects of gravitational lensing

Thesis submitted for the Degree of Doctor of Philosophy (Science)

In Physics



By

Rupa Basu

Roll No. PHD/17/PHY/05

Post Graduate and Research Department

of

St. Xavier's College (Autonomous), Kolkata

Affiliated to the **University of Calcutta**

2024

Dedicated to

My Parents

ACKNOWLEDGMENTS

I would like to use this space to convey my sincere appreciation for all the assistance and support that I have received during the course of this work. First and foremost, I would like to show my gratitude to my parents, to whom this thesis is dedicated.

I would like to thank my esteemed supervisor **Dr. Shibaji Banerjee**. Without his assistance, dedicated involvement in every step throughout the process, these papers would have never been accomplished. His insightful suggestions pushed me to sharpen my thinking, not only regarding my research related problems but in several aspects on the way of my life.

I am equally grateful to **Prof. Debasish Majumdar**, whose expertise was invaluable in formulating the research works. I feel very fortunate to have the opportunity to have him as a teacher as well as a collaborator. Several inferences expressed in this thesis are the results of long discussions with him.

I extend my heartfelt gratitude to our respected Father Principal of St. Xavier's College (Autonomous), Kolkata **Rev. Fr. (Dr.) Dominic Savio, S.J.** and our former respected Father Principal **Rev. Fr. (Dr.) John Felix Raj, S.J.** for their earnest concerns towards the progress of my thesis work and for providing me with all the necessary facilities at St. Xavier's College (Autonomous), Kolkata for persuasion of my Ph.D. thesis work. I also remain grateful to **Dr. Samrat Roy**, Ph.D. coordinator, for extending me valuable supports.

I am indebted to **Department of Science & Technology, Govt. of India**, for the financial support in terms of my fellowship and other grants in the form of Women Scientist Scheme (WOS-A) during the tenure of my Ph.D.

I would like to convey my sincere gratitude to **Prof. Sibaji Raha** and **Prof. Sanjay K. Ghosh**. Their valuable guidance helps me

a lot throughout my studies. I am really glad to have them as my collaborator.

I am very much fortunate to get associated with our department faculties. Their suggestions and inspirations help me a lot during this period of my academic career. Specially, I want to thank **Late Prof. Sailendra Narayan Roy Choudhury, Dr. Suparna Roy Chowdhury, Dr. Indranath Chaudhuri, Dr. Tapati Dutta, Dr. Soma Ghosh, Dr. Sarbari Guha.**

I would like to take this opportunity to acknowledge a few special people in my life. First and foremost, I would like to express my deepest gratitude to my husband, **Siddhartha Bhattacharyya**. Without his unwavering mental and financial support, I would not have been able to complete my Ph.D. He has always stood by me, especially during times of crisis. I am also deeply grateful to my **brother** and **sister-in-law** for their continuous encouragement throughout my Ph.D. journey; their support has been invaluable. Again a special thanks to my parents, **BABAMONI** and **MAA**, without whom I would not be who I am today. Their love and guidance have been the foundation of all my achievements. Lastly, I would like to acknowledge my niece, **Miska**, who has brought immense joy into my life and helped lift my spirits during times of depression.

I would also like to extend my heartfelt appreciation to my colleague, **Ashadul Halder**, who has been a constant presence throughout my journey, offering his support as both a friend and a brother.

To all of you, I express my endless gratitude and love.

Rupa Basu

Contents

Contents	vii
List of Figures	xi
List of Tables	xvii
1 Introduction	1
1.1 Basic of Cosmology	5
1.2 Cosmic History	10
1.2.1 Primordial Universe	10
1.2.2 Nucleosynthesis	11
1.2.3 Recombination	12
1.2.4 Dark Ages	12
1.2.5 First Stars	13
1.2.6 Reionization	14
1.2.7 Post-reionization	15
1.3 The Dark Matter Enigma	16
1.4 Evidence of Dark Matter	16
1.5 Nature of dark matter	40
1.5.1 Mass ranges of dark matter candidates	50
1.6 Detection technique of Dark Matter	52
1.7 Summary	60
2 21cm Cosmology	61
2.1 21cm Cosmology	61
2.2 21cm brightness temperature	64
2.3 Optical depth τ	68
2.4 Evolution of the global 21 cm signal	69
2.5 Summary	70
3 Annihilation Cross-Section of IDM Dark matter	73
3.1 Introduction	74
3.2 Thermal Evolution of intergalactic medium (IGM)	76
3.3 Variation of T_{21} with different parameters	81
3.4 Lower bound on annihilation cross-section of IDM	88

4	Bounds on Scattering cross-section of Two component dark matter	91
4.1	Introduction	92
4.2	Thermal Evolution	96
4.2.1	Heating Rates and Drag Terms	99
4.2.2	Energy Injection from Dark Matter Annihilation	100
4.3	Bounds on Scattering cross-section	101
5	Exploring Elder Dark Matter in the Context of 21cm Cosmology	107
5.1	Introduction	108
5.2	Elder dark matter model and its cannibalism property	110
5.3	Thermal evolution of 21cm signal	111
5.4	Effect of ELDER dark matter on 21cm line	112
5.4.1	DM-baryon elastic scattering ($\chi + SM \leftrightarrow \chi + SM$)	113
5.4.2	DM annihilation to SM ($\chi + \chi \leftrightarrow SM + SM$)	114
5.4.3	“3 \rightarrow 2” self-annihilation ($\chi\chi\chi \leftrightarrow \chi\chi$)	115
5.4.4	“2 \rightarrow 2” elastic self-scattering ($\chi\chi \leftrightarrow \chi\chi$)	116
5.5	Results and conclusion	118
6	Compact Astrophysical Objects	127
6.1	Introduction	128
6.2	Neutron Stars	129
6.2.1	Birth of a neutron star	130
6.2.2	Structure and composition of Neutron star	132
6.2.3	Observational constraints	134
6.3	Quark Stars	136
6.4	Massive Compact Halo Objects	137
6.5	Black Holes	138
6.6	Other Exotic stars	139
7	Detection of Isolated Neutron stars through HI signal	141
7.1	Introduction	141
7.2	Effect of gravitational lensing of 21cm line	144
7.2.1	Flux Density	144
7.2.2	Telescope and Background Noise	146
7.2.3	Gravitational Lensing Model	147
7.2.4	Mass of a Neutron Star	150
7.2.5	Optical Depth	151
7.2.6	Chance Coincidence	152
7.3	Result	153
7.4	Summary	158
8	Summary and Future Outlook	159

Bibliography	171
List of Publications	203

List of Figures

1.1	The schematic diagram of the components of the Universe.	4
1.2	The schematic diagram of evolution of Universe.	6
1.3	Different models of the expanding Universe.	7
1.4	(a) Galaxies inside the Coma Cluster (Photo credit: NASA/JPL-Caltech/L. Jenkins (GSFC)). (b) Virgo Cluster (Photo credit and copyright: Rogelio Bernal Andreo, deepskycolors.com.	19
1.5	Galaxy rotation curve of Messier 33. The yellow dashed line is the expected line from the visible disk, while the solid line represents the fitted line of observed points [35].	20
1.6	Galactic rotation curve of (a) Milky Way galaxy (Figure from Ref. [36]), (b) NGC 6503 galaxy (Figure from Ref. [37, 38].)	21
1.7	The all-sky cosmic microwave background radiation map from WMAP and Planck data. Both images show a temperature fluctuations of $\pm 300 \mu\text{K}$ around the average temperature 2.73 K. The top image represents the WMAP W-band CMB map while the bottom image is the Planck SMICA CMB map. (Photo credit: NASA / WMAP Science Team.)	23
1.8	The TT (temperature-temperature) angular power spectrum from nine-year WMAP data. The WMAP data are represented by black points and corresponding error bars. The red line describing the best fit model. The smoothed binned spectral function is shown using the gray region. (Photo credit: NASA / WMAP Science Team. [2])	24
1.9	The Bullet Cluster (Photo credit: NASA/CXC/CfA/M.Markevitch et al. [46])	25
1.10	Bending of incoming light due to the gravitational field of a massive object. The dashed lines show the apparent position of the light source. [53]	27
1.11	(a) The galaxy cluster CL0024+1654 produces multiple images of a distant blue galaxy (Photo credit: NASA, ESA, H. Lee & H. Ford (Johns Hopkins U.) [56]). (b) Horseshoe Einstein Ring from Hubble. The gravitational field of the red galaxy LRG 3-757 lenses the incoming light from a distant blue galaxy (Photo credit: ESA/Hubble, NASA).	28
1.12	The different regimes of gravitational lensing image distortion. The effect of lensing due to the passage of massive galaxies or clusters of galaxies results several distortions of the image of the circular source (in black and grey shadow) appeared to the observer [57]	29

1.13	Schematic diagram of gravitational microlensing.	29
1.14	The map of galaxies discovered by Sloan Digital Sky Survey (SDSS) showing the large-scale structure of the Universe. The radial distance from the centre of the circle representing the redshifts of the corresponding galaxies. (Photo credit: M. Blanton and SDSS)	30
1.15	The images give the dark matter distributions at large scale in the Universe obtained in the Millennium simulation. From the Millennium Simulation Project webpage. <i>URL : https://www.mpa-garching.mpg.de/galform/virgo/millennium/</i>	31
1.16	The predicted abundances of ^2H , ^3He , ^4He , ^7Li according to the standard model of Big Bang Nucleosynthesis (BBN). The bands denote the range of 95% confidence level (CL) for different values of (η). The yellow boxes in this plot represent the range of the observed abundances for those light elements. The pink (wide) vertical band denotes the BBN concordance range, while the blue (narrow) band indicates the CMB measure of the cosmic baryon density (From Ref. [63]).	34
1.17	Lyman-alpha Forest. Light rays from distant quasars (red dots) get partially absorbed as they pass through hydrogen gas of IGM. As a result, several absorption lines of hydrogen manifests in the spectrum of those quasar (the graph in this figure) as observed by telescope. (Photo Credit: Zosia Rostomian, Lawrence Berkeley National Laboratory; Nic Ross, BOSS Lyman-alpha team, Berkeley Lab; and Springel et al., Virgo Consortium and Max Planck Institute for Astrophysics.)	39
1.18	This figure depicts the mass ranges of dark matter and mediator particle candidates, experimental anomalies, and search techniques. Source: Figure adapted from [111]	51
1.19	Schematic diagram of the possible channels of dark matter detection.	53
1.20	The schematic diagram of the indirect detection of galactic dark matter halo.	56
1.21	Different dark matter halo profiles (see Table 1.2).	58
2.1	A visual representation illustrating the hyperfine transition occurring within the ground state of a neutral hydrogen atom [158].	62
2.2	A schematic representation illustrating the alteration in brightness temperature of light as it traverses through a medium [158].	64
2.3	The figures depict the evolution of fluctuations in the 21 cm signal (above) and the global 21 cm signal (below) under the condition where the background radiation is solely composed of the Cosmic Microwave Background Radiation (CMBR). <i>Photo credits: Pritchard & Loeb, Rep. Prog. Phys., 75, 086901, (2012) [159].</i>	69

2.4	Each profile, representing the brightness temperature T_{21} , is combined with its residuals and plotted against the redshift z along with the corresponding age of the Universe.. <i>Photo credits: Judd D. Bowman et al. [173].</i>	71
3.1	The variation in the 21-cm brightness temperature, T_{21} , across different redshifts is shown with the inclusion of dark matter (DM) annihilation effects alongside the standard thermal evolution. The different coloured lines represent varying IDM masses as indicated in the figure.	83
3.2	The variation in the 21-cm brightness temperature, T_{21} , across different redshifts includes the impact of DM-baryon elastic scattering in addition to the standard thermal evolution. Different colored lines correspond to various IDM masses as indicated in the figure.	84
3.3	(a) This panel depicts the variations in the 21-cm brightness temperature T_{21} at different redshifts, incorporating DM-baryon elastic scattering as an additional effect alongside the thermal evolution. The red points represent the computed values, while the blue line denotes the fitted curve. (b) Similarly, this panel illustrates the redshift values (z_{\min}) at which T_{21} reaches its minimum for each different IDM mass (m_χ). The solid green line traces the trends in the variation of z_{\min} across different IDM masses.	85
3.4	The left panel illustrates the changes in the 21cm absorption lines T_{21} , incorporating effects of dark matter annihilation and dark matter-baryon elastic scattering alongside thermal evolution. Each coloured line represents a different dark matter mass as specified in the figure. The right panel zooms in on the redshift range $80 \leq z \leq 120$, providing a detailed view of the variations depicted in the left panel.	85
3.5	(a) The figure illustrates the variation in the 21-cm brightness temperature T_{21} at different redshifts, considering only dark matter annihilation as an additional effect alongside thermal evolution. Red points denote computed values, while the blue line represents the fitted curve. (b) Similar to panel (a), this plot shows how the redshift values (z_{\min}) at which T_{21} reaches its minimum vary with different dark matter masses m_χ . The solid green line depicts the trend of z_{\min} with m_χ	86
3.6	(a) This panel depicts the variation in the 21-cm brightness temperature T_{21} at different redshifts, incorporating the combined effects of dark matter annihilation and dark matter-baryon scattering as additional factors influencing T_{21} , alongside the thermal evolution. The red points denote computed values, and the blue line represents the fitted curve. (b) In this panel, we present the variation of the redshift values (z_{\min}) at which T_{21} reaches its minimum for each different dark matter mass m_χ . The solid green line depicts the trend in the variation of z_{\min} with m_χ	86

3.7	The variation in the 21-cm absorption lines T_{21} due to the combined effect of different fractions of IDM masses f_{m_χ}	87
3.8	Variations of T_{21} across different fractions of IDM masses f_{m_χ}	88
3.9	The annihilation cross section $\langle\sigma v\rangle$ for various dark matter masses m_χ . The brown curve represents the range of $\langle\sigma v\rangle$ estimated from Planck experiments [206, 207].	90
4.1	The variation of brightness temperature the 21cm lines T_{21} due to the two component dark matter of different fractions of IDM masses f_{m_χ} . For each plot we considered the benchmark points described in Table 4.1. Different colour represents different fraction of IDM masses.	102
4.2	Variations of fraction of IDM mass with generic dark matter mass for a constant IDM mass at redshift $z = 17.2$ within the EDGES experimental result limit. Other parameters values were taken for this calculation is given in Table 4.1.	103
4.3	Variations of fraction of IDM mass with IDM dark matter mass for a constant generic DM mass at redshift $z = 17.2$ within the EDGES experimental result limit. Other parameters values were taken for this calculation is given in Table 4.1.	104
4.4	Variations of IDM dark matter- baryon scattering cross-section σ_{41}^χ with generic DM - baryon scattering cross-section σ_{41}^{DM} at redshift $z = 17.2$ within the EDGES experimental result limit. Other parameters values were taken for this calculation is $f_\chi = 0.2$, $m_\chi = 10$ GeV, 30 GeV and 80 GeV and $m_{DM} = 0.5$ GeV and 1 GeV.	106
5.1	(a) Evolution of the baryonic matter temperature (T_b) with redshift (z) for various selected model parameters. (b) Corresponding spin temperature (T_s) evolution with redshift (z) for the same set of model parameters. (c) Evolution of the brightness temperature (T_{21}) with redshift (z) for different chosen model parameters.	119
5.2	The parameter space in the α - η plane is examined for different values of m_χ in figs. (a) to (d): (a) $m_\chi = 0.01$ GeV, (b) $m_\chi = 0.02$ GeV, (c) $m_\chi = 0.05$ GeV, and (d) $m_\chi = 0.10$ GeV. Each plot assumes $\sigma_{41} = 0.25$	121
5.3	The allowed region in the $\eta - m_\chi$ parameter plane.	122
5.4	The permissible regions in the $\sigma_{41} - m_\chi$ plane are depicted for various selected values of η , accompanied by several constraints derived from different experiments.	123

5.5	Variations of the dark matter density parameter Ω_χ , normalized to the critical density of the Universe, are depicted for the dark matter particle χ as a function of η , considering four distinct mass values of χ . These are illustrated by solid colored lines. Additionally, dashed and dotted lines correspond to $\alpha = \alpha_{\max}$ and $\alpha = \alpha_{\min}(m_\chi)$ respectively, for each of the four mass cases, where the solid lines represent the average α values. The solid squares on the plots denote the EDGES observational result of the brightness temperature $T_{21}^{z=17.2} = -500$ mK.	125
6.1	Schematic diagram of neutron star core.	131
6.2	Schematic diagram of interior of neutron star core. [235]	132
6.3	The Event Horizon Telescope captured the first-ever image of a black hole, located at the center of the M87 galaxy. (Photo credit: Event Horizon Telescope Collaboration)	138
7.1	A simplified diagram illustrating the gravitational lensing of the HI signal by an isolated neutron star situated at a cosmological distance.	147
7.2	The left panel illustrates how the redshift of the neutron star varies with its position, while the right panel shows the corresponding changes in the optical depth fraction. These variations are considered for detecting the HI signal at Band-3 (represented by the red line) and Band-4 (depicted by the blue line) of the uGMRT.	154
7.3	The impact of the radius (upper panels) and position (lower panels) of an isolated neutron star on the signal-to-noise ratio $(SNR)_\mu$ for the HI signal expected to be detected at Band-3 (left column) and Band-4 (right column) of the uGMRT is illustrated. The black horizontal dashed line represents the threshold value of $(SNR)_\mu$, denoted as $SNR_{Th} = 5$.	155
7.4	The determination of the radius and position of an isolated neutron star is based on the signal-to-noise ratio $(SNR)_\mu$ of the HI signal, which is expected to be detected at Band-3 (left column) and Band-4 (right column) of the uGMRT. The white vertical dashed line indicates the standard neutron star radius of $R_{\text{peak}} = 10$ km.	157

List of Tables

1.1	Estimates of chronological periods, redshift values, and associated temperatures for key events in the Universe. <i>Table credit: Daniel Baumann [15]</i>	10
1.2	Density profiles of dark matter halo and corresponding parameters.	59
3.1	The relic density (Ω_c) and the corresponding annihilation cross section ($\langle\sigma v\rangle$) for various IDM dark matter masses (m_χ) are provided, ensuring that Ω_c falls within the 95% confidence interval of $\Omega_{c,0}$ as determined by the Planck experiment [45].	89
4.1	Benchmark values of generic dark matter masses m_{DM} , IDM mass m_χ , IDM-baryon scattering cross-section σ_0^χ and generic dark matter-baryon scattering cross-section σ_0^{DM}	101
5.1	Benchmark values for various parameters (m_χ , σ_{41} , α , and η) used in the plots of fig. 5.1.	118

Introduction

“Cosmology is peculiar among the sciences for it is both the oldest and the youngest. From the dawn of civilization man has speculated about the nature of the starry heavens and the origin of the world, but only in the present century has physical cosmology split away from general philosophy to become an independent discipline.”

-Gerald James Whitrow.

Over the past two decades, our comprehension of cosmology has reached new depths. Through observations spanning from the Universe’s infancy, about 400,000 years after the Big Bang, to its current age of 13.7 billion years, we have gained fundamental insights into its evolution. Yet, during the initial billion years, recent advancements in theory and instrumentation have expanded the horizons of our understanding in ways previously unimaginable. These developments have broadened the scope of research, refining our understanding across various facets of cosmology and high-energy astroparticle physics. From gravitational lensing to various possible dark matter models, dark energy models and 21 cm cosmology, among others, the commendable advancement has deepened our knowledge of the Universe’s intricacies.

Observational cosmology remains pivotal in testing theoretical predictions, leading to the refinement of cosmological models. For instance, observational data on dark matter has significantly influenced our understanding of the structure and the galaxy formations.

The evidence for dark energy emerged in the late 1990s during attempts to calibrate the Hubble diagram using Type I supernova [1] as standard candles. These findings were incorporated into the Λ CDM model, a six-parameter framework describing the cosmos's evolution in terms of its constituent components. Subsequent confirmation came from comprehensive studies of the cosmic microwave background, notably through experiments like WMAP [2].

The study of cosmological parameters is fundamental to our understanding of the Universe's structure, evolution, and ultimate fate. This discussion traces the development of these parameters, starting from the early conceptual framework proposed by Alan Sandage [3] to the more sophisticated models employed in modern cosmology [4]. In the mid-20th century, renowned astronomer Alan Sandage suggested that cosmology could be distilled into the search for two important factor namely the Hubble constant (H_0) and the deceleration parameter (q_0). The Hubble constant measures the rate of expansion of the Universe, while the deceleration parameter describes how the expansion rate changes over time. These two numbers were foundational because they encapsulated the most crucial aspects of cosmological dynamics and the Universe's large-scale structure. With advancements in observational cosmology, notably from the Cosmic Microwave Background (CMB) measurements by the Wilkinson Microwave Anisotropy Probe (WMAP) and Planck satellite [5, 6], the Lambda Cold Dark Matter (Λ CDM) model also known as the standard model of cosmology. Λ CDM is characterized by six or more key parameters [7]. We noted only six parameter in this section (*i*) Baryon Density ($\Omega_b h^2$)— the density of ordinary matter, (*ii*) Cold Dark Matter Density ($\Omega_{\text{CDM}} h^2$)— the density of dark matter, (*iii*) Dark Energy Density (Ω_Λ)— represented by the cosmological constant (Λ), it accounts for the accelerated expansion of the Universe, (*iv*) Hubble

Constant (H_0)— the current rate of expansion of the Universe, (v) Scalar Spectral Index (n_s)— describes the initial density fluctuations and (vi) Optical Depth (τ)— the measure of reionization’s effect on the CMB. This six-parameter model has been remarkably successful in explaining a wide range of cosmological observations .

While the Λ CDM model provides a robust framework, it is recognized that this model might be an approximation of a more complex reality. Extended cosmological models introduce additional parameters to address discrepancies and explore new physics. Some notable extended parameters include: Neutrino Masses ($\sum m_\nu$), Effective Number of Neutrino Species (N_{eff}), Equation of State Parameter for Dark Energy (ω) and so on. CMB measurements, Large-scale structure surveys, supernova observations and gravitational lensing like observational data give the precise measurement of cosmological parameters.

Despite the successes of the Λ CDM model, several tensions and open questions remain. For instance, discrepancies in the measured values of H_0 from different methods hint at possible new physics. Similarly, understanding the nature of dark matter and dark energy continues to be a major challenge. Future missions like the James Webb Space Telescope (JWST) [8], Euclid, and the Large Synoptic Survey Telescope (LSST) [9] are expected to provide further insights and possibly lead to new paradigms in cosmology.

Key modern observational endeavours continue to shape cosmology, contributing to ongoing advancements in the field. Nevertheless, A few observations from Robert Woodrow Wilson’s Nobel address may be echoed, which encapsulates the essence of these developments.

“Cosmology is a science which has only a few observable facts to work with.”

-Robert Woodrow Wilson.

In recent times, the Λ CDM cosmological model, described above has achieved remarkable success in understanding the evolution of cosmic history. This model sheds

light on various aspects, such as the production of light elements during Big Bang Nucleosynthesis, the spectrum of variation in the Cosmic Microwave Background Radiation from the early Universe, and the formation of structures like galaxies or galaxy clusters. Despite its significant achievements, the Λ CDM model gives rise to significant challenges, primarily due to the vast scale of the Universe, which defies any notion of a comprehensive survey at this point of time. The Universe still holds numerous unsolved mysteries compared to what we have already discovered. Dark Matter and Dark Energy stand out as two particularly enigmatic components. According to the current cosmological paradigm, ordinary baryonic matter constitutes only 4.9% of the Universe's total energy budget, while the remaining 95% comprises the mysterious dark matter and dark energy. Fig. 1.1 presents a pie chart for the the known energy budget of the Universe. Understanding the properties of these dark components continues to remain as puzzles for the humankind. The research presented in this dissertation aims to address many of these questions by developing and enhancing “21cm cosmology,” a novel experimental method capable of probing various cosmic epochs.

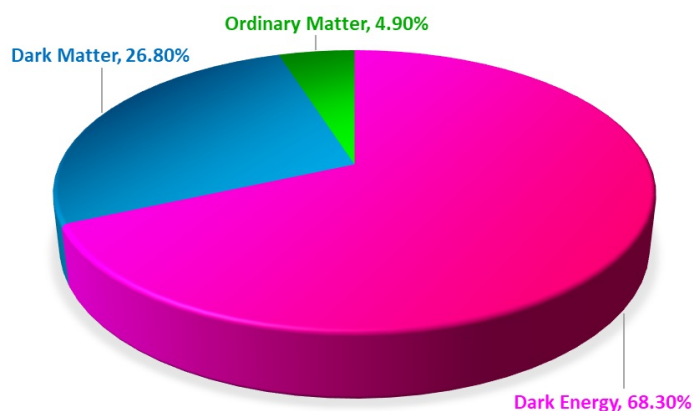


Figure 1.1: The schematic diagram of the components of the Universe.

1.1 Basic of Cosmology

“Look up at the stars and not down at your feet. Try to make sense of what you see, and wonder about what makes the Universe exist. Be curious.”

-Stephen Hawking.

We are currently experiencing a captivating era in cosmology and astrophysics, marked by unprecedented discoveries facilitated by new technological capabilities that allow us to explore the Universe in unprecedented detail. Through the combined efforts of missions like COBE, WMAP [2], ground-based CMB projects such as BICEP [10] and BOOMERANG [11], as well as surveys like 2dF/SDSS [12] and high-redshift supernova searches, we have been able to establish stringent constraints on cosmological parameters and develop a “Concordance Model”. This model serves as a robust framework for understanding the majority of observed cosmic phenomena.

However, it is becoming increasingly clear that traditional approaches may not yield the same level of insight as we move forward. As Steven Weinberg aptly put it,

“The effort to understand the Universe is one of the very few things that lifts human life a little above the level of farce, and gives it some of the grace of tragedy.”

-Steven Weinberg.

Several cosmological models, including Einstein’s initial notion of a static Universe, stemmed from his general theory of relativity, introduced in 1916. In 1927, Georges Lemaître (and independently Alexander Friedmann in 1922) derived solutions to Einstein’s field equations that described an expanding cosmos, challenging the prevailing static model. Edwin Hubble’s observational confirmation in 1929, demonstrating that distant galaxies are receding from us, provided tangible evidence for this expanding Universe. Despite Lemaître’s groundbreaking work, it received little attention until Eddington arranged for its translation and reissue in 1931.

Lemaître's contribution was pivotal, not only for introducing the concept of an expanding Universe (Fig. 1.2), which captured widespread interest, but also for his exploration of the origins and mechanisms driving this expansion. The Big Bang model, emerging from these foundational insights, offers precise and testable hypotheses, and its remarkable agreement with empirical observations instills confidence in its validity.

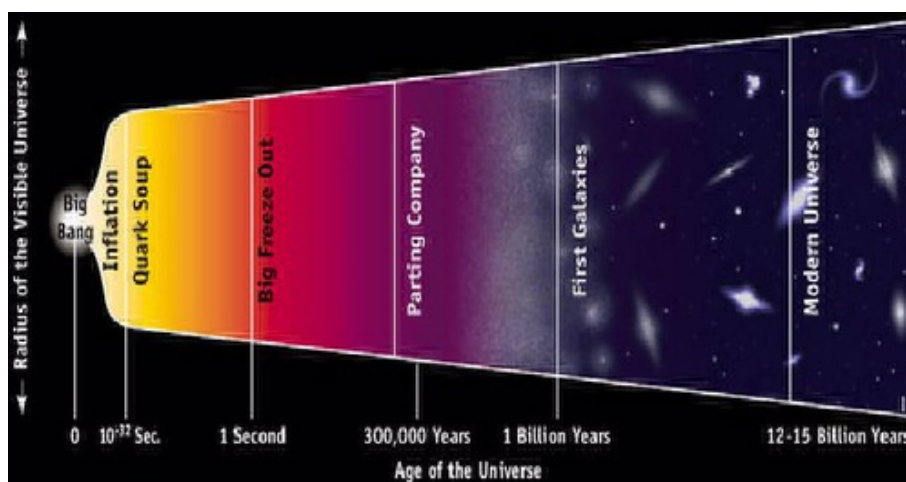


Figure 1.2: The schematic diagram of evolution of Universe.

Also several alternative models were proposed to explain the expansion of the Universe which is demonstrated in fig. 1.3.

The theoretical estimation of the Universe's expansion rate and evolution relies heavily on a fundamental concept known as the cosmic scale factor, denoted as $a(t)$. This dimensionless quantity serves as a crucial tool in cosmology, enabling us to understand the Universe's growth over time. It quantifies the relative size of the Universe at any given moment compared to its size at a reference time, typically denoted as t_0 .

In the context of the widely accepted Big Bang theory, which posits the Universe's origin from an intensely hot and dense state, all cosmic phenomena have unfolded subsequent to this initial event. The scale factor $a(t)$ provides a measure of this expansion, where $a(t) = 1$ at the present time t_0 , indicating the current size of the

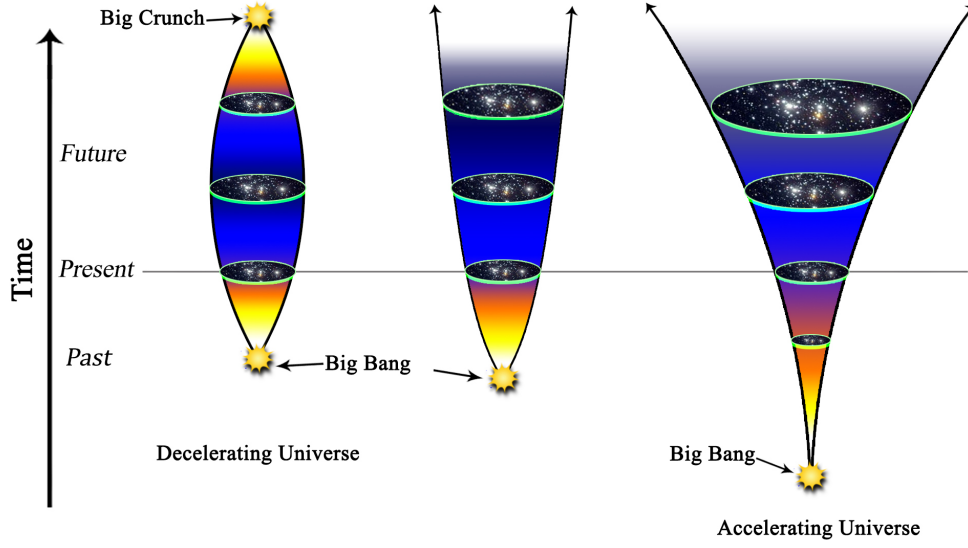


Figure 1.3: Different models of the expanding Universe.

Universe. For times after the present, $a(t) > 1$ suggests expansion, while $a(t) < 1$ implies contraction of the Universe.

By scrutinizing the behaviour of the scale factor over time, cosmologists can glean invaluable insights into the past and future evolution of the Universe, including the dynamics of cosmic structures and the rate of expansion. This comprehension forms the bedrock of our understanding of cosmology and the intricate history of the Universe.

The Friedman equations [13, 14] are central to the study of cosmological evolution, governing the Universe's expansion dynamics. These equations are represented as

$$H^2 = \left(\frac{\dot{a}}{a}\right)^2 = \frac{8\pi G}{3}\rho - \frac{K}{a^2} + \frac{\Lambda}{3} \quad (1.1)$$

$$\frac{\ddot{a}}{a} = -\frac{4\pi G}{3}(\rho + 3P) + \frac{\Lambda}{3} \quad (1.2)$$

These equations provide profound insights into the behaviour of the cosmic scale factor $a(t)$ which also is the expansion factor. Here, H serves as the expansion rate or Hubble parameter, signifying the rate of the Universe's expansion. In the

above, K represents the curvature constant and describes the geometry of the partial part of space-time ($K = +1, 0, -1$ corresponds to the close, flat and open Universes respectively). The cosmological constant is represented by Λ while ρ, P are the energy density and pressure density of fluids respectively, such that energy momentum tensor $T_{\nu}^{\mu} = \text{Diag}(-\rho, P, P, P)$. Cosmologists commonly use the scale factor a or the redshift z to measure temporal and spatial scales, linked to cosmic time through $a = \frac{1}{1+z}$ and $dz = -\frac{cdt}{(1+z)H(z)}$, respectively.

According to the widely accepted Big Bang theory, the Universe's existence originates from the very first cosmic event, known as the Big Bang. Approximately 10^{-35} seconds after this event, the Universe experienced an extremely rapid expansion known as "Cosmological Inflation", lasting for a very brief period of time, around up to the age $10^{-33} \sim 10^{-32}$ seconds of the Universe. Following this phase of rapid expansion, the Universe's expansion continued, albeit at a slower pace. Each component of the Universe's evolution exhibits distinct dependencies over time, allowing for the division of the cosmic timeline into different eras based on their dominant contributions.

In the early stages of the Universe, characterized by high redshifts (z), the dominance of the $(1+z)^4$ factor of radiation dictates the era of radiation domination. In radiation domination epoch, most of the energy constituents are coming from radiation and matter is mostly relativistic. Subsequently, the era of matter domination begins around the point of matter-radiation equality, approximately estimated as $1 + z_{\text{eq}} = \frac{\Omega_{\text{m}}}{\Omega_{\text{rad}}} \sim 3500$. Following this, the expansion of the Universe is primarily driven by non-relativistic matter until $1 + z_{\Lambda} = \left(\frac{\Omega_{\Lambda}}{\Omega_{\text{m}}}\right)^{1/3} \approx 1.3$, indicating the onset of the era of dark energy or Λ domination where the evolution of the scale factor for a dark energy-dominated Universe can be approximated as $a(t) \propto \exp(H_0 t)$. H_0 represents the present value of the Hubble parameter. This era continues until the present time, approximately 13.8 billion years after the Universe's inception.

The continuity equation, arising from conservation principles and represented by

$$\dot{\rho} + 3H(\rho + P) = 0, \quad (1.3)$$

This encapsulates the evolution of the Universe's energy content. It factors in contributions from various species characterized by their energy density (ρ_i) and pressure (P_i), with the equation of state ($w = \frac{P}{\rho}$) delineating each species' behavior and impact on the overall evolution. The expansion rate, modulated by the diverse contributions of these species and often expressed relative to the critical density ($\rho_c(z) = \frac{3H(z)^2}{8\pi G}$), sheds light on the dynamics and composition of the evolving Universe. This framework offers crucial insights into the roles played by radiation, non-relativistic matter, and the cosmological constant (Λ).

In the context of radiation, involving massless particles like photons or neutrinos in the early Universe, the pressure is expressed as $P_{\text{rad}} = \frac{1}{3}\rho_{\text{rad}}$. Consequently, in the absence of interactions, the equation without a specific label leads to a dependence on the scale factor where $\rho_{\text{rad}} \propto (1+z)^4$. Conversely, non-relativistic matter, encompassing both dark and baryonic matter, exerts negligible pressure, resulting in $\rho_m \propto (1+z)^3$. The contribution of Λ can be considered a manifestation of dark energy, characterized by constant energy density with $\dot{\rho}_\Lambda = 0$.

Considering the contributions from radiation, matter, and the dark energy ($i = \text{rad}, m, \Lambda$ respectively), the expansion rate can be expressed in terms of the energy density parameters ($\Omega_i = \frac{\rho_{i,0}}{\rho_{c,0}}$, where the subscript 0 indicates the current values) as the sum (with $K = 0$)

$$H^2 = H_0^2 (\Omega_{\text{rad}}(1+z)^4 + \Omega_m(1+z)^3 + \Omega_\Lambda) \quad (1.4)$$

The Hubble rate at present, denoted as H_0 , is conventionally represented as $H_0 = 100h \text{ km s}^{-1} \text{ Mpc}^{-1}$, with h being the reduced Hubble constant. From Cosmic Microwave Background (CMB) and Baryon Acoustic Oscillation (BAO) data, the value

Event	time	redshift	Temperature
Inflation	10^{-36} sec	-	-
Baryogenesis	-	-	$10^{12} \sim 10^{14}$ GeV
Electroweak phase transition	20 ps	10^{15}	100 GeV
QCD phase transition	20 μ s	10^{12}	150 MeV
Dark matter freeze-out	-	-	100 MeV
Neutrino Decoupling	1 sec	6×10^9	1 MeV
Electron-positron annihilation	6 sec	2×10^9	500 KeV
Big-Bang nucleosynthesis	3 minute	4×10^8	100 KeV
Matter-radiation equality	60 Kyr	3400	0.75 eV
Recombination	260 – 380 Kyr	1400 – 1100	0.33 – 0.26 eV
Photon decoupling	~ 380 Kyr	~ 1100	~ 0.27 eV
First stars formation	~ 100 Myr	~ 30	~ 7 meV
Reionization	~ 400 Myr	~ 11	~ 2.6 meV
Dark energy-matter equality	9 Gyr	0.4	0.33 meV
Present	13.8 Gyr	0	0.24 meV

Table 1.1: Estimates of chronological periods, redshift values, and associated temperatures for key events in the Universe. *Table credit: Daniel Baumann [15]*

of h is typically found to be approximately 0.693.

1.2 Cosmic History

In this section, we will provide a concise overview of the significant milestones in cosmic chronology, delineating the key epochs and transitions between them. Simplifying the comprehensive picture, we categorize the cosmic timeline into the following phases

1.2.1 Primordial Universe

Numerous theories have been proposed to explain the origin of the Universe, with the Big Bang theory emerging as the most widely accepted and evidence-supported explanation. According to this theory, the Universe undergoes various processes

within a time approximately 1 second subsequent to the initial cosmic explosion. In the initial seconds following the Big Bang, significant epochs transpire, including Planck, inflation, reheating, baryogenesis, the electroweak transition, and hadronization, among others. Given our focus on more recent developments, we will briefly overlook the details of this early epoch [16, 17, 18]. During the inflationary phase, the Universe experiences a rapid expansion driven by a scalar field or other exotic species, leading to a dramatic increase in size within an incredibly short duration, around 10^{-33} seconds. The fields responsible for inflation transition to particle and radiation species during the Reheating epoch, marking the onset of the radiation-dominated era. Throughout this period, the energy density is primarily governed by massless and nearly massless relativistic components like photons and neutrinos, which travel at or near the speed of light. This dominance extends over both matter density and dark energy. Subsequently, the Universe comprises a highly homogeneous plasma containing numerous species in thermal equilibrium. As the Universe continues to expand and undergoes adiabatic cooling, many of these species detach from the cosmic plasma. The minute fluctuations generated during inflation serve as the seeds from which cosmic structures evolve thereafter.

1.2.2 Nucleosynthesis

Big Bang Nucleosynthesis (BBN) [19, 20] refers to the synthesis of light nuclei that occurred during the early phases of the Universe, specifically within the first few minutes after the Big Bang. This process is significant because it is responsible for the formation of the lightest elements in the Universe, such as hydrogen, helium, and small traces of lithium and deuterium. During BBN, the extreme temperatures and densities allowed for the fusion of protons and neutrons into these light nuclei. The predictions of BBN regarding the primordial abundances of these light elements align closely with observations, strongly supporting the validity of the Big Bang cosmological model.

1.2.3 Recombination

Recombination [21, 22] is a pivotal event in cosmic history that occurred approximately 380,000 years after the Big Bang. At this point, the Universe had cooled sufficiently for electrons to combine with protons, forming neutral hydrogen atoms for the first time. Prior to recombination, the Universe was a hot, dense plasma consisting of free electrons and protons, making it opaque to light. This plasma era, known as the era of photon-baryon plasma, rendered the Universe opaque to electromagnetic radiation.

However, as the Universe expanded and cooled, it reached a critical temperature below 3000 Kelvin where electrons could bind to protons to form stable hydrogen atoms. This process, known as recombination, resulted in the decoupling of photons from matter. Photons were then able to travel freely through space, leading to the Universe becoming transparent.

The signature of this event is imprinted on the cosmic microwave background (CMB) radiation, which we observe today as a relic of the hot, dense early Universe. By studying the fluctuations in the CMB, scientists can glean valuable insights into the conditions of the Universe at the time of recombination, providing crucial information about its evolution and composition.

1.2.4 Dark Ages

The dark age commenced shortly after recombination in the early Universe, around the redshift $z \approx 1100$. During this period, the Universe cooled significantly, causing electrons to decouple from the cosmic background radiation. Consequently, the Universe became transparent to electromagnetic radiation, bathed in a nearly uniform reddish glow. Despite this transparency, the absence of large-scale structures meant there were no significant light sources apart from the cosmic background radiation.

However, due to cosmological redshift, the reddish (orange) glow of the cosmic microwave background (CMB) shifted further towards the red end of the spectrum as time progressed. Consequently, from the end of recombination until the birth of the first stars, the Universe remained dark, earning this period the title of Cosmic Dark Age [23, 24].

1.2.5 First Stars

The formation of the first stars [25, 26], also known as Population III stars, represents a critical milestone in cosmic history, marking the transition from a primordial Universe dominated by hydrogen and helium to one enriched with heavier elements. These stars are believed to have formed from primordial gas clouds composed almost exclusively of hydrogen and helium, with trace amounts of lithium.

The formation of Population III stars was likely triggered by the gravitational collapse of dense regions within these primordial gas clouds. Without the presence of heavier elements to cool the gas via molecular line emissions, the collapsing gas clouds could reach higher densities before fragmentation and star formation commenced. Consequently, the first stars were likely much more massive than those formed in later epochs, with masses potentially reaching hundreds of times that of the Sun.

The onset of nuclear fusion within these massive stars ignited intense nuclear reactions, leading to the emission of copious amounts of radiation. These Population III stars were short-lived compared to their lower-mass counterparts, burning through their nuclear fuel in a matter of millions of years before undergoing spectacular supernova explosions.

The demise of Population III stars played a crucial role in shaping the early Universe. Their explosive deaths ejected heavy elements synthesized during their lifetimes, enriching the surrounding interstellar medium with elements such as carbon, oxygen,

and iron. These enriched environments provided the raw materials necessary for the formation of subsequent generations of stars, including those with lower masses and longer lifetimes, like our Sun.

1.2.6 Reionization

Reionization stands as a pivotal epoch in cosmic history, marking the transition from the Universe's opaque, neutral state to one characterized by transparency and ionization. This process occurred roughly between 150 million to one billion years after the Big Bang and known as reionization epoch [27, 28].

During the early stages of cosmic evolution, following the era of recombination, the Universe consisted mainly of neutral hydrogen and helium atoms. However, the emergence of the first luminous sources, such as the first stars and galaxies, initiated a transformative period known as reionization. These sources emitted intense ultraviolet radiation, which ionized the surrounding neutral gas, stripping electrons from hydrogen and helium atoms and turning them into ions.

The reionization process gradually heated the intergalactic medium (IGM) and rendered it transparent to ultraviolet radiation. This allowed photons to travel freely across vast cosmic distances, marking the Universe's transition from an opaque to a transparent state.

Reionization profoundly influenced the subsequent evolution of cosmic structures. The ionization of hydrogen facilitated the transmission of radiation, enabling the formation of galaxies, stars, and other cosmic structures. Additionally, the heating of the IGM affected the dynamics of gas accretion onto galaxies and the formation of their internal structures.

Observational evidence for reionization comes from studies of the cosmic microwave background (CMB), distant quasars, and the Lyman-alpha forest in the spectra

of distant galaxies. These observations provide insights into the timeline and the sources responsible for driving the reionization process.

1.2.7 Post-reionization

Post-reionization denotes the epoch in cosmic history following the completion of the reionization process, which occurred approximately 150 million to one billion years after the Big Bang. This period witnessed significant transformations in the structure and dynamics of the Universe.

One notable consequence of post-reionization was the establishment of a fully ionized intergalactic medium (IGM). Furthermore, post-reionization heralded the era of cosmic dawn, during which the Universe became populated with a diverse array of galaxies, stars, and other astrophysical objects. These newly formed galaxies began to evolve and interact, giving rise to the rich tapestry of cosmic structures observed in the Universe today.

While our understanding of history of cosmic evolution and the constituents of the Universe has advanced significantly, we are still grappling with the challenge of identifying suitable candidates and understanding the characteristics of the predominant components, namely dark matter and dark energy. Despite the well-established theories describing the evolution of the cosmos, our comprehension of these enigmatic entities remains incomplete. In this thesis, our primary focus is to address the dark matter problem, given that it constitutes approximately 26.4% of the Universe's total energy content. Through rigorous investigation and analysis, we aim to shed light on the nature and potential candidates for dark matter, advancing our understanding of its role in shaping the cosmic landscape.

1.3 The Dark Matter Enigma

For decades, the elusive nature of Dark Matter (DM) has remained one of the most significant unresolved mysteries in modern physics. Various models, each proposing different types of particles, have been suggested to explain the formation of structures across different scales. Dark Matter, an enigmatic and non-luminous substance, reveals itself solely through its gravitational interactions with galaxies and stars. Its existence is now well-established, supported by extensive cosmological and astrophysical evidence, indicating that it comprises approximately 26.8% of the Universe's total mass-energy content.

The concept of dark matter was first introduced by Jan Oort in 1932 [29], who sought to explain the vertical motions of stars within the Milky Way. Later, in 1939, Horace Babcock's [30] measurements of the rotation curve of the Andromeda galaxy using optical spectroscopy suggested an increase in the mass-to-luminosity ratio with radial distance. This idea was further reinforced by Swiss physicist Fritz Zwicky, who, in the 1930s, studied the velocity distribution of galaxies within the Coma galaxy cluster [31]. Zwicky's observations highlighted significant discrepancies in the cluster's dynamics that could not be accounted for by visible mass alone. Additionally, observations by Sinclair Smith [32] in 1936 of the Virgo cluster echoed these findings, despite the challenges posed by the limited understanding of various astrophysical complexities at the time, which hindered the confirmation of dark matter's presence.

1.4 Evidence of Dark Matter

The concept of dark matter finds strong support within the realms of cosmology and astrophysics. Numerous astrophysical observations lend credence to the presence of dark matter, primarily grounded in gravitational effects. In the following section, we

outline a handful of the most compelling pieces of evidence supporting the existence of dark matter.

Motion of the Galaxies (Coma and Virgo Cluster)

The exploration into the existence of dark matter on the scale of galaxies and galaxy clusters heavily relies on the interplay between gravitational potential and kinetic energy. Swiss astronomer Fritz Zwicky undertook the task of estimating the dynamical masses of galaxies within clusters by measuring the velocity dispersion using Doppler shifts [31, 33]. In his analysis, he applied the virial theorem to the Coma cluster system. This theorem offers a straightforward relationship between the gravitational potential energy and kinetic energy of a gravitationally bound system.

The Hamiltonian of a non-relativistic, interacting system can be expressed as

$$H = \sum_i^n \frac{p_i^2}{2m_i} + V(r_i), \quad (1.5)$$

where r_i , m_i , v_i , V_i , and p_i represent the position, mass, velocity, potential energy, and momentum of the i^{th} particle, respectively. The notation $\langle \dots \rangle$ denotes averaging over time (Eq. 1.8). From eq. 1.5, we can deduce the relation

$$2T + U = 0, \quad (1.6)$$

where T and U denote kinetic energy and potential energy, respectively.

Assuming a spherically symmetric distribution of galaxies, the total gravitational potential of the galaxy cluster (regarded as a self-gravitating system) with mass M and radius R containing the galaxies is given by

$$U = -\frac{3}{5} \frac{GM^2}{R}. \quad (1.7)$$

Each galaxy in the cluster possesses certain velocities. Therefore, the total kinetic energy of the galaxy cluster can be expressed as

$$T = \frac{1}{2} M \langle v^2 \rangle, \quad (1.8)$$

where $\langle v^2 \rangle$ represents the average of the square of the velocities of galaxies within the cluster. By utilizing eq. 1.7 and eq. 1.8, one can estimate the total mass of the galaxy cluster, dependent on the radius R and the average velocity $\sqrt{\langle v^2 \rangle}$. Zwicky estimated the average velocity from seven galaxies in the Coma Cluster using Doppler shift [31, 33], yielding a mass of approximately $M \approx 1.9 \times 10^{13} M_{\odot}$. However, Zwicky derived a mass of $M \approx 8.0 \times 10^{11} M_{\odot}$ for the Coma Cluster based on the assumption of the stellar populations within the galaxy, which is approximately 400 times smaller than the previous estimation. Modern observations and methods allow for a more precise estimation of the Coma Cluster mass, yielding $\cong 1.6 \times 10^{14} M_{\odot}$ for a Hubble parameter $h = 0.673 \pm 0.012$, significantly larger than the previous estimate.

In 1936, Sinclair Smith conducted a similar investigation into the mass of the Virgo cluster [32], comprising several elliptical and lenticular galaxies. Smith's conclusions echoed those of Zwicky [32, 33]. Consequently, it can be inferred that these galaxy clusters (Coma Cluster and Virgo Cluster) harbor a substantial amount of invisible mass distribution, potentially constituting dark matter candidates.

Flattening of Rotation Curves of Spiral Galaxies

One of the most compelling pieces of evidence supporting the presence of Dark Matter (DM) within galaxies arises from the examination of their rotation curves, particularly those of spiral galaxies. These galaxies comprise various components,



Figure 1.4: (a) Galaxies inside the Coma Cluster (Photo credit: NASA/JPL-Caltech/L. Jenkins (GSFC)).
(b) Virgo Cluster (Photo credit and copyright: Rogelio Bernal Andreo, deepskycolors.com).

including a flat, rotating disc housing newly formed stars and interstellar matter, a central bulge composed of older stars with a supermassive black hole at its core, and near-spherical halos of stars. Additionally, the spiral arms of such galaxies extend from the center to the disc. In 1975, renowned American astronomer Vera Florence Cooper Rubin, along with fellow astronomers W. Kent Ford Jr. and Norbert Thonnard, brought to light a groundbreaking revelation [34]. Their investigation into the rotational curves of numerous spiral galaxies unveiled striking disparities between observed curves and those calculated solely based on the visible components of the galaxies. Their extensive studies led to the widespread acceptance of the existence of galactic dark matter. Notably, as early as 1959, Louise Volders had also identified similar inconsistencies, as illustrated in the case of the M33 galaxy (refer to fig. 1.5).

The rotation curve, or velocity curve, of a spiral galaxy illustrates the variation in orbital circular velocity of stars or gas clouds at different distances from the center. Analyses of the rotation curves of galaxies involve studying the relationship between the rotational velocity ($v(r)$) of a star within the galaxy and its radial distance (r) from the center.

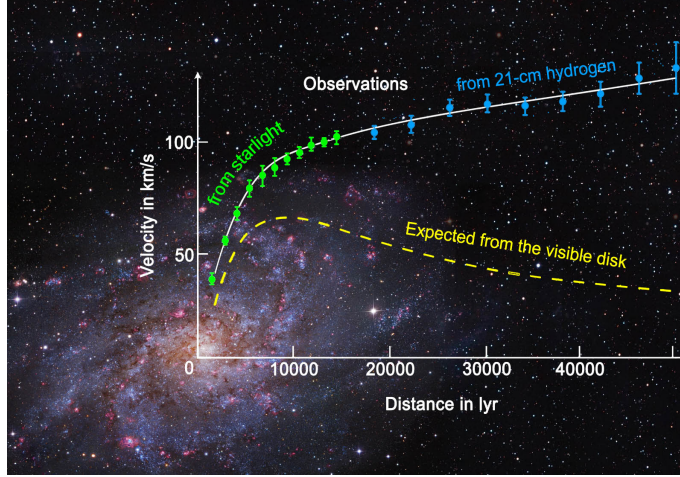


Figure 1.5: Galaxy rotation curve of Messier 33. The yellow dashed line is the expected line from the visible disk, while the solid line represents the fitted line of observed points [35].

To investigate these rotation curves, scientists measure the velocities of neutral hydrogen at varying distances by observing the Doppler shift of emission lines, such as hydrogen alpha in optical wavelengths or neutral hydrogen 21 cm in radio frequencies. By assuming spherical symmetry of the dark matter halo and applying Newtonian dynamics, specifically the law of circular motion, to the circular motion of a star, a balance between gravitational and centrifugal force fields can be expressed as

$$\frac{m_* v(r)^2}{r} = G \frac{M(r) m_*}{r^2}$$

or,

$$v(r) = \sqrt{\frac{GM(r)}{r}}. \quad (1.9)$$

In the equations above, m_* represents the mass of a star orbiting the galactic center at a radius r , and $M(r)$ denotes the mass encompassed within a spherical region of radius r around the galactic center, given by $M(r) = \int_{\text{sphere}} \rho dV$, where V is the volume and ρ is the average density of the central bulge of the galaxy. Eq. 1.9 suggests that the circular velocity $v(r) \propto r$ within the central bulge. Conversely, outside the central bulge, the velocity varies with r as $v(r) \propto 1/\sqrt{r}$ (illustrated by

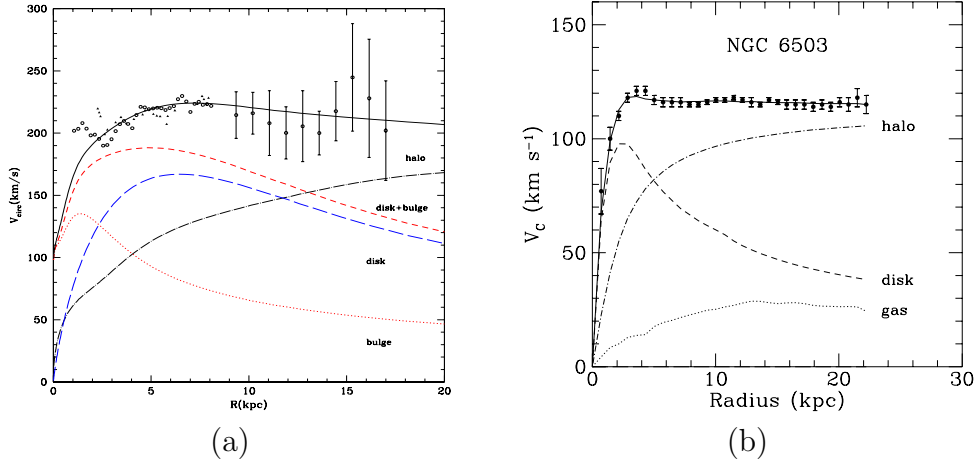


Figure 1.6: Galactic rotation curve of (a) Milky Way galaxy (Figure from Ref. [36]), (b) NGC 6503 galaxy (Figure from Ref. [37, 38].)

the yellow dashed line in fig. 1.5), considering that almost the entire mass of a spiral galaxy resides within the central bulge. However, observational evidence indicates that for higher values of r , $v(r) \propto r^0$ (refer to fig. 1.6a [36], fig. 1.6b [37, 38] and fig. 1.5 [35]). Consequently, an additional distribution of invisible matter must exist, influencing the nature of the rotation curve. This invisible or dark matter is believed to manifest in the form of a “dark matter halo.” The density profile of the galactic dark matter halo can be inferred by accommodating an approximately flat rotational curve, as deduced from observational evidence.

Cosmic Microwave Background

The most precise determination of the quantity of dark matter originates from observations of the cosmic microwave background (CMB). Serving as an echo of the moment when photons disengaged from matter in the early Universe, the CMB holds crucial information. This phenomenon was initially foreseen by Gamow in 1948 [39, 40] and serendipitously detected by Penzias and Wilson in 1965 [41, 42].

The CMB presents itself as a faint glow in microwave radiation, pervading the entire cosmos with almost perfect uniformity. Arising from the residual heat of the Big

Bang, the CMB emerged as thermal radiation once the Universe cooled sufficiently to become transparent to light and other electromagnetic waves, approximately 380,000 years post-Big Bang. During this epoch, the Universe brimmed with a hot, ionized gas.

Initially, the CMB did not manifest primarily as visible or ultraviolet light. However, over billions of years, the expansion of the Universe caused this radiation to undergo redshift, progressively stretching its wavelengths until it settled in the microwave band. Peaking at a wavelength of approximately 2 mm, the CMB boasts an almost ideal blackbody spectrum, corresponding to a temperature of 2.73 K.

Despite its remarkable uniformity, subtle polarizations and temperature fluctuations exist within the CMB. These faint features provide invaluable insights into the early Universe. Despite its near-perfect uniformity, this gas exhibits minute deviations (around 1 part in 10^5) from homogeneity. By scrutinizing the slight intensity variations of the CMB across the celestial sphere, with deviations of 1 part in 10^5 , researchers construct a detailed map of the early Universe [43, 44].

The data gathered from satellite-borne experiments such as Planck [5, 45] and WMAP (Wilkinson Microwave Anisotropy Probe) [2] provide crucial insights into the spectral anisotropies of the cosmic microwave background (CMB) (Fig. 1.7). These anisotropies, expressed in terms of spherical coordinates (θ, ϕ) , can be represented as,

$$\frac{\delta T}{T}(\theta, \phi) = \sum_{l=2}^{\infty} \sum_{m=-l}^l a_{lm} Y_{lm}(\theta, \phi). \quad (1.10)$$

The variance of the term $a_{lm} Y_{lm}(\theta, \phi)$ can be estimated as

$$C_l \equiv \langle |a_{lm}^2| \rangle \equiv \frac{1}{2l+1} \sum_{m=-l}^l |a_{lm}|^2. \quad (1.11)$$

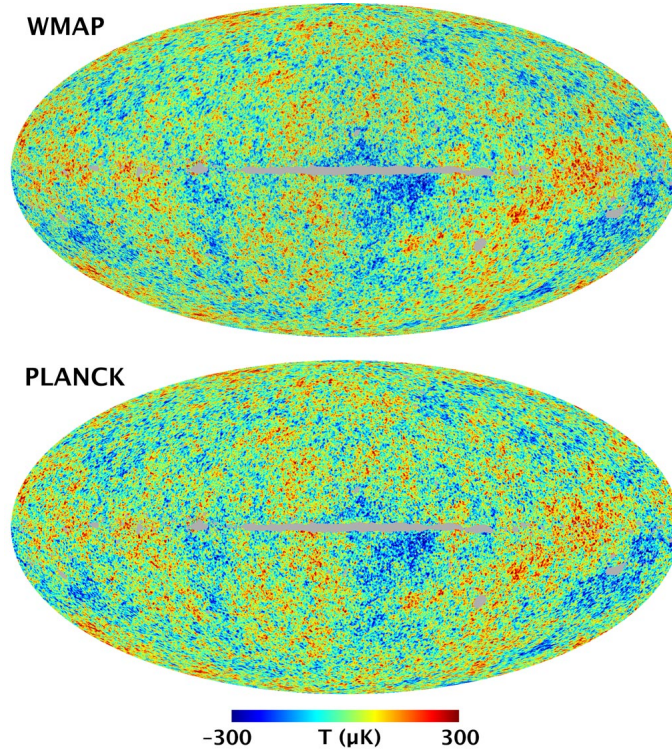


Figure 1.7: The all-sky cosmic microwave background radiation map from WMAP and Planck data. Both images show a temperature fluctuations of $\pm 300 \mu\text{K}$ around the average temperature 2.73 K . The top image represents the WMAP W-band CMB map while the bottom image is the Planck SMICA CMB map. (Photo credit: NASA / WMAP Science Team.)

Fig. 1.8 illustrates the variation of C_l (expressed as $l(l+1)C_l/2\pi$) with the multipole moment l . The red line represents the best-fitted spectra, while the black error bars depict the nine-year WMAP data points [2]. The shape of the power spectrum is influenced by the oscillations of the primordial hot gas, with the amplitude and frequency determined by its composition.

This demonstrative graph (Fig. 1.8) offers valuable insights into the constituents of the Universe. For instance, the ratio of heights between the first and second peaks provides information about the abundance of baryons (excluding baryonic dark matter), while the position of the first peak indicates the curvature of the Universe. Conversely, the third peak holds significance for various aspects related to dark matter.

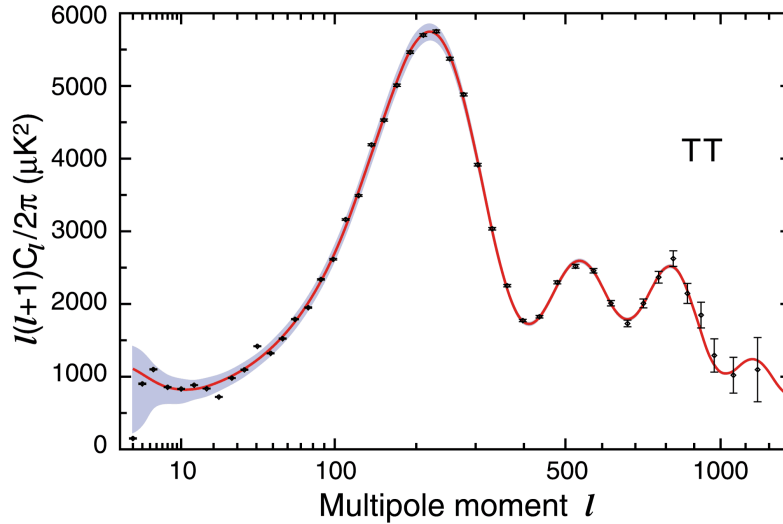


Figure 1.8: The TT (temperature-temperature) angular power spectrum from nine-year WMAP data. The WMAP data are represented by black points and corresponding error bars. The red line describing the best fit model. The smoothed binned spectral function is shown using the gray region. (Photo credit: NASA / WMAP Science Team. [2])

Bullet Cluster

The observation of galaxy clusters such as 1E0657-56 and 1E0657-558, commonly known as the Bullet Cluster [46, 47], stand as one of the most compelling pieces of evidence for the existence of dark matter [48]. The Bullet cluster comprises of two distinct clusters of galaxies that had undergone a collision event. The name “Bullet” arises from the dynamic interaction where a smaller subcluster traverses through the core of a larger subcluster, resembling the trajectory of a focussed bullet.

During this collision, the observable components of the clusters, including gas, galaxies, and stars, exhibit distinct behaviour from the elusive dark matter. However, the hot gas within the clusters, observable through X-ray telescopes, predominantly interacts electromagnetically due to its baryonic nature.

Consequently, the Bullet Cluster serves as a prominent example of dark matter lensing, providing compelling evidence for the presence of dark matter over alternative

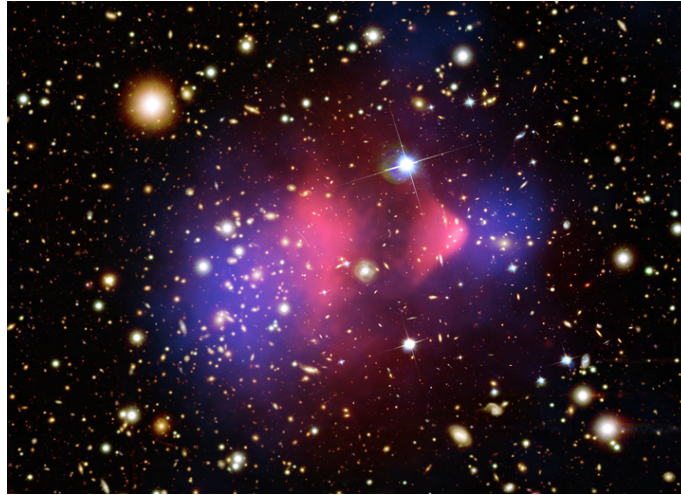


Figure 1.9: The Bullet Cluster
(Photo credit: NASA/CXC/CfA/M.Markevitch et al. [46])

hypotheses such as Modified Newtonian Dynamics (MOND) [49, 50] when applied to large galactic clusters.

Furthermore, the spatial offset observed between the center of total mass and the peaks of baryonic mass within the cluster, with a statistical significance of 8σ CL (confidence level), cannot be solely explained by modifications to gravitational forces. In theories like MOND, where dark matter is absent, the lensing effect would be expected to track the distribution of baryonic matter, such as the X-ray-emitting gas. However, observations reveal the strongest lensing effects occurring in two distinct regions near, and possibly coincident with, the locations of visible galaxies.

This discrepancy suggests that the majority of the mass in the cluster pair exists in the form of two regions of dark matter that have decoupled from the gas regions during the collision. These observations align with predictions of dark matter particles being weakly interacting in nature, apart from gravitational interactions, further bolstering the case for the existence of dark matter as a fundamental component of the Universe.

Multi-wavelength observations of the Bullet Cluster have yielded compelling evidence supporting the existence of dark matter. These observations reveal that during a high-velocity collision (approximately 4500 km/s [51]) between two clusters, the shape of the baryonic (visible) mass distribution undergoes significant perturbation, as depicted by the pink region in fig. 1.9. In stark contrast, the dark matter halos of the clusters pass through each other largely undisturbed.

The identifications of these invisible dark matter halos for the two clusters were made possible through the method of gravitational lensing. This phenomenon underscores the non-interacting nature of dark matter particles. While dark matter particles interact gravitationally with each other, the impact on the dark matter halos of the colliding clusters remains minimal. This is because the halos are expansive, resulting in low dark matter density within them, and thus insufficient gravitational influence to alter their shapes significantly.

Consequently, a substantial amount of dark matter concentrated in the blue zone, responsible for gravitational lensing, serves as strong evidence for non-interacting dark matter. This phenomenon is not unique to the Bullet Cluster; a similar observation has been documented at the MACS J0025.4-1222 cluster [52].

Gravitational Lensing

According to the principles of General Relativity, the presence of mass induces curvature in the surrounding space, defining what's known as geodesics. This curvature leads to the bending of light rays as they traverse through the gravitational field of massive objects. This phenomenon is referred to as gravitational lensing [54] (see fig. 1.10). Consequently, light from background objects can be lensed by foreground masses, resulting in the deflection of light rays towards an observer. In scenarios where an observer is situated in the foreground of such a lensing massive body, multiple or distorted images of background objects may be visualized. It was first

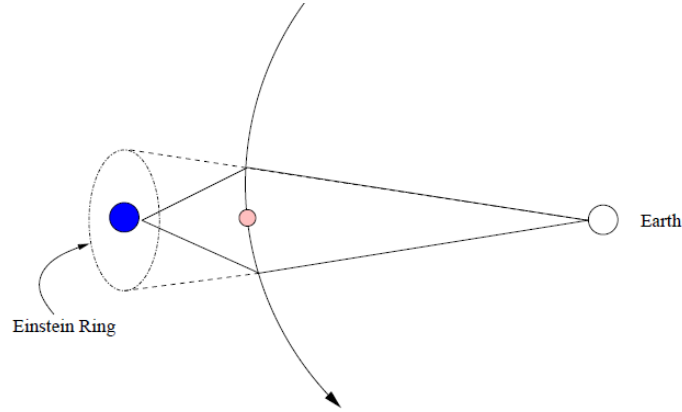


Figure 1.10: Bending of incoming light due to the gravitational field of a massive object. The dashed lines show the apparent position of the light source. [53]

proposed by Henry Cavendish in 1784 and subsequently addressed by Johann Georg von Soldner in 1804 within the framework of Newtonian gravity [54]. However, it was Albert Einstein who, in 1915, mathematically formalized this concept as part of his theory of relativity. The validation of gravitational lensing occurred on May 29th, 1919, when A. Eddington and F. Dyson confirmed Einstein’s predictions. The discovery of the ‘Twin Quasar’ (SBS 0957+561) was the first confirmed instance of gravitationally lensed objects [55], underscoring the significance of gravitational lensing in understanding the cosmos. Gravitational lensing can be categorized into three classes: strong, weak, and microlensing. Strong lensing occurs when the deflection of light is substantial due to the intense gravitational field of massive objects situated between the observer and the distant background object. This can result in observable effects such as multiple images, arcs, or even the formation of Einstein-Chwolson rings when the alignment between the distant object, lensing mass, and observer is precise (see fig. 1.11a and 1.11b). This Einstein ring has an angular separation given by

$$\theta_{\text{EC}} = \sqrt{\frac{4GM}{c^2} \frac{d_{\text{LS}}}{d_{\text{L}}d_{\text{S}}}}, \quad (1.12)$$

where G , c , and M represent the universal gravitational constant, the velocity of light in space, and the mass of the lensing body, respectively. Here, d_{L} and d_{S} denote

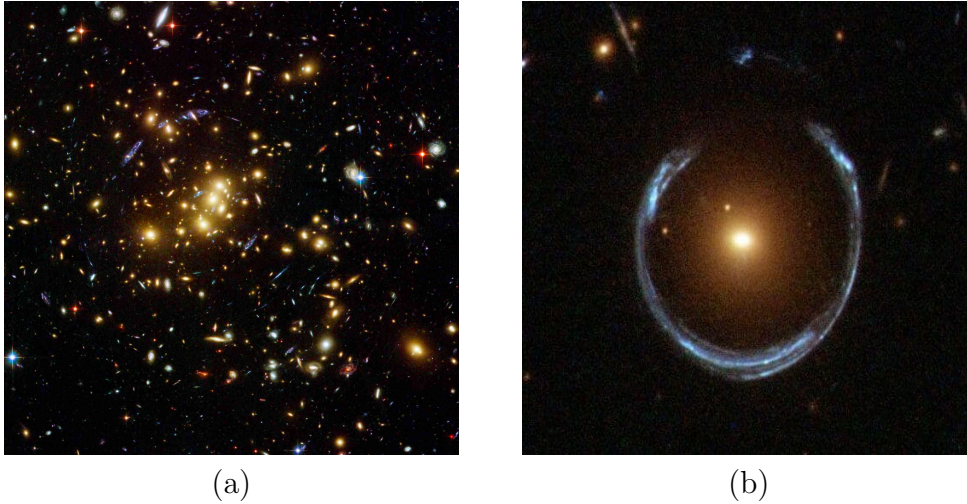


Figure 1.11: (a) The galaxy cluster CL0024+1654 produces multiple images of a distant blue galaxy (Photo credit: NASA, ESA, H. Lee & H. Ford (Johns Hopkins U.))[56]. (b) Horseshoe Einstein Ring from Hubble. The gravitational field of the red galaxy LRG 3-757 lenses the incoming light from a distant blue galaxy (Photo credit: ESA/Hubble, NASA).

the distances from the observer to the lensing body and to the background source, respectively, while $d_{LS} = d_S - d_L$.

Weak lensing, on the other hand, involves slight deflections of light rays due to the gravitational field (Fig. 1.12), insufficient to produce distinct images or arcs. Instead, it results in subtle distortions of background sources, requiring statistical analysis across a large number of sources to reconstruct the mass distribution effectively [54].

Microlensing, the third category, occurs when low-mass objects, such as planets or stars, pass between the observer and a background source. Although the deflection of light is challenging to detect directly, variations in the brightness of the background object as the lensing mass passes by can reveal the presence of the lensing mass (Fig. 1.13). Overall, gravitational lensing serves as a powerful tool for probing the distribution of mass in the cosmos, offering invaluable insights into the nature of dark matter and the dynamics of the Universe at large. Details analysis of effect of gravitational lensing is described in Sec. 7.

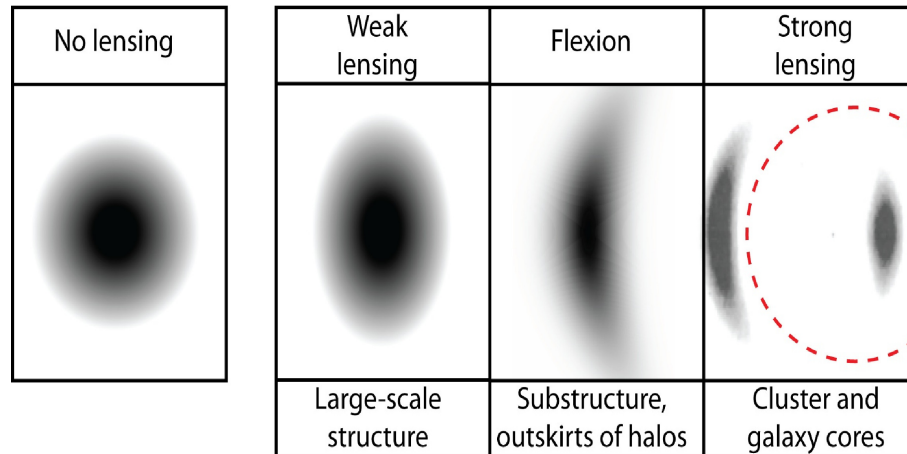


Figure 1.12: The different regimes of gravitational lensing image distortion. The effect of lensing due to the passage of massive galaxies or clusters of galaxies results several distortions of the image of the circular source (in black and grey shadow) appeared to the observer [57]

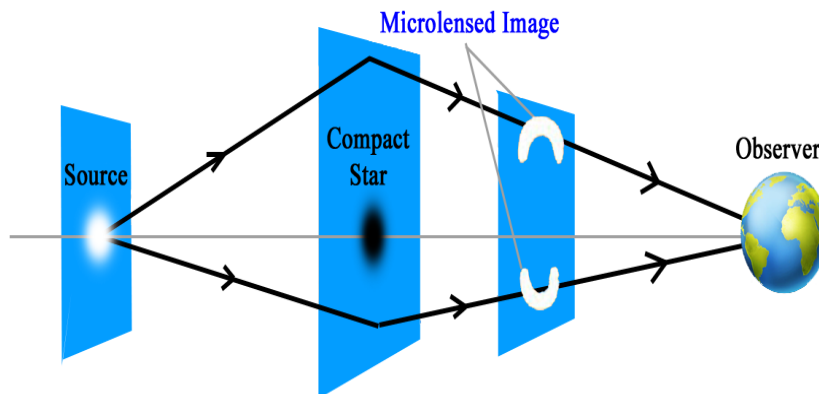


Figure 1.13: Schematic diagram of gravitational microlensing.

The Large Scale Structure of the Universe

Despite the theoretical premise of a homogeneous and isotropic Universe, the vast expanse of the Universe exhibits a rich tapestry of structures, ranging from galaxies to clusters and superclusters, all interconnected within a cosmic web of sheets, filaments, and voids (as depicted in fig. 1.14). These intricate formations have been meticulously explored through extensive surveys such as the 2-degree Field Galaxy Redshift Survey (2dF-GRS) [58, 59] and the Sloan Digital Sky Survey (SDSS)

(Fig. 1.14) [12]. Their arrangement reflects the gravitational clustering of matter since the inception of the Big Bang.

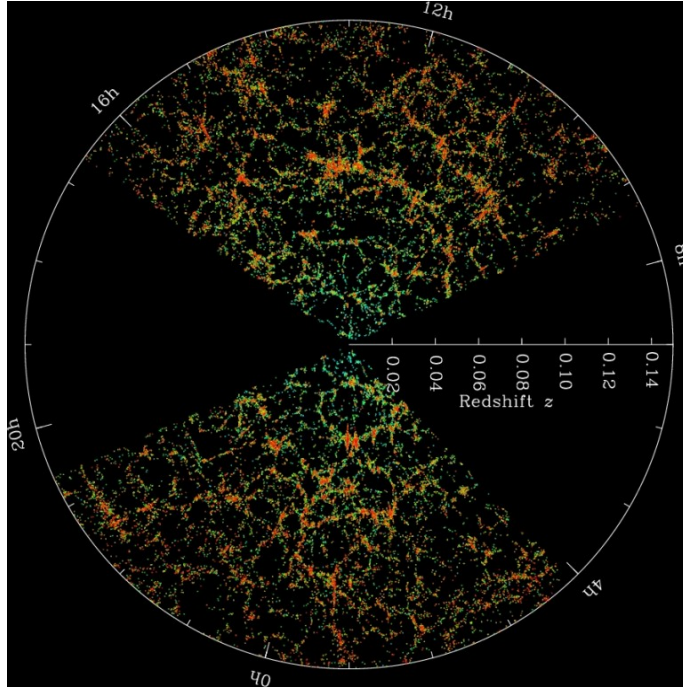


Figure 1.14: The map of galaxies discovered by Sloan Digital Sky Survey (SDSS) showing the large-scale structure of the Universe. The radial distance from the centre of the circle representing the redshifts of the corresponding galaxies. (Photo credit: M. Blanton and SDSS)

Cosmological simulations like Millenium [60], NFW [61], Aquarius [62] and many more like these vividly illustrate that the observed large-scale structure of luminous baryonic matter could only have arisen in the presence of a substantial amount of dark matter (reference fig. 1.15). Furthermore, to replicate the observed structures accurately, the majority of dark matter must exhibit characteristics of being cold and non-dissipative.

“Cold” dark matter particles are characterized by their non-relativistic motion and short free-streaming lengths, facilitating gravitational accumulation on small scales. This property enables them to serve as seeds for the formation of galaxies. Conversely, hot and warm dark matter, although potentially present in smaller fractions, lack the capacity to initiate such gravitational collapse effectively.

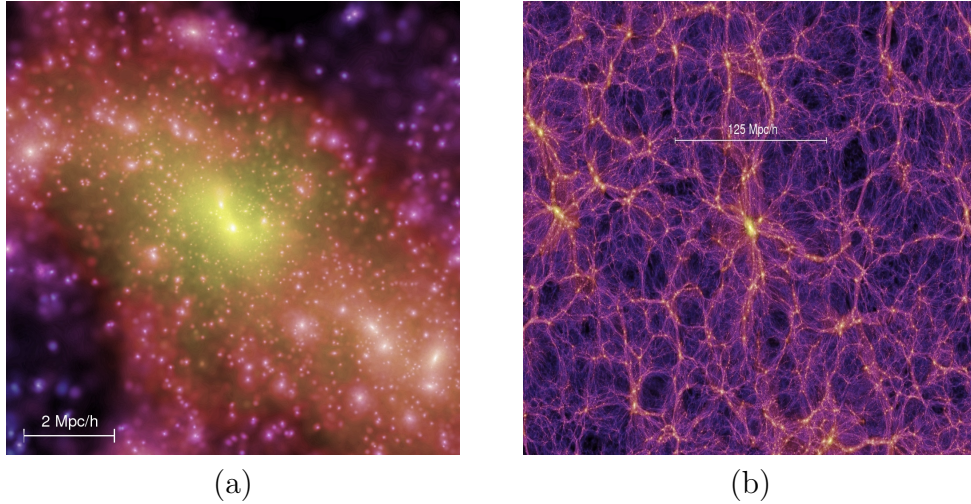


Figure 1.15: The images give the dark matter distributions at large scale in the Universe obtained in the Millennium simulation. From the Millennium Simulation Project webpage.

URL : <https://wwwmpa.mpa-garching.mpg.de/galform/virgo/millennium/>

Large-scale surveys offer insights into the distribution and composition of matter in the Universe. They reveal that the total matter density, encompassing both dark and luminous matter, is estimated to be approximately $\Omega_m \approx 0.315$. This density parameter holds crucial implications for the formation and evolution of cosmic structures.

Big Bang Nucleosynthesis

Big Bang nucleosynthesis (BBN) [20, 19, 21] is a pivotal epoch in the early Universe, occurring roughly between 1 second to 20 minutes after the Big Bang, when atomic nuclei were synthesized from protons and neutrons. During this brief period, the conditions were just right for nuclear fusion to occur, leading to the formation of the lightest elements in the periodic table. The synthesis of these elements laid the foundation for the chemical composition of the Universe as we know it today.

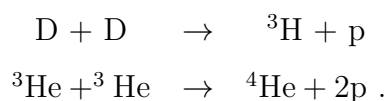
In the first few seconds, the Universe was incredibly hot and dense, with temperatures exceeding billions of degrees Celsius. In this early stages of the Universe,

atomic nuclei struggled to form due to extreme temperatures and densities. Instead, the space was filled with a seething mix of protons, neutrons, electrons, photons, and various short-lived particles. Occasionally, protons and neutrons collided and fused to create deuterium nuclei, which are heavier isotopes of hydrogen. However, the intense energy from high-temperature photons promptly disrupted these nascent nuclei, preventing their stable formation.

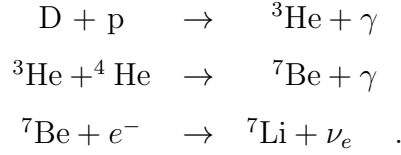
As the Universe progressed and its temperature gradually decreased, the prevalence of high-energy photons diminished, allowing deuterium nuclei to persist. The crucial factors governing Big Bang Nucleosynthesis (BBN) were the temperature and density of the Universe. These conditions played a vital role in overcoming the electromagnetic repulsion between positively charged protons, enabling them to come close enough for the strong nuclear force to bind them together. As the temperature dropped to approximately 100 keV, the fusion of protons (p) and neutrons (n) commenced, resulting in the formation of nuclei for several light elements. One of the first nuclear reactions was the synthesis of deuterium (a deuteron), which is a nucleus consisting of one proton and one neutron. This reaction primarily occurred through the collision of two protons, leading to the capture of a neutrino,



Helium-4, the most abundant element after hydrogen, was synthesized through a sequence of reactions involving the fusion of deuterium nuclei. This process typically involved the addition of two protons to a deuterium nucleus to form helium-4,



Helium-3, although less abundant than helium-4, was also produced during BBN through various reactions involving the fusion of deuterium and helium-3 nuclei,



From the above-mentioned reactions, we can infer that helium-4 (${}^4\text{He}$) emerged as the most abundant element, constituting around one-fourth of the mass fraction. Additionally, small amounts of deuterium (D), tritium (${}^3\text{H}$), lithium-6 (${}^6\text{Li}$), lithium-7 (${}^7\text{Li}$), and beryllium-7 (${}^7\text{Be}$) nuclei were also generated during this phase. This process of nuclei synthesis is known as “Big Bang Nucleosynthesis” (BBN).

One of the critical factors determining the outcome of BBN was the baryon-proton ratio (η), which influenced the synthesis of different elements. As the Universe expanded and cooled, the neutron-proton ratio decreased, affecting the types and abundances of nuclei produced. Baryon-to-photon ratio (η), which directly correlates with the baryon abundance of the Universe (Ω_b) which is $\eta \propto \Omega_b h^2$, where h represents the Hubble parameter, given by $h = H_0/(100, \text{km}, \text{s}^{-1}, \text{Mpc}^{-1})$ ⁱ⁾. Hence, the initial value of Ω_b can be determined through Big Bang Nucleosynthesis (BBN) by examining the actual primordial abundances of elements and accurately measuring h . Nevertheless, estimating the primordial abundances of light isotopes poses challenges, necessitating direct observations of exceptionally primitive systems.

As the Universe undergoes expansion, the pace of nucleosynthesis gradually decelerates until it ceases entirely a few minutes after the Big Bang, given the short lifespan of free neutrons (approximately 15 minutes). Consequently, the cosmic abundance of isotopes like ${}^2\text{H}$, ${}^3\text{He}$, ${}^4\text{He}$, and ${}^7\text{Li}$ stabilizes during this phase. However, following the cosmic dark age, the abundance of these light elements experiences perturbation due to stellar nucleosynthesis. Additionally, heavier elements such as C, N, O, and Fe are synthesized through this stellar process. Consequently, astrophysical environments with low metallicities serve as ideal candidates for investigating the primordial abundances of these light elements.

ⁱ⁾The baryon-to-photon ratio η is defined as $\eta \equiv \Omega_b h^2$, where h represents the Hubble parameter, given by $h = H_0/(100, \text{km}, \text{s}^{-1}, \text{Mpc}^{-1})$

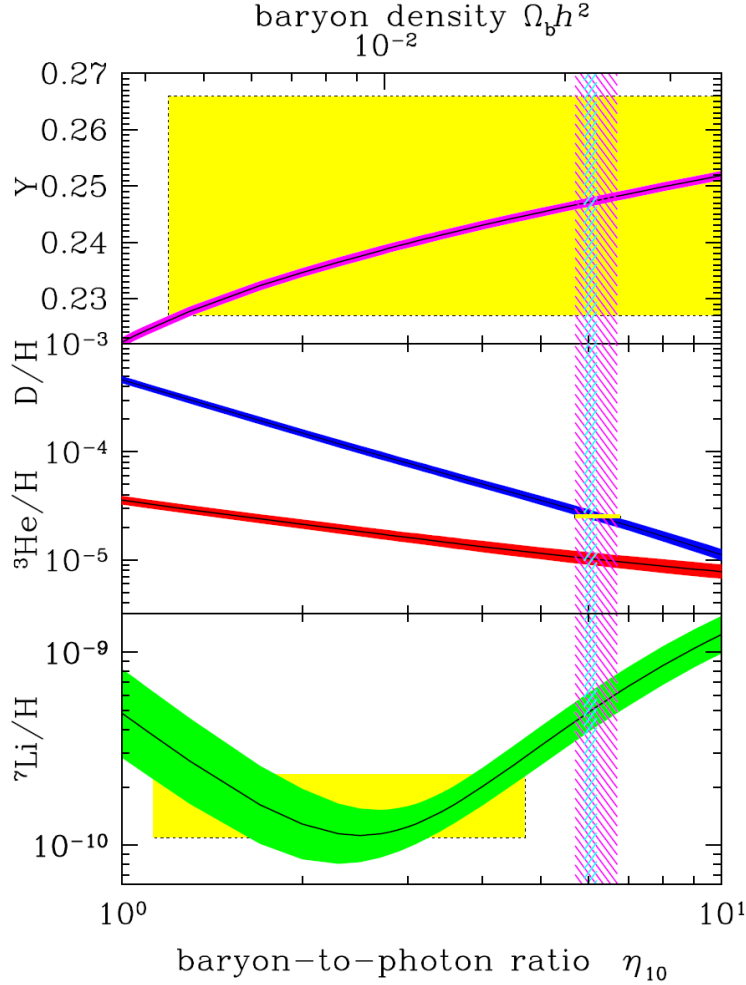


Figure 1.16: The predicted abundances of ${}^2\text{H}$, ${}^3\text{He}$, ${}^4\text{He}$, ${}^7\text{Li}$ according to the standard model of Big Bang Nucleosynthesis (BBN). The bands denote the range of 95% confidence level (CL) for different values of (η) . The yellow boxes in this plot represent the range of the observed abundances for those light elements. The pink (wide) vertical band denotes the BBN concordance range, while the blue (narrow) band indicates the CMB measure of the cosmic baryon density (From Ref. [63]).

Various theoretical and experimental studies have explored the primordial abundances of different baryonic elements as a function of η [64, 65]. The predicted data from nucleosynthesis indicates that, for $\eta \approx 6 \times 10^{-10}$, the calculated baryonic density amounts to 0.04 times the critical density of the Universe [66]. Such baryon density can be estimated much consistently from the measured abundances of deuterium and the helium isotopes. However, discrepancies arise for the lithium

isotopes, particularly lithium-7 (${}^7\text{Li}$), which is found to be under-abundant relative to the BBN predictions. Moreover, lithium-6 (${}^6\text{Li}$) is not expected to have been produced in BBN at all. These discrepancies may be resolved by considering non-standard BBN scenarios influenced by particle physics beyond the Standard Model, including certain dark matter models [67].

Various theoretical and experimental studies have explored the primordial abundances of different baryonic elements as a function of η (refer to fig. 1.16) [64, 65]. The predicted data from nucleosynthesis indicates that, for $\eta \approx 6 \times 10^{-10}$, the calculated baryonic density amounts to 0.04 times the critical density of the Universe [66]. However, observations of large-scale structure formation suggest that the matter density parameter is significantly higher ($\Omega_m \approx 0.29$) than this value. Consequently, the remaining portion of matter must exist in the form of dark matter. Furthermore, based on this estimation, it can be inferred that the predominant portion of dark matter is non-baryonic, exhibiting no interaction with electromagnetic fields. Nevertheless, there may still be a minor fraction of baryonic dark matter present in the form of low-luminosity astrophysical entities.

The presence of dark matter is indisputably inferred through independent measurements of Ω_m from large-scale structure formation and Ω_b from BBN. Since all luminous matter should be part of the baryonic matter content of the Universe, the difference between the measured quantities Ω_m (approximately 0.29) and Ω_b (approximately 0.04) implies that the leftover matter ($\Omega_{\text{leftover}} \approx 0.25$) must exist in the form of dark matter in the Universe. Moreover, this suggests that dark matter particles must predominantly be non-baryonic, lacking electromagnetic interaction and being dissipationless. It is important to note that a small portion of dark matter may be baryonic in nature.

X-ray Observation

One potential approach to investigate dark matter within galaxies and galaxy clusters involves probing their gravitational potential using X-ray observations. Galaxy clusters have enormous X-ray emitting gas inside them. These observations can also provide insights into the density distribution of the galaxy. To theoretically evaluate this technique, let us consider a scenario where a thin shell of hot X-ray emitting gas surrounds the galaxy, comprising stars, gas, and dark matter. The gravitational force exerted by the enclosed mass (including gas, stars, and dark matter) acts to pull the gas shell inward. Conversely, if the pressure within the gas shell decreases outward, it exerts an outward force. These opposing forces reach equilibrium in a state known as hydrostatic equilibrium, allowing estimation of the galaxy's gravitational mass through analysis of pressure gradients from X-ray observations. Any disparity between the gravitational mass and the visible mass of the galaxy could then indicate the presence of dark matter [68].

Let us consider the hypothetical scenario of an elliptical galaxy being spherically symmetric for simplicity. The gravitational force acting on the shell of hot gas at radius r (with width dr) due to the enclosed mass is given by

$$F_g(r) = \frac{GM(< r)M_s}{r^2} \quad (1.13)$$

Here, $M_s = 4\pi r^2 \rho_{\text{gas}}(r)dr$ represents the mass of the hot gas shell, where $M(< r)$ denotes the total enclosed mass inside the shell (including stars, gas, and dark matter), and dr is the shell's thickness. The pressure force on the surface, $F_p(r)$, can be expressed as

$$F_p(r) = 4\pi r^2(p(r) - p(r + dr)) = -4\pi r^2 \frac{dp}{dr} \quad (1.14)$$

In a state of hydrostatic equilibrium, the gravitational force and the pressure force balance each other, leading to the equation

$$\frac{GM(< r)}{r^2} = -\frac{1}{\rho_{\text{gas}}(r)} \frac{dp}{dr} \quad (1.15)$$

This equation can also be expressed in terms of gravitational potential (Φ) as

$$\nabla\Phi = -\frac{\nabla p}{\rho_{\text{gas}}} \quad (1.16)$$

The temperature of the hot gas ($T_{\text{gas}}(r)$) can be determined by modeling the X-ray spectrum as a function of position. Utilizing the fact that X-ray intensity is proportional to $\rho_{\text{gas}}^2 T_{\text{gas}}$, the radial gas density $\rho_{\text{gas}}(r)$ can be estimated. The pressure p is proportional to $\rho_{\text{gas}} T_{\text{gas}}$, and can be represented as

$$p = \frac{k_B T_{\text{gas}}}{\mu m_H} \rho_{\text{gas}} \quad (1.17)$$

Substituting the expression for p into the equilibrium equation, we obtain

$$\frac{1}{\rho_{\text{gas}}} \frac{dp}{dr} = \frac{k_B T_{\text{gas}}}{\mu m_H} \frac{1}{r} \frac{d \ln \rho_{\text{gas}}}{d \ln T_{\text{gas}}} + \frac{GM(< r)}{r^2} \quad (1.18)$$

The gravitational potential and mass distribution can be reconstructed from this equation. Additionally, an approximate expression for the density profile can be obtained if T_{gas} remains approximately constant. Assuming T_{gas} is constant, the right-hand side of the equation simplifies, leading to

$$\rho_{\text{tot}}(r) = \rho_0 \left(\frac{r_0}{r}\right)^{-2} \quad (1.19)$$

This enables a measurement of T_{gas} to constrain the total mass density ρ_{tot} . The stellar mass density (ρ_*) can be estimated from luminosity, and the gas density (ρ_{gas}) from X-ray emissivity. Consequently, the density of dark matter (ρ_{DM}) can also be

determined by subtracting ρ_{tot} , ρ_* , and ρ_{gas} . Detailed modeling using this method confirms that elliptical galaxies primarily consist of dark matter.

The hydrostatic equilibrium method, offering advantages over optical mass determination, has been utilized to determine the total gravitational mass and density distribution of galaxies. However, most X-ray observations of clusters lack spectral resolution, providing precise measurements of density rather than temperature. Notably, this method has been successfully applied to the M87 galaxy in the Virgo cluster [68], revealing a significant presence of dark matter. Yet, it remains unclear whether the dark matter halo is centered around the M87 galaxy or distributed throughout the entire cluster.

This approach has also been employed to estimate the mass of other clusters such as Coma and Perseus. The total mass of the Coma cluster, as derived by Hughes (1989) [69], lies within $2 \times 10^{15} M_{\odot}$, with a mass-to-light ratio $L_{\text{MB tot}}$ around $165 M_{\odot}/L_{\odot}$. However, estimated values carry high uncertainty due to limited spectral and spatial resolutions.

Lyman-alpha Forest

The Lyman-alpha ($\text{Ly}\alpha$) system serves as a valuable tool in cosmology [70, 71], providing insights into various physical phenomena, including the properties of dark matter. When an electron transitions from a higher energy state to the ground state in a hydrogen atom, Lyman-alpha spectral lines are emitted. Conversely, when hydrogen atoms encounter electromagnetic radiation of appropriate energy, the atoms absorb the energy, resulting in absorption lines in the spectrum. The large amount of neutral hydrogen in the intergalactic medium leads to a series of absorption lines, forming what is known as the Lyman-alpha forest (Fig. 1.17).

Discovered in 1970 by astronomer Roger Lynds during observations of the quasar 4C05.34 [72], the Lyman-alpha forest initially appeared to originate from interactions within Quasi Stellar Objects (QSOs) [73]. However, subsequent studies confirmed that it arises from the absorption of interstellar gas distribution in superclusters. The intensity of received spectra reveals dips at specific wavelengths,

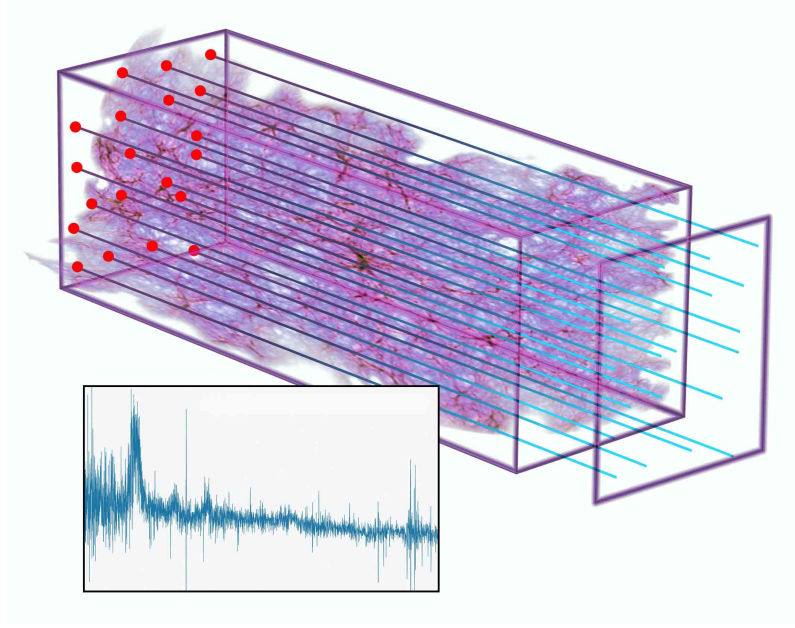


Figure 1.17: Lyman-alpha Forest. Light rays from distant quasars (red dots) get partially absorbed as they pass through hydrogen gas of IGM. As a result, several absorption lines of hydrogen manifests in the spectrum of those quasar (the graph in this figure) as observed by telescope. (Photo Credit: Zosia Rostomian, Lawrence Berkeley National Laboratory; Nic Ross, BOSS Lyman-alpha team, Berkeley Lab; and Springel et al., Virgo Consortium and Max Planck Institute for Astrophysics.)

indicating absorption due to neutral hydrogen. This absorption, known as optical depth, depends on the probability of hydrogen absorbing photons and the number of hydrogen atoms along the photon's path. The Lyman-alpha forest is observed in the spectra of distant, high-luminosity objects such as quasars, which emit various electromagnetic radiations.

As the Universe expands, photons emitted by quasars experience redshifts, causing the observed Lyman-alpha absorption lines to be redshifted as well. Consequently,

the Lyman-alpha forest provides information about the neutral hydrogen content of the intergalactic medium, allowing researchers to trace the positions of intervening hydrogen regions.

Before the proposal of dark matter, absorption systems were thought to be discrete gas clouds confined by the pressure of a hotter intercloud medium. However, this model failed to reproduce observed column densities and evolution with redshifts. The presence of dark matter, interacting gravitationally with interstellar matter, influences the formation of large-scale structures, which can be observed through the Lyman-alpha forest.

Cosmological simulations based on hierarchical structure formation models confirm the existence of cosmic web-like structures associated with the Lyman-alpha forest, further supporting the role of dark matter in structure formation. Additionally, observations of the forest disfavor the scenario of hot dark matter.

1.5 Nature of dark matter

While the precise identity and behavior of dark matter (DM) remain elusive, its existence is supported by various astrophysical observations primarily through gravitational effects. DM can be categorized based on several key aspects

- **Masses and velocities:** DM particles may have different masses and velocities, ranging from relativistic to non-relativistic. These properties are influenced by factors such as the DM particle's mass (m) and the Universal temperature at the time of freeze-out (T_f).
- **Particle nature:** The constituents of DM particles, including their particle nature, remain unknown. Understanding the fundamental particles that make up DM is crucial for unraveling its properties.

- Production mechanisms: DM can be generated through various production mechanisms, which shed light on its origins and distribution in the Universe.

At the freeze-out temperature, DM particles transition into relics with minimal interaction between them. Their motion at decoupling can be relativistic or non-relativistic, determined by factors such as their mass and the temperature of the Universe at freeze-out. Depending on the velocities of DM particles, they can be classified into different categories [74].

- **Hot Dark Matter**

Hot dark matter (HDM) particles are characterized by their relativistic velocities during the period of galaxy formation or structure formation. A dark matter candidate is classified as hot if its velocity is relativistic at the time of freeze-out. This is quantified by the parameter x_f , defined as the ratio of the freeze-out temperature (T_f) to the mass (m) of the dark matter particle, typically $\lesssim 3$ [13]. Hot dark matter particles have a tendency to suppress primordial density fluctuations below their free-streaming length, akin to the Silk damping effect observed during the recombination era due to the free-streaming of photons.

One potential candidate for hot dark matter is massive neutrinos, which are Standard Model neutrinos with non-zero mass in the eV range (usually less than 100 eV). The cosmological number density of hot dark matter particles is roughly comparable to that of microwave background photons, imposing an upper limit on their mass to a few tens of eV. Consequently, the free streaming of these relativistic particles erases fluctuations smaller than the scale of superclusters, approximately $10^{15} M_\odot$. Thus, the free-streaming length of hot dark matter particles, such as neutrinos, is on the order of the supercluster scale.

Furthermore, HDM predicts a top-down hierarchy in structure formation, where small-scale structures are formed through the fragmentation of larger

structures. However, this contradicts observations, as some galaxies older than superclusters have been observed. While neutrinos remain a potential candidate for HDM, their status is not yet confirmed due to constraints from observational limits on neutrino mass and their very low interaction cross-section, making their detection challenging. Although modern N-body simulations suggest that neutrinos alone cannot account for the observed large-scale structure formation of the Universe, as the density fluctuations in the early Universe need to be sustained to form structures like galaxies and galaxy clusters, strong constraints on HDM have been derived from observations such as the Lyman-alpha forest and data from WMAP or Planck missions.

- **Cold Dark Matter**

Cold dark matter (CDM) particles are characterized by their non-relativistic nature during the process of structure formation, allowing for the formation of small-scale clumps. In the CDM scenario, dark matter particles freeze out at temperatures much higher than their mass, resulting in non-relativistic velocities at freeze-out. This is reflected in the parameter x_f , which is much greater than 3 [13]. The free streaming of CDM particles is of minimal cosmological significance.

CDM particles are favored by simulations of large-scale structure formation, such as N-body simulations, as they can effectively explain observed phenomena like cluster abundance and galaxy-galaxy correlation functions. These particles are typically classified into two scenarios: heavy thermal remnants of annihilation processes, such as supersymmetric neutralinos, and a cold Bose condensate, such as axions. Among these possibilities, Weakly Interacting Massive Particles (WIMPs) are popular candidates for CDM, as they are motivated strongly by extensions of the Standard Model and are extensively studied in various particle physics models related to cold dark matter.

Despite its success, the CDM model faces several discrepancies between numerical predictions and observations [75], including the “missing satellite”

problem [76], the “core-vs-cusp” problem [77], and the “too-big-to-fail” problem [78]. These discrepancies have prompted investigations into alternative paradigms to CDM, such as warm dark matter or dark matter models with self-interactions, to address these challenges.

- **Warm Dark Matter** Warm dark matter (WDM) particles exhibit characteristics that lie between those of cold dark matter (CDM) and hot dark matter (HDM). The parameter x_f for WDM particles is approximately 3. Unlike CDM particles, which permit structure formation on small scales, and HDM particles, which lead to damping of primordial density fluctuations on small scales, WDM particles cause structure formation to occur both from above and below their free-streaming scale.

WDM particles interact weakly, albeit more strongly than neutrinos, and decouple from the thermal bath at temperatures much higher than the Quantum Chromodynamics (QCD) phase transition temperature. Consequently, WDM particles have lower number densities and higher masses compared to HDM particles. This characteristic allows for the survival of fluctuations corresponding to very large galaxy halos (around 10^{11} solar masses) during free streaming. The cutoff observed in the power spectrum $P(k)$ at large wave numbers (k) in the WDM scenario indicates the formation of small dark matter halos.

Examples of particles that fall into the category of WDM include very light gravitinos (associated with local supersymmetry breaking at around 10^6 GeV) and sterile neutrinos. Observations from high-redshift quasar spectra, such as those obtained from the Sloan Digital Sky Survey (SDSS) [12] observations of the Lyman-alpha forest [70], provide strong upper bounds on the thermal velocity or free-streaming length of WDM particles, thus establishing lower bounds on their masses [79].

An alternative to purely HDM or CDM is “**mixed**” dark matter, which combines aspects of both types to better align with observational data. Furthermore, proposals

involving primordial black holes, topological defects, and modifications of Newtonian gravity on large scales remain viable candidates for explaining dark matter and its effects, although they have yet to be experimentally ruled out.

The particle nature of dark matter constituents allows them to be categorized into two distinct sectors, namely

- **Baryonic Dark Matter**

If a dark matter candidate has a baryonic nature, it falls under the category of **baryonic dark matter**. This type of dark matter could potentially consist of particles such as neutrinos, neutrons, black holes, or objects similar to Jupiter. Dark matter halos around galaxies are considered to be the most plausible locations for dark baryons, as indicated by the presence of dark matter in galactic rotation curves. The observation of microlensing events in the Large Magellanic Cloud (LMC) [80, 81] also suggests the possible existence of baryonic dark matter in our Galaxy.

The density of visible matter (ρ_{vis}) in the Universe can be expressed as the sum over the luminosity function $\phi(L)$ and mass-to-light ratio $\Upsilon_{\text{vis}} = M_{\text{vir}}/L$ (M_{vir} is the mass and L is the luminosity) [82] of various galaxy types and hot gas in galaxy clusters and groups.

$$\rho_{\text{vis}} = \sum \int \phi(L) \Upsilon_{\text{vis}} dL, \quad (1.20)$$

Big Bang nucleosynthesis (BBN) provides insights into the formation and production of light elements in the Universe. The observed abundances of these light elements constrain the present density of baryons, suggesting that a significant portion of baryons may be missing from measurements and could constitute baryonic dark matter. The Planck satellite experiment [5, 45, 83], along with previous studies like COBE and WMAP [2], provides a more accurate estimate of the baryon density, including contributions from X-ray emitting gas

and luminous stars. This estimate aligns closely with values obtained from the mass-to-luminosity ratio and bounds derived from Big Bang Nucleosynthesis (BBN) theory.

X-ray data also suggests the presence of large amounts of baryonic gas within clusters and groups of galaxies, further constraining the density of baryonic dark matter. The primary candidates for baryonic dark matter include diffuse baryonic gas and dark stars (such as white dwarfs, neutron stars, or black holes). Since most baryons are expected to exist in gaseous form at the time of cluster formation, diffuse gas may harbor these dark baryons. However, such diffuse gaseous baryons are typically too cool to be detected. As a result, the existence of Massive Compact Halo Objects (MACHOs)[84], including small brown and black dwarf stars, unattached cold planets, and other compact objects, is also proposed as a possible explanation for baryonic dark matter.

- **Non-baryonic Dark Matter** Various observations, such as supernova measurements, cosmic microwave background (CMB) readings, and galaxy redshift surveys, provide precise measurements of the total matter (Ω_m) and energy (Ω_Λ) contents of the Universe. Conversely, the baryonic density (Ω_b) is determined through measurements of primordial nucleosynthesis and the CMB spectrum. But the calculated baryon density (Ω_b) is significantly lower than the total mass content (Ω_m), the disparity ($\Omega_m - \Omega_b$) is attributed to dark matter and the majority of dark matter is believed to be non-baryonic, classified as **non-baryonic dark matter** [85]. Recent observations from the Planck satellite indicate that non-baryonic dark matter constitutes approximately 26.8% of the total energy budget of the Universe [5, 45]. These non-baryonic dark matter particles exhibit weak interactions with Standard Model particles, making their detection challenging. As relics from the Big Bang, these particles must possess mass to align with the observed dark matter density of the Universe. However, the masses of non-baryonic dark matter particles remain unknown. Plausible candidates include exotic particles necessitating extensions of the

Standard Model, such as supersymmetric particles, Kaluza-Klein dark matter in extra dimensions, or other scalar and fermionic particles in theories beyond the Standard Model [86, 87, 88, 89]. Examples of such candidates include Q-balls [90, 91], WIMPZillas [92], Superheavy or Heavy Dark Matters (HDM) [93, 94], axions [95, 96], many others.

Dark matter particles can originate from processes occurring in the early Universe, with production happening through both thermal and non-thermal mechanisms. Thermal production occurs when dark matter particles are generated during the collisions of cosmic plasma at the radiation-dominated epoch. In contrast, non-thermal dark matter has a distinct production origin, resulting in an energy spectrum different from that of a thermal distribution. This type of dark matter is generated through processes such as the out-of-equilibrium decay of heavy unstable particles, bosonic coherent motion, or other mechanisms that do not adhere to thermal equilibrium.

- **Thermal Dark Matter**

In the early Universe, dark matter relics were primarily produced through thermal processes, wherein they originated from particles in thermal equilibrium. These relics were continuously generated and annihilated from the collisions of Standard Model (SM) particles, resulting in pairs of dark matter (DM) and anti-dark matter (anti-DM). This production and annihilation process involved interactions such as $\chi\bar{\chi} \leftrightarrow e^+e^-, \mu^+\mu^-, q\bar{q}, W^+W^-, ZZ, HH, \dots$. Initially, both forward and backward interactions occurred at equal rates, maintaining chemical and thermal equilibrium with the rest of the Universe.

However, as the Universe expanded, the interaction rate between dark matter particles decreased relative to the expansion rate. Consequently, dark matter particles became “frozen” or decoupled from the plasma of the Universe, transitioning into relic particles. The relic density of dark matter, as measured by experiments like the Planck satellite, indicates that dark matter is likely

massive and weakly interacting, often referred to as Weakly Interacting Massive Particles (WIMPs). This thermal process of dark matter production is synonymous with **thermal dark matter**.

Let us denote $\chi(\bar{\chi})$, m_χ ($m_{\bar{\chi}}$), and n_χ ($n_{\bar{\chi}}$) as the dark matter particle (antiparticle), mass, and number density, respectively. In the early Universe, when the temperature (T) was much higher than the dark matter mass ($T \gg m_\chi$), the dark matter number density followed its equilibrium value, n_χ^{eq} ⁱⁱ⁾. As the Universe expanded and the temperature decreased ($T < m_\chi$), the dark matter number density exponentially decreased following the Boltzmann factor,

$$n_\chi^{eq} = g \left(\frac{m_\chi T}{2\pi} \right)^{\frac{3}{2}} e^{-m_\chi/T}, \quad (1.21)$$

where ‘ g ’ represents the effective number of degrees of freedom at that particular epoch.

Both annihilation and production processes remained in equilibrium, with the common production rate given by $\Gamma_{ann} = \langle \sigma_{ann} v \rangle n_{eq}$. Here, σ_{ann} represents the WIMP annihilation cross-section, v is the relative velocity of annihilating WIMPs, and $\langle \dots \rangle$ denotes the average over the WIMP thermal distribution. However, as the Universe expanded further, the number density of WIMPs decreased, causing a decline in both production and annihilation rates. When the annihilation rate of WIMPs (Γ_{ann}) became smaller than the expansion rate of the Universe (H), chemical decoupling occurred, and the further production of WIMPs ceased. This decoupling temperature, known as the **freeze-out temperature**, determined the relic density of dark matter.

The relic density of dark matter (Ω_χ) after freeze-out inversely depended on the annihilation cross-section (σ_{ann}) as $\Omega_\chi \propto 1/\langle \sigma v \rangle$, where Ω_χ is the DM

ⁱⁱ⁾At such high temperatures (where $T \gg m_\chi$), the number density n_χ can be approximated as $n_\chi \approx \frac{1}{8\pi^2} \left(\frac{m_\chi T}{\hbar^3 c^3} \right) \int_0^\infty \frac{E^2 dE}{\exp\left(\frac{E}{k_B T}\right) - 1}$. Here, \hbar , c , and k_B represent the Planck constant, the speed of light in vacuum, and the Boltzmann constant, respectively. The expression simplifies to $n_\chi \sim T^3$ due to the exponential term in the integrand, which represents the Boltzmann factor.

density parameter [97]. The exact freeze-out temperature marked the point at which the number of WIMPs in a comoving volume remained approximately constant, signifying the decoupling of WIMPs from the cosmic plasma. The relic density and the maximum permissible cross-section of WIMP-like thermal dark matter impose an upper bound on the mass of dark matter particles, approximately around 10^5 GeV.

- **Non-thermal Dark Matter** Non-thermal dark matter, distinguished by its production mechanism, deviates from the thermal distribution of energy spectra [98]. One such mechanism involves the coherent motion of bosons, such as axions, originating from the oscillation of (pseudo)scalar fields. These fields, exhibiting coherent motion, are crucial for generating cold dark matter, requiring light bosons with lifetimes surpassing the age of the Universe.

Another avenue for non-thermal DM production involves the decay of heavy, unstable particles. When these particles decay out-of-equilibrium, they can generate non-thermal DM populations. Depending on whether the decay occurs in or out of thermal equilibrium, the resulting DM population can be thermal or non-thermal. Non-thermal DM candidates resulting from particle decay include neutralinos, axinos, gravitinos, and KK-gravitons, among others. DM of such kinds typically exhibits lower masses, often below 10^{-3} eV.

Gravitational effects can also contribute to non-thermal DM production. For instance, superheavy DM particles ($\sim 10^5 \leq \text{mass} \leq 10^{16}$ GeV) like WIMPZILLAs can be generated during the accelerated expansion of the Universe, akin to Hawking or Unruh radiation. These relics may arise during phase transitions, reheating after inflation, or bubble collisions [99]. WIMPZILLAs, characterized by masses much larger than the reheating temperature and around 10^{13} GeV, must have lifetimes exceeding the age of the Universe to persist as DM. The abundance of such superheavy dark matter candidates is suppressed as the power of the temperature-to-mass ratio [100].

Additionally, various other non-thermal DM candidates exist, including Pseudo Nambu-Goldstone bosons like Majorons, familons, branons, and dilatons, as well as Q-balls [90, 91], mirror matter DM [101], fuzzy CDM [102], CHAMPs [103, 104]. These diverse candidates highlight the complexity of DM origins and properties beyond the thermal paradigm [98].

Axions and axion-like particles (APLs) [105, 106] are other examples of non-thermal dark matter. Although at a higher temperature, axions are almost massless, at the QCD scale, the mass of the axion hovers near the minima of the axion potential. Such kinds of DMs are generally of lower masses ($\lesssim 10^{-3}$ eV).

- **SIMPs and ELDER** In recent analyses, another remarkable non-thermal dark matter candidate has emerged: SIMP [107] and ELDER [108, 109]. SIMP (Strongly Interacting Massive Particles) and ELDER (Elastically Decoupling Relic) represent intriguing alternatives to traditional WIMP (Weakly Interacting Massive Particles) models in the study of dark matter. These concepts suggest a departure from the conventional “WIMP miracle” scenario by proposing that dark matter particles may have masses closer to the QCD confinement scale, around $\Lambda_{\text{QCD}} \sim 100$ MeV, rather than the weak scale. In this framework, dark matter could manifest as mesons or baryons within a “mirror copy” of the standard QCD in a hidden sector, as proposed in twin Higgs models. The unique aspect of SIMP and ELDER models lies in their reliance on significant $3 \rightarrow 2$ processes, which alter the freeze-out dynamics and naturally lead to a relic abundance consistent with observational data. Details discussion in Chapter 5.

Particle dark matter candidates by simple extension of Standard Model

Simple particle physics models for particle dark matter can be constructed by simple extension of Standard Model. In this case the SM may be simply extended by one or more additional scalars or fermions or some other particles. In order that this(these) newly added particle(s) could be viable candidate(s) for dark matter,

first a suitable symmetry is generally imposed on this newly constructed model (by extending SM) to prevent the decay as also other interference on SM of the additional particle(s). The added particles to SM are often referred to as the dark sector while the SM sector is the usual visible sector. For Higgs portal models, the dark sector interacts with the SM or visible sector only via Higgs in such a way that SM results and predictions are not disturbed. This is envisaged by suitably constraining the unknown interaction couplings involving dark matter by imposing theoretical bounds (e.g. unitarity, vacuum stability, perturbativity etc.) and experimental bounds such as collider bounds (LEP and LHC), PLANCK limits on relic density, direct detection limits on dark matter etc. In this way the viability of the particle(s) of the added dark sector is established and allowed ranges of the values of unknown couplings related to the proposed dark matter candidates are fixed. This(These) additional particle(s) could be a singlet scalar, an SU(2) doublet scalar (that does not generate any vacuum expectation values (vev) on spontaneous symmetry breaking — the Inert Doublet Model or IDM [110]) or a fermion or a combination of many such proposed particles. The particle dark matter model could also include a new dark sector with suitable symmetries among many other possibilities.

1.5.1 Mass ranges of dark matter candidates

Dark matter eludes direct observation due to its lack of interaction with electromagnetic forces, setting it apart from visible baryonic elements. Consequently, alongside particle candidates like WIMPs and axions, various non-luminous or low-luminosity astrophysical entities such as MACHOs, brown dwarfs, and pure quark stars are also considered potential dark matter candidates. Both observational evidence and theoretical models suggest the existence of diverse types of dark matter throughout our Universe. Fig. 1.18 illustrates the mass ranges of these different dark matter types. Among these candidates, the Weakly Interacting Massive Particle (WIMP)

gravitationally during the early stages of the Universe [93, 113] or through spontaneous symmetry breaking at the Grand Unified scale [94, 99, 100, 113, 114, 115, 116]. Additionally, phase transitions occurring during the inflationary period of the Universe are proposed as potential sources for various non-thermal heavy dark matter candidates [99].

Furthermore, various alternative models propose different candidates for dark matter, including right-handed neutrinos, axions, and axion-like particles (APLs). These candidates typically have lower masses compared to other dark matter candidates, typically less than 1 MeV. The concept of the axion, with a mass around 10^{-3} eV, was introduced by Peccei–Quinn in 1977 [95, 96] to address the strong CP problem in QCD. Additionally, astrophysical objects such as primordial black holes (PBHs), MACHOs, and pure quark stars are considered as potential dark matter candidates due to their extremely low luminosity. Although the maximum masses of these astrophysical bodies are on the order of stellar mass, the mass of PBHs may decrease significantly over time due to Hawking radiation [117].

1.6 Detection technique of Dark Matter

Around the globe, there's a surge in concerted efforts to uncover elusive Dark Matter (DM) particles. While gravitational evidence hints at their existence, it's insufficient for detailed understanding. To probe further, scientists employ three primary methods, each offering unique insights into DM and its myriad conjectures.

Firstly, direct detection involves meticulously designed experiments on Earth, aiming to capture the faint signals of DM particles colliding with atomic nuclei. Conversely, indirect detection scrutinizes the cosmos for telltale signs of DM annihilation, manifested through observable products. Additionally, collider experiments offer another avenue, where high-energy collisions might birth DM particles amidst the debris of Standard Model (SM) interactions.

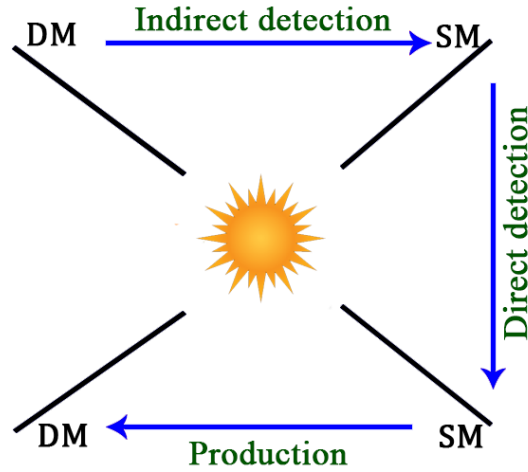


Figure 1.19: Schematic diagram of the possible channels of dark matter detection.

For effective detection, colliders like the LHC push boundaries, necessitating energy scales surpassing that of DM’s mass. Presently, the LHC operates at energies approaching the TeV scale, potentially within reach of DM detection. These distinct detection methodologies, depicted schematically in fig. 1.19, not only aim to confirm DM’s existence but also hold promise in unravelling its enigmatic nature.

• Direct Detection

The evidence supporting the existence of dark matter (DM) largely hinges on its gravitational interactions, with ongoing efforts worldwide to directly detect its elusive particles. A concept akin to detecting neutrinos directly by their elastic scattering with detector nuclei, proposed by Drukier and Stodolsky [118], suggests a potential method for direct DM detection. This approach involves searching for signatures of nuclear scattering, indicating a potential direct detection of DM. Galactic rotation curves suggest that DM forms an extended halo around galaxies, with our solar system moving through this halo, potentially exposing us to a flux of DM particles. If a DM particle interacts with a terrestrial detector, it can scatter off the nuclei of the detector material, causing recoil with energies typically in the range of a few keV due to the weak interaction strength. Detecting such low-energy recoils

requires experiments to be conducted in environments with minimal background noise, such as deep underground sites shielded from cosmic rays.

Various advanced technologies are under development to address the challenges of detecting DM, including the difficulty of detecting faint signals and the rarity of collisions. Different detection experiments employ diverse measurement techniques, such as scintillation, phonon excitation, ionization, or tracking the drifting of ionized charges in Time Projection Chambers (TPCs). Globally, extensive efforts are underway to probe for direct DM signals through experiments like DAMA [119, 120], CDMS (^{73}Ge) [121, 122], PICASSO, XENON [123, 124, 125, 126, 127], COUPP [128], LUX (Xe) [129], CLEAN (Ar, Ne), and DEAP (Ar) [130], among others. These experiments yield valuable data on scattering cross sections across different DM masses.

The type of interaction between DM and detector nuclei crucially influences direct detection signals, leading to spin-independent or spin-dependent interactions. Experiments like Edelweiss, DAMA/NaI [119, 120], CDMS, Xenon10 [123, 124], Xenon100 [125, 126, 127], [131, 132], KIMS [133, 134, 135] and CoGeNT focus on probing spin-independent interactions using heavy nuclei detectors, while NAIAD [136], SIMPLE, PICASSO [137], and Tokyo/NaF [138] investigate spin-dependent signals using light nuclei detectors. Additionally, variations in the Earth's diurnal and annual motion contribute to slight fluctuations in signal rates, which experiments like DAMA [119, 120] have attempted to detect and analyze.

• Indirect Detection

Dark matter particles have the potential to be gravitationally captured by massive celestial bodies like the Solar core or the galactic center. Within these bodies, dark matter particles may lose their velocity, potentially becoming trapped if their velocity drops below the body's escape velocity. Accumulating in significant quantities

within these sites, trapped dark matter can undergo pair annihilation, producing Standard Model particles as a result [93, 139, 140]. The annihilation products include (anti)protons, electrons, positrons, neutrinos, gamma rays, and other detectable particles. This process is particularly pronounced in regions with higher local dark matter densities, such as the galactic center or dwarf galaxies. However, challenges in indirect dark matter searches arise from astrophysical backgrounds and statistical fluctuations.

- **Neutrinos:** Neutrinos play a crucial role in probing various aspects of dark matter and stellar evolution. The annihilation and decay processes of dark matter particles generate a significant flux of neutrinos. Neutrinos have weak interactions with matter and are unaffected by celestial magnetic fields, allowing them to traverse astrophysical objects almost undisturbed. However, this property makes their detection challenging. Renowned detectors such as ANTARES, IceCube and Super-Kamiokande employ indirect methods to detect incoming neutrinos. In these experiments, high-energy neutrinos produce charged particles, like muons, as they propagate through ice, water, or rock. These energetic charged particles emit Cherenkov radiation while passing through the detectors, enabling estimation of the energy and direction of the parent neutrinos. Alternatively, tracking calorimeters, utilized in detectors like NUTEV, MINOS employ multiple layers of detector materials to track the direction of highly energetic neutrinos. While iron is a popular detector material due to its cost-effectiveness and density, liquid or plastic scintillators are also utilized for neutrino detection.
- **Antimatters:** Annihilation or decay processes of dark matter can result in the production of electron-positron and proton-antiproton pairs. While the Universe hosts numerous sources of electrons and protons, the presence of their antiparticles is relatively scarce. Consequently, an excess of antimatter could potentially signify the presence of dark matter sources. Unlike neutrinos and photons, antimatter particles are influenced by celestial and terrestrial

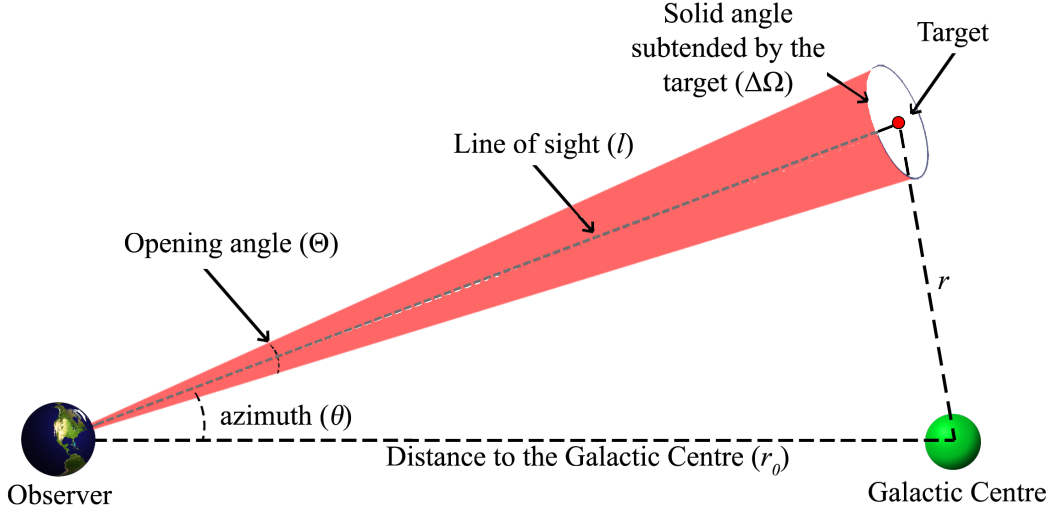


Figure 1.20: The schematic diagram of the indirect detection of galactic dark matter halo.

magnetic fields, leading to a diffuse spectrum when detected by ground-based instruments. To mitigate background flux, detectors can operate at higher altitudes using satellite-based or balloon-based experiments. Notable detectors such as PAMELA [141], HESS [142], HAWC [143], and CTA [144] and many more utilize these methods, with the latter observing Cherenkov radiation produced by charged particles during their traversal through Earth’s atmosphere.

- **Photons** Photons, though minimally affected by magnetic fields, experience attenuation over long distances. While the annihilation and decay of WIMP-like dark matter particles yield a significant number of high-energy photons, observing the full spectrum from the ground is challenging due to atmospheric opacity. Hence, space-based telescopes are more effective for high-energy photon detection. Satellites like EGRET and *Fermi*-LAT operate across a broad energy range (20 MeV-300 GeV). Conversely, ground-based gamma-ray telescopes like HESS, MAGIC [145], and CTA indirectly detect gamma-ray events through phenomena like Cherenkov radiation.

The flux observed from dark matter (DM) annihilation or decay is contingent upon

the total amount of dark matter contained within the solid angle $\Delta\Omega$, a quantity referred to as the \mathcal{J} -factor. This factor crucially hinges on the production mechanism of the emitted flux. For DM annihilation, the \mathcal{J} -factor is given by the integral

$$\mathcal{J}_{\text{ann}} = \int_{\text{l.o.s}} \rho(r)^2 dl \quad (1.22)$$

whereas for the decay process, it is expressed as

$$\mathcal{J}_{\text{dec}} = \int_{\text{l.o.s}} \rho(r) dl \quad (1.23)$$

The \mathcal{J} -factor associated with the DM decay process (\mathcal{J}_{dec}) is often denoted as the D -factor. In eqs. 1.22 and 1.23, $\rho(r)$ signifies the density of the DM halo at a radial distance r from the galactic center, assuming spherical symmetry in the distribution of the DM halo. The distance r from the galactic center can be represented in terms of the coordinates of the target object (r, θ) and the line of sight l as

$$r = \sqrt{l^2 + r_{\odot}^2 - 2lr_{\odot} \cos \theta} \quad (1.24)$$

Here, r_{\odot} denotes the distance between the galactic center and the observer, approximately representing the distance to the Sun.

The \mathcal{J} -factor, crucial for both annihilation and decay cases, is often represented in dimensionless form as

$$J_{\text{ann}} = \int_{\text{l.o.s}} \frac{1}{r_{\odot}} \left(\frac{\rho(r)}{\rho_{\odot}} \right)^2 dl \quad (1.25)$$

$$J_{\text{dec}} = \int_{\text{l.o.s}} \frac{1}{r_{\odot}} \frac{\rho(r)}{\rho_{\odot}} dl \quad (1.26)$$

Here, $\rho_{\odot} = 0.3 \text{ GeV}/\text{cm}^3$ denotes the average halo density near the Sun. These expressions enable the characterization of the \mathcal{J} -factor in terms of the density profile along the line of sight (l.o.s) within the halo.

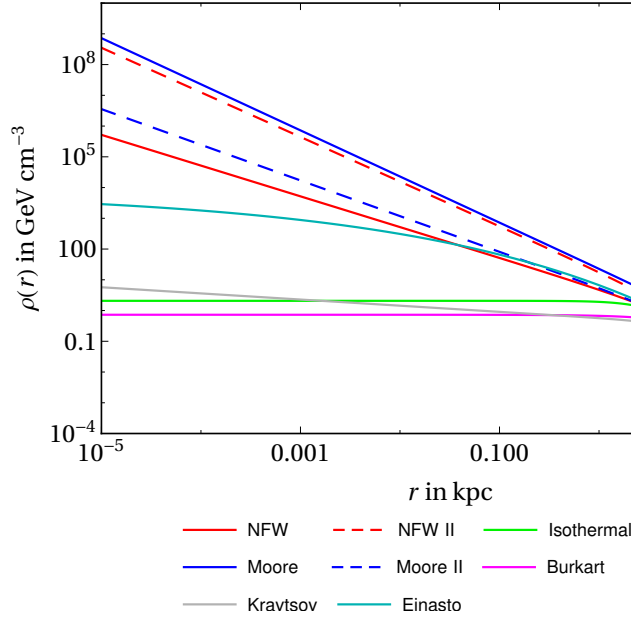


Figure 1.21: Different dark matter halo profiles (see Table 1.2).

The distribution of dark matter within the Universe is non-uniform, with dark matter halos predominantly surrounding galaxies. As one moves radially outward from the center of these galaxies, the density of dark matter increases. Additionally, numerical simulations suggest that the density of the dark matter halo decreases more rapidly in the outer regions of galaxies compared to the inner regions. Specifically, the density follows a power-law relationship, with density proportional to distance to the power of -3 in the outer region and -1 in the inner region [146]. To model this distribution, various spherically symmetric dark matter halo density profiles have been developed. These profiles offer an approximation of the distribution of dark matter around galaxies like our Milky Way. Table 1.2 presents some popular scaled halo density models for reference.

Among the various models describing dark matter halo density profiles, the first seven profiles can be represented by a generalized form known as the Hernquist profile

$$\rho(r) = \frac{\rho_s}{\left(\kappa + \left(\frac{r}{r_s}\right)^\gamma\right) \left(1 + \left(\frac{r}{r_s}\right)^\alpha\right)^{\frac{\beta-\gamma}{\alpha}}} \quad (1.27)$$

Model	$\rho(r)$	r_s (kpc)	ρ_s (GeV/cm ³)
NFW [147, 148]	$\rho_s \frac{r_s}{r} \left(1 + \frac{r}{r_s}\right)^{-2}$	20	0.259
NFW II [148]	$\rho_s \left(\frac{r_s}{r}\right)^{1.45} \left(1 + \left(\frac{r}{r_s}\right)^{0.8}\right)^{-1.5625}$	20	0.257
Isothermal [149]	$\frac{\rho_s}{1 + (r/r_s)^2}$	3.5	2.069
Moore [150]	$\rho_s \left(\frac{r_s}{r}\right)^{1.5} \left(1 + \left(\frac{r}{r_s}\right)^{1.5}\right)^{-1}$	20	0.256
Moore II [151]	$\rho_s \left(\frac{r_s}{r}\right)^{1.16} \left(1 + \frac{r}{r_s}\right)^{-1.84}$	30.28	0.108
Burkert [152, 153]	$\frac{\rho_s}{(1 + r/r_s)(1 + (r/r_s)^2)}$	12.67	0.729
Kravtsov [154]	$\rho_s \left(\frac{r_s}{r}\right)^{0.2} \left(1 + \left(\frac{r}{r_s}\right)^2\right)^{-1.4}$	10	0.361
Einasto [155]	$\rho_s \exp \left[-\frac{2}{\alpha} \left\{ \left(\frac{r}{r_s}\right)^\alpha - 1 \right\} \right]$	20	0.061

Table 1.2: Density profiles of dark matter halo and corresponding parameters.

Here, α , β , γ , and κ are model parameters, while r_s and ρ_s represent the scale distance and scale density, respectively. This general form encapsulates the diversity of density profiles observed in dark matter halos.

The NFW density profile, derived from cosmological N-body simulations, is widely utilized, yet it exhibits steepness near the galactic center. Profiles such as NFW II, Moore, and Moore II are even steeper in this region. However, observations of the galactic center indicate a flat halo density profile in the core of the galaxy. Density profiles like Isothermal, Burkert, and Kravtsov align with this observation. These profiles converge to different power laws at the core of the galactic halo. Aquarius simulations suggest a non-cuspy density profile at the galactic center, a trend better captured by the Einasto profile. For the Milky Way, the Einasto profile parameters are $r_s = 20$ kpc, $\rho_s = 0.061$ GeV/cm³, and $\alpha = 0.17$.

1.7 Summary

In this thesis, we aim to explore into various significant aspects of cosmology and astrophysics. This introductory chapter provides a foundational understanding of fundamental cosmology and dark matter. The subsequent chapters are structured as follows

- In Chapter 2, we expand upon the introduction to 21cm cosmology.
- Chapter 3 presents Inert Doublet Model for dark matter, exploring their lower bound on annihilation cross-section.
- Chapter 4 investigates multi-component dark matter Universe in the context of 21cm cosmology.
- Chapter 5 extends this study to examine the framework of self- interacting dark matter (ELDER), analysing bounds on the coupling parameter and its variation with other model parameters within the context of 21cm cosmology.
- Chapter 6 provides a brief introduction on compact objects.
- Chapter 7 explores the possible detection of 21cm signals through gravitational lensing of a compact star and bound their probability by uGMRT .
- Finally, Chapter 8 concludes the thesis, summarizing our findings and discussing possible future directions.

21cm Cosmology

“Something deeply hidden had to be behind things. ”
- Albert Einstein.

2.1 21cm Cosmology

The 21 cm signal presents a unique opportunity to delve into the era when the earliest luminous entities emerged, colloquially known as the first stars. This signal has been a subject of intense scrutiny for over seventy years, ever since its initial detection in 1951 [156]. The concept of the 21 cm line’s observability was first proposed by H. C. van de Hulst in 1945 [157], laying the groundwork for subsequent investigations.

However, exploring neutral hydrogen during the cosmic dawn and pre-cosmic dawn periods using the 21 cm signal presents distinct challenges and opportunities. During these epochs, observations manifest as absorption or emission features in the neutral hydrogen medium relative to the cosmic microwave background radiation (CMBR)

or background radiation, centered around a reference wavelength of 21 cm. This phenomenon is encapsulated in the concept of the 21 cm differential brightness temperature, which we will delve into in subsequent discussions.

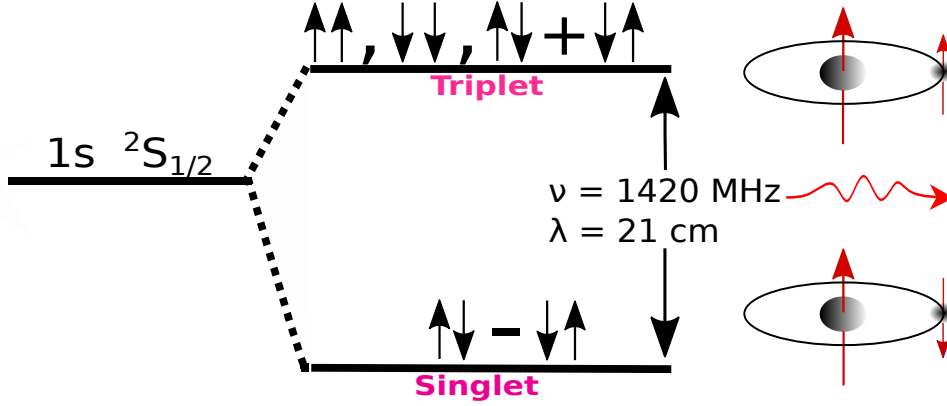


Figure 2.1: A visual representation illustrating the hyperfine transition occurring within the ground state of a neutral hydrogen atom [158].

Spin Temperature (T_s)

The 21 cm line marks the wavelength at which a hyperfine transition occurs between the singlet (1S) and triplet states of neutral hydrogen atoms. This transition corresponds to a frequency of 1420.4 MHz. When observing this transition at a redshift z , the frequency can be related to the present-day observed frequency as $1420.4/(1+z)$. During cosmic dawn, the Inter-Galactic Medium (IGM) is primarily composed of hydrogen, making it advantageous to study using the 21 cm signal. Under normal circumstances, the probability of a hyperfine state transition occurs roughly once every 10^7 years in the absence of external influences. However, the presence of exotic energy sources can significantly alter this transition and affect the spin temperature (T_s) of the hydrogen gas.

The spin temperature (T_s) [159] is defined by the ratio of the number densities of the singlet and triplet states of neutral hydrogen atoms

$$\frac{n_1}{n_0} = \frac{g_1}{g_0} \times \exp \left[-\frac{T_\star}{T_s} \right], \quad (2.1)$$

where n_1 and n_0 are the populations of the triplet and singlet states, respectively. $g_1 = 3$ and $g_0 = 1$ represent the statistical or spin degeneracies of the triplet and singlet states, respectively. The value of $T_\star (= \frac{hc}{k \lambda_{21\text{cm}}})$ is 0.068 Kelvin. The hyperfine splitting results in the suppression of the singlet state and the elevation of the triplet state.

In cosmological contexts, the spin temperature can be influenced by three main processes: background radio radiation, Ly α radiation from the first stars, and collisions involving hydrogen atoms, residual electrons, or protons. These processes occur at a fast rate compared to the de-excitation time of the line. Consequently, the spin temperature can be approximated by the equilibrium balance of these effects. In this scenario, the spin temperature T_s [159, 160] is given by

$$T_s^{-1} = \frac{T_R^{-1} + x_\alpha T_\alpha^{-1} + x_c T_{\text{gas}}^{-1}}{1 + x_\alpha + x_c}, \quad (2.2)$$

In the context of the discussed scenarios, several parameters contribute to the determination of the spin temperature (T_s).

Firstly, T_α represents the color temperature of Ly α radiation emitted by the first stars, while T_R denotes the background radio radiation temperature. T_R can also be represented as $T_\gamma (= 2.725 \times (1 + z) \text{ K})$. Additionally, T_{gas} stands for the gas temperature, encompassing neutral species, ions, electrons, or protons, all of which remain in thermal equilibrium.

Prior to the formation of the first luminous objects, there was no Ly α radiation present, implying $x_\alpha = 0$ and $T_\alpha = 0$. However, following the emergence of the first

luminous objects, their Ly α photons began to scatter with the gas, eventually bringing the Ly α radiation into local thermal equilibrium with the gas. Consequently, during the cosmic dawn era, the color temperature can be approximated as the gas temperature, $T_\alpha \approx T_{\text{gas}}$ [159, 161].

The Ly α coupling coefficient, denoted by x_α , arises due to the Wouthuysen-Field effect [161, 162, 163]. It can be expressed as $x_\alpha = P_{\text{TS}}^\alpha / P_{\text{TS}}^{\text{R}}$, where $P_{\text{TS}}^{\text{R}} = (1 + T_{\text{R}}/T_\star) A_{10}$, with $T_\star = 2\pi\nu_{\text{TS}} = 0.068$ K and $A_{10} = 2.85 \times 10^{-15} \text{ sec}^{-1}$ representing the Einstein coefficient [164, 165] for spontaneous emission from the triplet to the singlet state.

Considering $T_{\text{R}} \gtrsim 49$ K for all scenarios presented in the thesis, and $T_{\text{R}} \gg T_\star$ at the required redshift $z \sim 17$, P_{TS}^{R} can be approximated as $A_{10} \times (T_{\text{R}}/T_\star)$. Furthermore, $P_{\text{TS}}^\alpha = 4P_\alpha/27$, where P_α represents the rate of scattering of Ly α photons [159, 161].

Lastly, $x_{\text{c}} = P_{\text{TS}}^{\text{C}}/P_{\text{TS}}^{\text{R}}$ signifies the collisional coupling coefficient [161, 166, 167, 168]. resulting from the scattering between hydrogen atoms or the interaction of hydrogen atoms with other species such as electrons and protons. Thus, both the Ly α and collisional coupling coefficients are essential factors in the determination of the spin temperature [159].

2.2 21cm brightness temperature

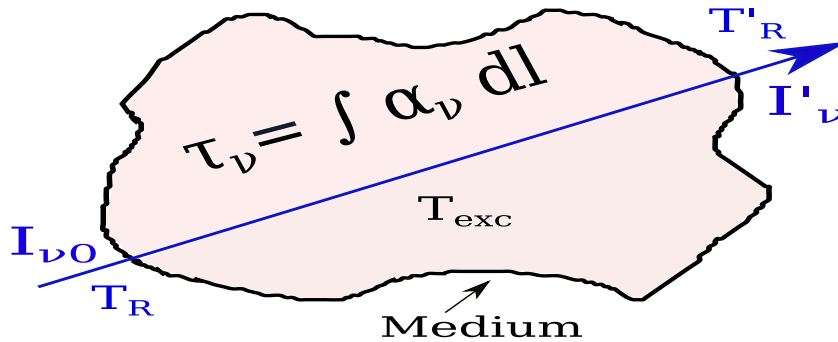


Figure 2.2: A schematic representation illustrating the alteration in brightness temperature of light as it traverses through a medium [158].

As previously discussed, during the cosmic dawn era, the 21 cm signal is observed as a differential brightness temperature. When light initially characterized by intensity ($I_{\nu 0}$) and brightness temperature (T_R , same as CMBR temperature T_γ) propagates through a medium with optical depth (τ_ν) and excitation temperature (T_{exc}), interactions with the medium can lead to absorption or emission. This interaction alters the final emergent intensity (I'_ν) and brightness temperature (T'_R). The discrepancy between the emergent brightness temperature (T'_R) and the initial brightness temperature (T_R) is termed the differential brightness temperature, which is what antennas observe

$$\delta T_B = T'_R - T_R. \quad (2.3)$$

In observations, observers detect the specific intensity of radiation at a given frequency [169]. As mentioned earlier, the initial frequency ν of light at a certain redshift z changes over time due to the Universe's expansion. At present, this frequency will be modified to $\nu/(1+z)$. Consequently, the frequency of light originating in the redshift range $z = 15 - 10$, with an initial frequency of 1420.4 MHz, will be suppressed to the order of 10^5 Hz. Comparatively, the frequency of the CMB peak is around 10^8 Hz, significantly higher than that of the 21 cm line. Hence, one can approximate the blackbody spectrum using the Rayleigh-Jeans limit. In this limit, the observed specific intensity of radiation at frequency ν is given by

$$I_\nu = \frac{4 \pi \nu^3}{\exp(2 \pi \nu/T) - 1} \quad (2.4)$$

,

$$I_\nu \equiv 2 \nu^2 T \quad [\text{only when } 2\pi\nu/T \ll 1] \quad (2.5)$$

T represents the brightness temperature of the blackbody. The emergent brightness

temperature, T'_R , as described in eq. 2.3, is influenced by both T_R and T_{exc} . Determining T'_R involves solving the radiative transfer equation. When light traverses through a medium, as depicted in Fig. 2.2, the alteration in its intensity (dI_ν) occurs due to absorption or emission over the distance travelled (dl) is expressed as

$$\frac{dI_\nu}{dl} = j_\nu - \alpha_\nu I_\nu, \quad (2.6)$$

In the context discussed above, the emission (j_ν) of light results from various processes such as spontaneous and stimulated emission. Conversely, absorption (α_ν) occurs due to interactions within the medium. Following the insights from Pritchard et al. [159] and Furlanetto et al. [170], the eq. 2.6 expressed as

$$\frac{dI_\nu}{d\tau_\nu} = S_\nu - I_\nu, \quad (2.7)$$

Here, $d\tau_\nu = \alpha_\nu dl$ and $S_\nu = j_\nu/\alpha_\nu$. Thus, the optical depth (τ_ν) can be defined as the integral of the absorption coefficient over the path length in the medium

$$\tau_\nu = \int \alpha_\nu dl, \quad (2.8)$$

Optical depth quantifies how much light is absorbed as it travels through the medium. By solving eq. 2.6 and incorporating eq. 2.4, one can derive T'_R as

$$T'_R = T_{\text{exc}} (1 - e^{-\tau_\nu}) + T_R e^{-\tau_\nu}. \quad (2.9)$$

The differential brightness temperature (δT_B), as defined in eq. 2.3, represents the change between T_{exc} and T_R as affected by the optical depth

$$\delta T_B = (T_{\text{exc}} - T_R) \times (1 - e^{-\tau_\nu}). \quad (2.10)$$

Considering the temperature of radiation in an expanding Universe, which is proportional to $(1+z)$, the redshifted differential brightness temperature for the present day can be expressed as

$$\delta T_B = \frac{T_{\text{exc}} - T_R}{1+z} \times (1 - e^{-\tau_\nu}). \quad (2.11)$$

In the specific case of hydrogen gas, with T_{exc} for the 21 cm line as T_s (defined in eq. 2.2), and considering τ_ν to be much less than 1 for neutral hydrogen gas (optically thin), Here we have denoted δT_B as T_{21} and replaced T_R by T_γ for the 21 cm line. Therefore, the 21 cm differential brightness temperature can be approximated as

$$T_{21} \simeq \frac{T_s - T_\gamma}{1+z} \times \tau_\nu. \quad (2.12)$$

The final expression for the global 21 cm differential brightness temperature obtain [159, 171, 172] as

$$T_{21} \simeq 27 x_{\text{HI}} (1 + \delta_b) \left(1 - \frac{T_\gamma}{T_s}\right) \left(\frac{0.15}{\Omega_m h^2} \frac{1+z}{10}\right)^{1/2} \left(\frac{\Omega_b h^2}{0.023}\right) \left[\frac{\delta_r v_r}{(1+z)H(z)}\right] \text{ mK}. \quad (2.13)$$

Here, $x_{\text{HI}} = n_{\text{HI}}/n_{\text{H}}$ represents the fraction of neutral hydrogen in the Universe, while Ω_m and Ω_b denote the dimensionless energy density parameters for total matter and baryons, respectively. δ_b represents the fractional overdensity in baryon and velocity gradient along the line of sight is denoted as $\delta_r v_r$.

Depending on the ratio T_R/T_s , three scenarios for the 21 cm signal can emerge: If $T_s = T_R$, then $T_{21} = 0$, indicating no signal. When $T_s > T_R$, emission spectra are observed, while $T_s < T_R$ results in absorption spectra.

2.3 Optical depth τ

The optical depth (τ) of interstellar neutral hydrogen gas concerning 21cm line radiation stands as a crucial parameter essential for determining the physical characteristics of the HI gas. Yet, obtaining this quantity poses significant challenges. The radiative transfer equation in the presence of emission and absorption of light as it traverses a medium, accounting for its path length (dl), is expressed as follows:

$$\frac{dI_\nu}{dl} = \frac{T_\star}{4\pi} \phi(\nu) [n_1 A_{10} + n_1 B_{10} I_\nu - n_0 B_{01} I_\nu], \quad (2.14)$$

where $T_\star = 2\pi\nu_{\text{TS}}$ and $\phi(\nu)$ represents the line profile of the light beam. The first term within the brackets accounts for spontaneous emission from the triplet to the singlet state, proportional to the population density of the triplet state. The second and third terms represent stimulated/induced emission and absorption, respectively. Comparing eqs. 2.14 and 2.6 and rewritten as

$$\alpha_\nu = \frac{T_\star}{4\pi} \phi(\nu) [n_0 B_{01} - n_1 B_{10}]. \quad (2.15)$$

To determine the optical depth of the hydrogen medium, integrate eq. 2.15 over dl (eq. 2.8):

$$\tau_\nu = \frac{3 A_{10}}{32\pi\nu_{\text{TS}}^2} \times \frac{T_\star}{T_s} \times n_{\text{HI}} \int \phi(\nu) dl, \quad (2.16)$$

where $n_{\text{HI}} = n_0 + n_1$. For hydrogen gas, the singlet state population density can be approximated as $n_0 \simeq n_{\text{HI}}/4$, and the ratio n_1/n_0 is given by eq. 2.1. Solving the integral in eq. 2.16 for a line profile $\phi(\nu) = 1/\Delta\nu$ with Doppler shift due to the moving medium, the optical depth for hydrogen obtain as

$$\tau_\nu = \frac{3 n_{\text{HI}}}{32\pi\nu_{\text{TS}}^3} \times \frac{T_\star}{T_s} \times \frac{A_{10}}{H(z) + (1+z)\delta_r v_r}. \quad (2.17)$$

Here, $\delta_r v_r$ is the proper velocity gradient along the line of sight. Substituting $n_{\text{HI}} = x_{\text{HI}} n_{\text{H}}$, with $n_{\text{H}} \simeq 8.5 \times 10^{-6} (1 + \delta_b) \Omega_b h^2 (1 + z)^3 \text{ cm}^{-3}$ and $H(z) = H_0 \sqrt{\Omega_m} (1 + z)^{3/2}$ for the matter-dominated era.

2.4 Evolution of the global 21 cm signal

In the Λ CDM cosmological model, it's typically assumed that the background radiation primarily consists of the Cosmic Microwave Background Radiation (CMBR), denoted as $T_{\text{R}} \equiv T_{\gamma}$. Here, T_{γ} represents the temperature of the CMBR. Consequently, in this section, we explore the evolution of the global 21 cm signal under the scenario where the background radiation is solely composed of the CMBR. In

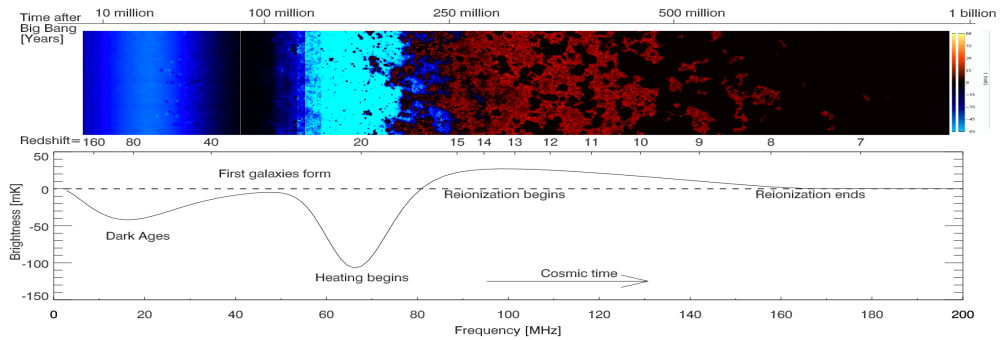


Figure 2.3: The figures depict the evolution of fluctuations in the 21 cm signal (above) and the global 21 cm signal (below) under the condition where the background radiation is solely composed of the Cosmic Microwave Background Radiation (CMBR). *Photo credits: Pritchard & Loeb, Rep. Prog. Phys., 75, 086901, (2012) [159].*

the cosmic timeline spanning from about $z = 200$ to $z = 1100$, residual free electrons from recombination enable Compton scattering, maintaining gas-CMB thermal coupling, hence $T_{\text{R}} = T_{\gamma}$. With high gas density, collisional coupling leads to $T_s = T_{\gamma}$, resulting in an expected absence of a detectable 21 cm signal ($T_{21} = 0$). But adiabatic cooling $T_{\text{R}} \propto (1 + z)^2$ during $40 \lesssim z \lesssim 200$ causes the temperature drop, leading to $T_{\text{R}} < T_{\gamma}$. Consequently, collisional coupling establishes $T_s < T_{\gamma}$, inducing $T_{21} \leq 0$ and an early absorption signal. Fluctuations in T_{21} are primarily driven

by density fluctuations, offering insights into initial conditions. As the first sources activate around $z \sim 30$, emitting Ly α photons and X-rays, a regime emerges where $T_s \sim T_R < T_\gamma$. An absorption signal prevails, with fluctuations driven by density variations and Ly α flux changes. With ongoing star formation, Ly α coupling eventually saturates ($x_\alpha \gtrsim 1$), leading to a strong coupling of gas. After around $z \sim 15$, the temperature of the gas begins to increase due to the emission of X-rays from the first stars. Consequently, the gas temperature surpasses that of the CMB, leading to observable emission spectra. As reionization concludes, the fraction of neutral hydrogen becomes extremely small, resulting in the absence of any observable signal. The residual neutral hydrogen is confined to dense regions within collapsed structures, which can be studied through the 21 cm forest—a counterpart to the Ly α forest.

2.5 Summary

Around $z \sim 200$, the gas temperature experiences adiabatic cooling, reaching approximately 7 K by $z = 17.2$, while the CMB temperature reaches about 49.6 K. According to eq. 2.13, this results in an absorption amplitude T_{21} of approximately -220 mK in the absence of any heating effects on the IGM gas from the first stars. Here, x_{HI} is assumed to be unity to calculate T_{21} . The neutral hydrogen fraction x_{HI} can be expressed as $1 - x_e$. At $z \sim 17$, the ionization fraction x_e is estimated to be on the order of $\mathcal{O}(10^{-3})$, indicating $x_{\text{HI}} \simeq 1$. Here, $x_e = n_e/n_{\text{H}}$ represents the ionization fraction, and n_e is the number density of residual free electrons.

The introduction of heating from radiation emitted by the first stars will elevate the gas temperature, subsequently diminishing the absorption amplitude of the 21 cm signal. Any exotic sources of energy can inject energy into the IGM, raising the gas temperature and potentially altering the absorption amplitude in the global 21 cm signal. This characteristic can establish stringent constraints on the properties of

such energy sources influencing the IGM. In the thesis, four works are considered, focusing on sterile neutrinos and primordial black holes as candidates for dark matter, and examining the constraints on their properties based on the global 21 cm signal. Additionally, two other works in the thesis investigate the strength of constraints on primordial magnetic fields that may have originated in the early Universe.

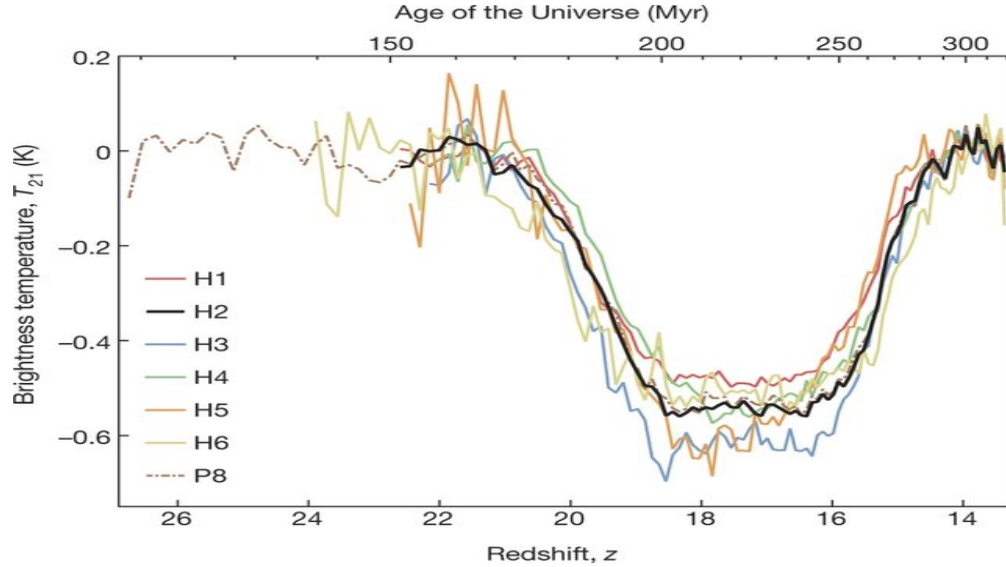


Figure 2.4: Each profile, representing the brightness temperature T_{21} , is combined with its residuals and plotted against the redshift z along with the corresponding age of the Universe.. *Photo credits: Judd D. Bowman et al. [173].*

In 2018, the Experiment to Detect the Global Epoch of Reionization Signature (EDGES)ⁱ⁾ collaboration announced an absorption profile for the 21 cm signal within the redshift range 15 – 20 [173]. The reported T_{21} was -500^{+200}_{-500} mK in the 15 – 20 redshift range, centred at 78 ± 1 MHz, forming a symmetric "U" shape (Fig. 2.4). This absorption amplitude is nearly half of what was predicted by theoretical models based on the Λ CDM framework (~ -220 mK). To reconcile the EDGES observation, it is suggested that either the cosmic background radiation temperature $T_{\text{CMB}} \gtrsim 104$ K is needed for the standard T_{gas} evolution, or $T_{\text{gas}} \lesssim 3.2$ K in the absence of any non-standard evolution of T_{CMB} [173]. However, there have been numerous articles

ⁱ⁾<https://www.haystack.mit.edu/astronomy/astronomy-projects/edges-experiment-to-detect-the-global-eor-signature/>

questioning the validity of the EDGES measurement [174, 175]. In this thesis, I have taken into account the absorption amplitude reported by the EDGES collaboration for some of the works (4, 5).

Annihilation Cross-Section of IDM Dark matter

The Inert Doublet Model (IDM) offers a potential particle dark matter (DM) candidate that aligns with current collider data and relic density constraints in three specific mass ranges: below 10 GeV, between 10 and 160 GeV, and above 500 GeV along with other coupling parameters (fixed using theoretical bounds and experimental bounds (*e.g.*, relic density results, direct detection bounds, collider bounds etc.)). There are various cosmological signals, that is difficult to interpret from known and well studied astrophysical and cosmological processes. Such phenomena includes γ -ray emission from Galactic Centre region, excess positron fraction, possible excess synchrotron radiation. In absence of any known astrophysical phenomena to explain the above, there are attempts in the literatures to explore the possibility that dark matter annihilation may produce the Standard Model particles which manifest as the excess signal.

It is also worthwhile to explore the effect of dark matter annihilation and scattering cross-section on 21cm HI signal from the early Universe. In this chapter this feature is addressed for IDM dark matter and bounds of IDM annihilation cross-section is analysed.

3.1 Introduction

In the Inert Doublet Model (IDM) [110, 176], an additional inert scalar doublet (referred to as the inert Higgs) is introduced alongside the Standard Model (SM). This extra SU(2) doublet does not obtain a vacuum expectation value (vev) during spontaneous symmetry breaking (SSB). A discrete Z_2 symmetry is applied to this added doublet, making it Z_2 even, while the SM particles are Z_2 odd. This symmetry ensures that the inert doublet cannot decay into SM fermions or contribute to their masses since it lacks a vev. Consequently, the Z_2 symmetry stabilizes the inert scalar, allowing interactions between dark matter candidates and the SM sector solely through the Higgs portal. The lighter neutral scalar from this inert doublet then serves as a viable dark matter candidate.

The IDM involves two scalar doublets: the conventional SM Higgs doublet (H_1) and the inert doublet (H_2). Under the Z_2 symmetry, H_2 remains invariant. The two SU(2) scalar doublets are expressed as:

$$H_1 = \begin{pmatrix} \phi^+ \\ h' + i\chi \end{pmatrix} \quad H_2 = \begin{pmatrix} H^+ \\ (S + iA)/\sqrt{2} \end{pmatrix}. \quad (3.1)$$

Here, ϕ^+ and H^+ are charged scalars, h' and χ are real scalars, S is a CP-even scalar, and A is a pseudoscalar. The interaction Lagrangian for the model is given by

$$\begin{aligned} \mathcal{L} \supset & m_{11}^2 H_1^\dagger H_1 + m_{22}^2 H_2^\dagger H_2 + \lambda_1 \left(H_1^\dagger H_1 \right)^2 + \lambda_2 \left(H_2^\dagger H_2 \right)^2 \\ & + \lambda_3 \left(H_1^\dagger H_1 \right) \left(H_2^\dagger H_2 \right) + \lambda_4 \left(H_2^\dagger H_1 \right) \left(H_1^\dagger H_2 \right) + \frac{\lambda_5}{2} \left[\left(H_2^\dagger H_1 \right)^2 + \left(H_1^\dagger H_2 \right)^2 \right] \end{aligned} \quad (3.2)$$

In this expression, m_{11} and m_{22} represent the mass terms, while the λ_i are various coupling parameters. In the IDM, which is a Higgs portal model, the interactions of dark matter are mediated by the Higgs boson, connecting the dark sector to the

visible sector. The couplings of dark matter to the Higgs are encapsulated in λ_3 , λ_4 , and λ_5 , combined as $\lambda_{L,L_1} = \frac{1}{2}(\lambda_3 + \lambda_4 \pm \lambda_5)$.

These parameters are constrained by both theoretical and experimental bounds. Theoretical constraints include the perturbativity bound ($|\lambda_i| < 4\pi$), vacuum stability conditions (e.g., $\lambda_{1,2} > 0$, $\lambda_3 > -2\sqrt{\lambda_1\lambda_2}$), and unitarity bounds (e.g., $\lambda_3 \pm \lambda_4 < 4\pi$). Experimental constraints arise from dark matter relic density measurements from Planck observational result, upper bounds on dark matter-nucleon scattering cross-sections from direct detection experiments, and collider constraints such as LEP I measurements of Z boson decay width.

Upon SSB, H_1 acquires a vev v , while H_2 does not. The physical scalars can then be expanded around the minima as

$$H_1 = \begin{pmatrix} \phi^+ \\ \frac{h+v+i\chi}{\sqrt{2}} \end{pmatrix} \quad H_2 = \begin{pmatrix} H^+ \\ \frac{S+iA}{\sqrt{2}} \end{pmatrix}. \quad (3.3)$$

In this scenario, h represents the physical Higgs boson. After performing a gauge transformation to unitary gauge, H_1 becomes $\begin{pmatrix} 0 \\ \frac{h+v}{\sqrt{2}} \end{pmatrix}$, with the Goldstone bosons being absorbed by the W^\pm and Z bosons to gain mass and longitudinal components. Both S and A could be dark matter candidates, but S is typically considered the lighter and thus the IDM dark matter candidate.

After SSB, the interaction vertices for IDM dark matter S and Higgs h include SSh and $SShh$ interactions, with couplings $g_{SSh} = \lambda_L v$ and $g_{SShh} = \frac{1}{2}\lambda_L$. These couplings are constrained by theoretical bounds, such as those ensuring vacuum stability and perturbativity, and by experimental results including relic density observations and direct detection experiments.

Recent studies, such as those by P. Stöcker et al., have discussed the constraints on these coupling parameters within Higgs portal models, considering data from Planck observations, direct detection experiments, and collider results. In this context, the

coupling parameters are constrained not only by experimental bounds but also by theoretical considerations, ensuring a consistent and viable model for dark matter.

We examine the scalar S as the dark matter candidate within the Inert Doublet Model (IDM) to account for the dark matter present in the Universe. We analyze the fluctuations in the brightness temperature of the 21-cm signal, given that the relic densities of IDM dark matter fall within the 95% confidence interval of the Planck observational data [45] for dark matter relic density. Our analysis incorporates the evolution of heat generated by dark matter annihilation [177, 178, 179] and dark matter-baryon elastic scattering [180, 181] during the dark ages, assessing its impact on the brightness temperature fluctuations T_{21} of the 21-cm signal.

Moreover, we explore scenarios where only a fraction of IDM dark matter participates in collision or annihilation processes, or both, affecting the brightness temperature T_{21} . We investigate how T_{21} varies for different fractions of IDM dark matter involved in these processes. In this particular scenario we had chosen the range of IDM dark mass between 10GeV to 900 GeV[182, 183].

3.2 Thermal Evolution of intergalactic medium (IGM)

The recent experiments [173, 184] have predicted the global 21-cm signal, though with some uncertainties. The fluctuations in this signal are measured by the differential brightness temperature, T_{21} , which is influenced by both the spin temperature T_s and the CMB temperature T_γ . The spin temperature T_s represents the excitation temperature of the 21-cm line and depends on the population ratio of the two hyperfine states of hydrogen. This temperature can be estimated by specific equations.

For our calculations, we approximate T_s by neglecting the Wouthuysen-Field effect, using the following formula [185]

$$T_s = \frac{(T_\gamma A_{10} + C_{10} T_\star) T_b}{A_{10} T_b + C_{10} T_\star} \quad (3.4)$$

where $T_\star = \frac{hc}{k\lambda_{21\text{cm}}} = 0.068 \text{ K}$, $A_{10} = 2.85 \times 10^{-15} \text{ s}^{-1}$ is the Einstein coefficient, and C_{10} is the collisional transition rate.

The evolution of temperatures in a charge-neutral Universe (where the abundances of protons and electrons, x_p and x_e , are equal) can be determined by tracking the temperature changes of both the dark matter fluid (T_χ) and the baryonic fluid (T_b) as the redshift varies. Incorporating the impact of heating or cooling on the baryonic and dark matter fluids resulting from dark matter interactions with baryons, the evolution equation is modified as [185, 180, 186, 187, 178]

$$(1+z) \frac{dT_b}{dz} = 2T_b + \frac{\Gamma_c}{H(z)} (T_b - T_\gamma) - \left(\frac{dE}{dV dt} \right)_{\text{inj}} \frac{1}{n_H} \frac{2f_{\text{heat}}(z)}{3H(z)(1+x_e+f_{\text{He}})} - \frac{2\dot{Q}_b}{3H(z)} \quad (3.5)$$

Here, $H(a)$ denotes the Hubble parameter. The term Γ_c is the Compton scattering rate, is influenced by the scattering interactions between CMB photons and residual free electrons. Given the significantly higher number density of CMB photons compared to residual free electrons, Compton scattering efficiently maintains thermal equilibrium between baryons and CMB photons. Thus, Γ_c depends on the electron fraction $x_e = \frac{n_e}{n_b}$ and is expressed as

$$\Gamma_c = \left(\frac{8\sigma_T a_r T_\gamma^4}{3m_e} \right) \frac{x_e}{1+f_{\text{He}}+x_e} \quad (3.6)$$

where σ_T is the Thomson cross-section, a_r is the radiation constant, and m_e is the electron mass. f_{He} signifies the relative abundance of helium nuclei, given by $f_{\text{He}} = n_{\text{He}}/n_H$. The term $(dE/dV dt)_{\text{inj}}$ refers to the energy injection rate per unit volume, while dQ_b/dt describes the heating rate of baryons in their rest frame. In

eq. (3.5), the third term accounts for the energy transfer rate due to dark matter annihilation, and the fourth term represents the contribution from dark matter-baryon elastic scattering.

Dark matter annihilation can significantly influence the evolution of baryon temperature (T_b). This process heats the baryons, thereby raising T_b and altering the differential brightness temperature spectrum (T_{21}). There are two primary mechanisms by which dark matter annihilation affects baryon temperature.

First, during the epoch of thermal decoupling from the CMB, dark matter annihilation increases the fraction of free electrons ($x_e = n_e/n_b$) beyond a certain threshold. The evolution of x_e can be described by

$$(1+z)\frac{dx_e}{dz} = \frac{C}{H(z)} (n_H \mathcal{A}_B x_e^2 - 4(1-x_e)\mathcal{B}_B e^{3E_0/(4T_\gamma)}) \quad (3.7)$$

where C is the Peebles factor [188], E_0 is the ground state energy of hydrogen, $\mathcal{A}_B(T_b, T_\gamma)$ is the effective recombination coefficient, and $\mathcal{B}_B(T_\gamma)$ is the effective photoionization rate to and from the excited state, respectively. A higher x_e delays CMB decoupling, resulting in an increased T_b since the baryons have less time to cool adiabatically.

Second, dark matter annihilation directly injects energy into the baryons, raising T_b . This direct heating mechanism is represented by the third term in eq. (3.5), which accounts for the contribution of dark matter annihilation to the evolution of baryon temperature.

Estimating the energy injection rate per unit volume $(dE/dV dt)_{\text{inj}}$ involves assuming that dark matter (DM) annihilates into standard model particles, thereby injecting energy into the Universe [178]. This process leads to additional ionization, excitation, and heating of the gas. Given a velocity-averaged annihilation cross section $\langle\sigma v\rangle$,

$dE/(dV dt)_{\text{inj}}$ is expressed as:

$$\left(\frac{dE}{dV dt}\right)_{\text{inj}} = \rho_\chi^2 B(z) f_\chi^2 \frac{\langle\sigma v\rangle}{M_\chi} \quad (3.8)$$

Here, f_χ represents the fraction of dark matter that undergoes annihilation into standard model particles, while ρ_χ denotes the dark matter density. Two distinct expressions for $B(z)$, the boost factor, are considered: $B(z) = 1 + 1.6 \times 10^5 a^{1.54} \text{Erfc}(\frac{1+z}{20.5})$ and $B(z) = 1 + 2.3 \times 10^6 a^{1.48} \text{Erfc}(\frac{1+z}{19.6})$ [178, 189]. The boost factor, crucially linked to structure formation, reflects the effective occurrence of DM annihilations across numerous small over-densities. As the spatial average of the annihilation rate relies on the square of dark matter densities, the boost factor enhances this dependence [190].

The energy injected by dark matter (DM) annihilation is primarily deposited into the baryons through ionization, excitation, and heating processes [178]. The dimensionless quantity f_{heat} in eq. (3.5) quantifies the efficiency of energy deposition into the baryons via heating. This efficiency depends on the DM mass and accounts for the time delay between energy injection and deposition. In our study, we distinguish between instantaneous and delayed energy deposition.

Instantaneous deposition implies that the energy produced by DM annihilation at a certain redshift is immediately transferred to the gas or background. Conversely, delayed deposition includes transfer functions accounting for the delay, as outlined in Ref. [191]. We estimate f_{heat} following the methods in [192, 191, 193], using the SCK approximation [178]. The f_{heat} is given by:

$$f_{\text{heat}} = f_{\text{eff}} \left(\frac{1 + 2x_e}{3}\right) \quad (3.9)$$

where f_{eff} is the fraction of energy from DM annihilation immediately transferred to the plasma. The values of f_{eff} are adopted from Refs. [191, 193] for photons and e^+e^-

pairs injected at keV-TeV energies, as detailed in the provided data sourceⁱ⁾. While $f(z)$, the ratio of deposited to injected power at redshift z , can be approximated by f_{eff} for WIMP dark matter [191], our calculations consider f_{eff} as a function of z [192, 191, 193, 179, 194]

The elastic scattering between dark matter (DM) and baryons influences the baryon temperature (T_b) and its evolution. This interaction can either cool or heat the baryons. Generally, when two fluids (such as DM and baryons) interact, the hotter fluid transfers energy to the cooler one until thermal equilibrium is reached. If the fluids are at the same temperature, no energy transfer occurs. A relative velocity between the two fluids introduces a friction term, which damps the motion and causes a loss in kinetic energy, thereby increasing the temperature of both fluids. The magnitude of this interaction effect depends on the initial relative velocity, which follows a Gaussian distribution with a variance of about 29 km s^{-1} at $z = 1010$. [180]. When DM and baryons interact at different temperatures, the colder DM gets heated, with the heating rate proportional to the temperature difference. If there is a relative velocity between DM and baryons, the friction term heats both DM and baryons regardless of their temperature difference. The baryon heating rate is given by [180]

$$\frac{dQ_b}{dt} = \frac{2 m_b \rho_\chi \sigma_0 e^{-\frac{r^2}{2}} (T_\chi - T_b)}{(m_\chi + m_b)^2 \sqrt{2\pi} u_{th}^3} + \frac{\rho_\chi}{\rho_m} \frac{m_\chi m_b}{m_\chi + m_b} V_{\chi b} \left(\frac{dV_{\chi b}}{dt} \right) \quad (3.10)$$

Here, m_χ and m_b are the masses of DM and baryons, respectively. ρ_χ is the energy density of DM, ρ_b is the energy density of baryons, and the total matter density is $\rho_m = \rho_b + \rho_\chi$. The term u_{th} represents the variance of the relative velocity between DM and baryons, estimated as $u_{th} \equiv \sqrt{T_b/m_b + T_\chi/m_\chi}$. The term $V_{\chi b}$ in eq. (3.10) is the drag term representing the relative velocity between DM and baryons.

ⁱ⁾<https://faun.rc.fas.harvard.edu/epsilon/>

The velocity-dependent cross-section can be expressed as $\sigma = \sigma_0(v/c)^n$, where n varies according to different dark matter interaction mechanisms, and c is the speed of light (in natural units, this simplifies to $\sigma = \sigma_0 v^n$). For dark matter with magnetic and/or electric dipole moments, n can be +2 or -2. Values of $n = 2, 1, 0, -1$ apply to scattering involving a Yukawa potential [195], and $n = -4$ is characteristic of millicharged dark matter interactions [196, 197]. The nature of baryon-dark matter scattering over a wide range of dark matter masses is extensively discussed in Ref. [198], with similar studies found in Refs. [199, 200, 201].

In our analysis, we parametrized the baryon-dark matter scattering cross-section σ as $\sigma = \sigma_0 v^{-4}$ [202, 180, 203]. Here, σ_0 represents the DM scalar scattering cross-section with baryons. The parameter σ_0 depends on the DM mass m_χ and scales as $\sigma_0 = (m_\chi/\text{GeV}) \times 10^{-42} \text{ cm}^{-2}$ [180].

Recent studies on the EDGES 21-cm signal also support a cross-section velocity dependence of $n = -4$ [180, 203, 204]. This particular value of n is prevalent in various dark matter interaction scenarios, including hadronically interacting DM, millicharged DM, and analyses of the Baryon Acoustic Oscillations (BAO) signal.

3.3 Variation of T_{21} with different parameters

Dark matter (DM) annihilation induces heating effects in baryons, directly injecting energy and raising the baryon temperature T_b . This increase in T_b influences the spin temperature T_s , subsequently affecting the 21-cm differential brightness temperature T_{21} . Additionally, DM-baryon elastic scattering contributes to heating due to the relative velocity between the particles, further elevating the baryon temperature and modifying T_{21} [178]

$$T_{21}(z) \approx 23 \left(1 - \frac{T_\gamma(z)}{T_s(z)}\right) \left(\frac{\Omega_b h^2}{0.02}\right) \left(\frac{0.15}{\Omega_m h^2}\right)^{1/2} \sqrt{\frac{1+z}{10}} x_{\text{HI}} \text{ mK}. \quad (3.11)$$

Here the quantity x_{HI} represents the fraction of hydrogen that is in a neutral state.

Initially, we focus on analysing the fluctuations in the 21cm brightness temperature T_{21} , specifically considering the influence of dark matter annihilation on the typical evolution of the baryon temperature (T_b). To achieve this, we modify eq. (3.5) by excluding the final term on the right-hand side, while retaining the term related to $\left(\frac{dE}{dVdt}\right)_{\text{inj}}$, as it accounts for the heat injection resulting from dark matter annihilation (as described in eq. (3.8)), whereas the former term with \dot{Q}_b represents the heating rate due to collisions between dark matter and baryons (as per eq. (3.10)). Solving eqs. (3.5-3.9) concurrently, with $T_\gamma(z) = T_\gamma^0 (1+z)$ (where $T_\gamma(z)$ denotes the background CMB temperature at redshift z and T_γ^0 is its present epoch value), the spin temperature T_s , and consequently T_{21} are calculated using eq. (3.4) and eq. (3.11) respectively. The baryon density parameter $\Omega_b (= \frac{\rho_b}{\rho_c}$, ρ_c being the critical density) and matter density parameter $\Omega_m (= \frac{\rho_m}{\rho_c})$ are assumed to follow $\Omega_b = 0.04 (1+z)^3$ and $\Omega_m = \Omega_\chi + \Omega_b = 0.30 (1+z)^3$ at varying redshifts for each of the chosen dark matter masses. The obtained results are graphically depicted in the left panel of fig. 3.1. Additionally, the right panel of fig. 3.1 zooms in on the truncated redshift range of $z \sim 15 - 30$, which broadly corresponds to the reionization epoch.

From fig. 3.1, it is evident that for IDM dark matter masses ranging from approximately 70 GeV to 80 GeV, a significant dip in the 21-cm brightness temperature fluctuation, T_{21} , is observed around redshift $z \sim 21$. This dip occurs during the reionization epoch. For other mass values outside the 70-80 GeV range, T_{21} drops to around -250 mK at a redshift of $z \sim 10$. At a redshift of $z \sim 1000$, the T_{21} temperature is approximately 0 mK across all IDM dark matter masses from 10 GeV to 990 GeV. This redshift marks the epoch of photon decoupling (CMB) and the beginning of the dark ages. The distinct behavior of T_{21} for IDM masses in the 70-80

GeV range is likely due to the resonance in interaction cross-sections, characteristic of Higgs portal dark matter.

Next, we examine the impact of baryon-dark matter (IDM) collisions on baryon temperature evolution and subsequently on the 21-cm temperature fluctuations T_{21} . In this scenario, the term related to dark matter annihilation is omitted, focusing instead on the heating rate due to dark matter-baryon collisions. By solving the coupled equations for a range of dark matter masses, we observe the variations in T_{21} throughout the dark ages, plotted in fig. 3.2.

In the left panel of fig. 3.2, we plot T_{21} variations with redshift z for IDM masses from 10 GeV to 80 GeV, including 550 GeV and 990 GeV. A dip in T_{21} is noticeable around redshift $z \sim 95$ for all masses. These variations are nearly degenerate except

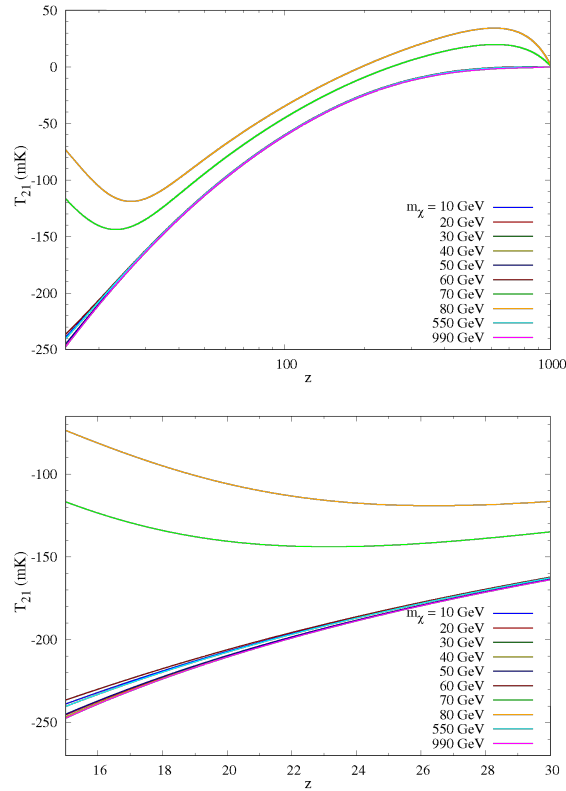


Figure 3.1: The variation in the 21-cm brightness temperature, T_{21} , across different redshifts is shown with the inclusion of dark matter (DM) annihilation effects alongside the standard thermal evolution. The different coloured lines represent varying IDM masses as indicated in the figure.

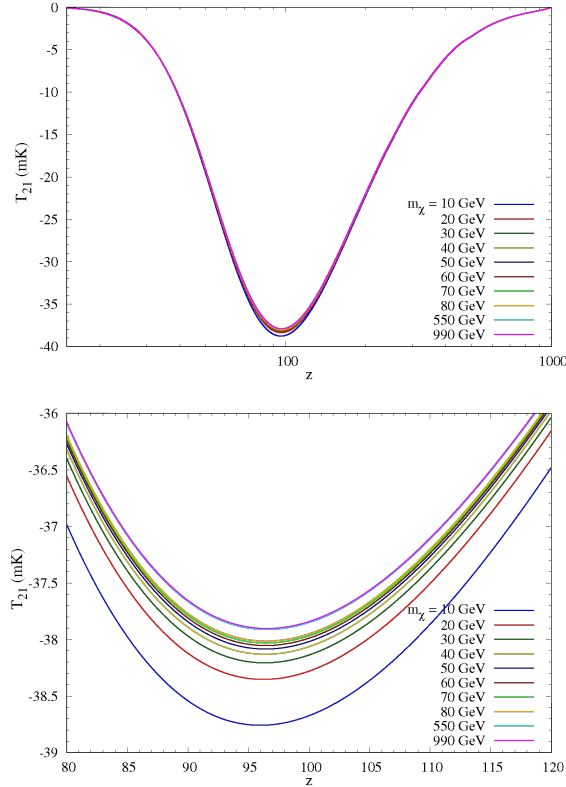


Figure 3.2: The variation in the 21-cm brightness temperature, T_{21} , across different redshifts includes the impact of DM-baryon elastic scattering in addition to the standard thermal evolution. Different colored lines correspond to various IDM masses as indicated in the figure.

near this minimum. The right panel, which zooms in on the $80 \leq z \leq 120$ range, shows that the minimum T_{21} increases with increasing dark matter mass.

Fig. 3.3(a) shows the relation $T_{21}|_{\min} = -41.76 + 3.87 \exp(-\frac{2.53}{m_{\chi}})$, fitting well with the observed minima of T_{21} as dark matter mass m_{χ} increases. Fig. 3.3(b) depicts the redshift z_{\min} at which these minima occur, also following a similar trend.

Next, we combine the effects of both dark matter annihilation and dark matter-baryon collisions, solving the equations to observe the combined impact on T_{21} . The results are shown in fig. 3.4. Unlike the annihilation-only scenario (Fig. 3.1), the combined effects eliminate the low-redshift feature of T_{21} , with minima around $z \sim 95$. The unique characteristics of IDM masses in the 70-80 GeV range are still evident, with T_{21} values differing from those for other masses.

Fig. 3.5(a) and (b) illustrate the variations of T_{21} minima with m_χ for dark matter annihilation alone, showing minimal variation outside the 70-80 GeV range. The corresponding redshift z_{\min} follows a similar pattern. In the combined scenario (Fig. 3.6(a) and (b)), the minima of T_{21} for 70-80 GeV masses occur at lower redshifts compared to other masses.

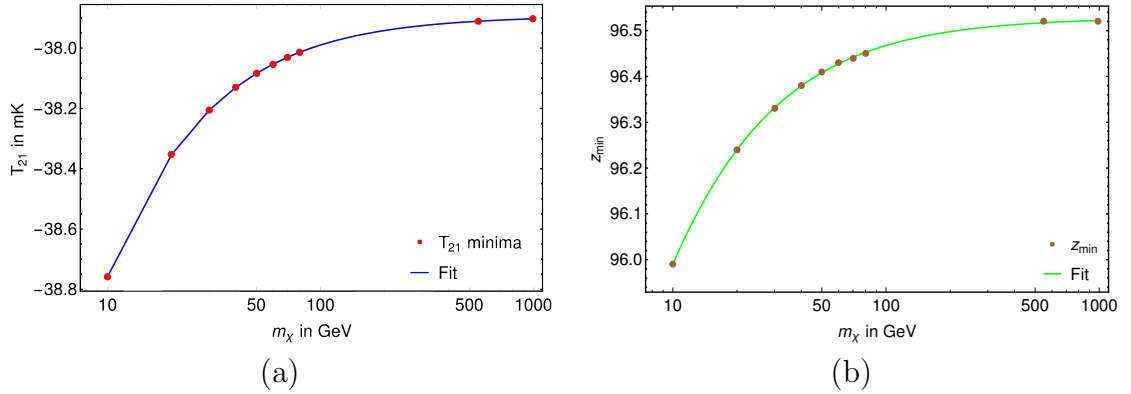


Figure 3.3: (a) This panel depicts the variations in the 21-cm brightness temperature T_{21} at different redshifts, incorporating DM-baryon elastic scattering as an additional effect alongside the thermal evolution. The red points represent the computed values, while the blue line denotes the fitted curve. (b) Similarly, this panel illustrates the redshift values (z_{\min}) at which T_{21} reaches its minimum for each different IDM mass (m_χ). The solid green line traces the trends in the variation of z_{\min} across different IDM masses.

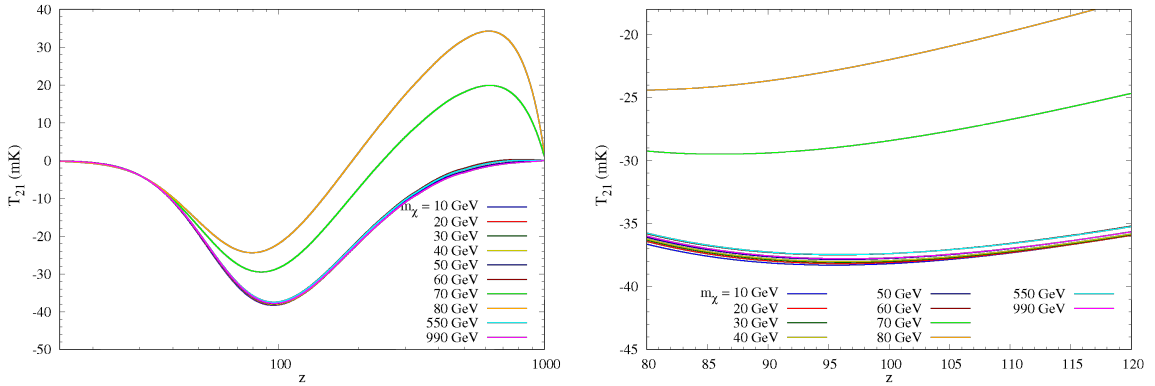


Figure 3.4: The left panel illustrates the changes in the 21cm absorption lines T_{21} , incorporating effects of dark matter annihilation and dark matter-baryon elastic scattering alongside thermal evolution. Each coloured line represents a different dark matter mass as specified in the figure. The right panel zooms in on the redshift range $80 \leq z \leq 120$, providing a detailed view of the variations depicted in the left panel.

We also explore the effects of IDM dark matter constituting only a fraction of the total dark matter content. For various IDM fractions, we compute T_{21} variations, shown in fig. 3.7. The results indicate that T_{21} decreases with decreasing IDM fraction, although the changes are less significant except for 70 and 80 GeV masses.

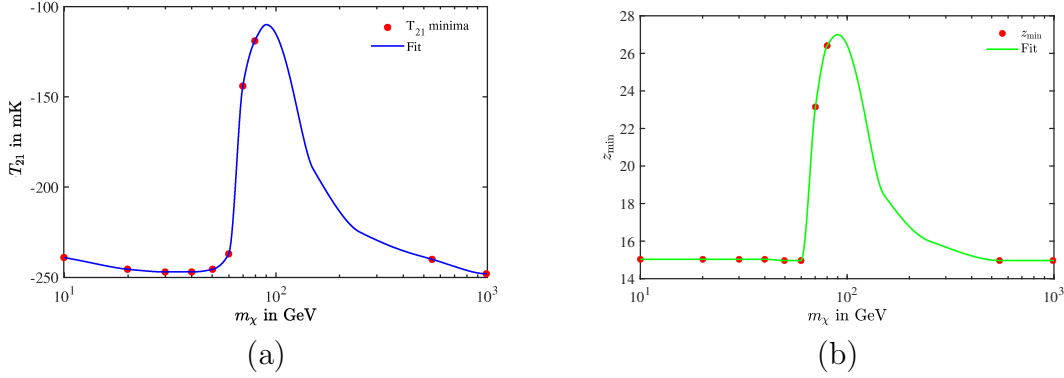


Figure 3.5: (a) The figure illustrates the variation in the 21-cm brightness temperature T_{21} at different redshifts, considering only dark matter annihilation as an additional effect alongside thermal evolution. Red points denote computed values, while the blue line represents the fitted curve. (b) Similar to panel (a), this plot shows how the redshift values (z_{\min}) at which T_{21} reaches its minimum vary with different dark matter masses m_χ . The solid green line depicts the trend of z_{\min} with m_χ .

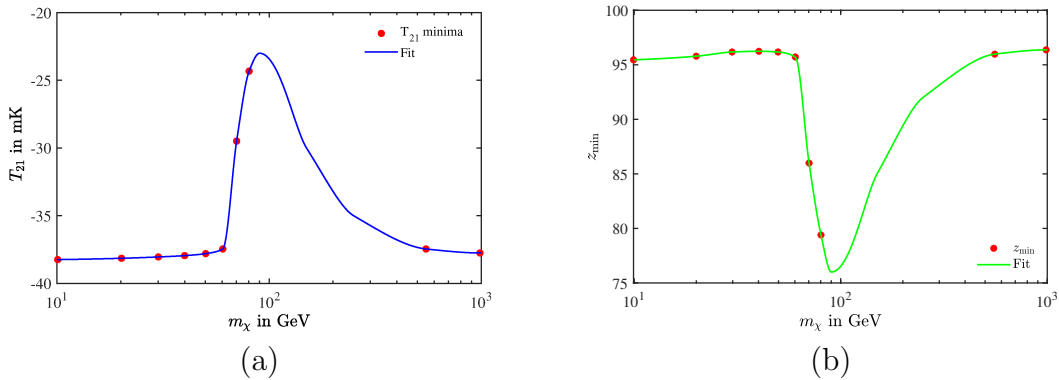


Figure 3.6: (a) This panel depicts the variation in the 21-cm brightness temperature T_{21} at different redshifts, incorporating the combined effects of dark matter annihilation and dark matter-baryon scattering as additional factors influencing T_{21} , alongside the thermal evolution. The red points denote computed values, and the blue line represents the fitted curve. (b) In this panel, we present the variation of the redshift values (z_{\min}) at which T_{21} reaches its minimum for each different dark matter mass m_χ . The solid green line depicts the trend in the variation of z_{\min} with m_χ .

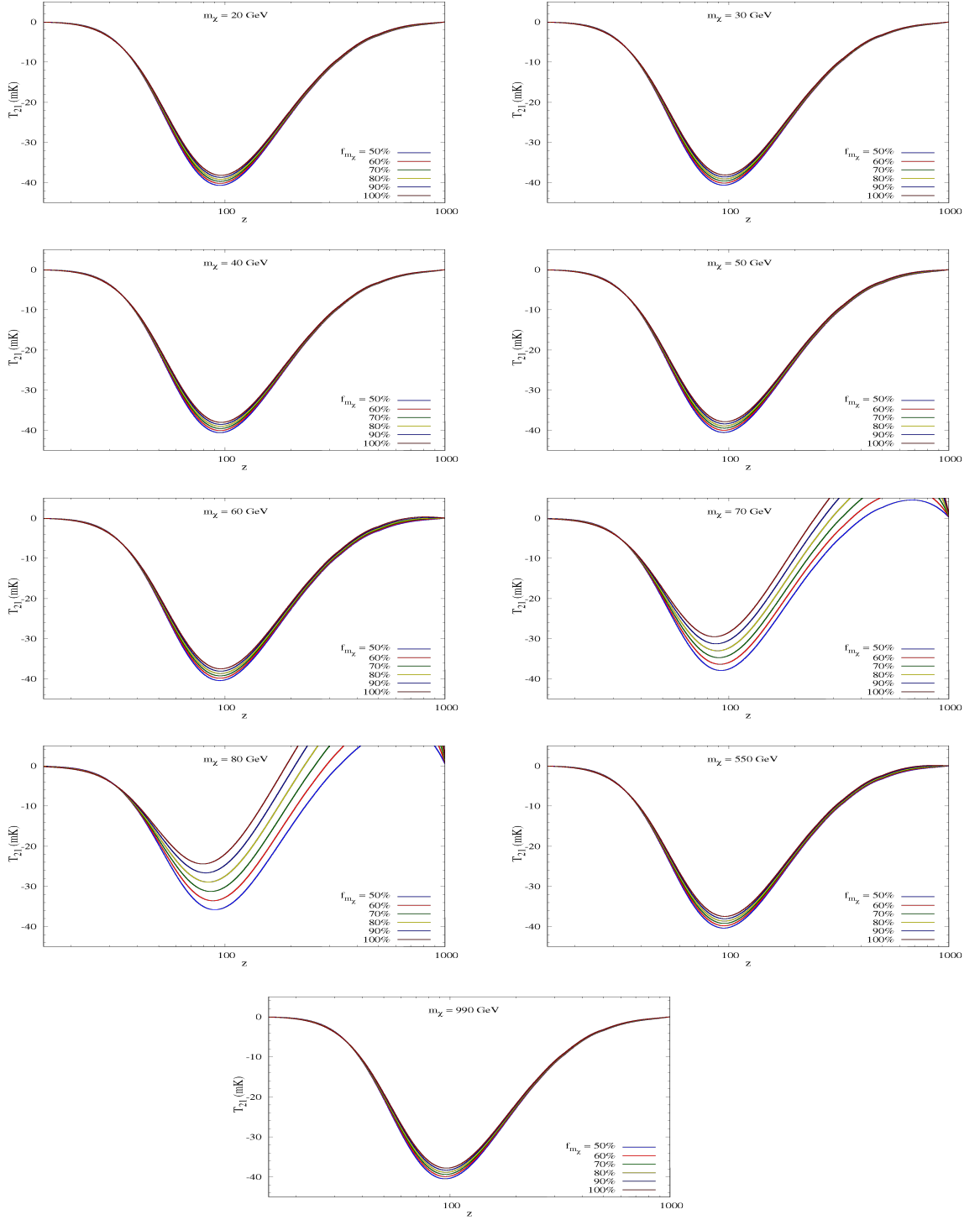


Figure 3.7: The variation in the 21-cm absorption lines T_{21} due to the combined effect of different fractions of IDM masses $f_{m_{\chi}}$.

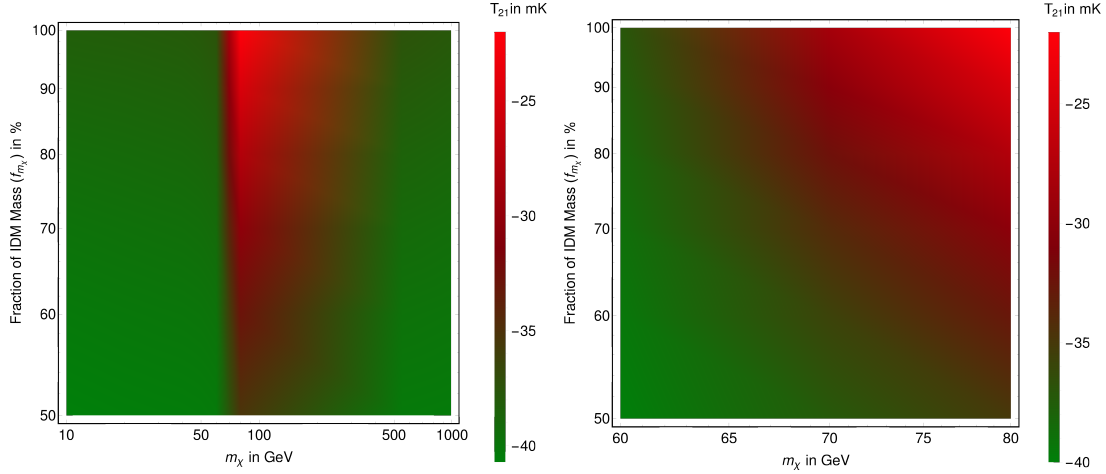


Figure 3.8: Variations of T_{21} across different fractions of IDM masses f_{m_x} .

Finally, fig. 3.8 provides a contour plot of T_{21} variations for different IDM fractions, highlighting the trends observed for various masses, particularly in the narrower 60-80 GeV range for clarity.

In summary, this analysis highlights the distinctive behaviour of 21-cm brightness temperature fluctuations for IDM dark matter masses, especially in the 70-80 GeV range, and underscores the combined effects of dark matter annihilation and collisions on T_{21} throughout cosmic history.

3.4 Lower bound on annihilation cross-section of IDM

The calculations outlined in Sec. 3.3 are based on the annihilation cross-sections of IDM masses provided in the Table 3.1

For the calculations, the mass of the Higgs portal IDM dark matter is initially set to a few tens of GeV. However, following the approach in Ref. [182, 183], which includes IDM dark matter masses in the hundreds of GeV, we have expanded our analysis to include higher mass IDM candidates ($\gtrsim 500$ GeV) [183]. The relic densities of these

m_χ (GeV)	Ω_c	$\langle\sigma v\rangle$ $\text{cm}^3 \text{s}^{-1}$
10	0.113	6.50×10^{-29}
20	0.116	7.72×10^{-29}
30	0.114	9.98×10^{-29}
40	0.116	1.65×10^{-28}
50	0.115	4.37×10^{-28}
60	0.116	1.40×10^{-27}
70	0.119	1.72×10^{-26}
80	0.113	2.59×10^{-26}
550	0.115	6.68×10^{-26}
990	0.113	4.88×10^{-26}

Table 3.1: The relic density (Ω_c) and the corresponding annihilation cross section ($\langle\sigma v\rangle$) for various IDM dark matter masses (m_χ) are provided, ensuring that Ω_c falls within the 95% confidence interval of $\Omega_{c,0}$ as determined by the Planck experiment [45].

IDM dark matter candidates were calculated using the microOMEGAS code [205] and compared with the relic densities obtained from Planck observational results [45]. We selected the IDM dark matter masses whose calculated relic densities fall within the 95% confidence limits of the Planck results. These masses, along with their corresponding annihilation cross-sections, are presented in Table 3.1. Additionally, fig. 3.9 displays the annihilation cross-sections for various IDM masses that meet the Planck relic density criteria within the 95% confidence limits.

Our calculated relic densities lie within the 95% confidence limit of the Planck experiment’s dark matter relic density (see Table 3.1). For different IDM dark matter fractions, we observed that for 100% IDM dark matter contribution, the dip in T_{21} for the combined effect reaches its minimum at $z \sim 95$ (Fig. 3.7). From these observations, we derived a lower bound on the IDM dark matter annihilation cross section. This lower bound lies within the range $\langle\sigma v\rangle \sim (6.5 \times 10^{-29}) - (4.88 \times 10^{-26}) \text{ cm}^3/\text{sec}$ for a DM mass range of $m_\chi \sim 10 - 990 \text{ GeV}$.

Also the evolution of T_{21} exhibits lower values at lower redshifts (z) when only dark matter annihilation effects are considered. Specifically, T_{21} shows a minimum around

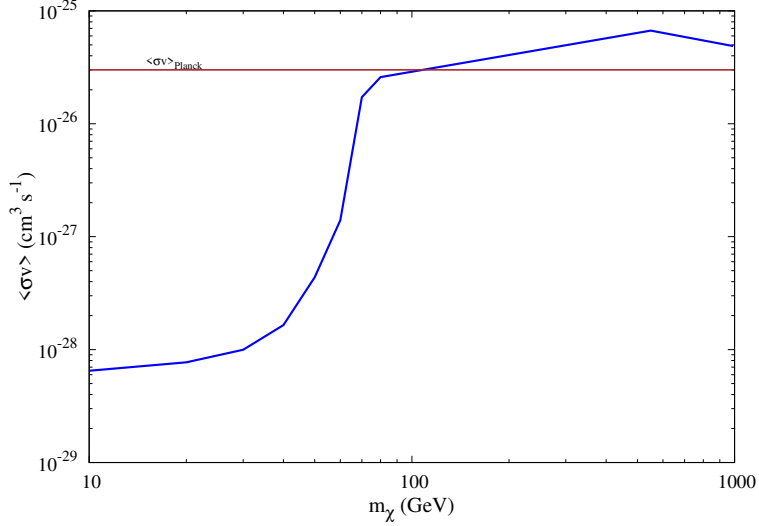


Figure 3.9: The annihilation cross section $\langle\sigma v\rangle$ for various dark matter masses m_χ . The brown curve represents the range of $\langle\sigma v\rangle$ estimated from Planck experiments [206, 207].

the epoch of reionization for dark matter masses in the range of approximately 70 to 80 GeV. The influence of baryon-dark matter collisions appears more pronounced at lower redshifts, manifesting as a dip in the T_{21} evolution around $z \sim 95$ for all chosen masses.

When both annihilation and collision effects are combined, the dominance of collision effects is noticeable around $z \sim 100$, beyond which annihilation effects become more prominent. The impact of different fractions of IDM on the evolution of T_{21} is generally minor for most chosen masses, except for IDM dark matter masses around 70 and 80 GeV. In these cases, variations in the minima of T_{21} with different fractions of IDM dark matter remain within approximately 20% to 25%.

These findings suggest that T_{21} shows heightened sensitivity in the IDM dark matter mass range of approximately 70 to 80 GeV when considering both dark matter collision and annihilation effects.

Bounds on Scattering cross-section of Two component dark matter

Two-component dark matter models propose that dark matter is composed of two distinct types of particles, each contributing to the total dark matter density in the Universe. This approach addresses limitations of single-component models by potentially explaining a wider range of astrophysical observations and anomalies. Each component in the model interacts through different mechanisms, such as weak or gravitational forces, allowing for a more complex and nuanced interaction profile with ordinary matter and among themselves. This dual-component framework enhances our understanding of dark matter's role in the cosmos, providing new avenues for theoretical research and experimental detection efforts. In this chapter, the thesis delves into the intricate interplay between two distinct components of dark matter namely generic dark matter and the Inert Doublet Model (IDM) which are mutually non-interactive. This scenario explores how these components interact with baryons within the cosmic landscape, impacting the thermal history and reionization epochs observed through the 21cm signal. By scrutinizing the annihilation and scattering properties specific to IDM, the study elucidates their contributions to cosmic evolution, offering crucial insights on bounds on dark matter-baryon cross-section for two

component dark matter using brightness temperature (T_{21}) reported by EDGES at reionization epoch.

4.1 Introduction

Despite being a well-established presence in the Universe, dark matter persists as a captivating mystery in astrophysics.. Researchers have proposed various candidates, such as weakly interacting massive particles (WIMPs) or axions, but conclusive evidence regarding the true nature of dark matter is yet to be discovered. Scientists continue to explore and conduct experiments to unravel this enigmatic aspect of the cosmos. The concept of multicomponent dark matter suggests that dark matter might not be made up of just one type of particle but could consist of various components with distinct properties. Recent analyses and studies have indeed hinted at the possibility of a multicomponent nature of dark matter, adding more complexity to the quest of understanding its composition and behaviour within the Universe. These findings open up new avenues for exploration and further research in the field of astrophysics. Exploring the potential existence of multicomponent dark matter adds depth to our understanding of the Universe's structure. In our recent works [185],[208] , this had been shown that there is a possibility of existence of multicomponent dark matter. Studying a two-component dark matter model, specifically involving an IDM dark matter alongside a generic type is worthwhile to explore. Investigating their existence and constraints within the context of the 21cm signal is an innovative way to understand their properties and potential interactions. The 21cm hydrogen absorption line, also known as the HI (atomic hydrogen) 21cm line, is a specific spectral line corresponding to the transition between two hyperfine energy levels of the ground state of neutral hydrogen atoms. Hydrogen atoms consist of a single proton in the nucleus and an electron orbiting the nucleus. The spins of the electron and the proton can align either parallel ($s = 0$ or singlet state) or antiparallel ($s = 1$ or triple state) to each other, resulting in different energy states within the ground state of the hydrogen atom. The 21cm line emerges as a significant probe for

comprehending the Universe's evolution owing to hydrogen constituting roughly 75% of the visible Universe. This spectral line proves instrumental in investigating cosmic processes, particularly in the observation of Cosmic Microwave Background Radiation (CMBR) and celestial entities like pulsars, enabling deeper insights into the Universe's developmental mechanisms. Given the Cosmic Microwave Background's temperature (T_γ) acting as the background, the brightness temperature (T_{21}) of the 21cm absorption line during the era of redshift z is expressed as

$$T_{21} = \frac{T_s - T_\gamma}{1 + z}(1 - e^{-\tau}) \quad (4.1)$$

The evolution of the 21cm brightness temperature T_{21} relies on both energy injection or heating and energy absorption or cooling within the system. Alterations in the background temperature T_γ or spin temperature T_s or both, modify the temperature T_{21} itself. Details of the discussion have been made in Chapter 2.

During the recombination era around redshift $z \sim 1100$, matter and radiation were expected to decouple, enabling photons to free stream. However, the substantial number of photons led to continued Compton scattering, coupling radiation to matter until about $z \sim 200$. Around this time, the Compton heating timescale surpassed the Hubble time, causing the matter temperature ($T_m \sim (1 + z)^2$) to decrease more rapidly than the radiation temperature ($T_\gamma \sim (1 + z)$).

The spin temperature (T_s), coupled to the background Cosmic Microwave Background (CMB), decoupled approximately at $z \sim 20$ during the reionization era with the emergence of the first stars. At this point, transitions from triplet to singlet states, mediated by Lyman-alpha ($\text{Ly}\alpha$) photons induced by the ultraviolet (UV) emission of the first stars through the Wouthuysen-Field effect, caused the spin temperature to align closely with the baryon temperature ($T_s \simeq T_b$).

The EDGES experiment [173] reported an excessive trough in the 21cm absorption line at a frequency of 78 MHz (redshifted 21cm line) within the cosmic dawn period

($14 < z < 20$). This anomaly, occurring at an average z of 17.2, exhibited a T_{21} measurement of $T_{21} = -500_{-500}^{+200}$ at the 99% confidence limit (C.L.), deviating significantly from the expected T_{21} ($T_{21} \simeq -200$ K) as per standard cosmology. Hence, the reported results by the EDGES experiment are approximately 3.8σ below the anticipated T_{21} value.

Given $T_{21} \sim T_s - T_\gamma$, the observed negative trough in T_{21} could occur if T_s decreases or T_γ increases. Dark matter-baryon collisions may modify T_s during the reionization epoch, whereas dark matter self-annihilation might impart heat to the system, ultimately altering T_{21} .

Our study addresses the observed excess trough in the 21cm temperature (T_{21}) due to dark matter-baryon collisions and dark matter annihilation. While previous studies [180, 209, 190, 170, 179, 178] have attempted to explain this anomaly using dark matter-baryon scattering and annihilation, our work specifically focuses on a two-component dark matter scenario. The two component dark matter model of Universe are the IDM dark matter and generic dark matter (~ 3 GeV) [203] which are *mutually non-interactive*. For IDM dark matter the lighter neutral scalar from this doublet, the inert Higgs, serves as the dark matter candidate, constituting one component of the two-component dark matter scenario. We also explore how different fractional components and masses of the IDM dark matter contribute to the 21cm signal. The IDM fraction and mass are constrained by the EDGES results at the 99% C.L., determining limits on the IDM's annihilation cross-section and masses within the EDGES's error limit (99%). Throughout, we ensure that the dark matter relic density, as determined by Planck satellite experiments [45], adheres to the constraints in our two-component dark matter scenario of the Universe.

The uncertainty in the global brightness temperature T_{21} detected by EDGES experiments has prompted investigations into the possible influence of dark matter, specifically its collisions with baryons and annihilations, which can exchange heat and subsequently modify T_s or T_γ . We consider a scenario where the Universe's

dark matter comprises IDM dark matter (with mass m_χ) and a generic dark matter candidate with mass m_{DM} . These two components do not interact with each other. The generic dark matter candidate is model-independent, and there is no mutual interaction between these two dark matter components.

The IDM model extends the scalar sector of the Standard Model by adding an extra SU(2) doublet that does not acquire a vacuum expectation value (vev) upon spontaneous symmetry breaking (SSB). After symmetry breaking and through appropriate unitary gauge transformations on the scalar doublets, we get

$$H_1 = \begin{pmatrix} 0 \\ \frac{h+v}{\sqrt{2}} \end{pmatrix}, \quad H_2 = \begin{pmatrix} H^+ \\ \frac{S+iA}{\sqrt{2}} \end{pmatrix}.$$

Here, h is the physical Higgs boson, while v is the vev. For the other doublet H_2 , S is a CP-even scalar and A is a pseudoscalar. Either S or A could be a viable dark matter candidate if their stability is ensured. To achieve this, a discrete Z_2 symmetry is imposed on the model, making the doublet H_2 Z_2 -even while the Standard Model (SM) particles are Z_2 -odd. Consequently, H_2 cannot decay into SM fermions and cannot induce mass to the fermions after SSB since H_2 does not obtain a vev.

The parameters of the model, which are the interaction couplings in the interaction Lagrangian, are constrained by theoretical bounds (such as perturbativity bound with coupling $|\lambda_i| < 4\pi$, vacuum stability, and unitarity bound) and experimental bounds, including the Planck results for dark matter relic density, collider bounds, and the upper limits on dark matter-nucleon scattering cross-section from direct dark matter search experiments. It is notable that the IDM model for dark matter is a Higgs portal model, meaning the dark matter scalar candidate in this model interacts with the SM through the Higgs portal. Details discussion of IDM dark matter and thermal evolution of 21cm brightness temperature were given in Chapter 3 and Chapter 2 respectively.

4.2 Thermal Evolution

Recent findings from the EDGES experiment have unveiled a notable absorption signal in the global 21cm hyperfine transition spectrum of neutral hydrogen at redshift $z = 17.2$ [173]. This absorption feature, detected around 78.2 MHz, aligns closely with the redshift $z \sim 17.2$ and exhibits a striking 3.8σ deviation from predictions based on the standard Λ CDM model. During the cosmic dawn epoch (approximately $15 \leq z \leq 35$) [210], especially around $z \sim 20$ when the first stars formed, cosmic hydrogen gas reached its coldest point prior to X-ray radiation influence. This radiation ionized neutral hydrogen, ending the 'Dark Ages' and initiating the reionization epoch, illuminating the Universe. The 21cm hydrogen line originates from the hyperfine transition between ortho (parallel spins) and para (anti-parallel spins) states of hydrogen's ground state. During reionization, the spin temperature T_s of hydrogen gas coupled with the cooler surroundings, resulting in the 21cm absorption line observed against the Cosmic Microwave Background (CMB) radio background. Whether the spin temperature aligns with the background radio temperature determines emission or absorption in the 21cm HI spectrum.

The discrepancy between experimental observations [173] and the predictions of the standard model [169] regarding the brightness temperature of redshifted 21cm hydrogen absorption spectra has spurred intense investigations into early Universe physics, particularly during the cosmic 'dark ages'. Given that approximately $\frac{3}{4}$ of the known Universe is composed of hydrogen gas, accurate 21cm measurements are crucial for understanding cosmic evolution and hydrogen gas temperature dynamics. The intensity of the 21cm signal hinges on the population ratio of triplet and singlet states, characterized by the spin temperature T_s , which is interlinked with the CMB temperature T_{CMB} and the optical depth τ of the intervening medium.

Around $z \sim 200$, cosmic gas decoupled from the CMB, experiencing a temperature decline below the radiation temperature due to adiabatic cooling. The unexpected cooling observed in the 21cm signal by EDGES provides a promising avenue for

probing cosmic history during the cosmic dawn era. Investigating the impact of baryon-dark matter interactions and the decay of dark matter during this epoch using the 21cm signal remains an active area of research. The global 21cm signal detected by EDGES during the cosmic dawn appeared notably cooler than anticipated by the standard Λ CDM cosmological model which may be attributed to a mechanism involving heat transfer from baryons or surroundings either by scattering or annihilation. This study focuses on two component dark matter scenarios, where interactions with baryons or surroundings could lead to substantial cooling or heating of the baryonic fluid once Lyman-alpha radiation becomes prevalent [203], but on the other hand they do not interact with one another.

Scenarios involving strong velocity-dependent dark matter-baryon scattering, such as Rutherford-like interactions, could yield distinctive 21cm signals during the cosmic dark ages while maintaining consistency with current astrophysical and cosmological constraints. Conversely, models involving Yukawa-type scattering potentials exhibit a velocity-dependent scattering cross-section $\sigma = \sigma_0 v^n$, where n varies depending on the nature of dark matter [198, 199, 200, 201, 211]. For instance, magnetized dark matter displays $n = \pm 2$, while millicharged dark matter exhibits $n = -4$ [196, 197, 212, 213, 214, 215]. This v^{-4} dependence is also evident in Rutherford-like dark matter-baryon scattering [180].

Dark matter (DM) components interact with baryons by heating them through DM annihilation and DM-baryon scattering. The total abundance of dark matter in the Universe at the current epoch is approximately $\Omega_{c,0} \approx 0.26$. Let f_χ and f_{DM} denote the fraction of ‘Inert Doublet Model’ dark matter (IDM) and the other model-independent dark matter component (which is described as generic dark matter in this chapter), respectively, such that $f_\chi + f_{DM} = 1$ and $\Omega_{c,0} h^2 = \Omega_\chi h^2 + \Omega_{DM} h^2$, representing the total abundance of dark matter. These two component are mutually interacting with each other but they are individually interact with baryon either through scattering or through annihilation. The total energy density of dark matter in the Universe, ρ_t , can be expressed as $\rho_t = f_\chi \rho_t + f_{DM} \rho_t$. Thus, the energy densities

of IDM dark matter (denoted in this chapter as χ) and the other generic component (denoted in this chapter as DM) are $f_\chi \rho_t$ and $f_{DM} \rho_t$, respectively.

To analyse the thermal evolution of the Universe, we compute the evolution of the dark matter temperatures T_χ and T_{DM} , and the baryon temperature T_b with cosmological redshift z . Considering energy injection from DM annihilation and baryon-DM scatterings for both IDM and the generic DM component, the evolution equations for T_χ , T_{DM} , and T_b [180] are given by

$$(1+z) \frac{dT_\chi}{dz} = 2T_\chi - \frac{2\dot{Q}_\chi}{3H(z)}, \quad (4.2)$$

$$(1+z) \frac{dT_{DM}}{dz} = 2T_{DM} - \frac{2\dot{Q}_{DM}}{3H(z)}, \quad (4.3)$$

$$(1+z) \frac{dT_b}{dz} = 2T_b + \frac{\Gamma_c}{H(z)} (T_b - T_\gamma) - \frac{2\dot{Q}_{b\chi}}{3H(z)} - \frac{2\dot{Q}_{bDM}}{3H(z)} - \frac{1}{H(z)} \frac{dE}{dVdt} \Big|_{\text{inj}_\chi} \frac{1}{n_H} \frac{2f_{\text{heat}}(z)}{3(1+x_e+f_{\text{He}})} - \frac{1}{H(z)} \frac{dE}{dVdt} \Big|_{\text{inj}_{DM}} \frac{1}{n_H} \frac{2f_{\text{heat}}(z)}{3(1+x_e+f_{\text{He}})}, \quad (4.4)$$

where \dot{Q}_χ and \dot{Q}_{DM} represent the heating rates due to IDM and other DM component interactions with baryons, respectively.

The evolution of x_e is given by

$$(1+z) \frac{dx_e}{dz} = \frac{C}{H(z)} (n_H \mathcal{A}_B x_e^2 - 4(1-x_e) \mathcal{B}_B e^{(-3E_0/4T_\gamma)}), \quad (4.5)$$

where C and E_0 are the Peebles factor and the ground state energy of hydrogen, respectively. The effective recombination coefficient $\mathcal{A}_B(T_b, T_\gamma)$ and the effective photoionization rate $\mathcal{B}_B(T_\gamma)$ account for recombination and photoionization processes.

4.2.1 Heating Rates and Drag Terms

The heating rates of baryons due to IDM and other DM components are $\dot{Q}_{b\chi}$ and \dot{Q}_{bDM} , respectively. The heating rates for DM components due to baryon-DM interactions are \dot{Q}_χ and \dot{Q}_{DM} . These rates depend on the temperature differences and relative velocities between the fluids. Following photon decoupling in the early Universe, dark matter and baryons develop a relative velocity $V_{\chi b}$, resulting in a drag effect between the two. Each dark matter can experience elastic scattering similar to Rutherford scattering, with a cross-section that varies significantly with velocity, described by v^{-4} [180, 203, 204]. The scattering cross-section is given by

$$\sigma = \sigma_0 v^{-4} = (\sigma_{41} \times 10^{-41} v^{-4}) \text{ cm}^2, \quad (4.6)$$

where the dimensionless parameter $\sigma_{41} = \frac{\sigma_0}{10^{-41}}$. The evolution equations for the drag terms $V_{\chi b} \equiv V_\chi - V_b$ and $V_{DMb} \equiv V_{DM} - V_b$ are

$$\frac{dV_{\chi b}}{dz} = \frac{V_{\chi b}}{1+z} + \frac{D(V_{\chi b})}{(1+z)H(z)}, \quad (4.7)$$

$$\frac{dV_{DMb}}{dz} = \frac{V_{DMb}}{1+z} + \frac{D(V_{DMb})}{(1+z)H(z)}, \quad (4.8)$$

where $D(V_{\chi b})$ and $D(V_{DMb})$ are the drag terms given by

$$D(V_{\chi b}) = \frac{d(V_{\chi b})}{dt} = \frac{\rho_m \sigma_0}{m_b + m_\chi} \frac{1}{V_{\chi b}^2} F(r), \quad (4.9)$$

$$D(V_{DMb}) = \frac{d(V_{DMb})}{dt} = \frac{\rho_m \sigma_1}{m_b + m_{DM}} \frac{1}{V_{DMb}^2} F_1(r_1). \quad (4.10)$$

In these equations, $\rho_m = \rho_b + \rho_\chi + \rho_{DM}$ and the functions $F(r)$ and $F_1(r_1)$ are given by

$$F(r) = \operatorname{erf}\left(\frac{r}{\sqrt{2}}\right) - \sqrt{\frac{2}{\pi}} r e^{-r^2/2}, \quad (4.11)$$

$$F_1(r_1) = \operatorname{erf}\left(\frac{r_1}{\sqrt{2}}\right) - \sqrt{\frac{2}{\pi}} r_1 e^{-r_1^2/2}, \quad (4.12)$$

with $r = V_{\chi b}/u_{\text{th}}$, $u_{\text{th}}^2 = T_b/m_b + T_\chi/m_\chi$, $r_1 = V_{DMb}/u_{\text{th}1}$, and $u_{\text{th}1}^2 = T_b/m_b + T_{DM}/m_{DM}$.

4.2.2 Energy Injection from Dark Matter Annihilation

The energy injection rate per unit volume from DM annihilation, which affects the baryons through ionization, heating, or excitation [170, 179], is given by

$$\left. \frac{dE}{dV dt} \right|_{\text{inj}_i} = f_i^2 \rho_{i,0}^2 (1+z)^6 \frac{\langle \sigma v \rangle_i}{m_i} \quad \text{where } i = \chi, DM \quad (4.13)$$

where ρ_i is the energy density of the interacting dark matter component i (IDM or the other component) and $\langle \sigma v \rangle$ is the velocity-averaged annihilation cross-section. The $\langle \sigma v \rangle_\chi$ is calculated using the microOMEGAS code [205] and tabulated in Chapter 3 in Table 3.1 and for generic DM is estimated by using the cosmic relic of the dark matter species [216, 217, 218].

The evolution equations for T_χ , T_{DM} , and T_b incorporate the effects of heating and drag due to baryon-DM interactions and energy injection from DM annihilation. These equations are coupled and depend on several cosmological parameters, including the Hubble parameter $H(z)$, the baryon-to-photon ratio x_e , and the relative velocities $V_{\chi b}$ and V_{DMb} . Solving these equations provides insights into the thermal

history of the Universe, particularly during epochs relevant to CMB observations and the formation of the cosmic structures.

4.3 Bounds on Scattering cross-section

To investigate the impact of baryon-dark matter interactions on the 21cm signal for two component dark matter which are mutually non-interacting, we set benchmark values for the baryon-DM scattering cross-section for both generic dark matter and Inert Doublet Model dark matter (IDM). The allowed range for the brightness temperature T_{21} is chosen as -500^{+200}_{-500} mK. The mass range for generic dark matter is taken as $0 < m_{\text{DM}} \leq 3$ GeV, while the IDM mass range is $10 \leq m_{\chi} \leq 80$ GeV. The benchmark value for the scattering cross-section is set to $\sigma_0^{(DM,\chi)} = 1 \times 10^{-41}$ cm², therefore $\sigma_{41}^{(DM,\chi)} = \frac{\sigma_0^{(DM,\chi)}}{10^{-41}}$. The benchmark values for our analysis is .

m_{DM} (GeV)	m_{χ} (GeV)	σ_0^{DM} (cm ²)	σ_0^{χ} (cm ²)
0.5	10-80	1×10^{-41}	1×10^{-41}
1.0	10-80	1×10^{-41}	1×10^{-41}
1.3	10-80	1×10^{-41}	1×10^{-41}

Table 4.1: Benchmark values of generic dark matter masses m_{DM} , IDM mass m_{χ} , IDM-baryon scattering cross-section σ_0^{χ} and generic dark matter-baryon scattering cross-section σ_0^{DM} .

In the present case, two components of dark matter is considered, one of these is Inert Doublet Model or IDM dark matter and other is generic dark matter. While the mass of the IDM DM can be any things between ~ 20 to 80 GeV [110], the mass of the generic DM could only vary upto about 3 GeV[203]. Thus the dominant effect of IDM on the 21cm signal brightness temperature will be via the self annihilation of IDM DM while the scattering of baryons with DM dominates in the case of generic dark matter. While the former process involving the IDM DM is associated with the heating of baryons, the latter process involves cooling of the baryons, takes away the heat from baryon.

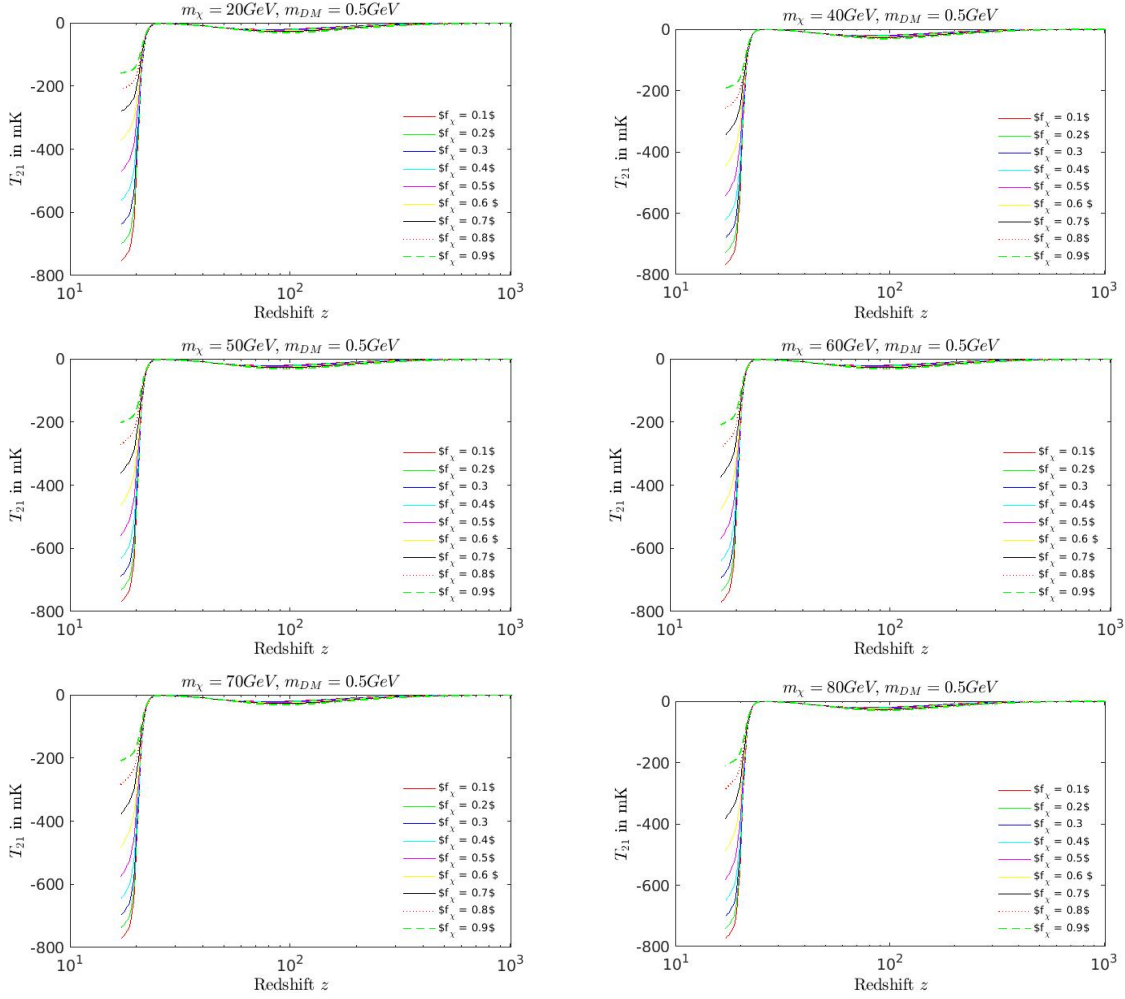


Figure 4.1: The variation of brightness temperature the 21cm lines T_{21} due to the two component dark matter of different fractions of IDM masses f_{m_χ} . For each plot we considered the benchmark points described in Table 4.1. Different colour represents different fraction of IDM masses.

As we can see from fig. 4.1, as the fraction of IDM component of the present two component dark matter scenario, the temp T_{21} tends to increase more in the redshift region of interest (in the reionization epoch). This is evident from fig. 4.2(a) where IDM fraction f_χ is plotted against the mass m_{DM} of generic dark matter that satisfy the different T_{21} temperature (colour code). In addition, this fig. 4.2(a) also demonstrates the effect of the variation of m_{DM} on the fractional component of IDM. This can be seen that, more the value of m_{DM} is (within ~ 3 GeV, as for $m_{DM} > 3$ GeV, the calculated T_{21} goes beyond the observed range of T_{21} by EDGES), more

is the IDM fraction required for T_{21} to be within the EDGES result for T_{21} . This means, more massive the generic DM is, more dominant is its cooling effect which is compensated by the heating effect of IDM.

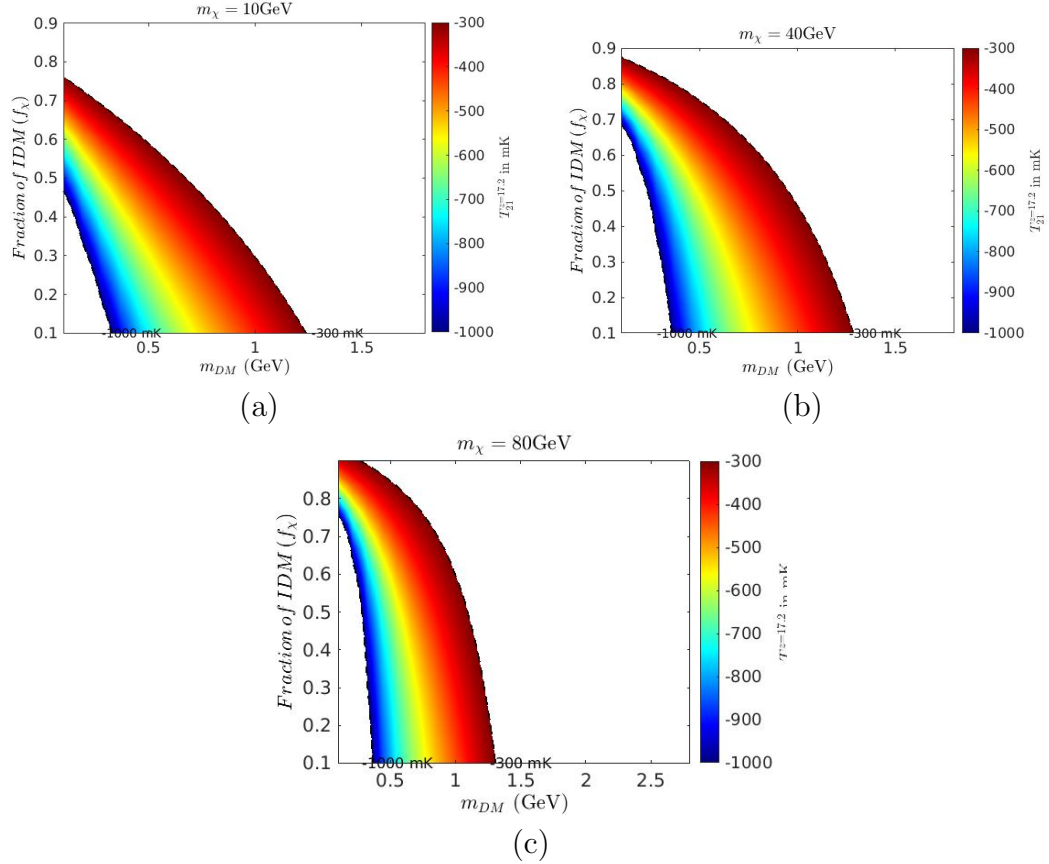


Figure 4.2: Variations of fraction of IDM mass with generic dark matter mass for a constant IDM mass at redshift $z = 17.2$ within the EDGES experimental result limit. Other parameters values were taken for this calculation is given in Table 4.1.

Fig. 4.2(b) and fig. 4.2(c) are similar to fig. 4.2(a) but for different fixed IDM masses. From fig. 4.2(a)-4.2(c), it can be concluded that massive the the IDM dark matter, more fraction of its is required to obtained a particular T_{21} value. Also, the central value of T_{21} as given by EDGES experiment is achieved when the given generic dark matter mass is around 0.75 GeV.

As IDM masses varies, we can see that there is a upper bound for generic dark matter masses for the brightness temperature will be within the range of EDGES

experiment result ($T_{21} = -500^{+200}_{-500}$) mK for a constant scattering cross-section for both IDM and generic DM. In our work, the evaluated upper bound of generic dark matter mass for the scattering cross-section $\sigma_0^\chi = \sigma_0^{DM} = 1 \times 10^{-41}$ can not be more than ~ 1.3 GeV. This put an upper bound for generic dark matter mass.

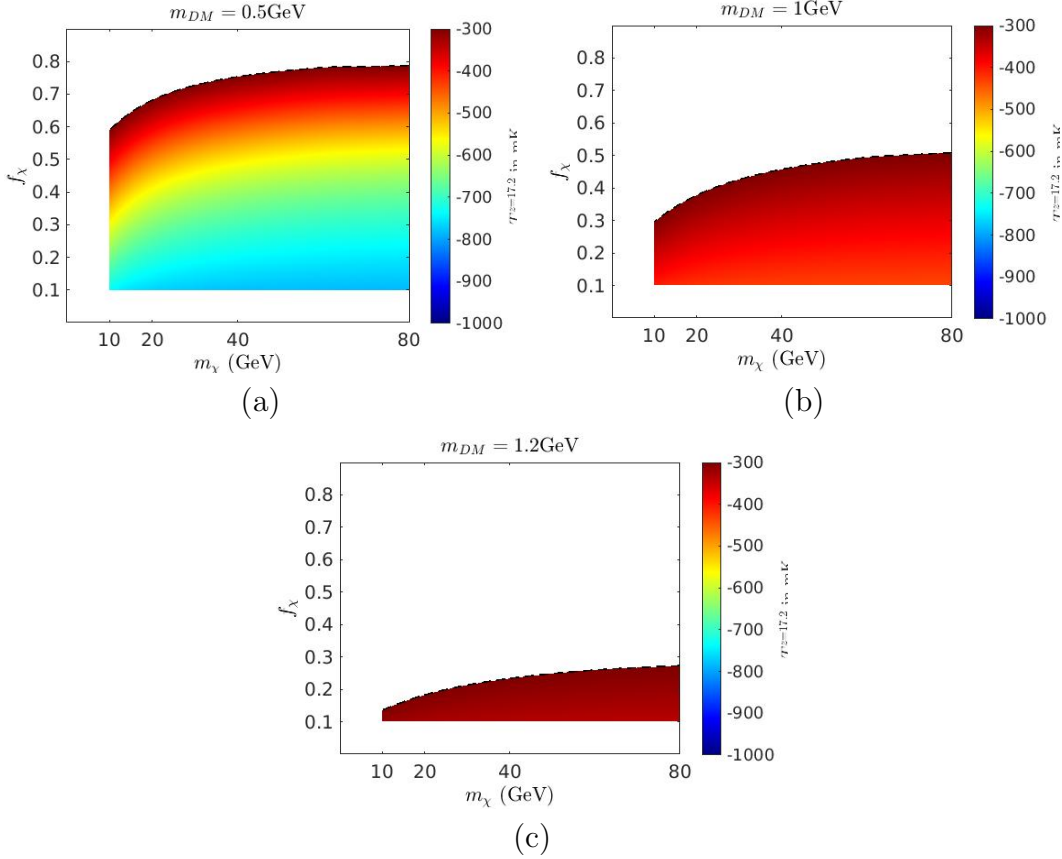


Figure 4.3: Variations of fraction of IDM mass with IDM dark matter mass for a constant generic DM mass at redshift $z = 17.2$ within the EDGES experimental result limit. Other parameters values were taken for this calculation is given in Table 4.1.

Adopting the benchmark values of σ_0^χ and σ_0^{DM} from Table 4.1, the calculations are made using eqs. 4.2, 4.3 and 4.4 to obtain the variations of IDM mass fraction corresponds to the IDM mass for different generic dark matter masses. The results are shown in fig. 4.3. Needless to mention that the plots of fig. 4.3 are obtained using the bounds on brightness temperature T_{21} (-1000 mk to -300 mK) of EDGES experiments results at redshift 17.2. From fig. 4.3(a), we can see that the fraction of IDM dark matter almost becomes constant at higher IDM masses, and the bound

on 21cm brightness temperature from EDGES experiments also constraints a bound on fractional mass of IDM dark matter for which EDGES results has been satisfied. From fig. 4.3, we can conclude that for a particular set of benchmark points (Table 4.1) there is upper bounds of the fraction of IDM contributions. These upper bounds are $f_\chi \sim 0.75, 0.45$ and 0.25 for the figs. 4.3(a), (b) and (c) respectively. It has been seen from fig. 4.3 that as the generic dark matter mass increases, the allowed region for the fraction of mass shifts towards the lower value (colour band) of brightness temperature of EDGES results. This can be understood from the facts that higher m_χ gives rise to more heating effect which is compensated by the cooling effect due to the given generic dark matter masses.

According to fig. 4.1 to fig. 4.3, we have concluded that when generic dark matter mass is 0.5 GeV and fraction of IDM mass is 0.2 , all the IDM mass ranges (10 GeV - 80 GeV) lie within the bound of brightness temperature predicted by the EDGES experiments ($T_{21}^{z=17.2} = -500|_{-500}^{+200}$) at the redshift $z = 17.2$. This happens because at the given redshift $z = 17.2$, the cooling effect is much more than the heating effect. Hence for the further analysis we adopt the fraction of IDM mass $f_\chi = 0.2$ and $m_{DM} = 0.5$.

Fig. 4.4(a) to fig. 4.4(d) demonstrate the allowed region in $\sigma_{41}^\chi - \sigma_{41}^{DM}$ plane for fixed values of m_{DM} , m_χ and fraction of IDM mass f_χ . One notices from these plots the allowed region is barely contracted with σ_{41}^{DM} as m_{DM} values change from 0.5 GeV (Fig. 4.4(a)) to 1 GeV (Fig. 4.4(d)). Hence from these changes and using the limits of T_{21} from EDGES result at $z = 17.2$, we have set an upper and a lower bound for σ_{41}^{DM} , beyond which the EDGES result is not satisfied. So the range of σ_0^{DM} is $\sim 3 \times 10^{-42} \lesssim \sigma_0^{DM} \lesssim 10^{-39} \text{ cm}^2$. This is also evident that when m_{DM} is shifted from 0.5 GeV to 1 GeV, the central value (and the values at its uncertainty) of T_{21} (as reported by EDGES experiments) is always towards the upper limit of T_{21} range. This is caused by enhanced heating effect by a more massive generic DM component. Also from fig. 4.4, we calculated an upper boundary of IDM-baryon

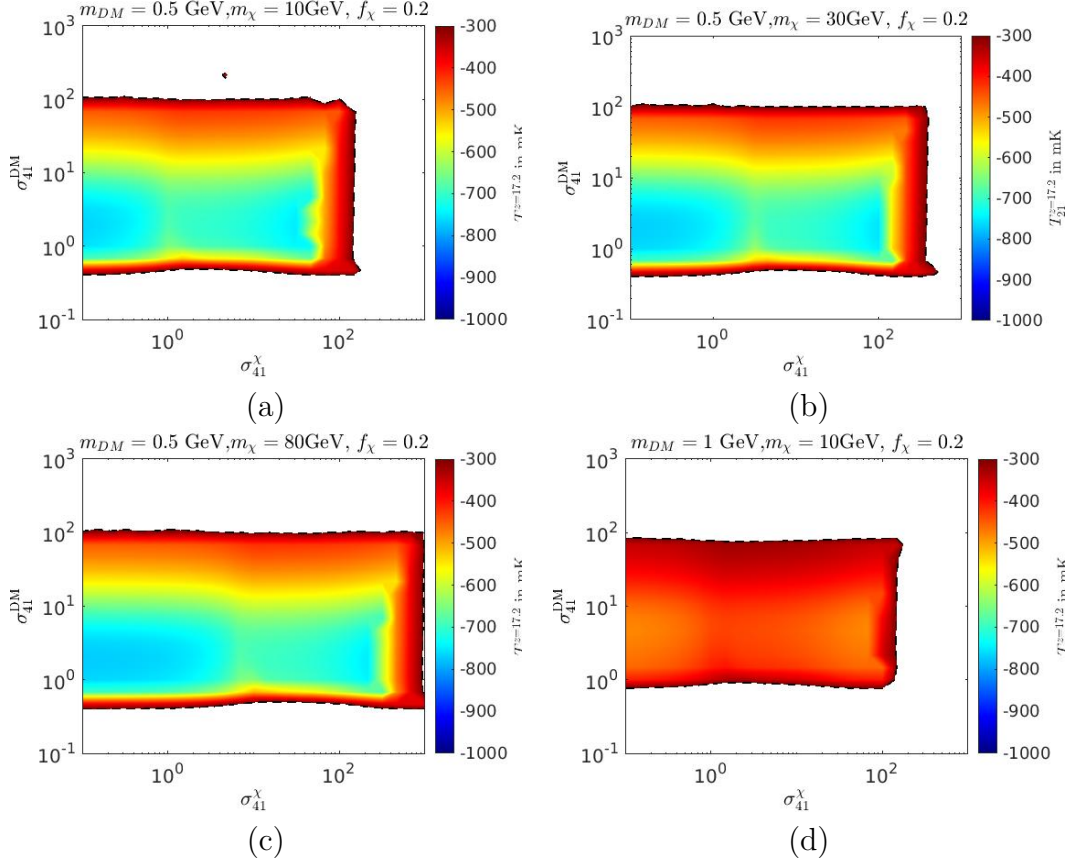


Figure 4.4: Variations of IDM dark matter- baryon scattering cross-section σ_{41}^x with generic DM - baryon scattering cross-section σ_{41}^{DM} at redshift $z = 17.2$ within the EDGES experimental result limit. Other parameters values were taken for this calculation is $f_\chi = 0.2$, $m_\chi = 10$ GeV, 30 GeV and 80 GeV and $m_{DM} = 0.5$ GeV and 1 GeV.

scattering cross-section σ_0^x for above mentioned particular benchmark points. The upper value of IDM-baryon scattering cross-section $\sigma_0^x < 10^{-38} \text{cm}^2$.

In summary, this thesis offers extensive insights into the intricate interplay between baryon-dark matter interactions and their implications for the 21cm signal, elucidating the varying impacts of different dark matter scenarios on cosmic reionization and the thermal history of the Universe.

Exploring Elder Dark Matter in the Context of 21cm Cosmology

Elastically Decoupling Relic (ELDER) dark matter is a cold thermal relic whose present-day abundance is primarily determined by its elastic scattering cross-section with Standard Model (SM) particles. The predicted mass of ELDER dark matter ranges from a few to several hundred MeV, with an elastic scattering cross-section in the range of $10^3 - 1$ fb.

Similar to the Strongly-Interacting Massive Particle (SIMP) model for dark matter, ELDER presents a well-defined target for future searches of sub-GeV dark matter and dark photons. This dark matter is explored in this chapter in the context of the EDGES result for 21cm HI signal from the reionization era of the Universe. This has been discussed earlier (2) that EDGES experiments reported a visual dip in the HI 21cm line brightness temperature at the reionization era. This dip has been explored by taking into consideration the effect of dark matter-baryon scattering, dark matter self annihilation and additionally dark matter self scattering. In this context the bounds on dark matter self scattering coupling are addressed using the EDGES results.

5.1 Introduction

Observations from the EDGES experiment have revealed a significant absorption signal in the global 21cm hyperfine transition spectrum of neutral hydrogen around redshift $z = 17.2$ [173]. This absorption spectrum, centred at a frequency of approximately 78.2 MHz, corresponds to the redshift $z \sim 17.2$. The reported result from EDGES indicates a 3.8σ deviation from the prediction of the standard Λ CDM model.

During the epoch of cosmic dawn (approximately $15 \leq z \leq 35$) [210], particularly around $z \sim 20$ when the first stars formed, the cosmic hydrogen gas was at its coolest point before being influenced by X-ray radiation. This radiation ionized the neutral hydrogen, marking the end of the “Dark Ages” and the onset of the reionization epoch, illuminating the Universe. The 21cm hydrogen line arises from the hyperfine transition between the ortho (parallel spins of proton and electron) and para states (anti-parallel spins) of hydrogen’s ground state. During reionization, the spin temperature T_s of hydrogen gas was coupled to the cooler gas, causing the 21cm absorption line to appear against the Cosmic Microwave Background (CMB) radio background. Whether the spin temperature is greater or less than the background radio temperature determines whether an emission or absorption line is observed in the 21cm H1 spectrum.

The discrepancy between experimental and standard model predictions of the brightness temperature of the redshifted 21cm hydrogen absorption spectra has spurred investigations into the early Universe, particularly during the cosmic dark ages. Given that the known Universe is composed of approximately 75% hydrogen gas, measurements of the 21cm transition are crucial for understanding both cosmic evolution and the temperature dynamics of hydrogen gas. The intensity of the 21cm signal depends on the population ratio of the triplet and singlet states, described by the spin temperature T_s , which relates to the CMB temperature T_{CMB} and the optical depth τ of the medium through which the radiation passes.

Around $z \sim 200$, the cosmic gas decoupled from the CMB, and its temperature dropped below the radiation temperature due to adiabatic cooling. The unexpected cooling observed in the 21cm signal by EDGES presents a promising probe to understand cosmic history during the cosmic dawn era. The impact of baryon-dark matter interactions, as well as the effects of dark matter decay during this era, are also subjects of investigation using the 21cm signal from that epoch.

The global 21cm signal detected by EDGES during the cosmic dawn era appeared at a temperature significantly lower than expected from the standard cosmological model (Λ CDM).

The observed cooling of the gas reported by EDGES could potentially be caused by a process involving heat absorption from baryons. If the exchange of heat between dark matter and baryons led to this cooling effect, it suggests that dark matter-baryon scattering could be responsible. For this to occur, the mass of the dark matter should be comparable to or less than the mass of baryons. Dark matter annihilation could also contribute to heat exchange with the surroundings. In this study, we consider sub-GeV dark matter, where the scattering of such particles with baryons could significantly cool the baryonic fluid once Lyman- α radiation becomes effective [203].

Strong velocity-dependent dark matter-baryon scattering, such as Rutherford-like scattering, could produce a pronounced 21cm signal during the cosmic dark ages while remaining consistent with astrophysical and cosmological constraints today. However, scenarios involving Yukawa-type scattering potentials exhibit a velocity-dependent scattering cross-section $\sigma = \sigma_0 v^n$, where n can vary depending on the nature of dark matter [198, 199, 200, 201, 211]. For instance, magnetized dark matter exhibits $n = \pm 2$, while millicharged dark matter shows $n = -4$ [196, 197, 212, 213, 214, 215]. This v^{-4} dependence also applies to Rutherford-like dark matter-baryon scattering [180].

In addition to dark matter-Standard Model (SM) scattering, dark matter can undergo self-interactions. The self-scattering of dark matter may also influence the brightness temperature of the 21cm absorption line. In this study, we consider two types of self-interaction namely elastic self-scattering $\chi\chi \rightarrow \chi\chi$ and self-annihilation $\chi\chi\chi \rightarrow \chi\chi$ [108, 109].

Self-interacting dark matter provides a compelling window into the dark sector of the Universe beyond the Standard Model gauge group. When the relic density of dark matter is determined by either the cross-section of elastic scattering with SM particles or the cross-section of self-interaction processes that change the number of dark matter particles, the scenario is referred to as Elastically Decoupling Relic (ELDER) dark matter. In this case, the mass of dark matter m_χ is typically around the QCD confinement scale (between 10 MeV and 100 MeV). In this work, we consider all four interactions mentioned above to be active in the early Universe ($\Gamma > H$, where Γ is the respective interaction rate and H is the Hubble parameter) until ELDER dark matter becomes non-relativistic. Under these conditions, the interaction rates for processes such as $\chi + \text{SM} \rightarrow \chi + \text{SM}$, $\chi\chi \rightarrow \chi\chi$, and $\chi\chi\chi \rightarrow \chi\chi$ decay exponentially, while elastic scattering interaction rates ($\chi + \text{SM} \rightarrow \chi + \text{SM}$) vary more gradually.

5.2 Elder dark matter model and its cannibalism property

While the presence of dark matter (DM) in the Universe is well-established, its particle nature and interaction properties remain elusive. Among the prominent candidates for dark matter are Weakly Interacting Massive Particles (WIMPs), which are often theorized using frameworks beyond the Standard Model (SM), such as supersymmetry, extra-dimensional theories, or straightforward extensions of the SM.

Typically, WIMPs are thermal relics whose density is determined by a process called thermal decoupling.

Dark matter can also be categorized based on its decoupling processes from the Universe's SM plasma. For example, “freeze-out” DM like WIMPs undergoes a decoupling process dominated by annihilation into SM particles (e.g., $\chi + \chi \rightarrow \text{SM} + \text{SM}$). However, other scenarios include “freeze-in” DM, where the particle density approaches equilibrium density over time. In scenarios where DM decoupling involves not only annihilation but also elastic scattering and self-annihilation, new DM models emerge.

One such model is the ELDER (Elastically Decoupling Relic) DM, where the decoupling is governed by four key processes 1. DM annihilation to SM particles ($\chi + \chi \leftrightarrow \text{SM} + \text{SM}$). 2. DM-baryon elastic scattering ($\chi + \text{SM} \leftrightarrow \chi + \text{SM}$). 3. $3 \rightarrow 2$ self-annihilation ($\chi\chi\chi \leftrightarrow \chi\chi$). 4. $2 \rightarrow 2$ elastic self-scattering ($\chi\chi \leftrightarrow \chi\chi$).

5.3 Thermal evolution of 21cm signal

In this model, the relic density of DM is primarily determined by elastic scattering. As the Universe cools to temperatures below the DM mass ($T_{\text{Univ}} < m_\chi$), the equilibrium density of DM particles drops exponentially, leading to the decoupling of annihilation processes. However, self-annihilation and elastic scattering continue to keep DM in thermal equilibrium with the SM plasma. Eventually, as the Universe expands, self-annihilation processes like $\chi\chi\chi \rightarrow \chi\chi$ maintain a nearly constant temperature for DM, despite the decoupling of elastic scattering. This self-annihilation process is referred to as “cannibalism,” where three DM particles interact to form two, releasing energy that maintains the DM temperature.

The relic density of ELDER DM depends on the cross-sections of self-interaction and elastic scattering processes. For DM with mass in the range of 10 to 100 MeV, the relic abundance [108] is given by

$$\Omega_\chi \sim \frac{10^6 m_{\text{MeV}} \exp(-10 \epsilon_{-9}^{1/2} m_{\text{MeV}}^{-1/4})}{1 + 0.07 \log \alpha}. \quad (5.1)$$

Here, α is the coupling strength for $3 \rightarrow 2$ self-annihilation, $\epsilon_{-9}(= \epsilon/10^{-9})$ is the coupling strength for $2 \rightarrow 2$ self-scattering, and $m_{\text{MeV}} = \frac{m_\chi}{1\text{MeV}}$ is the parametrized mass of DM in MeV. Recent studies indicate that for ELDER DM, the coupling strength α should lie within the range $0.5 \frac{m_\chi}{10\text{MeV}} \leq \alpha \leq 73$.

The 21cm signal originates from the hyperfine transition of hydrogen atoms between their two spin states ($s = 0$ and $s = 1$). The intensity of this absorption spectrum is described by the brightness temperature T_{21} , which is expressed as

$$T_{21} = \frac{T_s - T_\gamma}{1 + z} (1 - e^{-\tau}), \quad (5.2)$$

where τ is the optical depth, T_γ is the background temperature, and T_s is the spin temperature at redshift z .

The theoretical brightness temperature of the 21cm signal at $z = 17.2$ (T_{21}^{Th}) is approximately $T_{21}^{Th} \sim -200$ mK when $T_s = T_b$ (the baryon temperature). However, the EDGES experiment reported a significantly lower brightness temperature $T_{21}^{EDGES} = -500^{+200}_{-500}$ mK, with a confidence level of 99%. This discrepancy, almost 3.8σ , indicates a need to explore beyond the standard cosmological models to understand the observed cooling of the hydrogen gas.

5.4 Effect of ELDER dark matter on 21cm line

The brightness temperature T_{21} is influenced by variations in the background temperature T_γ , the spin temperature T_s , or both. At redshift $z \sim 1100$, photons

should free-stream; however, due to the high photon density, radiation remains coupled to matter via Compton scattering until $z \sim 200$. Once the Compton heating timescale exceeds the Hubble time, decoupling of matter and radiation occurs. Post-decoupling, the temperatures of matter and dark matter decrease more rapidly ($T_{m/\chi} \sim (1+z)^2$) compared to the radiation temperature ($T_\gamma \sim (1+z)$).

In the absence of interactions, the temperature evolution for standard model (SM) gas and dark matter (DM) can be described by the following equations, respectively [219, 159]

$$(1+z) \frac{dT_b}{dz} = 2T_b + \frac{\Gamma_c}{H(z)} (T_b - T_\gamma), \quad (5.3)$$

$$(1+z) \frac{dT_\chi}{dz} = 2T_\chi, \quad (5.4)$$

where Γ_c represents the Compton scattering rate.

This study examines the impact on T_{21} when incorporating four ELDER dark matter processes, including DM-baryon elastic scattering and DM annihilation to SM particles.

5.4.1 DM-baryon elastic scattering ($\chi + SM \leftrightarrow \chi + SM$)

After photon decoupling in the early Universe, dark matter and baryons acquire a relative velocity $V_{\chi b}$, leading to a drag effect between them. Dark matter and baryons may undergo Rutherford-like elastic scattering, with the cross-section strongly dependent on velocity, expressed as v^{-4} . The scattering cross-section is

$$\sigma = \sigma_0 v^{-4} = (\sigma_{41} \times 10^{-41} v^{-4}) \text{ cm}^2, \quad (5.5)$$

where $\sigma_{41} = \frac{\sigma_0}{10^{-41}}$ is dimensionless. The relative velocity $V_{\chi b}$ is the difference between the bulk DM velocity V_χ and baryon velocity V_b , i.e., $V_{\chi b} = V_\chi - V_b$. The initial condition $V_{\chi b0} = 10^{-4}c$ at $z = 1010$ is used in our calculations.

Scattering between hotter baryons and colder DM heats the DM. The rate of change of relative velocity $D(V_{\chi b})$, and the heating rates of baryons \dot{Q}_b and DM \dot{Q}_χ , are given by [180]

$$\frac{dV_{\chi b}}{dt} = -D(V_{\chi b}) = \frac{\rho_m \sigma_0}{m_b + m_\chi} \frac{1}{V_{\chi b}^2} F(r), \quad (5.6)$$

$$\frac{dQ_b}{dt} = \dot{Q}_b = \frac{2m_b \rho_\chi \sigma_0 e^{-r^2/2} (T_\chi - T_b)}{(m_b + m_\chi)^2 \sqrt{2\pi} u_{th}^3} + \frac{\rho_\chi}{\rho_b + \rho_\chi} \frac{m_\chi m_b}{m_\chi + m_b} V_{\chi b} D(V_{\chi b}), \quad (5.7)$$

$$\frac{dQ_\chi}{dt} = \dot{Q}_\chi = \frac{2m_\chi \rho_b \sigma_0 e^{-r^2/2} (T_b - T_\chi)}{(m_b + m_\chi)^2 \sqrt{2\pi} u_{th}^3} + \frac{\rho_b}{\rho_b + \rho_\chi} \frac{m_\chi m_b}{m_\chi + m_b} V_{\chi b} D(V_{\chi b}), \quad (5.8)$$

where ρ_χ and ρ_b are the DM and baryon densities, respectively, and $\rho_m = \rho_\chi + \rho_b$. m_b and m_χ are the average masses of baryons and DM, respectively, with temperatures T_b and T_χ . The term r is defined as $r = V_{\chi b}/u_{th}$, with $u_{th} = \sqrt{T_b/m_b + T_\chi/m_\chi}$. The function $F(r)$ is

$$F(r) = \text{erf}(r/\sqrt{2}) - \sqrt{2/\pi} r e^{-r^2/2}. \quad (5.9)$$

Equation 5.6 can be rewritten as

$$\frac{dV_{\chi b}}{dz} = \frac{V_{\chi b}}{1+z} + \frac{D(V_{\chi b})}{(1+z)H(z)}. \quad (5.10)$$

5.4.2 DM annihilation to SM ($\chi + \chi \leftrightarrow SM + SM$)

DM annihilation into SM particles can inject energy into the Universe, affecting the gas temperature (T_b) by heating, ionizing, or exciting the gas [219, 220]. The rate of energy injection from annihilation depends on the velocity-averaged s-wave annihilation cross-section $\langle \sigma v \rangle$ and is given by

$$\left(\frac{dE}{dV dt} \right)_{\text{inj}} = f_\chi^2 \rho_{\chi,0}^2 (1+z)^6 \frac{\langle \sigma v \rangle}{m_\chi}, \quad (5.11)$$

where f_χ is the DM fraction (assumed to be 1), and the two annihilating particles are indistinguishable. The deposited energy is related to the injected energy by

$$\left(\frac{dE}{dVdt}\right)_{\text{dep}} = f_c(z) \left(\frac{dE}{dVdt}\right)_{\text{inj}}, \quad (5.12)$$

where $f_c(z)$ is the deposition efficiency at redshift z [192, 191, 193, 221, 185, 222]. The fractions of energy deposited into baryon heating and gas ionization are $\chi_h = (1 + 2x_e)/3$ and $\chi_i = (1 - x_e)/3$, respectively [223, 224, 225, 177].

5.4.3 “3 → 2” self-annihilation ($\chi\chi\chi \leftrightarrow \chi\chi$)

Initially, DM particles are in thermal and chemical equilibrium with SM particles, but as the Universe expands and cools, the DM temperature drops below their mass. The 3 → 2 self-annihilation process, where three DM particles annihilate to form two, helps maintain chemical equilibrium even when elastic scattering with SM particles is insufficient. This ”cannibalization” decreases the number of DM particles and releases kinetic energy, which is then transferred to the SM gas via DM-SM elastic scattering. The self-annihilation cross-section is parametrized as [108, 109]

$$\langle\sigma_{3\rightarrow 2}v^2\rangle = \frac{\alpha^3}{m_\chi^5}, \quad (5.13)$$

where m_χ is the DM mass and α is the coupling constant. The excess energy transfer rate to SM particles is

$$\dot{Q}_{32} \sim \Gamma_{32}m_\chi = n_\chi^2\langle\sigma_{3\rightarrow 2}v^2\rangle m_\chi, \quad (5.14)$$

with $\Gamma_{32} = n_\chi\langle\sigma_{3\rightarrow 2}v^2\rangle$ being the annihilation rate.

5.4.4 “2 → 2” elastic self-scattering ($\chi\chi \leftrightarrow \chi\chi$)

The $\chi\chi \leftrightarrow \chi\chi$ interaction, also known as “2 → 2” elastic self-scattering, does not alter the number of dark matter particles. This process decouples after the “3 → 2” self-annihilation event. Both interactions in the dark sector exchange energy among dark matter particles, and heat is transferred to the standard model (SM) gas through DM-SM elastic scattering. The rate of heat transfer is expressed as

$$\dot{Q}_{22} \sim \Gamma_{22} v_\chi^2 T_\chi, \quad (5.15)$$

where the interaction rate for “2 → 2” self-scattering is

$$\Gamma_{22} = n_\chi \langle \sigma_{2 \rightarrow 2} v \rangle, \quad (5.16)$$

and the cross-section is parametrized as

$$\langle \sigma_{2 \rightarrow 2} v \rangle = \frac{\epsilon^2}{m_\chi^2}, \quad (5.17)$$

with ϵ being the coupling constant.

Both “2 → 2” self-scattering and “3 → 2” self-annihilation occur exclusively within the dark sector, affecting only the thermal evolution of dark matter. The thermal evolution due to “2 → 2” interactions can be described by

$$\zeta_{22} = -\frac{2}{3} \frac{\dot{Q}_{22}}{(1+z)H(z)n_\chi}. \quad (5.18)$$

Impact on Brightness Temperature (T_{21})

To investigate the effect of these processes on the brightness temperature T_{21} , we numerically solve the system of coupled differential eqs. (5.3, 5.4, 5.6, 5.7, 5.8, 5.10) for different redshifts, considering the heating contributions from 3 → 2 and 4 → 2

self-annihilation, as well as DM annihilation to SM particles and elastic scattering with baryons. The total energy injection rate into the baryons is modified to include these additional heating terms. By solving these equations, we can determine the evolution of the gas temperature T_b , DM temperature T_χ , and relative velocity $V_{\chi b}$, which in turn allows us to compute the brightness temperature T_{21} .

Incorporating the effects of both “3 → 2” and “2 → 2” interactions, the evolution equations for temperatures and ionization fraction become

$$(1+z)\frac{dT_\chi}{dz} = 2T_\chi - \frac{2}{3H(z)}\frac{dQ_\chi}{dt} + (1+z)(\kappa_{32} + \zeta_{22}) \quad (5.19)$$

$$(1+z)\frac{dT_b}{dz} = 2T_b + \frac{\Gamma_c}{H(z)}(T_b - T_\gamma) - \frac{2}{3H(z)}\frac{dQ_b}{dt} - \frac{1}{H(z)}\left(\frac{dE}{dVdt}\right)_{\text{dep}} \frac{\chi_h}{n_H} \frac{2}{3(1+x_e+f_{\text{He}})} \quad (5.20)$$

The ionization fraction ($x_e = \frac{n_e}{n_b}$) evolves as

$$\frac{dx_e}{dz} = \frac{1}{(1+z)H(z)} \left[C_P \left(n_H \alpha_B x_e^2 - 4(1-x_e)\beta_B e^{-\frac{3E_0}{4k_B T_\gamma}} \right) - I_{\text{heat}}(z) \right], \quad (5.21)$$

where n_H is the number density of hydrogen and n_e is the number density of free electrons. The Peebles-C factor (C_P) is nearly unity, and α_B and β_B are the effective recombination coefficient and the effective photoionization rate, respectively. The heating term $I_{\text{heat}}(z)$ represents the heat involved in ionizing the baryons

$$I_{\text{heat}}(z) = \chi_i \frac{1}{n_b E_0} \left(\frac{dE}{dVdt} \right)_{\text{dep}}. \quad (5.22)$$

These results will provide insights into the potential modifications of the 21 cm signal due to ELDER dark matter processes, offering a window into the properties and interactions of dark matter in the early Universe.

m_χ (GeV)	σ_{41}	α	$\eta = \frac{\epsilon}{m_\chi^{-0.5}}$ (GeV ^{-0.5})
0.015	0.25	1	1.05×10^{-7}

Table 5.1: Benchmark values for various parameters (m_χ , σ_{41} , α , and η) used in the plots of fig. 5.1.

5.5 Results and conclusion

In this study, we explore several intriguing aspects of 'ELDER' dark matter within the framework of the 21cm brightness temperature scenario. ELDER dark matter affects four primary interactions that subsequently influence the temperature of the baryonic fluid and, thus, the 21cm signal's brightness temperature. The most critical interaction among these is the dark matter-baryon interaction, which reduces the temperature disparity between the baryonic and dark matter fluids. The dark matter candidate under consideration may cool the baryons through elastic scattering with standard model (SM) particles.

In contrast, the other interactions associated with ELDER dark matter, such as dark matter annihilation ($\chi\chi \rightarrow \text{SM SM}$), dark matter self-scattering ($\chi\chi \rightarrow \chi\chi$), and dark matter self-annihilation ($\chi\chi \rightarrow \chi\chi\chi$), tend to heat the baryons. This heating can occur either directly, as in the case of dark matter annihilation into SM particles ($\chi\chi \rightarrow \text{SM SM}$), or indirectly, through dark matter self-scattering and self-annihilation ($\chi\chi \rightarrow \chi\chi$ and $\chi\chi \rightarrow \chi\chi\chi$).

To incorporate the effects of ELDER dark matter, we solve a set of coupled equations (Eqs. 5.10, 5.19, 5.20, and 5.21) to obtain the thermal evolution of the baryonic temperature (T_b) and the dark matter temperature (T_χ). For this analysis, we assume that at $z \approx 1010$, the dark matter fluid's temperature is negligible, while the baryonic temperature (T_b) is approximately equal to the radiation temperature (T_γ), reflecting the tight coupling between baryons and radiation prior to recombination.

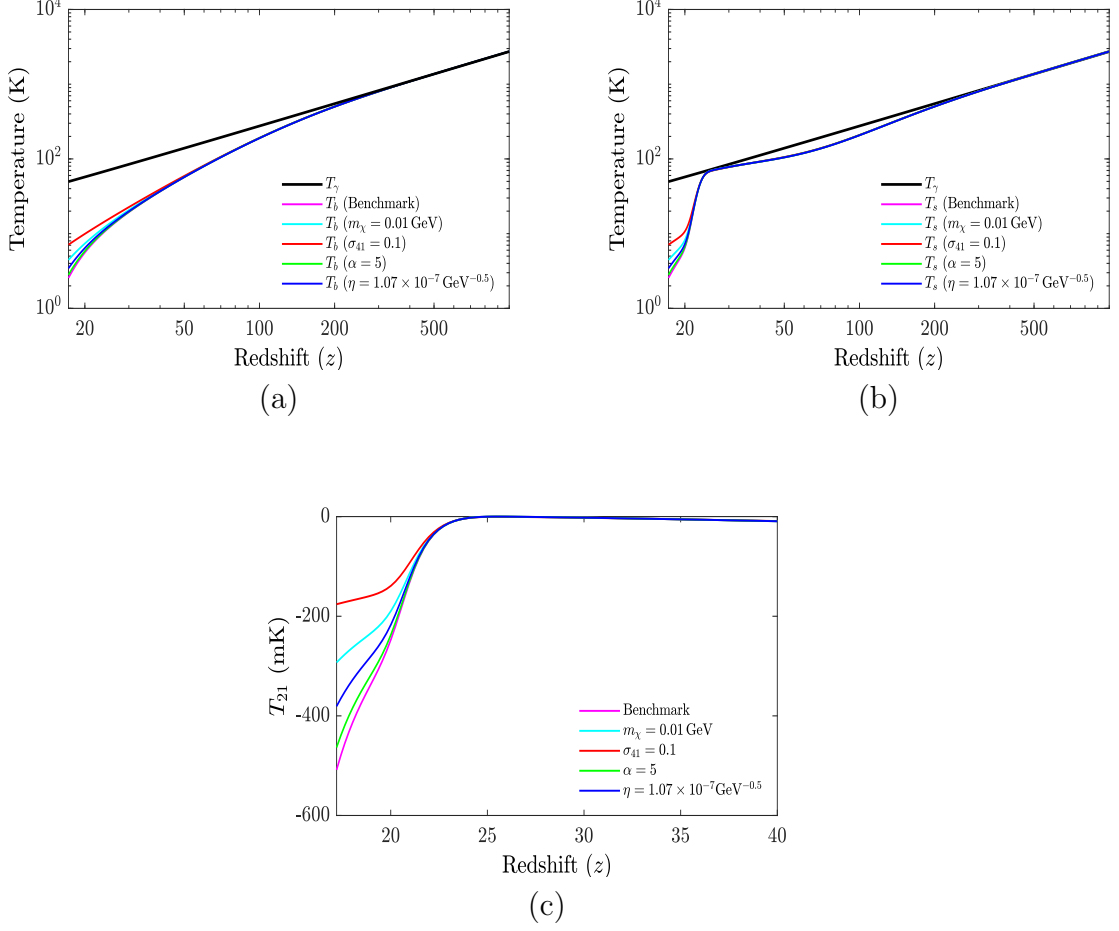


Figure 5.1: (a) Evolution of the baryonic matter temperature (T_b) with redshift (z) for various selected model parameters. (b) Corresponding spin temperature (T_s) evolution with redshift (z) for the same set of model parameters. (c) Evolution of the brightness temperature (T_{21}) with redshift (z) for different chosen model parameters.

The baryon temperature (T_b) and spin temperature (T_s) are obtained through numerical solutions of the coupled differential equations (Eqs. 5.10, 5.21, 5.19, and 5.20) as detailed in Section 7.3. For this study, we adopt benchmark values for the parameters listed in Table 5.1. Notably, η is expressed in terms of ϵ .

Fig. 5.1 illustrates the calculated variations of T_b , T_s , and T_{21} with redshift z . These results are compared against variations with different parameter values such as m_χ

and σ_{41} . In fig. 5.1(a), the magenta line depicts T_b versus z using the benchmark values from Table 5.1. Variations due to changes in individual parameters while keeping others fixed at the benchmark values are also shown. Similarly, fig. 5.1(b) and fig. 5.1(c) display variations of T_s and T_{21} , respectively.

In all plots of fig. 5.1, the background temperature T_γ (black line) versus z is included for reference. Notably, T_b shows limited sensitivity to parameter variations, with minor fluctuations ($\sim 2^\circ\text{K}$ to 7°K) observed for $z \lesssim 30$. During reionization, as shown in fig. 5.1(a), the spin temperature rapidly transitions from T_γ to T_b due to the Wouthuysen-Field effect. Similarly, fig. 5.1(b) indicates minimal parameter dependency for T_s versus z for $z \lesssim 22$.

Regarding T_{21} (Fig. 5.1(c)), variations due to parameter changes exhibit more significant effects compared to T_b and T_s . For instance, at $z \sim 17.5$, T_{21} shifts from -500 mK to -410 mK when adjusting the strength parameter η for the $2 \rightarrow 2$ process.

These findings underscore the distinct impacts of parameter variations on T_{21} compared to T_b and T_s .

We now extend our analysis to constrain the parameters ϵ , η , and α (representing various self-interaction parameters) using observational results from EDGES for the brightness temperature T_{21} at $z = 17.2$ ($-300 \text{ mK} \geq T_{21} \geq -1000 \text{ mK}$). To facilitate this, we introduce $T_{21}^{z=17.2}$, denoting the brightness temperature T_{21} specifically at $z = 17.2$.

Fig. 5.2 illustrates the permissible regions in the α - η parameter plane for different values of the dark matter mass $m_\chi = 0.01 \text{ GeV}$, 0.02 GeV , 0.05 GeV , and 0.10 GeV , as depicted in panels (a), (b), (c), and (d) of the figure, respectively. Each panel corresponds to a specific m_χ , and the colour coding in the plots represents different values of $T_{21}^{z=17.2}$, with the colour index provided at the bottom of fig. 5.2.

In all panels of fig. 5.2, the regions coloured in white denote areas that are ruled out based on the EDGES observational constraints. It is evident from fig. 5.2 that

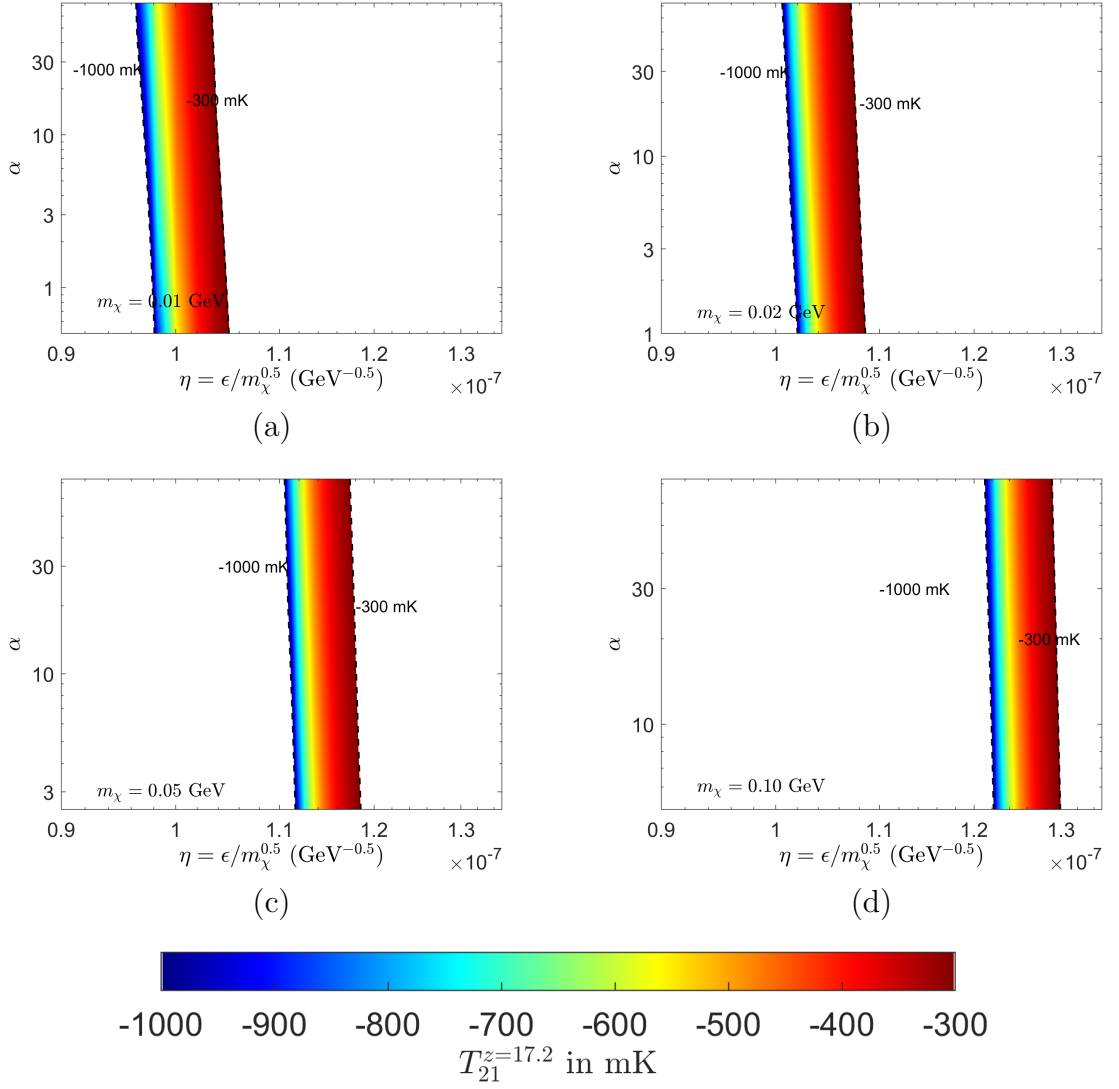


Figure 5.2: The parameter space in the α - η plane is examined for different values of m_χ in figs. (a) to (d): (a) $m_\chi = 0.01$ GeV, (b) $m_\chi = 0.02$ GeV, (c) $m_\chi = 0.05$ GeV, and (d) $m_\chi = 0.10$ GeV. Each plot assumes $\sigma_{41} = 0.25$.

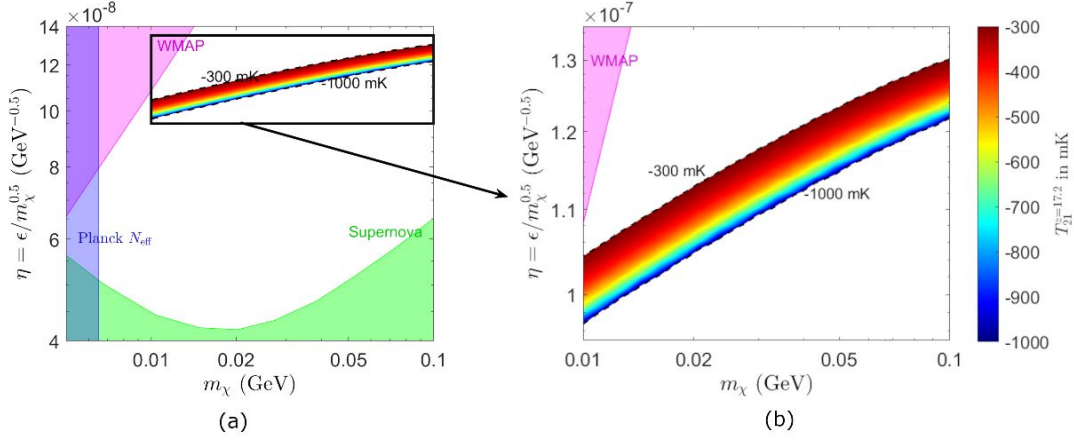


Figure 5.3: The allowed region in the $\eta - m_\chi$ parameter plane.

for higher values of m_χ , $T_{21}^{z=17.2}$ decreases across individual points in the α - η plane, consequently shifting the allowed region towards higher values of η .

Moreover, the allowed zone tends to cover the entire permissible range of α (α_{\min} to α_{\max}) and shows minimal dependence on α . However, slight variations are observed for lower dark matter masses m_χ , as depicted in panels (a) and (b) of fig. 5.2.

It should be noted that all plots in fig. 5.2 maintain $\sigma_{41} = 0.25$ throughout for consistency.

From fig. 5.2, it is evident that as m_χ increases, higher values of η are required to achieve a desired value of T_{21} . The allowed zone in fig. 5.2 shifts towards higher values of η as m_χ increases from fig. 5.2(a) to fig. 5.2(d). Additionally, it is noticeable from fig. 5.2 that to achieve a specific variation in T_{21} (within -1000 mK and -300 mK), the parameter α varies less compared to η . Hence, T_{21} exhibits greater sensitivity to η than to α . These computations are performed with σ_{41} fixed at 0.25.

In these calculations, η and m_χ are systematically varied while solving the coupled differential equations with a fixed σ_{41} and α . Here, $\sigma_{41} = 0.25$ is chosen. To determine α for each set of η and m_χ , the range of α is identified, and the average value $\alpha = \frac{\alpha_{\max} + \alpha_{\min}}{2}$ is employed in computing T_{21} for that specific $\eta - m_\chi$ configuration.

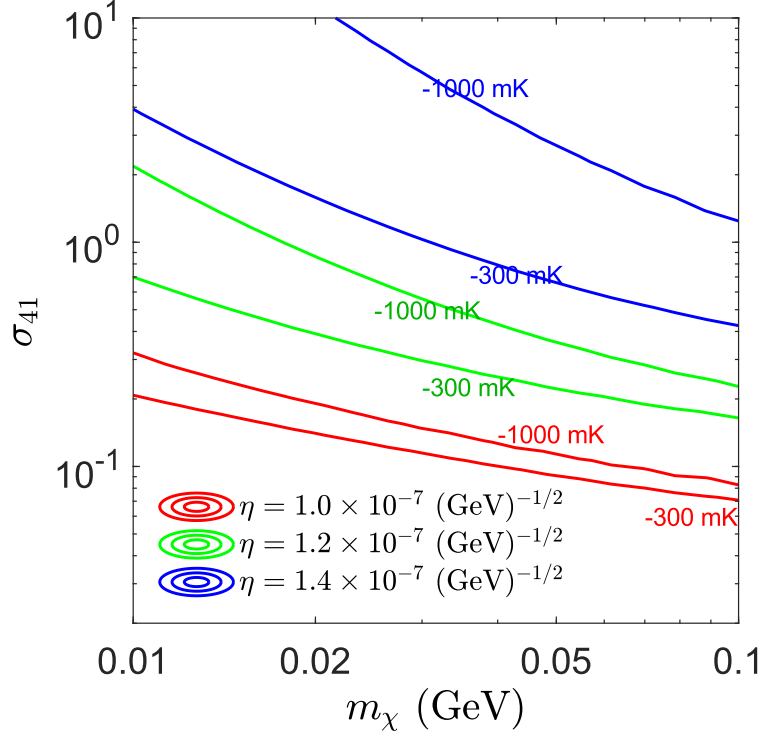


Figure 5.4: The permissible regions in the $\sigma_{41} - m_\chi$ plane are depicted for various selected values of η , accompanied by several constraints derived from different experiments.

Fig. 5.3 also includes comparisons with bounds obtained from Supernova observations and the WMAP results, as detailed in Ref. [108]. The bounds from Supernova arise due to the trapping of dark matter χ within the SN core through χ scattering on photons, imposing constraints on ϵ [108]. The WMAP constraint is derived from the bounds shown in Ref. [108] and depicted in fig. 5.3 within the current study.

Fig. 5.3 highlights that the constraints derived from our calculations using EDGES 21cm observations align with the SN and WMAP constraints on ϵ . Specifically, in fig. 5.3(b), the lower bound on ϵ , obtained from the process $\gamma\gamma \rightarrow \chi\chi$ at SN, is illustrated in terms of η for comparison [108]. This overlap underscores that the $\eta - m_\chi$ parameter space permitted by the observational constraints of the 21cm line during the reionization epoch also respects the SN cooling constraint, as well as the PLANCK and WMAP constraints on ϵ .

The permissible region is also assessed in the $\sigma_{41} - m_\chi$ parameter space for three distinct values of η . In fig. 5.4, the allowed zones corresponding to $\eta = 1.0 \times 10^{-7} \text{ GeV}^{-1/2}$, $\eta = 1.2 \times 10^{-7} \text{ GeV}^{-1/2}$, and $\eta = 1.4 \times 10^{-7} \text{ GeV}^{-1/2}$ are plotted across the range of dark matter masses $0.01 \text{ GeV} < m_\chi < 0.1 \text{ GeV}$. These plots also incorporate various experimental constraints. Similar to the methodology used in fig. 5.2, the values of α for different m_χ are determined by averaging the permissible range of α .

From fig. 5.4, it is evident that the allowed region narrows at lower values of η . Conversely, the region expands and becomes more pronounced at higher values of η . Additionally, it is observed that the region corresponding to higher values of η tends to occupy the higher σ_{41} regime. This trend is associated with the increase in η , which influences the rate of dark matter self-interactions $\chi\chi \rightarrow \chi\chi$, thereby potentially injecting more heat ($\langle\sigma v\rangle \sim \frac{c^2}{m_\chi^2}$). Conversely, as m_χ decreases, $\langle\sigma v\rangle_{\chi\chi \rightarrow \chi\chi}$ increases, necessitating an increase in the dark matter-baryon scattering process to counterbalance this heating effect, as illustrated in fig. 5.4.

We further expand our analysis to determine the density parameter Ω_χ for ELDER-type cold dark matter candidates across different values of η . In fig. 5.5, Ω_χ is scaled relative to Ω_{dm} , the dark matter density parameter for the entire Universe as determined by PLANCK [45]. The solid red line in fig. 5.5 represents $\Omega_\chi/\Omega_{\text{dm}}$ for $m_\chi = 0.01 \text{ GeV}$, calculated at $\alpha = (\alpha_{\text{max}} + \alpha_{\text{min}}(m_\chi))/2$ as previously described. The corresponding values for $\alpha = \alpha_{\text{max}}$ and $\alpha = \alpha_{\text{min}}(m_\chi)$ are shown by the red dotted and dashed lines, respectively. Similar variations of Ω_χ with η are depicted for the other three m_χ values (0.02 GeV in green, 0.05 GeV in blue, and 0.10 GeV in magenta), with each set of lines representing a specific m_χ value. In each set, the solid line of a particular color corresponds to $\alpha = (\alpha_{\text{max}} + \alpha_{\text{min}})/2$, while the dashed and dotted lines show the variations for $\alpha = \alpha_{\text{max}}$ and $\alpha = \alpha_{\text{min}}(m_\chi)$, respectively.

In fig. 5.5, solid squares of respective colors denote the values in the $\Omega_\chi/\Omega_{\text{DM}} - \eta$ plane that match the central value of the EDGES experimental result ($T_{21}^{z=17.2} = -500$

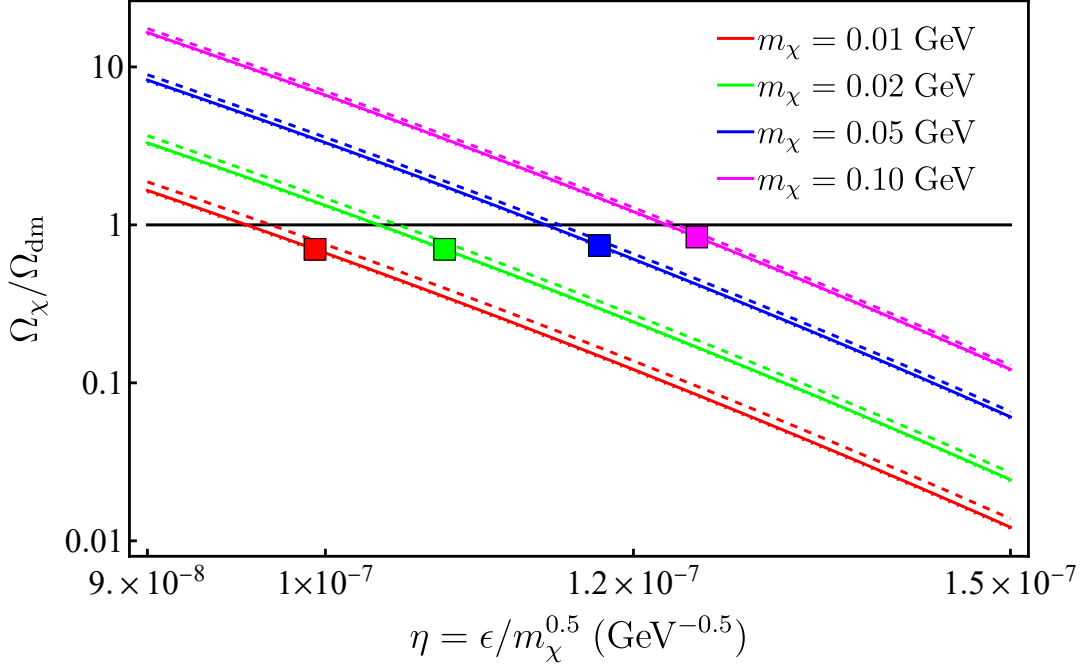


Figure 5.5: Variations of the dark matter density parameter Ω_χ , normalized to the critical density of the Universe, are depicted for the dark matter particle χ as a function of η , considering four distinct mass values of χ . These are illustrated by solid colored lines. Additionally, dashed and dotted lines correspond to $\alpha = \alpha_{\max}$ and $\alpha = \alpha_{\min}(m_\chi)$ respectively, for each of the four mass cases, where the solid lines represent the average α values. The solid squares on the plots denote the EDGES observational result of the brightness temperature $T_{21}^{z=17.2} = -500$ mK.

mK) for each m_χ considered. It is observed that for all four chosen m_χ values, the best-fit points lie within the range $\Omega_{\text{DM}} < 1$. This indicates the presence of other dark matter components in the Universe, suggesting the potential existence of multi-component dark matter systems.

It should be noted that the “3 \rightarrow 2” process within the ELDER scenario is considerably less significant compared to the “2 \rightarrow 2” process. Even when setting the parameter α , which governs the “3 \rightarrow 2” interaction strength, to zero, it has been verified that the outcomes remain unchanged. The cross-section for the “2 \rightarrow 2”

process is constrained by observations from the Bullet Cluster and halo shapes, ensuring that $\frac{\sigma_{\chi\chi\rightarrow\chi\chi}}{m_\chi} \lesssim 1 \text{ cm}^2/\text{g}$. This constraint is crucial for explaining the observed small-scale structure through N-body simulations. Therefore, the self-scattering of dark matter plays a pivotal role in the process of Universe structure formation.

Compact Astrophysical Objects

In the realm of 21cm cosmology, there is ongoing exploration into the predictions concerning compact astrophysical objects. These objects, which include neutron stars, white dwarfs, black holes, and more exotic varieties like quark stars and boson stars, are pivotal due to their extreme densities. This compactness leads to the manifestation of unique phenomena that play a crucial role in high-energy astrophysics and cosmology.

Specifically, in the context of 21cm cosmology, the study of these compact objects becomes significant as they may influence the distribution of dark matter and affect the observed 21cm signal from the early Universe. Their properties, such as non-luminosity or low-luminosity in the case of black holes and other similar compact objects, also make them potential candidates for contributing to baryonic dark matter. Thus, exploring the predictions regarding these compact objects offer valuable insights in the understanding of both the formation and evolution of the structures in the Universe, as well as the nature of dark matter itself. In this chapter these aspects have been addresses exploring the 21cm HI signal.

6.1 Introduction

Compact astrophysical objects represent the final stages of stellar evolution, encompassing familiar entities like neutron stars, white dwarfs, and black holes, as well as more exotic ones such as quark stars, preon stars, and boson stars. These objects are extraordinarily dense, leading to the emergence of extreme phenomena that hold great importance in high-energy astrophysics and cosmology. Many of these compact objects, such as black holes, MACHOs (Massive Astrophysical Compact Halo Objects), and black dwarfs (spent white dwarfs), are characterized by their non-luminous or low-luminous nature. These types of astrophysical bodies are often considered potential candidates for baryonic dark matter.

Renowned English astronomer and physicist Sir Arthur Stanley Eddington discussed the discovery of the first observed white dwarf, Sirius B, in his book "The Internal Constitution of the Stars" (1926) [226]. However, the actual discovery of the first white dwarf occurred earlier in 1914 by W. S. Adam. Subsequently, in 1931, S. Chandrasekhar developed a comprehensive model of white dwarfs by incorporating the relativistic effects of degenerate electrons [227]. Chandrasekhar also calculated the maximum possible mass for white dwarfs, known as the "Chandrasekhar limit," set at $1.4 M_{\odot}$ in his analysis.

White dwarfs represent the first compact stars to have been identified. It is estimated that more than 95% of stars will enter this phase at the culmination of their lifecycle. Current models suggest there are approximately $\sim 10^{10}$ white dwarfs in our Milky Way galaxy today [228]. Typically, a main-sequence star with a mass between $0.07 M_{\odot}$ and $10 M_{\odot}$ [229, 230] transitions into a white dwarf as it exhausts its hydrogen core and begins fusing heavier elements, shedding its outer layers. This process results in a planetary nebula dissipating into space, leaving behind a compact white dwarf core sustained by electron degeneracy pressure, which stabilizes its collapse depending on its core density. If the white dwarf's mass exceeds the Chandrasekhar limit, electron degeneracy pressure cannot prevent gravitational collapse, leading to

a transformation into a neutron star. Additionally, if a white dwarf is part of a binary system, it may accrete mass from its companion star, potentially surpassing the Chandrasekhar limit and transforming into a neutron star.

Due to their high compactness, white dwarfs exhibit surface gravities hundreds of thousands of times greater than that of Earth. They emit light over billions of years but eventually cool down to become black dwarfs, devoid of energy to radiate further. Given the Universe's age of 13.6×10^9 years, no observational evidence of black dwarfs has been recorded to date.

6.2 Neutron Stars

“Things changed with the discovery of neutron stars and black holes - objects with gravitational fields so intense that dramatic space and time-warping effects occur. ”

-Paul Davies

The discovery of pulsars in 1967 [231] and their subsequent identification as rotating neutron stars in 1968-69 sparked significant interest in neutron star physics [232]. These objects are now understood to be the remnants of supernova explosions, representing the final stage in the evolution of massive stars. Neutron stars exhibit extreme properties: their surface matter density is around 10^4 g/cm^3 , and at their core, the density can exceed normal nuclear matter density ($\rho_o \approx 2.8 \times 10^{14} \text{ g/cm}^3$). At these high densities, exotic forms of matter, such as hyperons, quark-hadron mixed phases, and Bose-Einstein condensates of kaons, may exist.

Neutron stars [233, 234] also possess incredibly strong magnetic fields (10^{12} G), rapid rotation periods (ranging from milliseconds to seconds), and extremely low spin-down rates (10^{-15}). Such extreme conditions cannot be replicated in terrestrial laboratories, making neutron stars exceptional natural laboratories for studying matter under these extreme conditions.

Numerous theoretical models have been proposed to describe the properties of neutron star matter. However, only a model that accurately interprets all observational data will ultimately prevail.

6.2.1 Birth of a neutron star

Neutron stars are the final products of stellar evolution, believed to form during supernova explosions. A star typically spends most of its luminous life in the hydrogen-burning phase, where hydrogen fusion produces helium and releases vast amounts of thermal energy in the core. This outward thermal pressure balances the inward gravitational pull, stabilizing the star. Once the hydrogen in the core is depleted, the star collapses under its own gravity. The core heats up during this collapse, and when the temperature becomes high enough, helium fusion begins in the core while hydrogen continues to burn in an outer shell.

For stars with masses up to about 8 times the mass of the sun ($8 M_{\odot}$), the burning process cannot proceed beyond helium fusion as the core temperature never gets high enough for further fusion. Helium burning mainly produces carbon and oxygen, and these reactions are extremely temperature-sensitive. A slight rise in temperature can significantly increase the reaction rate, making the star unstable and causing large pulsations that eventually expel the star's outer envelope into the interstellar medium. The remaining carbon-oxygen core contracts under gravity but cannot ignite carbon fusion due to mass loss. It ultimately becomes a white dwarf, where gravity is balanced by electron degeneracy pressure.

In more massive stars (greater than $8 M_{\odot}$), the core undergoes successive stages of fusion, burning elements such as carbon, neon, oxygen, magnesium, and silicon. This creates an onion-like structure with concentric burning shells. The innermost shell contains iron-group elements (Fe, Ni, Co), the end products of silicon burning (Fig. 6.1). Fusion stops at iron (^{56}Fe) since it is the most stable nucleus, and iron

burning is not energetically favourable. Without fusion, there is no outward thermal pressure to counteract gravity, causing the core to collapse. As the core gains mass from the surrounding shells, it eventually exceeds the **Chandrasekhar limit** ($1.4 M_{\odot}$), and electron degeneracy pressure can no longer support it.

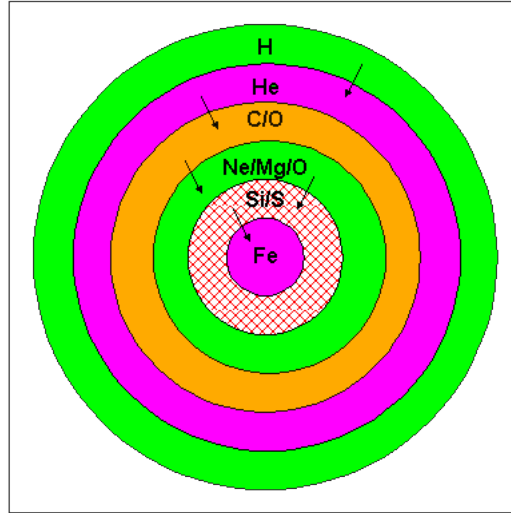


Figure 6.1: Schematic diagram of neutron star core.

The core's density increases until inverse beta decay becomes favourable, where protons capture electrons to form neutrons and neutrinos. This process depletes electrons, reducing electron degeneracy pressure and accelerating the collapse. Neutrinos initially escape the star quickly but become trapped as the density reaches approximately 10^{12} g/cm^3 . When the core's density exceeds nuclear density ($\sim 2.8 \times 10^{14} \text{ g/cm}^3$), nuclei dissolve into nuclear matter. The repulsion between nucleons and the degeneracy pressure of nucleons, electrons, and neutrinos then halt further compression, creating a shock wave that expels the star's outer layers in a supernova explosion.

If the star's initial mass is more than $20 M_{\odot}$, the remaining core collapses into a black hole. For less massive stars, the remnant forms a neutron star. Newly formed neutron stars are extremely hot, with temperatures ranging from 10^{11} to 10^{12} K. They cool rapidly by emitting trapped neutrinos, reducing their temperature to 10^9

to 10^{10} K within a day. Over time, neutron stars continue to cool more slowly through neutrino emission and later through photon emission.

6.2.2 Structure and composition of Neutron star

In a cold neutron star, the matter is in its absolute ground state, meaning its energy cannot be reduced by any strong, weak, or electromagnetic processes. The composition of this ground state changes significantly with increasing density. The interior structure of a neutron star can be divided into several distinct layers (Fig. 6.2).

At the surface, there is an atmosphere only a few centimetres thick, composed of plasma primarily containing hydrogen, helium, and possibly traces of heavier elements. Although this layer holds a negligible fraction of the star's total mass, it is crucial for observations as the electromagnetic and thermal radiation spectra we detect originate from this region.

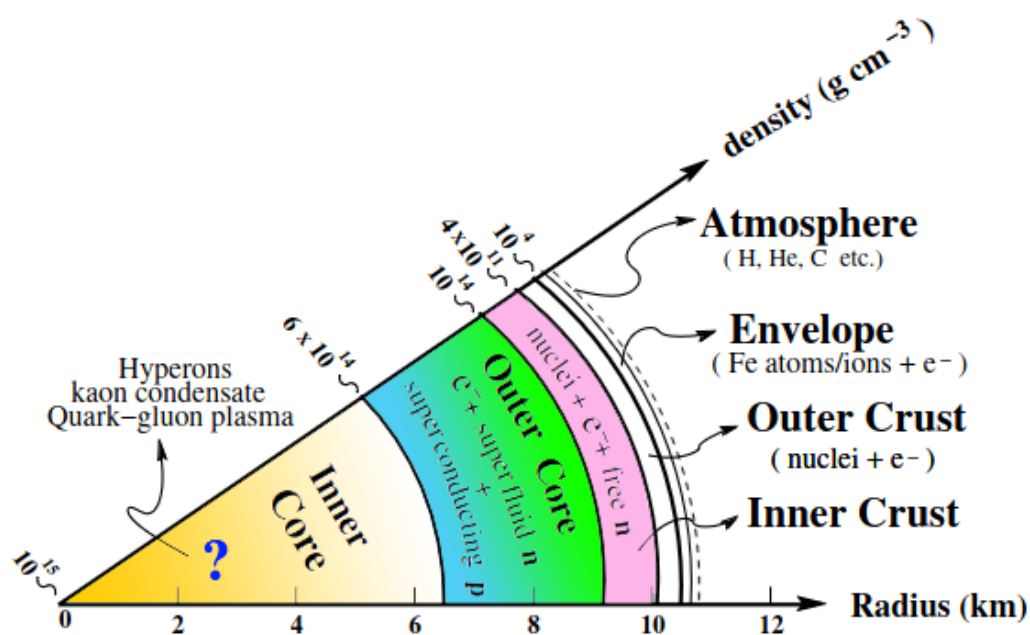


Figure 6.2: Schematic diagram of interior of neutron star core. [235]

Just below the atmosphere lies a thin envelope a few meters thick, consisting of ionized ^{56}Fe atoms and a gas of non-relativistic electrons. At a density of about 10^4 g/cm^3 , ^{56}Fe nuclei become completely ionized, marking the start of the outer crust, which extends a few hundred meters. In this outer crust, nuclei are arranged in a body-centered cubic (bcc) lattice, surrounded by a gas of free electrons that become relativistic at densities above 10^7 g/cm^3 . Initially, ^{56}Fe is the equilibrium nucleus, but as density increases, the nuclei become more neutron-rich through electron capture processes. At around $4 \times 10^{11} \text{ g/cm}^3$, neutrons begin to drip out of the nuclei, marking the neutron drip point and the transition to the inner crust.

The inner crust, which is about a kilometer thick, consists of neutron-rich nuclei immersed in a neutron gas and a uniform electron gas. As density increases, the number of free neutrons and the volume fraction occupied by the nuclei grow. Near the bottom of the crust, where this volume fraction exceeds 50%, the nuclei may transition through various shapes such as cylindrical, slab, cylindrical bubble, and spherical bubble forms—known as the pasta phase [236, 237, 238]. Beyond a density of about 10^{14} g/cm^3 , nuclei dissolve into nuclear matter, defining the crust-core boundary.

The outer core of the neutron star extends up to a density of about $2\rho_0$ (where $\rho_0 \approx 2.8 \times 10^{14} \text{ g/cm}^3$), spanning a few kilometers. It comprises a uniform mixture of neutrons, protons, electrons, and muons, where the electrons and muons form ideal Fermi gases and the neutrons and protons constitute a strongly interacting Fermi liquid. In this region, neutrons may exhibit superfluidity while protons may demonstrate superconductivity.

The inner core, the densest part of the neutron star, along with the outer core, accounts for most of the star's mass. The exact composition and equation of state (EOS) of this region are highly model-dependent. It has been proposed that at such extreme densities, various exotic forms of matter such as hyperons, quark-hadron mixed phases, and Bose-Einstein condensates of kaons might appear.

6.2.3 Observational constraints

The theory of many-body interactions in dense matter is still incomplete, resulting in numerous theoretical models that propose different equations of state (EOS) for neutron star matter. To validate these models, we rely on observations of neutron stars, as the extreme conditions within their interiors cannot be replicated on Earth. Critical observational data include the masses and radii of neutron stars. Each EOS predicts a distinct mass-radius relationship and a specific maximum mass for neutron stars. Therefore, precise measurements of these parameters can eliminate models that fail to align with observed values.

Models incorporating exotic particles within the neutron star core tend to yield softer EOSs, resulting in a smaller predicted maximum mass compared to models excluding such particles. Recent precise measurements have indicated a neutron star mass of $1.97 \pm 0.04 M_{\odot}$ [239], significantly higher than previously measured values, leading to the exclusion of several theoretical models that predicted lower maximum masses.

Neutron stars emit radiation across the entire electromagnetic spectrum, providing valuable information about their surface temperature, chemical composition, magnetic field strength, mass, and radius. Most neutron stars are observed as radio pulsars, with over two thousand identified by 2008 [240], including 186 in binary systems. These binaries fall into two categories: pulsar-neutron star (PSR+NS) and pulsar-white dwarf (PSR+WD) systems.

Additionally, neutron stars in X-ray binaries, where they accrete matter from a companion star, are significant for observations. X-ray binaries are classified into high mass X-ray binaries (HMXBs) and low mass X-ray binaries (LMXBs). In HMXBs, the companion star is a massive star with a mass greater than $10 M_{\odot}$, whereas in LMXBs, the companions are lighter than the sun.

These observational constraints are essential for refining theoretical models and advancing our understanding of neutron star properties and the fundamental physics governing their behaviour.

- **Mass and Radius Measurements** - The most accurately measured masses of neutron stars come from observations of binary systems, particularly double neutron star systems and neutron star-white dwarf systems. The heaviest confirmed neutron star has a mass around $2.14 M_{\odot}$ (PSR J0740+6620 [241]), setting a lower bound on the maximum mass.

The radius of neutron stars can be inferred from X-ray observations of thermonuclear bursts and from fitting the thermal emission of neutron star surfaces. The recent NICER (Neutron star Interior Composition Explorer) [242] observations suggest radii in the range of 11-13 kilometers for neutron stars around $1.4 M_{\odot}$.

- **Moment of Inertia**- The moment of inertia provides information about the distribution of mass within the neutron star and is sensitive to the equation of state (EOS). Measurements from double pulsar systems, like the binary system PSR J0737-3039 [243], are valuable for constraining this property.
- **Surface Temperature and Cooling Rates** - Neutron stars cool over time, primarily through neutrino emission from the core and photon emission from the surface. Observations of surface temperatures, especially from young neutron stars and X-ray observations, provide insights into the cooling mechanisms and interior composition.
- **Gravitational Waves** - The detection of gravitational waves from neutron star mergers (e.g., GW170817 [244]) provides information on the tidal deformability, which is sensitive to the neutron star's internal structure and EOS. The tidal de-formability parameter, inferred from these observations, helps constrain the stiffness of the EOS.

- **Other constraints** - Observations of neutron stars through various phenomena provide crucial insights into their properties. X-ray bursts and quasi-periodic oscillations (QPOs) in low-mass X-ray binaries (LMXBs) reveal information about accretion processes, magnetic fields, and the surface characteristics of neutron stars, indirectly helping to estimate their mass and radius. The precise timing properties of pulsars, including their period and period derivative, shed light on magnetic field strength, age, and spin evolution, with millisecond pulsars setting constraints on maximum rotation rates and the equation of state (EOS). Neutron stars exhibit a wide range of magnetic field strengths, from 10^8 to 10^{15} gauss, influencing their emission mechanisms and rotational dynamics; magnetars, with exceptionally strong magnetic fields, offer unique observational constraints on magnetic field decay and energy release. Observations of pulsar glitches and QPOs in magnetar flares provide valuable data on the superfluid properties of the neutron star crust and its interactions with the core. Additionally, neutron star mergers, detected by gravitational wave observatories, yield comprehensive information about the masses, radii, and EOS of these stars, with electromagnetic counterparts like kilonovae offering further insights into their composition and nucleosynthesis processes. By integrating data from these diverse observations, astronomers and physicists can rigorously constrain neutron star properties, enhancing our understanding of the extreme states of matter they contain.

6.3 Quark Stars

The Universe is populated with objects that challenge common understanding, among which quark stars are particularly exotic [245]. First predicted in 1965 by Soviet physicists D.D. Ivanenko and D.F. Kurdgelaidze [246], quark stars are some of the most peculiar celestial bodies. They are thought to form in the dense cores of massive neutron stars, with primordial strange stars being another potential source.

As quarks are the fundamental building blocks of matter, quark stars are significantly more compact than typical neutron stars. According to an analytical study by Banerjee et al. [247], in extreme cases, a quark star's Schwarzschild radius can be up to $\frac{3}{8}$ of its total radius.

Typically, neutron stars represent the final stage in the evolution of massive stars. However, if the star's gravitational pull is strong enough to overcome neutron degeneracy pressure, it can collapse further, forcing neutrons into an ultra-dense quark phase. Alternatively, quark stars can form from the accumulation of ambient quark matter in the presence of sufficient strange quarks [245, 248].

6.4 Massive Compact Halo Objects

In the early twentieth century, observations based on lensing and microlensing [80, 249] suggested the presence of non-luminous objects in the Milky Way's halo, known as Massive Compact Halo Objects (MACHOs). These stellar-mass objects, which do not emit radiation, exhibit a wide range of masses from approximately 6×10^{-8} to $15 M_{\odot}$ [250]), although most commonly they fall within the range of $0.5_{-0.2}^{+0.3} M_{\odot}$ [81, 251]. .

MACHOs have been proposed as candidates for baryonic dark matter. It is hypothesized that MACHOs may originate from primordial strange quark nuggets, which have a mass around 10^{44} GeV [250]. These quark nuggets are believed to have formed during the quark-hadron phase transition, which occurred when the Universe cooled to about 100 MeV [245, 84], roughly 10^{-5} seconds after the Big Bang. This coalescence process [84] suggests an intriguing link between early Universe conditions and the dark matter content observed in the present day.

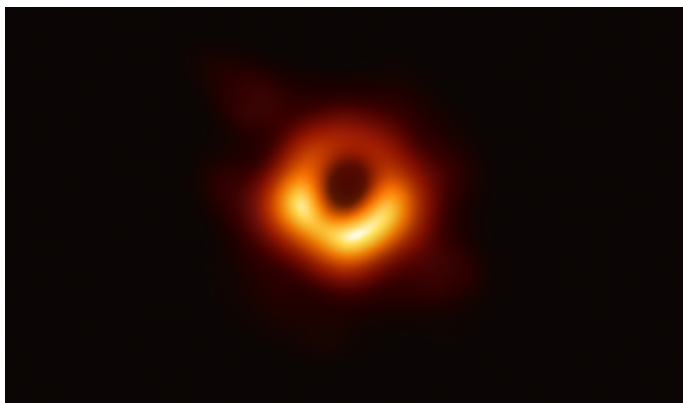


Figure 6.3: The Event Horizon Telescope captured the first-ever image of a black hole, located at the center of the M87 galaxy. (Photo credit: Event Horizon Telescope Collaboration)

6.5 Black Holes

The concept of a “Dark Star,” now known as a black hole, was first introduced by British philosopher John Michell in 1783 within the framework of Newtonian gravity. Nearly 200 years later, in 1965, Roger Penrose provided a mathematical description of this phenomenon using Einstein’s theory of relativity. Black holes [252] are among the most enigmatic entities in the Universe, characterized by their extreme compactness and intense gravitational pull, which prevents even light from escaping.

Black holes are believed to form from the gravitational collapse of massive stars. When a star exhausts its nuclear fuel, its core collapses under the force of gravity. In some instances, the star’s mass becomes so concentrated that the escape velocity at its surface equals the speed of light. Consequently, the star ceases to emit or reflect any electromagnetic radiation, rendering it invisible and thus a black hole.

Fig. 6.3 depicts the first-ever image of a black hole, captured by the Event Horizon Telescope Collaboration in 2019. Although this image shows a supermassive black hole, black holes can vary widely in mass. Primordial black holes (PBHs), for example, can be significantly lighter than stellar-mass black holes. The concept of PBHs was first introduced by Soviet scientists Y.B. Zel’dovich and I.D. Novikov

[253]. These black holes are thought to form from the collapse of overdense regions in the early Universe [254, 255, 256, 257].

The critical threshold for such overdensity can be characterized by the Jeans length $R_j = \sqrt{\frac{1}{3G\rho}}$. The density fluctuation $\delta\rho$ must meet the condition $\delta_{\min} \leq \delta\rho \leq \delta_{\max}$, where δ_{\max} and δ_{\min} represent the maximum and minimum values of the density contrasts. This fluctuation is expressed as $\rho = \rho_c + \delta\rho$, where ρ_c is the critical density for collapse. The gravitational fluctuations during the inflationary epoch are considered the most plausible explanation for the formation of PBHs [258, 259, 260, 261, 262, 263, 264].

In addition to standard scenarios, several alternative hypotheses for PBH formation exist, including the collapse of domain walls and cosmic strings, [265, 266, 267] and the fragmentation of scalar condensation [268, 269, 270].

6.6 Other Exotic stars

In addition to the compact stellar objects mentioned earlier, there exists a category of exotic compact stars composed of elementary particles beyond protons, electrons, neutrons, and muons [271, 272]. Quark stars, briefly discussed in the preceding section, are one such example. Other intriguing candidates in this category include preon stars, boson stars, and Planck stars [273]. Preons, hypothesized as fundamental components of leptons and quarks, can form extremely dense preon stars with densities potentially exceeding 10^{23} g/cm³ due to early Universe density fluctuations or gravitational collapse within massive stars [274, 275]. Boson stars, peculiar among compact objects, are theorized to be transparent and lack event horizons like black holes, causing gravitational lensing due to their immense gravitational fields possibly sustained by transparent axions or Helium-4 nuclei [276, 271, 277]. Planck stars, proposed by Carlo Rovelli and Francesca Vidotto in 2014 [273], are highly hypothetical objects where quantum-gravitational pressure counterbalances

their mass, potentially emitting detectable signals of quantum gravitational origin. These exotic celestial bodies remain largely theoretical, challenging to detect through conventional cosmic-ray signals. The future of space-based gravitational wave astronomy holds promise for advancing our understanding and potentially discovering these enigmatic astrophysical entities.

Detection of Isolated Neutron stars through HI signal

In this chapter, alongside the analysis of particle dark matter within the framework of 21cm cosmology, we investigate the detection prospects of non-luminous compact objects, particularly neutron stars, through gravitational lensing of the HI signal. We propose a methodology to detect the lensed 21cm signal by an isolated neutron star and subsequently calculate the necessary mass, radius, and position of the neutron star to observe such lensing effects. This exploration bridges theoretical cosmology with observational astrophysics, offering insights into the potential use of gravitational lensing to probe compact objects and their impact on cosmological observations.

7.1 Introduction

Neutral atomic hydrogen (HI) is essential for understanding the Universe's evolution, providing critical insights into the formation and dynamics of galaxies [278, 279, 280].

HI signals also trace the distribution of matter throughout the cosmos. Studies indicate that redshifted HI signals from the post-reionization era ($z < 6$) are particularly valuable for understanding structure formation, as they originate from dense, self-shielded regions of neutral hydrogen [281]. However, detecting HI signals is challenging due to their weak strength relative to foreground and background noise, limiting observations to the local Universe. Only a few studies [282, 283] have successfully detected HI signals at redshifts beyond $z \sim 0.1$, providing limited information on HI's role in more distant cosmic environments.

In recent decades, our understanding of the cosmic evolution of neutral hydrogen is expected to undergo a significant transformation. Several advanced radio telescopes are being developed to observe the HI spectral line at high redshifts. These include the Australian Square Kilometre Array Pathfinder (ASKAP) [284], the Square Kilometre Array [285], MeerKAT [286], the upgraded Karl G. Jansky Very Large Array [287], the Westerbork Synthesis Radio Telescope (WSRT) with the APERTure Tile In Focus project (APERTIF)[288], the upgraded Karl G. Jansky Very Large Array [287] and the upgraded Giant Metrewave Radio Telescope (uGMRT) [289]. These instruments will enable deep HI surveys, allowing for the detection of individual galaxies at redshifts up to $z \sim 1$ and beyond. This will facilitate studies of HI in galaxies at unprecedented scales and distances. The increased observational capacity will necessitate new analytical frameworks to accommodate the dynamics of an evolving Universe, ensuring accurate data interpretation and advancing our comprehension of cosmic phenomena.

HI radiation also offers significant potential for gravitational lensing studies. Research has shown that if the Epoch of Reionization (EoR) occurred at redshift $z \sim 8$ or later, large-scale radio arrays like the SKA could measure the lensing convergence power spectrum and refine standard cosmological parameters [290]. During the EoR, the neutral hydrogen fraction is high, and HI gas is not limited to individual galaxies. At lower redshifts, the HI fraction decreases significantly, with the gas primarily residing within discrete galaxies. In this regime, the distribution of HI is modelled

as discrete sources clustered according to the Cold Dark Matter (CDM) paradigm. This modelling is crucial for measuring lensing from HI radiation post-reionization. The evolution of the HI fraction with redshift is still debated, significantly affecting the expected lensing signal-to-noise ratio (S/N).

In this study, we explore the HI signal from a distant galaxy, providing essential information about the properties of neutral hydrogen sources and the intergalactic medium (IGM) at various redshifts. The uGMRT, with its 30 parabolic dishes of 45 meters each arranged in a “Y” shaped pattern and operating in four frequency bands (125-250 MHz, 250-500 MHz, 550-850 MHz, and 1060-1460 MHz), is an excellent instrument for detecting such HI signals. Each frequency band has system noise dependent on various factors, including system temperature, antenna gain, frequency bandwidth, and integration time. Additionally, foreground radio sources create noise several orders of magnitude higher than the HI signal. Techniques to mitigate these foreground sources have been discussed in the literature [291, 292, 293].

Recently, Chakraborty et al. [282] reported detecting the HI signal from a neutral hydrogen source in a galaxy at redshift $z \sim 1.3$ using the uGMRT’s Band-4. This observation suggests that the signal was magnified, allowing it to surpass the foreground and system noise levels of the telescope. Strong gravitational lensing is one potential method for magnifying weak HI signals. Chakraborty et al. noted the nature and redshift of the lensing medium but did not provide further details.

In this analysis, we present a method to quantify the size and position of the lensing object using the lensed HI signal detected at different uGMRT frequency bands. While various astrophysical objects such as MACHOs and black holes can lens the HI signal, we focus on neutron stars as potential lensing objects. Our proposed method is applicable to any radio telescope with similar specifications.

7.2 Effect of gravitational lensing of 21cm line

We explore a model of strong gravitational lensing, where a neutron star amplifies the HI signal from a distant galaxy, making it detectable across various frequency bands of the uGMRT. The discussion includes several key aspects: the flux of the HI signal from the distant galaxy, the noise from the telescope and background that suppresses this signal, the gravitational lensing model used to amplify the signal beyond the noise level for detection at uGMRT, the relationship between a neutron star's mass and radius and its impact on signal amplification, the optical depth indicating the likelihood of signal detection, and the chance coincidences crucial for the amplification of the HI signal as detected by uGMRT.

7.2.1 Flux Density

The brightness of a radio signal is typically measured by its flux, given by $S = \frac{L}{4\pi D_L(z)^2}$, where L represents the luminosity and $D_L(z)$ is the luminosity distance of the source. The luminosity distance is related to the co-moving distance by $D_L(z) = (1+z) D_M(z)$. In this study, we examine a neutral hydrogen source within a distant galaxy at a cosmological distance with redshift z . We assume that three-fourths of the HI atoms are in the upper hyperfine state, emitting HI signals with a spontaneous emission rate of A_{HI} . The number of HI atoms involved in this emission can be estimated from the source's luminosity using $n_{\text{HI}} = \frac{4L}{3h \nu_{\text{HI}} A_{\text{HI}}}$, where h is the Planck constant and $\nu_{\text{HI}} = 1420$ MHz is the HI emission frequency. To estimate the HI column density, which represents the number of HI atoms per unit area along the line of sight to the galaxy, we use $N_{\text{HI}} = \frac{n_{\text{HI}}}{\Omega_{\text{beam}} D_A(z)^2}$. Here, Ω_{beam} is the solid angle of the telescope beam, varying with different frequency bands, and $D_A(z)$ is the angular diameter distance of the galaxy, related to the co-moving distance by $D_A(z) = \frac{D_M(z)}{(1+z)}$. Combining these equations, the HI flux from a galaxy at redshift z

can be calculated as

$$S_{\text{HI}}(z) = \frac{3 h \nu_{\text{HI}} A_{\text{HI}} N_{\text{HI}} \Omega_{\text{beam}}}{16\pi (1+z)^4} \quad (7.1)$$

where Ω_b , Ω_m , and Ω_{HI} are the cosmological density parameters for baryons, matter, and neutral hydrogen, respectively. In this context, A_{HI} is the spontaneous emission rate of HI, which equals $2.88 \times 10^{-15} \text{ s}^{-1}$, h is the Planck constant, valued at $6.63 \times 10^{-34} \text{ J} \cdot \text{Hz}^{-1}$, and ν_{HI} is the HI emission frequency, which is 1420 MHz. Wolfe et al. (2005) proposed that damped Lyman-alpha systems serve as reservoirs of neutral hydrogen, playing a crucial role in the formation of galaxies at cosmological distances.

Damped Lyman-alpha systems are known to contribute significantly to the HI column density, N_{HI} , whereas Lyman-alpha systems are optically thin at the Lyman limit [294]. For this study, we use a saturated value of $N_{\text{HI}} = 2 \times 10^{20} \text{ cm}^{-2}$ [295, 296] as the HI column density for damped Lyman-alpha systems. The HI flux from a distant galaxy also depends on the solid angle Ω_{beam} covered by the telescope beam, which is given by $d\Omega_{\text{beam}} = A(\theta) \sin \theta d\theta d\phi$ and is influenced by the antenna beam pattern $A(\theta)$. For the uGMRT, this pattern is approximated by a Gaussian function $A(\theta) = \exp(-\theta^2/\theta_0^2)$, where $\theta_0 = 0.6 \theta_{\text{FWHM}}$ and θ_{FWHM} denotes the full width at half maximum of the beam pattern, which varies across different frequency bands.

The redshift of the neutral hydrogen source is related to the observational frequency ν_{obs} by the relation $z = \frac{\nu_{\text{HI}}}{\nu_{\text{obs}}} - 1$. For the uGMRT, the frequency bands correspond to specific redshift ranges: $4.68 \leq z \leq 10.83$ for B2, $1.84 \leq z \leq 4.46$ for B3, $0.67 \leq z \leq 1.58$ for B4, and $0 \leq z \leq 0.34$ for B5. However, in this analysis, we focus on HI signals from self-shielded dense pockets of neutral hydrogen in the post-reionization era, where the redshift is $z < 6$. Therefore, we exclude B2 from our consideration. We also exclude B5 since our focus is on detecting HI flux from galaxies at larger cosmological distances in the post-reionization era. We define a characteristic redshift z_c , based on the central frequencies of B3 and B4, with $z_c = 2.73$ for B3 and $z_c = 1.03$ for B4. For these characteristic redshifts, the HI flux [297] values are $S_{\text{HI}}(z_c) = 0.41 \text{ Jy}$ for B3 and 1.09 Jy for B4.

7.2.2 Telescope and Background Noise

The detection of the faint HI signal is challenged by significant interference from telescope noise, which is predominantly influenced by foreground and background sources. These sources include extragalactic point sources, galactic synchrotron radiation, and both galactic and extragalactic free-free emissions [298, 292, 293]. The noise level of a radio telescope can be determined through the use of the radiometer equation [299]

$$\Delta S = \frac{T_{sys} + T_{BG}}{N_A G \sqrt{(n_P T_{samp} \Delta\nu)}} \quad (7.2)$$

In this context, n_P , N_A , and T_{samp} represent the number of polarizations, the number of antennas, and the sampling time for an observation, respectively. These parameters are independent of the frequency band; for instance, $N_A = 14$, $n_P = 2$, and $T_{samp} = 0.671$ seconds remain constant for both B3 and B4. The antenna gain G varies across the frequency bands of the uGMRT. For this analysis, we use the minimum value of G for each band to assess the maximum possible telescope noise. Specifically, G is 0.38 K Jy^{-1} for B3 and 0.35 K Jy^{-1} for B4 [289]. The system temperature T_{sys} varies across the frequency ranges of each uGMRT band. To maximize the telescope noise, we use the highest value of T_{sys} for each band. Specifically, T_{sys} is set to 165 K for B3 and 100 K for B4 [289]. The frequency bandwidth $\Delta\nu$, also referred to as the usable bandwidth, varies across the different frequency bands of the uGMRT. For B3, the bandwidth is 120 MHz , while for B4, it is 200 MHz [289].

Foreground and background astrophysical sources contribute significantly to the telescope noise, represented by the noise temperature T_{BG} , which is calculated using Eq. 7.2. The value of T_{BG} depends on the observational frequency ν_{obs} , generally decreasing with increasing frequency. The sky temperature for foreground and background noise at an observational frequency of $78 \pm 1 \text{ MHz}$ is approximately 6000 K using the EDGES telescope [173]. This temperature would be lower for the B3 and

Fig. 7.1 illustrates the gravitational lensing of the HI signal by a compact object, specifically an isolated neutron star for this analysis. In the diagram, the source “S” emits the HI signal, which travels along the path “SP” and is deflected at the point “P” by the lensing object “L”. The observer “O” then receives the signal along the path “PO”, forming an image of “S” at “I”. The line “ON” represents the line-of-sight (LOS) between the observer and the compact object. The angular positions of the source “S” and its image “I” relative to “ON” are denoted as β and θ , respectively. It is assumed that both the source and its image lie on the same plane perpendicular to “ON”.

The bending of the signal path is characterized by the impact parameter ξ , which indicates the closest approach of the signal to the lensing object, and the bending angle α relative to “PS”.

For cosmological sources and lensing objects, the angular diameter distance is used instead of their physical distance. For a source at redshift z , the angular diameter distance is given by $D(z) = (1+z)^{-1} \int_0^z dz' (c/H(z'))$, where $H(z)$ is the Hubble parameter and c is the speed of light. In fig. 7.1, the angular diameter distances from “O” to “L” and “S” are denoted as D_L and D_S , respectively, while D_{LS} is the distance between “S” and “L”. Since both “S” and “L” are at cosmological distances, D_{LS} is not simply $D_S - D_L$. The distances of the image and source from “ON” are βD_S and θD_S , respectively, with the separation between “I” and “S” being αD_{LS} .

We define a parameter γ as $D_L = \gamma D_S$, which indicates the relative position of the lensing object. Here, $\gamma \rightarrow 0$ means the lensing object is close to the observer, while $\gamma \rightarrow 1$ indicates it is close to the source. The redshift of the lensing object, z_L , depends on γ and the redshift of the source, z_S , where a fixed γ and z_S determine a constant z_L . Therefore, D_{LS} and D_L are functions of γ and z_S , while D_S depends only on z_S .

The angular position θ of the lensed image is given by

$$\theta_{\pm} = \frac{\beta}{2} \left[1 \pm \sqrt{1 + \left(\frac{2\theta_E}{\beta} \right)^2} \right] \quad (7.3)$$

where β is the angular position of the source and θ_E is the Einstein radius. This equation indicates that two images of the source are formed with angular positions θ_+ and θ_- relative to “ON”. The image at θ_+ is outside the Einstein radius, while the image at θ_- is inside it. Observations may detect varying flux levels from these images, with typically more flux received from the image at θ_+ . Einstein’s angle θ_E is influenced by the mass of the lensing object and the angular diameter distances of the source and lensing object from the observer

$$\theta_E = \left[\frac{4GM_L(R)}{c^2} \left(\frac{D_{LS}(\gamma, z_S)}{D_L(\gamma, z_S) D_S(z_S)} \right) \right]^{1/2} \quad (7.4)$$

where G represents the universal gravitational constant, c is the speed of light in a vacuum, and $M_L(R)$ denotes the total mass of the lensing object, which depends on its radius as detailed later in this paper. The parameters D_{LS} , D_L , and D_S have been previously defined. Eq. 7.4 shows that Einstein’s angle θ_E is influenced by the parameters R , γ , and z_S .

As discussed, strong gravitational lensing magnifies the HI signal flux due to the massive compact object “L” (see fig. 7.1). The amplified flux can be expressed as $S_{\mu} = \mu \times S_{\text{HI}}$, where μ is the magnification factor, and S_{HI} is calculated using eq. 7.1. The signal-to-noise ratio $(SNR)_{\text{HI}}$, which is the ratio of S_{HI} to ΔS , is unaffected by the lens’s magnification. Consequently, the amplified signal-to-noise ratio, $(SNR)_{\mu}$, is scaled similarly: $(SNR)_{\mu} = \mu \times (SNR)_{\text{HI}}$.

We previously noted that strong gravitational lensing creates two images of “S” (Fig. 7.1) due to the lensing object “L”, one inside and one outside the Einstein circle. This means the magnification factor μ will differ for each image. For a given angular position of the source “S” (Fig. 7.1), the magnification factor can be

computed using

$$\mu_{\pm} = \frac{\beta^2 + 2\theta_E^2}{2\beta\sqrt{\beta^2 + 4\theta_E^2}} \pm \frac{1}{2} \quad (7.5)$$

where μ_+ and μ_- are the magnification factors for the images formed outside and inside the Einstein circle, respectively. It follows that the signal-to-noise ratio $(SNR)_{\mu}$ will be higher for the image outside the Einstein circle compared to the one inside. Since θ_E (Eq. 7.4) depends on R , γ , and z_S , the magnification factors μ_{\pm} also depend on these parameters. For simplicity, we will consider only the image outside the Einstein circle for two reasons: (A) the angular separation θ_- is very close to β , making it challenging to differentiate both images due to the limited field-of-view of the uGMRT, and (B) the flux from the image inside the Einstein circle (S_{μ}), with magnification factor μ_- , may be too weak to detect.

7.2.4 Mass of a Neutron Star

We previously established that Einstein's angle θ_E (Eq. 7.4) is influenced by the mass of the lensing object. Consequently, both θ_+ (Eq. 7.3) and μ_+ (Eq. 7.5) also vary with the mass of the lensing object. In this analysis, we use a neutron star, a dense and compact object, as the lensing medium, where its mass is a nonlinear function of its radius. The mass $M_L(R)$ of a neutron star can be determined numerically by solving the Tolman-Oppenheimer-Volkoff (TOV) equations [300], given by:

$$\frac{dP}{dR} = -\frac{GM_L(R)}{R^2} \rho \left(1 + \frac{P}{\rho c^2}\right) \left(1 + \frac{4\pi R^3 P}{M_L(R)c^2}\right) \left(1 - \frac{2GM_L(R)}{c^2 R}\right)^{-1} \quad (7.6)$$

where P , ρ , and R represent the pressure, density, and radius of the neutron star, respectively. The relationship between pressure P and density ρ is given by a polytropic equation $P = K\rho^{\Gamma}$, with K being a constant and Γ the polytropic exponent defined as $\Gamma = 1 + \frac{1}{n}$, where n is the polytropic index. The hydrostatic equilibrium within the neutron star, as described by [301], is expressed through

$$\frac{dM_L}{dR} = 4\pi R^2 P \quad (7.7)$$

We numerically solve these coupled differential equations, using parameters such as a core density $\rho_c = 2.5 \times 10^{17} \text{ kg m}^{-3}$ and a polytropic exponent $\Gamma = \frac{5}{3}$ for the neutron star. The resulting mass $M_L(R)$ initially increases with radius R , reaches a maximum, and then decreases. For the chosen values, the maximum mass $M_L(R)$ is approximately $2M_\odot$ at a radius of around 10 km, denoted as R_{peak} .

7.2.5 Optical Depth

We now focus on the optical depth parameter, τ , which quantifies the likelihood of detecting the lensed HI signal with a radio telescope at a given observational frequency. The optical depth is influenced by the density and position of the lensing object along the line of sight (LOS) and is expressed as

$$\tau = \int_0^{z_S} d\chi(z) (1+z)^2 n_L \sigma(z) \quad (7.8)$$

Here, $\chi(z)$ denotes the co-moving distance for an object at redshift z , n_L represents the co-moving number density of the lensing material, and $\sigma(z)$ is the cross section of the lensing medium for the incoming HI signal at redshift z .

In a flat Λ CDM cosmology, the equation for τ can be reformulated as

$$\tau(z_S, \gamma) = \frac{3}{2} \Omega_{CO} f \int_0^{z_S} dz \frac{(1+z)^2 H_0^2 D_{LS}(z, \gamma) D_L(z)}{c H(z) D_S(z)} \quad (7.9)$$

In this equation, $H(z) = H_0 \sqrt{\Omega_M(1+z)^3 + \Omega_\Lambda}$ is the Hubble parameter, where H_0 , Ω_M , and Ω_Λ are the Hubble constant, dark matter density parameter, and dark energy density parameter, respectively. The values for these parameters are sourced

from Planck results [45]. The dimensionless parameter f is close to unity, and the density parameter of compact objects Ω_{CO} is typically ≤ 0.1 [302]. The equation indicates that τ depends on the redshift of the neutral hydrogen source (z_S) and the position of the lensing object, as determined by the parameter γ .

7.2.6 Chance Coincidence

Up to this point, we have examined how to estimate the signal-to-noise ratio ($(SNR)_\mu$) of the HI signal amplified through gravitational lensing by a compact neutron star for various frequency bands of the uGMRT. The analysis assumes a neutral hydrogen source at redshift z_S with its signal further amplified by a neutron star located at redshift z_L . We have seen that the neutron star's mass, which is a function of its radius, plays a crucial role in this amplification, and the angular position of the image also significantly affects the HI signal's amplification. The neutron star's mass can be estimated using the Tolman-Oppenheimer-Volkoff (TOV) equations [300].

In addition to the mass of the lensing object, the angular position of the source (β) impacts the HI signal amplification. As previously noted, β is defined relative to the line-of-sight (LOS) of the observation (refer to fig. 7.1). According to the amplification formula in eq. 7.5, both amplification and $(SNR)_\mu$ increase dramatically as β decreases. However, this paper does not show these trends explicitly.

We have determined a maximum allowed value for β , denoted as β_{\max} , above which the HI signal amplification becomes insufficient for detection at various uGMRT frequency bands. The value of β_{\max} varies depending on the frequency band, size, and position of the lensing object. For instance, with a lensing object size of $R = 10$ km and $\gamma = 0.5$, β_{\max} is 9.23×10^{-26} rad for B3 and 9.86×10^{-26} rad for B4. These values indicate that β_{\max} is extremely small across all considered frequency bands, suggesting that the source must be very close to the LOS for the HI signal to be detected.

This scenario aligns with the concept of “chance coincidence,” previously discussed in studies such as [303].

7.3 Result

We analyze how variations in several lensing parameters impact the detection of the HI signal across different frequency bands (B3 and B4) of the uGMRT. Our focus is on the redshift (z_L) of the neutron star, which acts as the lensing object, and its dependence on the parameter γ , which indicates the lensing object’s position.

The left panel of fig. 7.2 illustrates how z_L changes with γ (ranging from 0.1 to 0.9) for various redshifts of the neutral hydrogen source situated in distant galaxies. We use characteristic redshifts z_c for the different observational bands of the uGMRT: $z_c = 2.73$ for B3 and $z_c = 1.03$ for B4, represented by different colored lines.

Our findings show that z_L increases as γ increases for all frequency bands of the GMRT. For a given γ , the trend of z_L with γ is quite similar for B3 (red line) and B4 (blue line). Specifically, across the entire range of γ , the maximum z_L is 0.77 for $\gamma = 0.9$ with B4, while the minimum z_L is approximately 0.04 for $\gamma = 0.1$, which is nearly the same for both B3 and B4.

This indicates that the redshift of the neutron star used as a lensing object for detecting the amplified HI signal at the uGMRT falls within the range of 0.04 to 0.77 for different frequency bands.

We next examine how the optical depth varies with the position of the neutron star, which acts as the lensing object. The optical depth (τ) plays a crucial role in determining the likelihood of detecting the amplified HI signal, and it is influenced by factors such as the redshift (z_S) of the neutral hydrogen source, the position (γ) of the neutron star along the line of sight, and the density parameter (Ω_{CO}) of

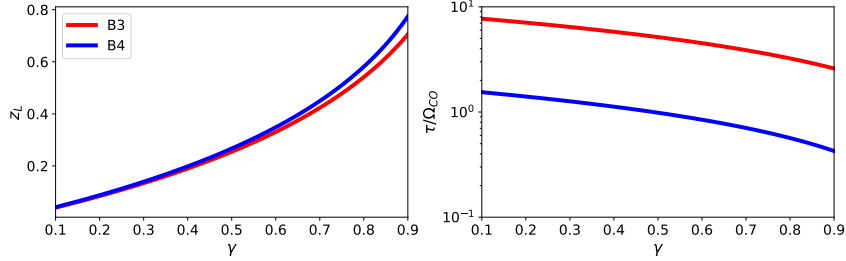


Figure 7.2: The left panel illustrates how the redshift of the neutron star varies with its position, while the right panel shows the corresponding changes in the optical depth fraction. These variations are considered for detecting the HI signal at Band-3 (represented by the red line) and Band-4 (depicted by the blue line) of the uGMRT.

compact objects. Although the exact value of Ω_{CO} is not precisely known, previous study [302] suggests an upper limit of $\Omega_{CO} \leq 0.1$.

We investigate how τ/Ω_{CO} varies with γ for different source redshifts, using characteristic redshifts corresponding to different frequency bands of the uGMRT. The right panel of fig. 7.2 illustrates this variation of τ/Ω_{CO} with γ ($0.1 \leq \gamma \leq 0.9$) for different neutral hydrogen source redshifts. The red and blue lines represent the optical depth fraction for detecting the amplified HI signal at Band-3 ($z_c = 2.73$) and Band-4 ($z_c = 1.03$), respectively.

For all frequency bands examined, τ/Ω_{CO} decreases as γ increases. This indicates that the likelihood of detecting the amplified HI signal is higher when the neutron star is closer to the observer. Specifically, for a fixed γ , τ/Ω_{CO} is highest for Band-3 and lowest for Band-4. This suggests that the probability of detecting the amplified HI signal is greater when the neutral hydrogen source is more distant from the observer and diminishes when the source is closer.

Across the entire range of γ , the maximum value of τ/Ω_{CO} is 7.72 for $\gamma = 0.1$ with Band-3, while the minimum value is 0.43 for $\gamma = 0.9$ with Band-4. Considering the upper limit of Ω_{CO} , the maximum and minimum values of the optical depth are $\tau_{\max} = 0.77$ and $\tau_{\min} = 0.04$, respectively. Therefore, the optimal conditions for

detecting the amplified HI signal occur at Band-3 ($z_c = 2.73$) when the neutron star is situated closer to the observer.

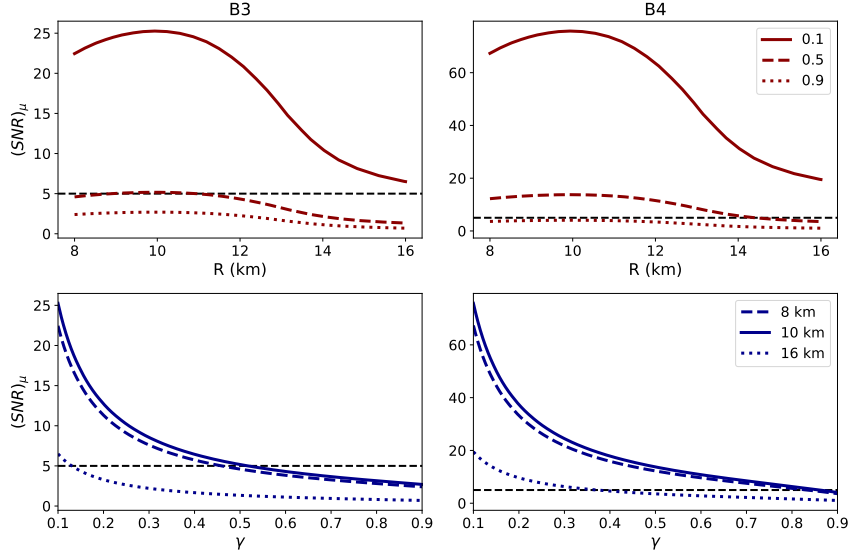


Figure 7.3: The impact of the radius (upper panels) and position (lower panels) of an isolated neutron star on the signal-to-noise ratio $(SNR)_\mu$ for the HI signal expected to be detected at Band-3 (left column) and Band-4 (right column) of the uGMRT is illustrated. The black horizontal dashed line represents the threshold value of $(SNR)_\mu$, denoted as $SNR_{Th} = 5$.

The amplification of the HI signal through gravitational lensing by an isolated neutron star is influenced primarily by two key parameters: the star’s mass and its position along the line of sight (LOS). Earlier discussions have highlighted the necessity for the neutral hydrogen source to be close to the LOS, meaning $\beta \rightarrow 0$, to ensure that the amplified HI signal is detectable across different frequency bands of the uGMRT—a condition known as “chance coincidence.” Consequently, we exclude the parameter β from our analysis of HI signal amplification.

The neutron star’s mass is intricately linked to its radius, which can be estimated using the Tolman-Oppenheimer-Volkov (TOV) equation. We convert the amplification strength into the observed signal-to-noise ratio $(SNR)_\mu$ for detection at various uGMRT frequency bands. Thus, the observed $(SNR)_\mu$ is significantly affected by the neutron star’s size and its position along the LOS.

Fig. 7.3 illustrates how $(SNR)_\mu$ varies with the neutron star's radius and position along the LOS for the detection of the amplified HI signal at Band-3 (left column) and Band-4 (right column). The upper panels depict $(SNR)_\mu$ as a function of neutron star radius (R) for different values of γ (0.1, 0.5, 0.9), which cover the entire range of γ . The lower panels show how $(SNR)_\mu$ changes with γ for different neutron star radii (8 km, 10 km, 16 km), spanning the full range of R . A threshold value for $(SNR)_\mu$, denoted as $SNR_{Th} = 5$, is indicated by black horizontal dashed lines; any $(SNR)_\mu$ below this threshold is not considered a valid detection.

Initially, we examine the variation of $(SNR)_\mu$ with R for detecting the amplified HI signal across different frequency bands. For Band-3 ($z_c = 2.73$), $(SNR)_\mu$ increases with R until it reaches a peak near $R_{max} \approx 10$ km, after which it begins to decrease. The steepness of this curve varies with γ , being steeper for $\gamma = 0.1$ and flatter for $\gamma = 0.9$. The peak $(SNR)_\mu$ value also varies with γ ; it is highest ($SNR_{max} = 25.26$) for $\gamma = 0.1$ and lowest ($SNR_{min} = 2.69$) for $\gamma = 0.9$. For a range of $8 \text{ km} \leq R \leq 16 \text{ km}$, $(SNR)_\mu$ is above SNR_{Th} only for $\gamma = 0.1$ and below this threshold for $\gamma = 0.9$, while $(SNR)_\mu$ exceeds SNR_{Th} for $\gamma = 0.5$ only if $R \lesssim 11$ km.

For Band-4 ($z_c = 1.03$), similar trends are observed. $(SNR)_\mu$ exceeds SNR_{Th} for $\gamma = 0.1$ with $8 \text{ km} \leq R \leq 16 \text{ km}$, and for $\gamma = 0.5$ with $R \lesssim 14 \text{ km}$. However, for $\gamma = 0.9$, $(SNR)_\mu$ remains below SNR_{Th} across the entire range of R . The maximum and minimum $(SNR)_\mu$ values are 75.74 and 4.06, respectively.

Next, we analyze the variation of $(SNR)_\mu$ with γ for different uGMRT frequency bands. For Band-3, $(SNR)_\mu$ decreases with increasing γ . The qualitative nature of the $(SNR)_\mu$ vs. γ plot is similar for $R = 10$ km and 8 km, but differs significantly for $R = 16$ km. For a fixed γ , $(SNR)_\mu$ is maximized at $R = 10$ km and minimized at $R = 16$ km, with $R \approx 10$ km being denoted as R_{peak} , the optimal radius for maximum signal amplification. The value of γ_{cut} , the upper limit of γ for which $(SNR)_\mu$ remains above SNR_{Th} , varies with R , showing $\gamma_{cut} \approx 0.46, 0.51, \text{ and } 0.13$ for $R = 8$ km, 10 km, and 16 km, respectively.

For Band-4, γ_{cut} is approximately 0.84, 0.86, and 0.37 for $R = 8$ km, 10 km, and 16 km, respectively. Generally, γ_{cut} increases as the redshift of the neutral hydrogen source decreases.

In summary, a neutron star with a radius between 8 km and 16 km, positioned close to the observer, can amplify the HI signal from a distant neutral hydrogen source with a redshift ranging from 0.13 to 2.73, making it detectable at various uGMRT frequency bands. This amplification is influenced by the neutron star's radius, with $R_{\text{peak}} = 10$ km consistently providing the highest $(SNR)_{\mu}$, regardless of the source redshift. This radius will be used as the standard for further analysis.

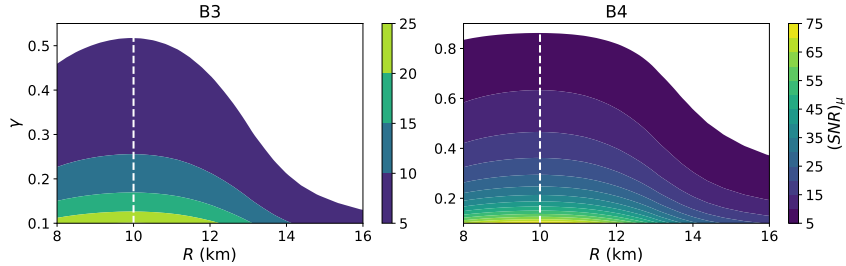


Figure 7.4: The determination of the radius and position of an isolated neutron star is based on the signal-to-noise ratio $(SNR)_{\mu}$ of the HI signal, which is expected to be detected at Band-3 (left column) and Band-4 (right column) of the uGMRT. The white vertical dashed line indicates the standard neutron star radius of $R_{\text{peak}} = 10$ km.

We have explored how various lensing parameters, including the position and radius of a neutron star, impact the amplification of the HI signal detected at different frequency bands of the uGMRT. In this section, we examine how detecting an amplified HI signal with a specific signal-to-noise ratio $(SNR)_{\mu}$ at a given frequency band can help constrain the radius and position of the neutron star responsible for the amplification.

Fig. 7.4 illustrates the relationship between $(SNR)_{\mu}$ and the parameters γ (position) and R (radius) of the neutron star for different frequency bands of the uGMRT. The white vertical dashed line denotes the standard radius of the neutron star, $R_{\text{peak}} = 10$ km. For instance, consider the scenario at Band-3 (left panel). If an HI

signal with $z_c = 2.73$ is detected with an $(SNR)_\mu$ of 10, it suggests that a neutron star with a radius close to $R_{\text{peak}} \approx 10$ km and positioned at $\gamma = 0.25$ is responsible for the amplification. However, if the neutron star's radius deviates from R_{peak} , the corresponding value of γ would adjust accordingly.

The value of γ generally increases with the neutron star's radius, reaching a peak before decreasing with further increases in R . Thus, the maximum allowed γ typically corresponds to the standard radius R_{peak} for a given $(SNR)_\mu$. Similar predictions can be made for Band-4 (right panel). For an HI signal detected with $(SNR)_\mu = 10$ at $z_c = 1.03$, a neutron star with $\gamma = 0.63$ and $R = R_{\text{peak}} \approx 10$ km could be responsible for the amplification.

In summary, the detection of an HI signal at a specific frequency band with a given $(SNR)_\mu$ allows us to infer the neutron star's position and radius. Although γ and R are closely correlated, using the standard radius R_{peak} provides a robust constraint on the position γ of the neutron star.

7.4 Summary

Detecting the HI signal from distant galaxies is challenging due to its low strength compared to background noise. Gravitational lensing by an isolated neutron star is a key method for such amplification. We present a technique to estimate the neutron star's size and position using the signal-to-noise ratio of the amplified HI signal detected at uGMRT's Band-3 and Band-4. Our findings indicate optimal amplification with a neutron star of radius 10 km and suggest constraints on the neutron star's position based on the HI signal's detection. For further validation, we propose cross-checking these estimates with pulsar observations in the same sky location. If no pulsar is detected, alternative massive compact objects might be responsible for the amplification. Future work will explore the amplification potential of accreting neutron stars in binary systems.

Summary and Future Outlook

“To raise new questions, new possibilities, to regard old problems from a new angle, requires creative imagination and marks real advance in science.”

-Albert Einstein

The 21cm signal serves as a powerful tool in cosmology, offering valuable insights into both the early and late stages of the Universe. It provides a window into the era of galaxy and star formation, offering a glimpse into the cosmic dawn. Within the framework of this thesis, various parameters of cosmological significance have been investigated using the global 21cm signal during this pivotal cosmic epoch. The 21cm line, arising from the hyperfine transition of neutral hydrogen, holds particular significance in this context.

The EDGES collaboration reported a 21 cm differential brightness temperature of $T_{21} = -500^{+200}_{-500}$ mK at a redshift of $z = 17.2$ [173], corresponding to a gas temperature of $T_{\text{gas}}(z = 17.2) = 3.26^{+1.94}_{-1.58}$ K when considering $T_s = T_{\text{gas}}$. In the Λ CDM framework, the gas temperature at $z = 17.2$ is expected to be around 7 K, resulting in

a differential brightness temperature of $T_{21}(z = 17.2) \approx -220$ mK (ref. (2.13)). However, there exists tension between the theoretical predictions based on the Λ CDM model and the EDGES observation, suggesting the need to increase the ratio of T_R/T_s . Several mechanisms have been proposed to achieve this, including increasing the background radiation or cooling the gas [180, 203, 304, 194, 179, 305, 178], although these possibilities remain subject to debate.

Dark matter constitutes approximately 85% of the total matter content in the Universe, yet its microscopic properties remain elusive. Over the past decades, numerous dark matter models have been proposed to account for various astrophysical phenomena. However, the fundamental nature of dark matter remains unresolved.

The doctoral research works have explored high energy astrophysical dark matter model (IDM, ELDER), seeking to constrain their properties through the absorption feature observed in the 21 cm differential brightness temperature during the cosmic dawn era. In the context of thermal dark matter models, the Inert Doublet Dark Matter model (IDM) stands out as a promising candidate. Our research aims to constrain the parameters related to energy injection and relic density within this model, with a specific focus on the velocity-averaged annihilation cross-section across various IDM dark matter masses. Through meticulous analysis, our objective is to provide insights into the viability of IDM as a dark matter candidate, while also elucidating the constraints and limitations imposed by relic density considerations. This study delves into the impact of baryon-dark matter collisions and dark matter annihilation on the 21cm signal during the dark ages leading up to the reionization era while neglecting Wouthuysen-Field effect [163]. The focus is on a specific particle dark matter candidate arising from an extended Standard Model of particle physics, featuring an inert scalar doublet. In this inert doublet model (IDM), the lighter of the neutral scalars serves as the dark matter candidate, influencing the evolution of the 21cm Hydrogen line during the dark ages.

Chapter 3 investigation explores how different fractions of IDM dark matter affect

the 21 cm temperature, considering both instantaneous and delayed energy deposition from dark matter annihilation. In our examination of dark matter (DM) annihilation, we observed that the energy is transferred to the system through either instantaneous or delayed deposition mechanisms. Notably, we found that with instantaneous energy deposition, there is an activation of the boost factor, which enhances the effects of DM annihilation. However, in cases where energy deposition is delayed, the boost factor does not exert a prominent effect. Accounting for contributions from thermal evolution, DM annihilation and DM-baryon elastic scattering, the evolution of the baryon temperature and resulting 21 cm temperature fluctuations (T_{21}) are computed. In the analysis, we observed that the T_{21} signal tends to decrease at lower redshift regions when only the effects of dark matter annihilation are considered. Specifically, the evolution of T_{21} exhibits a minimum value at lower redshifts, approximately around the epoch of reionization, particularly for dark matter masses within the range of approximately 70 to 80 GeV. Additionally, the influence of baryon-dark matter collisions appears to be more pronounced in regions characterized by lower redshifts. For all selected dark matter masses, there is a notable dip observed in the T_{21} evolution around a redshift of approximately 95. When both the collision and annihilation effects are combined, the dominance of collision effects is evident around a redshift of approximately 100, beyond which annihilation effects become more prominent. Furthermore, the impact of varying fractions of Inert Doublet Dark Matter (IDM) on the evolution of T_{21} is relatively minor for most chosen masses, except for IDM dark matter masses of approximately 70 and 80 GeV. In these cases, the variations in the minima of T_{21} with different IDM dark matter fractions are within approximately 20% to 25%. This suggests that T_{21} exhibits greater sensitivity in the IDM dark matter mass range of approximately 70 – 80 GeV when considering both dark matter collision and annihilation effects.

Using the micrOMEGAs code, the IDM dark matter annihilation cross-section and

relic density are estimated, ensuring consistency with Planck experiment observations. Lower bounds for the annihilation cross-section are derived, providing insights into the parameter space for IDM dark matter masses ranging from tens to hundreds of GeV. The estimated minimum value for the annihilation cross-section should fall within the interval $\langle\sigma v\rangle \sim (6.5 \times 10^{-29}) - (4.88 \times 10^{-26}) \text{ cm}^3/\text{sec}$ for dark matter masses ranging from $m_\chi \sim 10$ to 990 GeV.

The effects of dark matter-baryon collisions and annihilation are analyzed separately, considering IDM dark matter masses across different ranges. Additionally, the combined effects are investigated, revealing distinct behaviours in the evolution of T_{21} across varying redshifts and IDM dark matter masses. The study underscores the sensitivity of T_{21} to IDM dark matter masses in the region of approximately 70-80 GeV.

The exploration of Inert Doublet Model (IDM) dark matter and two-component dark matter scenarios intertwines crucial aspects of cosmic evolution and dark matter physics. IDM, characterized by its inert scalar doublet within the Standard Model, serves as a prominent candidate for dark matter, impacting the cosmic 21cm signal through its annihilation and interaction processes.

In the context of two-component dark matter, where IDM and generic dark matter coexist without mutual interactions, the thesis establishes fundamental benchmarks for their respective roles in shaping the 21cm brightness temperature (T_{21}). IDM's presence significantly influences T_{21} dynamics during cosmic reionization, particularly through its annihilation effects, which heat baryonic matter and alter the thermal history of the Universe.

Moreover, the study identifies constraints on generic dark matter mass (m_{DM}) to ensure consistency with experimental observations like those from the EDGES collaboration. These constraints not only validate theoretical models but also highlight the intricate balance between heating and cooling effects within the two-component framework.

By linking IDM's distinctive characteristics with the broader implications of two-component dark matter scenarios, the thesis underscores how different dark matter models interact with baryonic matter and influence the evolution of the 21cm signal. This interconnected approach enriches our understanding of dark matter's role in cosmic structure formation and the intricate dynamics of the early Universe.

Chapter 4 investigates the impact of baryon-dark matter interactions on the 21cm signal, focusing on two-component dark matter scenarios where the components—generic dark matter and Inert Doublet Model (IDM) dark matter—are mutually non-interacting. Benchmark values for the baryon-dark matter scattering cross-sections were set for both types, with IDM masses ranging from 10 to 80 GeV and generic dark matter masses up to 3 GeV. The scattering cross-sections were fixed at $\sigma_0^{(\text{DM},\chi)} = 1 \times 10^{-41} \text{ cm}^2$.

The study reveals several key findings: - The presence of IDM dark matter significantly influences the 21cm brightness temperature (T_{21}) through its annihilation processes, contributing to baryon heating. Fig. 4.2(a) illustrates that as the fraction of IDM dark matter increases, T_{21} tends to rise during the reionization epoch, crucially affecting its temperature profile. The analysis in fig. 4.3 indicates an upper limit on the generic dark matter mass ($m_{\text{DM}} \lesssim 1.3 \text{ GeV}$) for T_{21} to remain consistent with the EDGES experiment's findings ($T_{21} = -500_{-500}^{+200} \text{ mK}$ at $z = 17.2$). Notably, as generic dark matter mass increases, the permissible range for IDM fraction decreases, highlighting the balancing act between heating and cooling effects. Based on the results in fig. 4.1, a specific scenario with $m_{\text{DM}} = 0.5 \text{ GeV}$ and $f_\chi = 0.2$ allows all IDM masses (10 GeV - 80 GeV) to align with the EDGES temperature bounds at $z = 17.2$.

Additionally, figs. 4.4(a)-(d) delineate the $\sigma_{41}^\chi - \sigma_{41}^{\text{DM}}$ parameter space, showing minimal contraction in the allowed region as m_{DM} varies from 0.5 GeV to 1 GeV. These plots establish upper and lower bounds for σ_{41}^{DM} based on EDGES constraints, with

$\sigma_0^{\text{DM}} \sim 3 \times 10^{-42} \lesssim \sigma_0^{\text{DM}} \lesssim 10^{-39} \text{ cm}^2$. The values of T_{21} tend towards the upper limits of the EDGES range as generic dark matter mass increases, driven by enhanced heating effects.

Furthermore, an upper limit of $\sigma_0^{\chi} < 10^{-38} \text{ cm}^2$ for IDM-baryon scattering cross-sections has been derived from the benchmark points.

In conclusion, this thesis provides comprehensive insights into the interplay between baryon-dark matter interactions and the 21cm signal, shedding light on how different dark matter scenarios impact cosmic reionization and thermal history.

Two-component dark matter scenarios, which encompass generic dark matter alongside the Inert Doublet Model (IDM), provide a dual perspective on dark matter interactions within the early Universe. IDM, as a specific dark matter candidate, remains non-interacting with generic dark matter, influencing the thermal history and reionization epochs through its distinct annihilation and scattering properties. This scenario is pivotal for understanding the intricate interplay between different dark matter components and their collective impact on cosmic evolution, particularly as inferred from the 21cm brightness temperature (T_{21}).

In contrast, ‘Elastically Decoupling Dark Matter’ (ELDER) dark matter introduces a novel paradigm with self-interactions that actively alter dark matter dynamics and structure formation. These self-scattering properties are crucial in shaping small-scale structures and can significantly affect the observable signatures in the 21cm signal. By modifying the distribution and density profiles of dark matter, ELDER dark matter not only influences the evolution of cosmic structures but also enhances the potential observability of dark matter effects through radio astronomy experiments.

Thus, while two-component dark matter models highlight the diversity of dark matter interactions, ELDER dark matter underscores the role of self-interactions in shaping both large-scale cosmological features and small-scale structures, offering

profound insights into the nature and behavior of dark matter in the early Universe. Integrating these perspectives enriches our understanding of dark matter’s fundamental properties and its implications for cosmic evolution.

The exploration of the global 21cm line of neutral hydrogen offers valuable insights into the reionization era following the “Dark Ages.” This measure, specifically the brightness temperature of the 21cm line (T_{21}), is influenced by various factors, including interactions between dark matter and baryons, as well as self-interaction processes within dark matter itself. Chapter 5 delves into these self-scattering and self-annihilation phenomena within the context of the global 21cm line signal, spanning from the cosmic dawn era to the onset of the first star formation. Specifically, the 21 cm differential brightness temperature have been analysed , ensuring it remains within a certain range around its observed value of EDGES experiment [173] (approximately -500^{+200}_{-500} mK) at redshift 17.2. This constraint provides valuable insights into the properties and characteristics of self-interacting dark matter as potential constituents of dark matter.

Primarily focus has been given on two types of processes namely “2 \rightarrow 2” and “3 \rightarrow 2” and their interaction strengths have been explored in the context of the brightness temperature (T_{21}) results obtained from the 21cm line during the cosmic dawn. Referred to as ELDER dark matter, this self-interacting dark matter model sheds light on the prevalence of “2 \rightarrow 2” interactions over “3 \rightarrow 2” cannibalistic processes. The disparity in the required strength parameter α between these processes underscores the dominance of “2 \rightarrow 2” interactions in affecting T_{21} .

Through this analysis, we delineate the permissible regions for the “2 \rightarrow 2” strength parameter and the mass of dark matter (m_χ). Notably, the interaction strength normalized by dark matter mass increases with mass. Furthermore, we observe an influence of “2 \rightarrow 2” interactions on the cross-section of dark matter-baryon elastic scattering. This is reflected in the shifting regions of $(\sigma_{41} - m_\chi)$ space concerning EDGES T_{21} results, particularly as the value of η increases.

It is noteworthy that the density of dark matter (Ω_χ) required to align with EDGES results consistently falls below the total dark matter density (Ω_{DM}) determined by PLANCK experiments. This suggests the potential existence of other dark matter components across various mass ranges within the Universe.

In contrast, the “3 \rightarrow 2” process within the ELDER scenario appears less significant compared to “2 \rightarrow 2” interactions. Even when the strength parameter α is set to zero, the overall results remain largely unchanged. The constrained cross-section for the “2 \rightarrow 2” process, derived from observations such as the Bullet Cluster and halo shapes, holds significance in explaining small-scale structures via N-body simulations. Thus, the self-scattering dynamics of dark matter emerge as pivotal contributors to the structural evolution of the Universe.

Gravitational lensing, a consequence of Einstein’s theory of general relativity, magnifies celestial objects such as neutron stars, affecting the observable properties of the 21cm signal. The thesis explores how gravitational lensing can amplify these signals, enhancing our ability to detect and study cosmic phenomena with radio telescopes like the uGMRT.

Neutron stars, compact remnants of supernovae, play a dual role in this study: as potential lenses for gravitational amplification and as independent probes of cosmic conditions through their interactions with the 21cm signal. Their precise positioning and characteristics offer insights into the distribution of dark matter and other cosmic structures, bridging theoretical models with observational data.

Detecting the HI signal in radio astronomy is challenging due to its extremely low strength compared to foreground and background noises. Recent studies have reported detections of this signal at various radio telescopes, suggesting magnification through mechanisms like strong gravitational lensing, quantified by the signal-to-noise ratio (SNR).

Chapter 7 presents a method to estimate the position and size of the lensing medium using the SNR of the HI signal, considering detection at different uGMRT frequency bands (Band-3 and Band-4). We analyse the effects of lensing parameters—such as size, mass, and position of the neutron star, as well as detection probability—on the SNR and its variation across frequency bands.

Our research reveals critical insights into the gravitational lensing of the HI-21cm signal by isolated neutron stars. Our analysis indicates a strong potential for detecting the HI signal from distant galaxies with high signal-to-noise ratios using the uGMRT, particularly noting that Band-4 provides a better signal-to-noise ratio compared to Band-3. To achieve adequate amplification of the HI signal, the neutral hydrogen source must be near the line of sight between the observer and the isolated neutron star, with the neutron star’s redshift falling in the range of $0.04 \leq z_L \leq 0.77$ depending on the source’s redshift. Additionally, the amplification is maximized for a neutron star with a radius of 10 km and decreases for a radius of 16 km, regardless of its position along the line of sight. We also identified an upper boundary for the neutron star’s position beyond which effective amplification is not achievable. This upper limit varies with the neutron star’s radius and the redshift of the HI source. Our analysis provides a method to determine the position and size of an isolated neutron star by using the signal-to-noise ratio of the amplified HI signal detected in Band-3 and Band-4, assuming a fixed radius ($R = 10$ km), or conversely, to deduce the radius if the position is determined through other means.

We also explore the possibility of cross-validating the estimated parameters of the neutron star responsible for amplifying the HI signal by observing pulsars in the same region of the sky. Given the predicted redshift range, the necessary luminosity for such an extragalactic pulsar is approximately $\sim 10^{32}$ erg s⁻¹, which is much higher than that of the brightest pulsars detected so far. This makes simultaneous detection of the pulsar and amplified HI signal challenging at radio frequencies. However, such a high-luminosity pulsar might be detectable in the X-ray band [306]. In this context, multi-messenger astronomy could be applied, where the HI signal is detected in the

radio band and the corresponding pulsar emission is observed in the X-ray band from the same sky location. Previous studies [307, 308] provide methodologies for estimating the redshift and radius of isolated neutron stars emitting X-ray pulsar signals. We propose to use the detection of amplified HI signals in the radio band to cross-validate the position and size of the neutron star through pulsar observations in the X-ray band from the same location.

Further studies will explore amplification by other massive compact objects, such as accreting neutron stars in binary systems, which is beyond the scope of this thesis.

Future Prospects

The analyses discussed in this thesis have been centered on two sectors, namely IDM and ELDER, of contemporary significance, which are primarily concerned with the identification of signatures of dark matter candidates based on extensions of the standard model of particle physics in 21cm data. In addition to the analysis of dark matter signatures, a theoretical investigation was conducted involving the detection of Gravitational Lensing signatures of isolated Neutron stars in uGMRT based on the analysis of the Global HI-21cm Signal.

The experience gained from these works has facilitated the investigation of several aspects of high energy and astroparticle physics through the analysis of data from next-generation telescopes like the SKA (Square Kilometer Array) and HERA (Hydrogen Epoch of Reionization Array), which will provide better resolution and sensitivity. Furthermore, more efficient noise reduction techniques can be developed to properly analyze faint signals and compare the outcomes with experiments being conducted at LHC and future colliders.

On the theoretical front, the development and testing of more dark matter models inspired by particle physics theory within the current framework, and addressing extended questions involving the study of the Epoch of Reionization, formation of the cosmic web, and investigating how dark matter influences the large-scale structure of the Universe have been pursued.

In the final part of the thesis, the detection of compact astrophysical objects using gravitational lensing of the 21cm signal was investigated. Efforts can be extended to shed more light on their composition and their belonging to the dark sector of the Universe.

The future outlook for 21cm astronomy and dark matter physics appears promising, supported by ongoing technological advancements and collaborative efforts spanning diverse disciplines. The emerging possibilities in cosmology perceived as a pathway

towards refining models and simulations, enhancing deeper insights into how dark matter physics influences cosmic structures, with the potential to extend the boundaries of current physical paradigms.

Bibliography

- [1] D. Branch and B. Patchett, “*Type i supernovae*”, *Mon. Not. Roy. Astron. Soc.* **161** 71--83 (1973).
- [2] C. L. Bennett, D. Larson, J. L. Weiland, N. Jarosik, G. Hinshaw, N. Odegard et al., “*NINE-YEAR WILKINSON MICROWAVE ANISOTROPY PROBE (WMAP) OBSERVATIONS: FINAL MAPS AND RESULTS*”, *Astrophys. J. suppl.* **208** 20 (Sep, 2013), [[arXiv:1212.5225](#)].
- [3] A. R. Sandage, “*Cosmology: A search for two numbers*”, *Physics Today* **23** 34--41 (1970).
- [4] Y. L. Bolotin, V. Cherkaskiy, O. Lemets, D. Yerokhin and L. Zazunov, “*Cosmology in terms of the deceleration parameter. part i*”, *arXiv preprint arXiv:1502.00811*, (2015).
- [5] Planck Collaboration, Ade, P. A. R. et al., “*Planck 2015 results - xiii. cosmological parameters*”, *Astron. Astrophys.* **594** A13 (2016), [[arXiv:1502.01589](#)].
- [6] N. Planck Collaboration, Aghanim, Y. Akrami, M. Ashdown, J. Aumont, C. Baccigalupi, M. Ballardini et al., “*Planck 2018 results-vi. cosmological parameters*”, *Astronomy & Astrophysics* **641** A6 (2020).
- [7] O. Lahav and A. R. Liddle, “*The cosmological parameters*”, *arXiv preprint astro-ph/0406681*, (2004).

- [8] J. P. Gardner, J. C. Mather, M. Clampin, R. Doyon, M. A. Greenhouse, H. B. Hammel et al., “*The james webb space telescope*”, *Space Science Reviews* **123** 485--606 (2006).
- [9] J. A. Tyson, “*Large synoptic survey telescope: overview*”, *Survey and Other Telescope Technologies and Discoveries* **4836** 10--20 (2002).
- [10] H. C. Chiang, P. A. Ade, D. Barkats, J. O. Battle, E. M. Bierman, J. J. Bock et al., “*Measurement of cosmic microwave background polarization power spectra from two years of bicep data*”, *Astrophys. J.* **711** 1123 (2010).
- [11] G. Polenta, P. A. Ade, A. Balbi, J. Bock, J. Bond, J. Borrill et al., “*Boomerang results*”, *Advances in Space Research* **36** 1064--1069 (2005).
- [12] M. Tegmark, M. R. Blanton, M. A. Strauss, F. Hoyle, D. Schlegel, R. Scoccimarro et al., “*The three-dimensional power spectrum of galaxies from the sloan digital sky survey*”, *Astrophys. J.* **606** 702{740 (May, 2004), [[arXiv:astro-ph/0310725](https://arxiv.org/abs/astro-ph/0310725)].
- [13] E. Kolb and M. Turner, *The Early Universe*. Avalon Publishing, 1994.
- [14] E. J. Copeland, M. Sami and S. Tsujikawa, “*Dynamics of dark energy*”, *International Journal of Modern Physics D* **15** 1753--1935 (2006).
- [15] D. Baumann, *Cosmology*. Cambridge University Press, 2022.
- [16] G. Montani, *Primordial cosmology*. World Scientific, 2011.
- [17] J. Rafelski, J. Birrell, A. Steinmetz and C. T. Yang, “*A short survey of matter-antimatter evolution in the primordial universe*”, *Universe* **9** 309 (2023).
- [18] K. S. Thorne, “*Primordial element formation, primordial magnetic fields, and the isotropy of the universe*”, *Astrophysical Journal*, vol. 148, p. 51 **148** 51 (1967).

-
- [19] B. D. Fields, P. Molaro and S. Sarkar, “*Big-bang nucleosynthesis*”, *arXiv preprint arXiv:1412.1408*, (2014).
- [20] B. Fields and S. Sarkar, “*Big-bang nucleosynthesis (particle data group mini-review)*”, *arXiv preprint astro-ph/0601514*, (2006).
- [21] E. Kolb and M. Turner, “*The early universe addison-wesley*”, *Redwood City*, (1990).
- [22] W. Keel, “*The early universe: From recombination to reionisation*”, *Astrophysics Update* **139** (2003).
- [23] A. Loeb, “*The dark ages of the universe*”, *Scientific American* **295** 46--53 (2006).
- [24] J. Miralda-Escudé, “*The dark age of the universe*”, *Science* **300** 1904--1909 (2003).
- [25] V. Bromm and R. B. Larson, “*The first stars*”, *Annu. Rev. Astron. Astrophys.* **42** 79--118 (2004).
- [26] V. Bromm, “*Formation of the first stars*”, *Reports on Progress in Physics* **76** 112901 (2013).
- [27] S. Zaroubi, “*The epoch of reionization*”, *The first galaxies: theoretical predictions and observational clues* 45--101 (2012).
- [28] T. R. Choudhury, “*A short introduction to reionization physics*”, *General Relativity and Gravitation* **54** 102 (2022).
- [29] J. H. Oort, “*The force exerted by the stellar system in the direction perpendicular to the galactic plane and some related problems*”, *bain* **6** 249 (Aug., 1932).
- [30] H. W. Babcock, “*The rotation of the Andromeda Nebula*”, *Lick Observatory Bulletin* **498** 41-51 (Jan., 1939).

- [31] F. Zwicky, “Die Rotverschiebung von extragalaktischen Nebeln”, *Helvetica Physica Acta* **6** 110–127 (Jan., 1933).
- [32] S. Smith, “The mass of the virgo cluster”, *Astrophysical Journal*, vol. 83, p. 23 **83** 23 (1936).
- [33] F. Zwicky, “On the Masses of Nebulae and of Clusters of Nebulae”, *Astrophys. J.* **86** 217 (Oct., 1937).
- [34] V. C. Rubin, J. Ford, W. K. and N. Thonnard, “Extended rotation curves of high-luminosity spiral galaxies. IV. Systematic dynamical properties, Sa - \dot{z} Sc.”, *Astrophys. J. Lett.* **225** L107–L111 (Nov., 1978).
- [35] E. Corbelli and P. Salucci, “The extended rotation curve and the dark matter halo of M33”, *Mon. Not. Roy. Astron. Soc.* **311** 441–447 (Jan, 2000), [[arXiv:astro-ph/9909252](https://arxiv.org/abs/astro-ph/9909252)].
- [36] A. Klypin, H. Zhao and R. S. Somerville, “Lambda CDM-based models for the Milky Way and M31 I: Dynamical models”, *Astrophys. J.* **573** 597–613 (Jul, 2002), [[arXiv:astro-ph/0110390](https://arxiv.org/abs/astro-ph/0110390)].
- [37] M. Kamionkowski, “Possible relics from new physics in the early universe: Inflation, the cosmic microwave background, and particle dark matter”, in *Workshop on The Early and Future Universe*, 6, 1998. [[arXiv:astro-ph/9809214](https://arxiv.org/abs/astro-ph/9809214)].
- [38] K. G. Begeman, A. H. Broeils and R. H. Sanders, “Extended rotation curves of spiral galaxies: dark haloes and modified dynamics”, *Mon. Not. Roy. Astron. Soc.* **249** 523–537 (04, 1991).
- [39] G. Gamow, “The origin of elements and the separation of galaxies”, *Phys. Rev.* **74** 505–506 (Aug, 1948).
- [40] G. Gamow, “The Evolution of the Universe”, *Nature* **162** 680–682 (1948).

-
- [41] A. A. Penzias and R. W. Wilson, “A Measurement of Excess Antenna Temperature at 4080 Mc/s.”, *Astrophys. J.* **142** 419–421 (July, 1965).
- [42] A. A. Penzias and R. W. Wilson, “Measurement of the flux density of cas a at 4080 mc/s.”, *Astrophysical Journal*, vol. 142, p. 1149 **142** 1149 (1965).
- [43] W. Hu and S. Dodelson, “Cosmic microwave background anisotropies”, *Annual Review of Astronomy and Astrophysics* **40** 171–216 (2002).
- [44] D. Samtleben, S. Staggs and B. Winstein, “The cosmic microwave background for pedestrians: A review for particle and nuclear physicists”, *Annu. Rev. Nucl. Part. Sci.* **57** 245–283 (2007).
- [45] N. Aghanim, Y. Akrami, M. Ashdown, J. Aumont, C. Baccigalupi, M. Ballardini et al., “Planck 2018 results - vi. cosmological parameters”, *Astron. Astrophys.* **641** A6 (Sep, 2020), [[arXiv:1807.06209](https://arxiv.org/abs/1807.06209)].
- [46] D. Clowe, M. Bradač, A. H. Gonzalez, M. Markevitch, S. W. Randall, C. Jones et al., “A direct empirical proof of the existence of dark matter”, *Astrophys. J.* **648** L109 (2006).
- [47] D. Clowe, A. Gonzalez and M. Markevitch, “Weak-lensing mass reconstruction of the interacting cluster 1e 0657–558: Direct evidence for the existence of dark matter”, *Astrophys. J.* **604** 596 (2004).
- [48] M. Markevitch, A. H. Gonzalez, D. Clowe, A. Vikhlinin, W. Forman, C. Jones et al., “Direct constraints on the dark matter self-interaction cross section from the merging galaxy cluster 1e 0657–56”, *Astrophys. J.* **606** 819 (2004).
- [49] M. Milgrom, “A modification of the newtonian dynamics as a possible alternative to the hidden mass hypothesis”, *Astrophysical Journal, Part 1 (ISSN 0004-637X)*, vol. 270, July 15, 1983, p. 365–370. Research supported by the US-Israel Binational Science Foundation. **270** 365–370 (1983).

- [50] B. Famaey and S. S. McGaugh, “*Modified newtonian dynamics (mond): observational phenomenology and relativistic extensions*”, *Living reviews in relativity* **15** 1--159 (2012).
- [51] G. Madejski, “*Recent and future observations in the x-ray and gamma-ray bands: Chandra, suzaku, glast, and nustar*”, *AIP Conference Proceedings* **801** 21-30 (2005), [[arXiv:astro-ph/0512012](#)].
- [52] M. Bradač, S. W. Allen, T. Treu, H. Ebeling, R. Massey, R. G. Morris et al., “*Revealing the properties of dark matter in the merging cluster MACS j0025.4-1222*”, *Astrophys. J.* **687** 959–967 (Nov, 2008), [[arXiv:0806.2320](#)].
- [53] S. Banerjee, “*Some aspects of strange matter in astrophysics*”, 2014.
- [54] Wikisource, “*Translation: on the deflection of a light ray from its rectilinear motion — wikisource,*”, 2021.
- [55] D. Walsh, R. F. Carswell and R. J. Weymann, “*0957+ 561 a, b: twin quasistellar objects or gravitational lens?*”, *Nature* **279** 381--384 (1979).
- [56] M. J. Jee, H. C. Ford, G. D. Illingworth, R. L. White, T. J. Broadhurst, D. A. Coe et al., “*Discovery of a ringlike dark matter structure in the core of the galaxy cluster cl 0024+17*”, *Astrophys. J.* **661** 728–749 (Jun, 2007), [[arXiv:0705.2171](#)].
- [57] R. Massey, T. Kitching and J. Richard, “*The dark matter of gravitational lensing*”, *Reports on Progress in Physics* **73** 086901 (2010).
- [58] S. Cole, W. J. Percival, J. A. Peacock, P. Norberg, C. M. Baugh, C. S. Frenk et al., “*The 2df galaxy redshift survey: power-spectrum analysis of the final data set and cosmological implications*”, *Mon. Not. Roy. Astron. Soc.* **362** 505{534 (Sep, 2005), [[arXiv:astro-ph/0501174](#)].

- [59] M. Colless, G. Dalton, S. Maddox, W. Sutherland, P. Norberg, S. Cole et al., “*The 2dF Galaxy Redshift Survey: spectra and redshifts*”, *Mon. Not. Roy. Astron. Soc.* **328** 1039–1063 (12, 2001), [[arXiv:astro-ph/0106498](#)].
- [60] V. Springel, S. D. M. White, A. Jenkins, C. S. Frenk, N. Yoshida, L. Gao et al., “*Simulations of the formation, evolution and clustering of galaxies and quasars*”, *Nature* **435** 629–636 (Jun, 2005), [[arXiv:astro-ph/0504097](#)].
- [61] J. F. Navarro, “*The structure of cold dark matter halos*”, in *Symposium-international astronomical union*, vol. 171, pp. 255–258, Cambridge University Press, 1996.
- [62] V. Springel, J. Wang, M. Vogelsberger, A. Ludlow, A. Jenkins, A. Helmi et al., “*The Aquarius Project: the subhaloes of galactic haloes*”, *Mon. Not. Roy. Astron. Soc.* **391** 1685–1711 (Dec, 2008), [[arXiv:0809.0898](#)].
- [63] PARTICLE DATA GROUP collaboration, K. A. Olive et al., “*Review of Particle Physics*”, *Chin. Phys. C* **38** 090001 (2014).
- [64] A. Coc, E. Vangioni-Flam, P. Descouvemont, A. Adahchour and C. Angulo, “*Updated big bang nucleosynthesis compared with wilkinson microwave anisotropy probe observations and the abundance of light elements*”, *Astrophys. J.* **600** 544–552 (Jan, 2004), [[arXiv:astro-ph/0309480](#)].
- [65] F. Iocco, G. Mangano, G. Miele, O. Pisanti and P. D. Serpico, “*Primordial nucleosynthesis: From precision cosmology to fundamental physics*”, *Phys. Rept.* **472** 1–76 (Mar, 2009), [[arXiv:0809.0631](#)].
- [66] J. Dunkley, E. Komatsu, M. R.olta, D. N. Spergel, D. Larson, G. Hinshaw et al., “*Five-year wilkinson microwave anisotropy probe observations: Likelihoods and parameters from the wmap data*”, *Astrophys. J. suppl.* **180** 306–329 (Feb, 2009), [[arXiv:0803.0586](#)].
- [67] K. Jedamzik and M. Pospelov, “*Big bang nucleosynthesis and particle dark matter*”, *arXiv preprint arXiv:0906.2087*, (2009).

- [68] G. Bertone, D. Hooper and J. Silk, “Particle dark matter: Evidence, candidates and constraints”, *Physics reports* **405** 279--390 (2005).
- [69] J. P. Hughes, “The mass of the coma cluster-combined x-ray and optical results”, *Astrophysical Journal, Part 1 (ISSN 0004-637X)*, vol. 337, Feb. 1, 1989, p. 21-33. Research supported by the Smithsonian Institution. **337** 21--33 (1989).
- [70] P. McDonald, U. Seljak, S. Burles, D. J. Schlegel, D. H. Weinberg, R. Cen et al., “The $Ly\alpha$ forest power spectrum from the sloan digital sky survey”, *Astrophys. J. suppl.* **163** 80 (2006).
- [71] D. H. Weinberg, R. Dave, N. Katz and J. A. Kollmeier, “The lyman- α forest as a cosmological tool”, in *AIP Conference Proceedings*, vol. 666, pp. 157–169, American Institute of Physics, 2003.
- [72] R. Lynds, “The absorption-line spectrum of 4c 05.34”, *Astrophysical Journal*, vol. 164, p. L73 **164** L73 (1971).
- [73] G. Burbidge, “The quasi-stellar objects”, *American Scientist* **55** 282--295 (1967).
- [74] M. Taoso, G. Bertone and A. Masiero, “Dark matter candidates: a ten-point test”, *J. Cosmol. Astropart. Phys.* **2008** 022 (2008).
- [75] F. Mayet, D. Santos and C. Tao, “Astrophysical constraints on dark matter”, *European Astronomical Society Publications Series* **53** 97--104 (2012).
- [76] J. Bullock, “Notes on the missing satellites problem”, *Local Group Cosmology* **20** 95 (2013).
- [77] W. De Blok et al., “The core-cusp problem”, *Advances in Astronomy* **2010**, (2010).

-
- [78] M. Boylan-Kolchin, J. S. Bullock and M. Kaplinghat, “*Too big to fail? the puzzling darkness of massive milky way subhaloes*”, *Mon. Not. Roy. Astron. Soc.: Letters* **415** L40--L44 (2011).
- [79] M. Viel, J. Lesgourgues, M. G. Haehnelt, S. Matarrese and A. Riotto, “*Constraining warm dark matter candidates including sterile neutrinos and light gravitinos with wmap and the lyman- α forest*”, *Phys. Rev. D* **71** 063534 (2005).
- [80] C. Alcock, C. W. Akerlof, R. A. Allsman, T. S. Axelrod, D. P. Bennett, S. Chan et al., “*Possible gravitational microlensing of a star in the large magellanic cloud*”, *Nature* **365** 621–623 (Oct, 1993), [[arXiv:astro-ph/9309052](https://arxiv.org/abs/astro-ph/9309052)].
- [81] C. Alcock, R. A. Allsman, D. R. Alves, T. S. Axelrod, A. C. Becker, D. P. Bennett et al., “*The macho project: Microlensing results from 5.7 years of large magellanic cloud observations*”, *Astrophys. J.* **542** 281–307 (Oct, 2000), [[arXiv:astro-ph/0001272](https://arxiv.org/abs/astro-ph/0001272)].
- [82] M. Persic and P. Salucci, “*The baryon content of the universe*”, *Mon. Not. Roy. Astron. Soc.* **258** 14P–18P (Sep, 1992), [[arXiv:astro-ph/0502178](https://arxiv.org/abs/astro-ph/0502178)].
- [83] N. Mandolesi, F. Villa and L. Valenziano, “*The planck satellite*”, *Advances in Space Research* **30** 2123--2128 (2002).
- [84] S. Banerjee, A. Bhattacharyya, S. K. Ghosh, S. Raha, B. Sinha and H. Toki, “*Massive compact halo objects from the relics of the cosmic quark-hadron transition*”, *Mon. Not. Roy. Astron. Soc.* **340** 284–288 (Mar, 2003), [[arXiv:astro-ph/0211560](https://arxiv.org/abs/astro-ph/0211560)].
- [85] P. Gondolo, “*Non-baryonic dark matter*”, in *Frontiers of Cosmology: Proceedings of the NATO Advanced Study Institute on The Frontiers of Cosmology Cargèse, France 8–20 September 2003*, pp. 279–333. Springer, 2005.

- [86] H.-C. Cheng, J. L. Feng and K. T. Matchev, “*Kaluza-Klein dark matter*”, *Phys. Rev. Lett.* **89** 211301 (2002).
- [87] G. Servant and T. M. P. Tait, “*Is the lightest Kaluza-Klein particle a viable dark matter candidate?*”, *Nucl. Phys.* **B650** 391–419 (2003).
- [88] D. Hooper, G. Zaharijas, D. P. Finkbeiner and G. Dobler, “*Prospects For Detecting Dark Matter With GLAST In Light Of The WMAP Haze*”, *Phys. Rev.* **D77** 043511 (2008).
- [89] D. Majumdar, “*Relic densities for Kaluz-Klein dark matter*”, *Mod. Phys. Lett.* **A18** 1705–1710 (2003).
- [90] T. Lee and Y. Pang, “*Nontopological solitons*”, *Physics Reports* **221** 251–350 (Nov, 1992).
- [91] S. Coleman, “*Q-balls*”, *Nuclear Physics B* **262** 263–283 (Dec, 1985).
- [92] E. W. Kolb, D. J. H. Chung and A. Riotto, “*WIMPzillas!*”, *AIP Conf. Proc.* **484** 91–105 (1999), [[arXiv:hep-ph/9810361](https://arxiv.org/abs/hep-ph/9810361)].
- [93] M. Kachelrieß, O. E. Kalashev and M. Y. Kuznetsov, “*Heavy decaying dark matter and IceCube high energy neutrinos*”, *Phys. Rev. D* **98** 083016 (Oct, 2018), [[arXiv:1805.04500](https://arxiv.org/abs/1805.04500)].
- [94] D. J. H. Chung, E. W. Kolb and A. Riotto, “*Superheavy dark matter*”, *Phys. Rev. D* **59** 023501 (Nov, 1998), [[arXiv:hep-ph/9802238](https://arxiv.org/abs/hep-ph/9802238)].
- [95] R. D. Peccei and H. R. Quinn, “*CP conservation in the presence of pseudoparticles*”, *Phys. Rev. Lett.* **38** 1440–1443 (Jun, 1977).
- [96] R. D. Peccei and H. R. Quinn, “*Constraints imposed by CP conservation in the presence of pseudoparticles*”, *Phys. Rev. D* **16** 1791–1797 (Sep, 1977).
- [97] D. Majumdar, *Dark Matter: An Introduction*. Taylor & Francis, 2014.

-
- [98] H. Baer, K.-Y. Choi, J. E. Kim and L. Roszkowski, “Dark matter production in the early universe: beyond the thermal wimp paradigm”, *Physics Reports* **555** 1--60 (2015).
- [99] D. J. H. Chung, P. Crotty, E. W. Kolb and A. Riotto, “Gravitational production of superheavy dark matter”, *Phys. Rev. D* **64** 043503 (Jul, 2001), [[arXiv:hep-ph/0104100](https://arxiv.org/abs/hep-ph/0104100)].
- [100] D. J. H. Chung, E. W. Kolb and A. Riotto, “Production of massive particles during reheating”, *Phys. Rev. D* **60** 063504 (Aug, 1999), [[arXiv:hep-ph/9809453](https://arxiv.org/abs/hep-ph/9809453)].
- [101] S. I. Blinnikov, “Mirror matter and other dark matter models”, *Physics-Uspekhi* **57** 183 (2014).
- [102] W. Hu, R. Barkana and A. Gruzinov, “Fuzzy cold dark matter: the wave properties of ultralight particles”, *Phys. Rev. Lett.* **85** 1158 (2000).
- [103] M. Fairbairn, A. Kraan, D. Milstead, T. Sjöstrand, P. Skands and T. Sloan, “Stable massive particles at colliders”, *Physics Reports* **438** 1--63 (2007).
- [104] M. Pospelov and A. Ritz, “Resonant scattering and recombination of pseudodegenerate wimps”, *Phys. Rev. D—Particles, Fields, Gravitation, and Cosmology* **78** 055003 (2008).
- [105] D. J. Marsh, “Axion cosmology”, *Physics Reports* **643** 1--79 (2016).
- [106] P. W. Graham, I. G. Irastorza, S. K. Lamoreaux, A. Lindner and K. A. van Bibber, “Experimental searches for the axion and axion-like particles”, *Annual Review of Nuclear and Particle Science* **65** 485--514 (2015).
- [107] Y. Hochberg, E. Kuflik, T. Volansky and J. G. Wacker, “Mechanism for thermal relic dark matter of strongly interacting massive particles”, *Phys. Rev. Lett.* **113** 171301 (Oct, 2014).

- [108] E. Kuflik, M. Perelstein, N. Rey-Le Lorier and Y.-D. Tsai, “Elastically decoupling dark matter”, *Phys. Rev. Lett.* **116** 221302 (2016).
- [109] E. Kuflik, M. Perelstein, N. R.-L. Lorier and Y.-D. Tsai, “Phenomenology of elder dark matter”, *J. High Energy Phys.* **2017** 1--30 (2017).
- [110] L. Lopez Honorez and C. E. Yaguna, “The inert doublet model of dark matter revisited”, *J. High Energy Phys.* **2010** 46 (Sep, 2010).
- [111] M. Battaglieri, A. Belloni, A. Chou, P. Cushman, B. Echenard, R. Essig et al., “Us cosmic visions: New ideas in dark matter 2017: Community report”, 2017.
- [112] K. Griest and M. Kamionkowski, “Unitarity limits on the mass and radius of dark-matter particles”, *Phys. Rev. Lett.* **64** 615--618 (Feb, 1990).
- [113] V. A. Kuzmin and I. I. Tkachev, “Ultrahigh-energy cosmic rays, superheavy long-lived particles, and matter creation after inflation”, *JETP* **68** 271-275 (Aug, 1998), [[arXiv:hep-ph/9802304](#)].
- [114] D. J. H. Chung, E. W. Kolb and A. Riotto, “Nonthermal supermassive dark matter”, *Phys. Rev. Lett.* **81** 4048-4051 (Nov, 1998), [[arXiv:hep-ph/9805473](#)].
- [115] G. Gelmini and P. Gondolo, “Dm production mechanisms”, [[arXiv:1009.3690](#)].
- [116] G. Bertone, *Particle dark matter: observations, models and searches*. Cambridge University Press, 2010, DOI:10.1017/CBO9780511770739.
- [117] S. W. HAWKING, “Black hole explosions?”, *Nature* **248** 30-31 (Mar, 1974).
- [118] A. Drukier and L. Stodolsky, “Principles and applications of a neutral-current detector for neutrino physics and astronomy”, *Phys. Rev. D* **30** 2295 (1984).

-
- [119] DAMA collaboration, R. Bernabei et al., “*First results from DAMA/LIBRA and the combined results with DAMA/NaI*”, *Eur. Phys. J. C* **56** 333–355 (Aug, 2008), [[arXiv:0804.2741](#)].
- [120] R. Bernabei et al., “*Dark matter particles in the Galactic halo: Results and implications from DAMA/NaI*”, *Int. J. Mod. Phys.D* **13** 2127–2160 (Dec, 2004), [[arXiv:astro-ph/0501412](#)].
- [121] CDMS collaboration, Z. Ahmed et al., “*Search for Axions with the CDMS Experiment*”, *Phys. Rev. Lett.* **103** 141802 (Oct, 2009), [[arXiv:0902.4693](#)].
- [122] CDMS-II collaboration, Z. Ahmed et al., “*Dark Matter Search Results from the CDMS II Experiment*”, *Science* **327** 1619–1621 (Feb, 2010), [[arXiv:0912.3592](#)].
- [123] XENON COLLABORATION collaboration, J. Angle et al., “*First results from the xenon10 dark matter experiment at the gran sasso national laboratory*”, *Phys. Rev. Lett.* **100** 021303 (Jan, 2008), [[arXiv:0706.0039](#)].
- [124] E. Aprile and T. Doke, “*Liquid xenon detectors for particle physics and astrophysics*”, *Rev. Mod. Phys.* **82** 2053–2097 (Jul, 2010).
- [125] E. Aprile et al., “*First dark matter results from the xenon100 experiment*”, *Phys. Rev. Lett.* **105**, (Sep, 2010).
- [126] XENON100 collaboration, E. Aprile et al., “*Dark Matter Results from 100 Live Days of XENON100 Data*”, *Phys. Rev. Lett.* **107** 131302 (Sep, 2011), [[arXiv:1104.2549](#)].
- [127] E. Aprile et al., “*The xenon100 dark matter experiment*”, *Astropart. Phys.* **35** 573–590 (Apr, 2012), [[arXiv:1107.2155](#)].
- [128] E. Behnke, J. I. Collar, P. S. Cooper, K. Crum, M. Crisler, M. Hu et al., “*Spin-dependent wimp limits from a bubble chamber*”, *Science* **319** 933–936 (Feb, 2008), [[arXiv:0804.2886](#)].

- [129] LUX collaboration, D. S. Akerib et al., “*First results from the LUX dark matter experiment at the Sanford Underground Research Facility*”, *Phys. Rev. Lett.* **112** 091303 (Mar, 2014), [[arXiv:1310.8214](#)].
- [130] M. Boulay, B. Cai and the Deap/Clean Collaboration, “*Dark matter search at SNOLAB with DEAP-1 and DEAP/CLEAN-3600*”, *J. Phys. Conf. Ser.* **136** 042081 (Nov, 2008).
- [131] UKDMC collaboration, T. Sumner, “*Direct dark matter searches: DRIFT and ZEPLIN*”, *PoS HEP2005* 003 (2006).
- [132] V. N. Lebedenko et al., “*Result from the First Science Run of the ZEPLIN-III Dark Matter Search Experiment*”, *Phys. Rev. D* **80** 052010 (Sep, 2009), [[arXiv:0812.1150](#)].
- [133] KIMS collaboration, H. S. Lee et al., “*Limits on WIMP-nucleon cross section with CsI(Tl) crystal detectors*”, *Phys. Rev. Lett.* **99** 091301 (Aug, 2007), [[arXiv:0704.0423](#)].
- [134] S. C. Kim et al., “*New Limits on Interactions between Weakly Interacting Massive Particles and Nucleons Obtained with CsI(Tl) Crystal Detectors*”, *Phys. Rev. Lett.* **108** 181301 (Apr, 2012), [[arXiv:1204.2646](#)].
- [135] KIMS collaboration, H. S. Lee et al., “*First limit on wimp cross section with low background csi(tl) crystal detector*”, *Phys. Lett. B* **633** 201–208 (Feb, 2006), [[arXiv:astro-ph/0509080](#)].
- [136] G. Alner et al., “*Limits on wimp cross-sections from the naiad experiment at the boulby underground laboratory*”, *Phys. Lett. B* **616** 17–24 (Jun, 2005), [[arXiv:hep-ex/0504031](#)].
- [137] S. Archambault et al., “*Searching for dark matter with picasso*”, *Physics Procedia* **61** 107–111 (2015).

-
- [138] A. Takeda et al., “Limits on the WIMP - nucleon coupling coefficients from dark matter search experiment with NaF bolometer”, *Phys. Lett. B* **572** 145–151 (Oct, 2003), [[arXiv:astro-ph/0306365](#)].
- [139] S. Ando and K. Ishiwata, “Constraints on decaying dark matter from the extragalactic gamma-ray background”, *J. Cosmol. Astropart. Phys.* **2015** 024–024 (May, 2015), [[arXiv:1502.02007](#)].
- [140] M. Pandey, D. Majumdar, A. Halder and S. Banerjee, “Mass and Life Time of Heavy Dark Matter Decaying into IceCube PeV Neutrinos”, *Phys.Lett.B* **797** 134910 (2019), [[arXiv:1905.08662](#)].
- [141] P. Picozza et al., “Pamela - a payload for antimatter matter exploration and light-nuclei astrophysics”, *Astropart. Phys.* **27** 296–315 (Apr, 2007), [[arXiv:astro-ph/0608697](#)].
- [142] G. Pühlhofer, F. Leuschner and H. Salzmänn, “Hess: The high energy stereoscopic system”, in *Handbook of X-ray and Gamma-ray Astrophysics*, pp. 2745–2785. Springer, 2024.
- [143] J. Goodman and P. Huentemeyer, “The high-altitude water cherenkov detector array—hawc”, in *Handbook of X-ray and Gamma-ray Astrophysics*, pp. 1–26. Springer, 2023.
- [144] C. Bigongiari, C. Consortium et al., “The cherenkov telescope array”, *Nuclear and particle physics proceedings* **279** 174--181 (2016).
- [145] M. Garzarczyk, M. Collaboration et al., “The major atmospheric gamma-ray imaging cherenkov telescope”, *Nuclear Instruments and Methods in Physics Research Section A: Accelerators, Spectrometers, Detectors and Associated Equipment* **639** 33--36 (2011).
- [146] J. Shen, R. M. Rich, J. Kormendy, C. D. Howard, R. D. Propris and A. Kunder, “OUR MILKY WAY AS a PURE-DISK GALAXY—a

- CHALLENGE FOR GALAXY FORMATION”, *Astrophys. J.* **720** L72–L76 (Aug, 2010), [[arXiv:1005.0385](#)].
- [147] J. F. Navarro, C. S. Frenk and S. D. M. White, “The Structure of cold dark matter halos”, *Astrophys. J.* **462** 563–575 (1996), [[arXiv:astro-ph/9508025](#)].
- [148] J. F. Navarro, C. S. Frenk and S. D. M. White, “A Universal Density Profile from Hierarchical Clustering”, *Astrophys. J.* **490** 493–508 (Dec., 1997), [[arXiv:astro-ph/9611107](#)].
- [149] J. N. Bahcall and R. M. Soneira, “The universe at faint magnitudes. I. Models for the Galaxy and the predicted star counts.”, *Astrophys. J. suppl.* **44** 73–110 (Sep, 1980).
- [150] B. Moore, F. Governato, T. Quinn, J. Stadel and G. Lake, “Resolving the Structure of Cold Dark Matter Halos”, *Astrophys. J. Lett.* **499** L5–L8 (May, 1998), [[arXiv:astro-ph/9709051](#)].
- [151] J. Diemand, B. Moore and J. Stadel, “Convergence and scatter of cluster density profiles”, *Mon. Not. Roy. Astron. Soc.* **353** 624–632 (Sep, 2004), [[arXiv:astro-ph/0402267](#)].
- [152] A. Burkert, “The structure of dark matter halos in dwarf galaxies”, *Astrophys. J.* **447**, (Jul, 1995), [[arXiv:astro-ph/9504041](#)].
- [153] P. Salucci et al., “Dwarf spheroidal galaxy kinematics and spiral galaxy scaling laws”, *Mon. Not. Roy. Astron. Soc.* **420** 2034–2041 (Feb, 2012), [[arXiv:1111.1165](#)].
- [154] A. V. Kravtsov, A. A. Klypin, J. S. Bullock and J. R. Primack, “The cores of dark matter–dominated galaxies: Theory versus observations”, *Astrophys. J.* **502** 48–58 (Jul, 1998), [[arXiv:astro-ph/9708176](#)].

-
- [155] J. Einasto, “Influence of the atmospheric and instrumental dispersion on the brightness distribution in a galaxy”, *Trudy Inst. Astrofiz. Alma-Ata* **51** 8 (1965).
- [156] H. I. Ewen and E. M. Purcell, “Observation of a line in the galactic radio spectrum: Radiation from galactic hydrogen at 1,420 mc./sec.”, *Nature* **168** 356--356 (1951).
- [157] H. Van de Hulst, “Radiogolven uit het wereldruim: Ii. herkomst der radiogolven; radiogolven uit het wereldruim: Ii. herkomst der radiogolven; radio waves from space.”, *Nederlandsch Tijdschrift voor Natuurkunde* **11** 210--221 (1945).
- [158] P. K. Natwariya, “21 cm line astronomy and constraining new physics”, *arXiv preprint arXiv:2301.02655*, (2023).
- [159] J. R. Pritchard and A. Loeb, “21 cm cosmology in the 21st century”, *Rep. Prog. Phys.* **75** 086901 (jul, 2012).
- [160] J. R. Pritchard and S. R. Furlanetto, “Descending from on high: Lyman-series cascades and spin-kinetic temperature coupling in the 21-cm line”, *Mon. Not. Roy. Astron. Soc.* **367** 1057--1066 (2006).
- [161] G. B. Field, “Excitation of the hydrogen 21-cm line”, *Proceedings of the IRE* **46** 240--250 (1958).
- [162] S. A. Wouthuysen, “On the excitation mechanism of the 21-cm (radio-frequency) interstellar hydrogen emission line.”, *Astron. J.* **57** 31-32 (Jan., 1952).
- [163] C. M. Hirata, “Wouthuysen-Field coupling strength and application to high-redshift 21-cm radiation”, *Mon. Not. Roy. Astron. Soc.* **367** 259-274 (03, 2006).

- [164] Y. Ali-Haïmoud and C. M. Hirata, “*Ultrafast effective multilevel atom method for primordial hydrogen recombination*”, *Phys. Rev. D* **82** 063521 (Sep, 2010).
- [165] Y. Ali-Haïmoud and C. M. Hirata, “*Hyrec: A fast and highly accurate primordial hydrogen and helium recombination code*”, *Phys. Rev. D* **83** 043513 (Feb, 2011), [[arXiv:1011.3758](https://arxiv.org/abs/1011.3758)].
- [166] Q. Yuan, B. Yue, X.-J. Bi, X. Chen and X. Zhang, “*Leptonic dark matter annihilation in the evolving universe: constraints and implications*”, *J. Cosmol. Astropart. Phys* **2010** 023--023 (oct, 2010).
- [167] M. Kuhlen, P. Madau and R. Montgomery, “*The spin temperature and 21 cm brightness of the intergalactic medium in the pre-reionization era*”, *Astrophys. J.* **637** L1--L4 (jan, 2006).
- [168] W. Yang, S. Pan, S. Vagnozzi, E. D. Valentino, D. F. Mota and S. Capozziello, “*Dawn of the dark: unified dark sectors and the EDGES cosmic dawn 21-cm signal*”, *J. Cosmol. Astropart. Phys* **2019** 044--044 (nov, 2019).
- [169] J. R. Pritchard and A. Loeb, “*21 cm cosmology in the 21st century*”, *Rept. Prog. Phys.* **75** 086901 (2012).
- [170] S. R. Furlanetto, S. P. Oh and F. H. Briggs, “*Cosmology at low frequencies: The 21 cm transition and the high-redshift universe*”, *Physics reports* **433** 181--301 (2006).
- [171] A. Mesinger, S. Furlanetto and R. Cen, “*21cmfast: a fast, seminumerical simulation of the high-redshift 21-cm signal*”, *Mon. Not. Roy. Astron. Soc.* **411** 955--972 (2011).
- [172] M. Zaldarriaga, S. R. Furlanetto and L. Hernquist, “*21 centimeter fluctuations from cosmic gas at high redshifts*”, *Astrophys. J.* **608** 622 (2004).

-
- [173] J. D. Bowman, A. E. E. Rogers, R. A. Monsalve, T. J. Mozdzen and N. Mahesh, “*An absorption profile centred at 78 megahertz in the sky-averaged spectrum*”, *Nature* **555** 67–70 (Mar, 2018).
- [174] S. Singh, J. Nambissan T, R. Subrahmanyam, N. Udaya Shankar, B. Girish, A. Raghunathan et al., “*On the detection of a cosmic dawn signal in the radio background*”, *Nature Astronomy* **6** 607–617 (2022).
- [175] R. F. Bradley, K. Tauscher, D. Rapetti and J. O. Burns, “*A ground plane artifact that induces an absorption profile in averaged spectra from global 21 cm measurements, with possible application to edges*”, *Astrophys. J.* **874** 153 (2019).
- [176] S. Banerjee, F. Boudjema, N. Chakrabarty, G. Chalons and H. Sun, “*Relic density of dark matter in the inert doublet model beyond leading order: The heavy mass case*”, *Phys. Rev. D* **100** 095024 (Nov, 2019), [[arXiv:1906.11269](https://arxiv.org/abs/1906.11269)].
- [177] S. R. Furlanetto, S. P. Oh and E. Pierpaoli, “*The Effects of Dark Matter Decay and Annihilation on the High-Redshift 21 cm Background*”, *Phys. Rev. D* **74** 103502 (2006).
- [178] G. D’Amico, P. Panci and A. Strumia, “*Bounds on dark-matter annihilations from 21-cm data*”, *Phys. Rev. Lett.* **121** 011103 (2018).
- [179] H. Liu and T. R. Slatyer, “*Implications of a 21-cm signal for dark matter annihilation and decay*”, *Phys. Rev. D* **98** 023501 (2018).
- [180] J. B. Muñoz, E. D. Kovetz and Y. Ali-Haïmoud, “*Heating of baryons due to scattering with dark matter during the dark ages*”, *Phys. Rev. D* **92** 083528 (Oct, 2015).
- [181] C. Dvorkin, K. Blum and M. Kamionkowski, “*Constraining dark matter-baryon scattering with linear cosmology*”, *Phys. Rev. D* **89** 023519 (2014).

- [182] J. Kalinowski, W. Kotlarski, T. Robens, D. Sokolowska and A. F. Żarnecki, “Benchmarking the inert doublet model for $e^+ e^-$ colliders”, *Journal of High Energy Physics* **2018** 1–21 (2018).
- [183] S. Banerjee, F. Boudjema, N. Chakrabarty, G. Chalons and H. Sun, “Relic density of dark matter in the inert doublet model beyond leading order: The heavy mass case”, *Phys. Rev. D* **100** 095024 (2019).
- [184] S. Singh, J. Nambissan T., R. Subrahmanyam, N. Udaya Shankar, B. S. Girish, A. Raghunathan et al., “On the detection of a cosmic dawn signal in the radio background”, *Nature Astronomy* **6** 607–617 (May, 2022).
- [185] R. Basu, M. Pandey, D. Majumdar and S. Banerjee, “Bounds on dark matter annihilation cross-sections from inert doublet model in the context of 21-cm cosmology of dark ages”, 2021. 10.1142/S0217751X21501633.
- [186] A. Halder and M. Pandey, “Probing the effects of primordial black holes on 21-cm EDGES signal along with interacting dark energy and dark matter–baryon scattering”, *Mon. Not. Roy. Astron. Soc.* **508** 3446–3454 (10, 2021), [[arXiv:2101.05228](https://arxiv.org/abs/2101.05228)].
- [187] S. Galli, T. R. Slatyer, M. Valdes and F. Iocco, “Systematic uncertainties in constraining dark matter annihilation from the cosmic microwave background”, *Phys. Rev. D* **88** 063502 (Sep, 2013).
- [188] P. J. E. Peebles, “Recombination of the Primeval Plasma”, *Astrophys. J.* **153** 1 (July, 1968).
- [189] C. Evoli, A. Mesinger and A. Ferrara, “Unveiling the nature of dark matter with high redshift 21 cm line experiments”, *J. Cosmol. Astropart. Phys.* **2014** 024 (2014).
- [190] V. Poulin, P. D. Serpico and J. Lesgourgues, “Dark matter annihilations in halos and high-redshift sources of reionization of the universe”, *J. Cosmol. Astropart. Phys.* **2015** 041 (2015).

-
- [191] T. R. Slatyer, “*Indirect Dark Matter Signatures in the Cosmic Dark Ages II. Ionization, Heating and Photon Production from Arbitrary Energy Injections*”, *Phys. Rev. D* **93** 023521 (2016).
- [192] M. S. Madhavacheril, N. Sehgal and T. R. Slatyer, “*Current Dark Matter Annihilation Constraints from CMB and Low-Redshift Data*”, *Phys. Rev. D* **89** 103508 (2014).
- [193] H. Liu, G. W. Ridgway and T. R. Slatyer, “*Code package for calculating modified cosmic ionization and thermal histories with dark matter and other exotic energy injections*”, *Phys. Rev. D* **101** 023530 (2020).
- [194] T. R. Slatyer and C.-L. Wu, “*Early-universe constraints on dark matter-baryon scattering and their implications for a global 21 cm signal*”, *Phys. Rev. D* **98** 023013 (2018).
- [195] M. R. Buckley and P. J. Fox, “*Dark matter self-interactions and light force carriers*”, *Phys. Rev. D* **81** 083522 (Apr, 2010).
- [196] B. Holdom, “*Two $u(1)$'s and ϵ charge shifts*”, *Phys. Lett. B* **166** 196–198 (1986).
- [197] E. J. Chun, J.-C. Park and S. Scopel, “*Dark matter and a new gauge boson through kinetic mixing*”, *J. High Energy Phys.* **2011**, (Feb, 2011).
- [198] C. Dvorkin, T. Lin and K. Schutz, “*The cosmology of sub-meV dark matter freeze-in*”, 2020.
- [199] E. O. Nadler, V. Gluscevic, K. K. Boddy and R. H. Wechsler, “*Constraints on dark matter microphysics from the milky way satellite population*”, *Astrophys. J.* **878** L32 (Jun, 2019).
- [200] A. Bhoonah, J. Bramante, F. Elahi and S. Schon, “*Calorimetric dark matter detection with galactic center gas clouds*”, *Phys. Rev. Lett.* **121** 131101 (Sep, 2018).

- [201] E. D. Kovetz, V. Poulin, V. Gluscevic, K. K. Boddy, R. Barkana and M. Kamionkowski, “*Tighter limits on dark matter explanations of the anomalous edges 21 cm signal*”, *Phys. Rev. D* **98** 103529 (Nov, 2018).
- [202] U. Mukhopadhyay, D. Majumdar and K. K. Datta, “*Probing interacting dark energy and scattering of baryons with dark matter in light of the edges 21-cm signal*”, *Phys. Rev. D* **103** 063510 (Mar, 2021).
- [203] R. Barkana, “*Possible interaction between baryons and dark-matter particles revealed by the first stars*”, *Nature* **555** 71--74 (2018).
- [204] M. S. Mahdawi and G. R. Farrar, “*Constraints on dark matter with a moderately large and velocity-dependent dm-nucleon cross-section*”, *J. Cosmol. Astropart. Phys* **2018** 007{007 (Oct, 2018).
- [205] G. Bélanger, F. Boudjema, A. Goudelis, A. Pukhov and B. Zaldivar, “*micromegas5. 0: Freeze-in*”, *Computer Physics Communications* **231** 173--186 (2018).
- [206] L. Lopez-Honorez, O. Mena, S. Palomares-Ruiz and A. C. Vincent, “*Constraints on dark matter annihilation from cmb observations before planck*”, *J. Cosmol. Astropart. Phys.* **2013** 046 (2013).
- [207] M. Kawasaki, K. Nakayama and T. Sekiguchi, “*Cmb constraint on dark matter annihilation after planck 2015*”, *Physics Letters B* **756** 212--215 (2016).
- [208] R. Basu, D. Majumdar, A. Halder and S. Banerjee, “*Addressing the self-interaction for elder dark matter from the 21-cm signal*”, 2023.
- [209] J. R. Pritchard and A. Loeb, “*Evolution of the 21 cm signal throughout cosmic history*”, *Phys. Rev. D* **78** 103511 (Nov, 2008).

-
- [210] L. Koopmans, J. Pritchard, G. Mellema, F. Abdalla, J. Aguirre, K. Ahn et al., “*The cosmic dawn and epoch of reionization with the square kilometre array*”, *Prec. Sci. AASKA14* 001 (2015).
- [211] G. D. Mack, J. F. Beacom and G. Bertone, “*Towards closing the window on strongly interacting dark matter: Far-reaching constraints from earth’s heat flow*”, *Phys. Rev. D* **76** 043523 (Aug, 2007).
- [212] A. Aboubrahim, P. Nath and Z.-Y. Wang, “*A cosmologically consistent millicharged dark matter solution to the EDGES anomaly of possible string theory origin*”, *J. High Energy Phys.* **12** 148 (2021).
- [213] R. Barkana, N. J. Outmezguine, D. Redigolo and T. Volansky, “*Strong constraints on light dark matter interpretation of the edges signal*”, *Phys. Rev. D* **98** 103005 (Nov, 2018).
- [214] A. Berlin, D. Hooper, G. Krnjaic and S. D. McDermott, “*Severely constraining dark-matter interpretations of the 21-cm anomaly*”, *Phys. Rev. Lett.* **121** 011102 (Jul, 2018).
- [215] T. R. Slatyer and C.-L. Wu, “*Early-universe constraints on dark matter-baryon scattering and their implications for a global 21 cm signal*”, *Phys. Rev. D* **98** 023013 (Jul, 2018).
- [216] A. Halder, S. S. Pandey and A. S. Majumdar, “*Global 21-cm brightness temperature in viscous dark energy models*”, *JCAP* **10** 049 (2022), [[arXiv:2207.09177](https://arxiv.org/abs/2207.09177)].
- [217] A. Gupta, D. Majumdar and A. Halder, “*KM3NeT upper bounds of detection rates of solar neutrinos from annihilations of dark matter at the solar core*”, *Mod. Phys. Lett. A* **37** 2250233 (2022), [[arXiv:2203.13697](https://arxiv.org/abs/2203.13697)].
- [218] P. Gondolo and G. Gelmini, “*Cosmic abundances of stable particles: Improved analysis*”, *Nuclear Physics B* **360** 145–179 (1991).

- [219] H. Liu and T. R. Slatyer, “Implications of a 21-cm signal for dark matter annihilation and decay”, *Phys. Rev. D* **98** 023501 (Jul, 2018).
- [220] N. Hiroshima, K. Kohri, T. Sekiguchi and R. Takahashi, “Impacts of new small-scale n -body simulations on dark matter annihilations constrained from cosmological 21-cm line observations”, *Phys. Rev. D* **104** 083547 (Oct, 2021).
- [221] S. K. Acharya and R. Khatri, “CMB and BBN constraints on evaporating primordial black holes revisited”, *J. Cosmol. Astropart. Phys* **06** 018 (2020).
- [222] S. J. Clark, B. Dutta, Y. Gao, Y.-Z. Ma and L. E. Strigari, “21 cm limits on decaying dark matter and primordial black holes”, *Phys. Rev. D* **98** 043006 (Aug, 2018).
- [223] Y. Yang, “Constraints on primordial black holes and curvature perturbations from the global 21-cm signal”, *Phys. Rev. D* **102** 083538 (Oct, 2020).
- [224] K. J. Mack and D. H. Wesley, “Primordial black holes in the dark ages: Observational prospects for future 21cm surveys”, 2008. [arXiv:0805.1531](https://arxiv.org/abs/0805.1531).
- [225] L. Zhang, X. Chen, M. Kamionkowski, Z.-G. Si and Z. Zheng, “Constraints on radiative dark-matter decay from the cosmic microwave background”, *Phys. Rev. D* **76** 061301(R) (Sep, 2007).
- [226] A. S. Eddington, *The Internal Constitution of the Stars*. 1926.
- [227] S. Chandrasekhar, “The Maximum Mass of Ideal White Dwarfs”, *Astrophys. J.* **74** 81 (July, 1931).
- [228] R. Napiwotzki, “The galactic population of white dwarfs”, in *J. Phys. Conf. Ser.*, vol. 172 of *Journal of Physics Conference Series*, p. 012004, June, 2009. [[arXiv:0903.2159](https://arxiv.org/abs/0903.2159)], [DOI:10.1088/1742-6596/172/1/012004](https://doi.org/10.1088/1742-6596/172/1/012004).
- [229] A. Heger, C. L. Fryer, S. E. Woosley, N. Langer and D. H. Hartmann, “How massive single stars end their life”, *Astrophys. J.* **591** 288–300 (Jul, 2003), [[arXiv:astro-ph/0212469](https://arxiv.org/abs/astro-ph/0212469)].

-
- [230] G. Fontaine, P. Brassard and P. Bergeron, “*The Potential of White Dwarf Cosmochronology*”, *Publications of the Astronomical Society of the Pacific* **113** 409–435 (Apr., 2001).
- [231] A. Hewish, S. J. Bell, J. D. Pilkington, P. Frederick Scott and R. A. Collins, “*Observation of a rapidly pulsating radio source*”, in *A Source Book in Astronomy and Astrophysics, 1900–1975*, pp. 498–504. Harvard University Press, 1979.
- [232] T. Gold, “*Pulsars and the origin of cosmic rays*”, *Phil. Tran. Roy. Soc. London. Ser. A* **277** 453--461 (1975).
- [233] J. M. Lattimer and M. Prakash, “*The physics of neutron stars*”, *Science* **304** 536--542 (2004).
- [234] W. Becker et al., *Neutron stars and pulsars*, vol. 357. Springer, 2009.
- [235] R. Nandi, “*Studies on some aspects of neutron stars—from crust to core*”, *Ph. D. Thesis*, (2012).
- [236] D. Ravenhall, C. Pethick and J. Wilson, “*Structure of matter below nuclear saturation density*”, *Phys. Rev. Lett.* **50** 2066 (1983).
- [237] M.-a. Hashimoto, H. Seki and M. Yamada, “*Shape of nuclei in the crust of neutron star*”, *Prog. th. phys.* **71** 320--326 (1984).
- [238] K. Oyamatsu, “*Nuclear shapes in the inner crust of a neutron star*”, *Nucl. Phys. A* **561** 431--452 (1993).
- [239] P. B. Demorest, T. Pennucci, S. Ransom, M. Roberts and J. Hessels, “*A two-solar-mass neutron star measured using shapiro delay*”, *nature* **467** 1081--1083 (2010).
- [240] R. N. Manchester, G. B. Hobbs, A. Teoh and M. Hobbs, “*The Australia Telescope National Facility Pulsar Catalogue*”, *Astron. J.* **129** 1993–2006 (Apr, 2005), [[arXiv:astro-ph/0412641](https://arxiv.org/abs/astro-ph/0412641)].

- [241] M. C. Miller, F. Lamb, A. Dittmann, S. Bogdanov, Z. Arzoumanian, K. Gendreau et al., “*The radius of psr j0740+ 6620 from nicer and xmm-newton data*”, *Astrophys. J. Lett.* **918** L28 (2021).
- [242] K. C. Gendreau, Z. Arzoumanian, P. W. Adkins, C. L. Albert, J. F. Anders, A. T. Aylward et al., “*The neutron star interior composition explorer (nicer): design and development*”, in *Space telescopes and instrumentation 2016: Ultraviolet to gamma ray*, vol. 9905, pp. 420–435, SPIE, 2016.
- [243] A. Lyne, “*A review of the double pulsar-psr j0737-3039*”, *Chinese Journal of Astronomy and Astrophysics* **6** 162 (2006).
- [244] B. P. Abbott, R. Abbott, T. Abbott, F. Acernese, K. Ackley, C. Adams et al., “*Gw170817: observation of gravitational waves from a binary neutron star inspiral*”, *Phys. Rev. Lett.* **119** 161101 (2017).
- [245] E. Witten, “*Cosmic separation of phases*”, *Phys. Rev. D* **30** 272–285 (Jul, 1984).
- [246] D. Ivanenko and D. Kurdgelaidze, “*Hypothesis concerning quark stars*”, *Astrophysics* **1** 251--252 (1965).
- [247] S. Banerjee, S. K. Ghosh and S. Raha, “*The chandrasekhar limit for quark stars*”, *J. Phys. G* **26** L1 (2000), [[arXiv:astro-ph/0001246](https://arxiv.org/abs/astro-ph/0001246)].
- [248] M. Malheiro, M. Fiolhais and A. Taurines, “*Metastable strange matter and compact quark stars*”, *J. Phys. G* **29** 1045–1052 (Apr, 2003), [[arXiv:astro-ph/0304096](https://arxiv.org/abs/astro-ph/0304096)].
- [249] E. Aubourg, P. Bareyre, S. Bréhin, M. Gros, M. Lachièze-Rey, B. Laurent et al., “*Evidence for gravitational microlensing by dark objects in the galactic halo*”, *Nature* **365** 623–625 (Oct, 1993).
- [250] P. Tisserand, L. Le Guillou, C. Afonso, J. N. Albert, J. Andersen, R. Ansari et al., “*Limits on the macho content of the galactic halo from the eros-2*

-
- survey of the magellanic clouds*”, *Astron. Astrophys.* **469** 387–404 (Apr, 2007), [[arXiv:astro-ph/0607207](https://arxiv.org/abs/astro-ph/0607207)].
- [251] W. Sutherland, “*Gravitational microlensing—a report on the macho project*”, *Rev. Mod. Phys.* **71** 421–434 (Jan, 1999), [[arXiv:astro-ph/9811185](https://arxiv.org/abs/astro-ph/9811185)].
- [252] S. Hawking and W. Israel, *Three Hundred Years of Gravitation*. Philosophiae Naturalis, Principia Mathematica. Cambridge University Press, 1989.
- [253] Y. B. Zel’dovich and I. D. Novikov, “*The Hypothesis of Cores Retarded during Expansion and the Hot Cosmological Model*”, *Soviet Astronomy* **10** 602 (Feb., 1967).
- [254] M. Y. Khlopov, “*Primordial black holes*”, *Res. Astron. Astrophys.* **10** 495–528 (may, 2010).
- [255] K. M. Belotsky, A. E. Dmitriev, E. A. Esipova, V. A. Gani, A. V. Grobov, M. Y. Khlopov et al., “*Signatures of primordial black hole dark matter*”, *Mod. Phys. Lett. A* **29** 1440005 (2014).
- [256] K. M. Belotsky, V. I. Dokuchaev, Y. N. Eroshenko, E. A. Esipova, M. Y. Khlopov, L. A. Khromykh et al., “*Clusters of primordial black holes*”, *Eur. Phys. J. C* **79** 246 (Mar, 2019).
- [257] J. García-Bellido, “*Massive primordial black holes as dark matter and their detection with gravitational waves*”, *J. Phys: Conf. Ser.* **840** 012032 (may, 2017).
- [258] P. Ivanov, P. Naselsky and I. Novikov, “*Inflation and primordial black holes as dark matter*”, *Phys. Rev. D* **50** 7173–7178 (Dec, 1994).
- [259] B. J. Carr and J. E. Lidsey, “*Primordial black holes and generalized constraints on chaotic inflation*”, *Phys. Rev. D* **48** 543–553 (Jul, 1993).

- [260] B. J. Carr, J. H. Gilbert and J. E. Lidsey, “Black hole relics and inflation: Limits on blue perturbation spectra”, *Phys. Rev. D* **50** 4853--4867 (Oct, 1994).
- [261] J. García-Bellido, A. Linde and D. Wands, “Density perturbations and black hole formation in hybrid inflation”, *Phys. Rev. D* **54** 6040--6058 (Nov, 1996).
- [262] A. Taruya, “Parametric amplification of density perturbations in the oscillating inflation model”, *Phys. Rev. D* **59** 103505 (Apr, 1999).
- [263] S. Pi, Y. li Zhang, Q.-G. Huang and M. Sasaki, “Scalaron from r^2 -gravity as a heavy field”, *J. Cosmol. Astropart. Phys* **2018** 042--042 (may, 2018).
- [264] B. A. Bassett and S. Tsujikawa, “Inflationary preheating and primordial black holes”, *Phys. Rev. D* **63** 123503 (May, 2001), [[arXiv:hep-ph/0008328](https://arxiv.org/abs/hep-ph/0008328)].
- [265] C. J. Hogan, “Massive black holes generated by cosmic strings”, *Phys. Lett. B* **143** 87 - 91 (1984).
- [266] A. Polnarev and R. Zembowicz, “Formation of primordial black holes by cosmic strings”, *Phys. Rev. D* **43** 1106--1109 (Feb, 1991).
- [267] K. ichi Maeda, K. Sato, M. Sasaki and H. Kodama, “Creation of schwarzschild-de sitter wormholes by a cosmological first-order phase transition”, *Phys. Lett. B* **108** 98 - 102 (1982).
- [268] E. Cotner and A. Kusenko, “Primordial black holes from supersymmetry in the early universe”, *Phys. Rev. Lett.* **119** 031103 (Jul, 2017).
- [269] E. Cotner, A. Kusenko and V. Takhistov, “Primordial black holes from inflaton fragmentation into oscillons”, *Phys. Rev. D* **98** 083513 (Oct, 2018).
- [270] E. Cotner and A. Kusenko, “Primordial black holes from scalar field evolution in the early universe”, *Phys. Rev. D* **96** 103002 (Nov, 2017).

-
- [271] E. W. Kolb and I. I. Tkachev, “*Axion miniclusters and bose stars*”, *Phys. Rev. Lett.* **71** 3051–3054 (Nov, 1993), [[arXiv:hep-ph/9303313](#)].
- [272] F. Sandin, *Exotic phases of matter in compact stars*. PhD thesis, Luleå tekniska universitet, 2007.
- [273] C. Rovelli and F. Vidotto, “*Planck stars*”, *Int. J. Mod. Phys.D* **23** 1442026 (Oct, 2014), [[arXiv:1401.6562](#)].
- [274] I. D’Souza and C. Kalman, *Preons: Models of Leptons, Quarks and Gauge Bosons as Composite Objects*. World Scientific, 1992.
- [275] J. Hansson and F. Sandin, “*Preon stars: A New class of cosmic compact objects*”, *Phys. Lett. B* **616** 1–7 (Jun, 2005), [[arXiv:astro-ph/0410417](#)].
- [276] S. Clark, “*Holy moley (astronomers taking a first peek at our galaxy’s black heart might be in for a big surprise)*”, 15 July 2017.
- [277] E. Braaten, A. Mohapatra and H. Zhang, “*Dense Axion Stars*”, *Phys. Rev. Lett.* **117** 121801 (2016), [[arXiv:1512.00108](#)].
- [278] L. Staveley-Smith and T. Oosterloo, “*Hi science with the square kilometre array*”, *arXiv preprint arXiv:1506.04473*, (2015).
- [279] H.-S. Kim, J. S. B. Wyithe, C. Power, J. Park, C. d. P. Lagos and C. Baugh, “*The $h\ i$ mass function as a probe of photoionization feedback on low-mass galaxy formation*”, *Mon. Not. Roy. Astron. Soc.* **453** 2315–2325 (2015).
- [280] S.-L. Blyth, J. Van Der Hulst, M. Verheijen, H. Members, B. Catinella, F. Fraternali et al., “*Exploring neutral hydrogen and galaxy evolution with the ska*”, *arXiv preprint arXiv:1501.01295*, (2015).
- [281] J. Bagla, N. Khandai and K. K. Datta, “*H i as a probe of the large-scale structure in the post-reionization universe*”, *Mon. Not. Roy. Astron. Soc.* **407** 567–580 (2010).

- [282] A. Chakraborty and N. Roy, “Detection of hi 21 cm emission from a strongly lensed galaxy at $z 1.3$ ”, *Mon. Not. Roy. Astron. Soc.* **519** 4074--4081 (2023).
- [283] A. Chowdhury, N. Kanekar, J. N. Chengalur, S. Sethi and K. Dwarakanath, “Hi 21-centimetre emission from an ensemble of galaxies at an average redshift of one”, *Nature* **586** 369--372 (2020).
- [284] S. Johnston, R. Taylor, M. Bailes, N. Bartel, C. Baugh, M. Bietenholz et al., “Science with askap: The australian square-kilometre-array pathfinder”, *Experimental astronomy* **22** 151--273 (2008).
- [285] P. Dewdney, W. Turner, R. Millenaar, R. McCool, J. Lazio and T. Cornwell, “Ska1 system baseline design”, *Document number SKA-TEL-SKO-DD-001 Revision 1*, (2013).
- [286] J. L. Jonas, “Meerkat—the south african array with composite dishes and wide-band single pixel feeds”, *Proceedings of the IEEE* **97** 1522--1530 (2009).
- [287] M. Lacy, S. Baum, C. Chandler, S. Chatterjee, T. Clarke, S. Deustua et al., “The karl g. jansky very large array sky survey (vlass). science case and survey design”, *Publications of the Astronomical Society of the Pacific* **132** 035001 (2020).
- [288] M. Verheijen, T. Oosterloo, W. Van Cappellen, L. Bakker, M. Ivashina and J. van der Hulst, “Apertif, a focal plane array for the wsrt”, in *AIP Conference Proceedings*, vol. 1035, pp. 265–271, American Institute of Physics, 2008.
- [289] Y. Gupta, B. Ajithkumar, H. Kale, S. Nayak, S. Sabhapathy, S. Sureshkumar et al., “The upgraded gmrt: opening new windows on the radio universe”, *Current Science* **707**--714 (2017).
- [290] R. B. Metcalf and S. White, “Cosmological information in the gravitational lensing of pregalactic h i”, *Mon. Not. Roy. Astron. Soc.* **394** 704--714 (2009).

-
- [291] A. Ghosh, S. Bharadwaj, S. S. Ali and J. N. Chengalur, “Gmrt observation towards detecting the post-reionization 21-cm signal”, *Mon. Not. Roy. Astron. Soc.* **411** 2426--2438 (2011).
- [292] T. Di Matteo, R. Perna, T. Abel and M. J. Rees, “Radio foregrounds for the 21 centimeter tomography of the neutral intergalactic medium at high redshifts”, *Astrophys. J.* **564** 576 (2002).
- [293] S. S. Ali, S. Bharadwaj and J. N. Chengalur, “Foregrounds for redshifted 21-cm studies of reionization: Giant meter wave radio telescope 153-mhz observations”, *Mon. Not. Roy. Astron. Soc.* **385** 2166--2174 (2008).
- [294] M. Rauch, “The lyman alpha forest in the spectra of quasistellar objects”, *Annual Review of Astronomy and Astrophysics* **36** 267--316 (1998).
- [295] A. M. Wolfe, E. Gawiser and J. X. Prochaska, “Damped $ly\alpha$ systems”, *Annu. Rev. Astron. Astrophys.* **43** 861--918 (2005).
- [296] C. Péroux, M. Dessauges-Zavadsky, S. D’Odorico, T.-S. Kim and R. G. McMahon, “A homogeneous sample of sub-damped lyman α systems—ii. statistical, kinematic and chemical properties”, *Mon. Not. Roy. Astron. Soc.* **345** 480--496 (2003).
- [297] M. Meyer, A. Robotham, D. Obreschkow, T. Westmeier, A. R. Duffy and L. Staveley-Smith, “Tracing hi beyond the local universe”, *Publications of the Astronomical Society of Australia* **34** e052 (2017).
- [298] A. Ghosh, S. Bharadwaj, S. S. Ali and J. N. Chengalur, “Improved foreground removal in gmrt 610 mhz observations towards redshifted 21-cm tomography”, *Mon. Not. Roy. Astron. Soc.* **418** 2584--2589 (2011).
- [299] D. R. Lorimer and M. Kramer, *Handbook of pulsar astronomy*, vol. 4. Cambridge university press, 2005.

- [300] J. R. Oppenheimer and G. M. Volkoff, “On massive neutron cores”, *Physical Review* **55** 374 (1939).
- [301] S. L. Shapiro and S. A. Teukolsky, *Black holes, white dwarfs, and neutron stars: The physics of compact objects*. John Wiley & Sons, 2008.
- [302] P. Schneider, “Upper bounds on the cosmological density of compact objects with sub-solar masses from the variability of quasars”, *Astronomy and Astrophysics (ISSN 0004-6361)*, vol. 279, no. 1, p. 1-20 **279** 1--20 (1993).
- [303] T. D. Saini, S. Bharadwaj and S. K. Sethi, “Using gravitational lensing to study high redshift clouds at high redshift”, *Astrophys. J.* **557** 421 (2001).
- [304] H. Tashiro, K. Kadota and J. Silk, “Effects of dark matter-baryon scattering on redshifted 21 cm signals”, *Phys. Rev. D* **90** 083522 (2014).
- [305] A. Mitridate and A. Podo, “Bounds on dark matter decay from 21 cm line”, *J. Cosmol. Astropart. Phys.* **2018** 069 (2018).
- [306] F. M. Walter, S. J. Wolk and R. Neuhäuser, “Discovery of a nearby isolated neutron star”, *Nature* **379** 233--235 (1996).
- [307] J. A. Pons, F. M. Walter, J. M. Lattimer, M. Prakash, R. Neuhäuser and P. An, “Toward a mass and radius determination of the nearby isolated neutron star *rx j185635-3754*”, *Astrophys. J.* **564** 981 (2002).
- [308] D. L. Kaplan, M. Van Kerkwijk and J. Anderson, “The distance to the isolated neutron star *rx j0720. 4-3125*”, *Astrophys. J.* **660** 1428 (2007).

List of Publications

Papers included in Thesis

1. “**Bounds on dark matter annihilation cross-sections from inert doublet model in the context of 21-cm cosmology of dark ages**”, [Rupa Basu](#), Madhurima Pandey, Debasish Majumdar and Shibaji Banerjee, published on *International Journal of Modern Physics A*, DOI: 10.1142/S0217751X21501633.
2. “**Addressing the self-interaction for ELDER dark matter from the 21-cm signal**”, [Rupa Basu](#), Debasish Majumdar, Ashadul Halder and Shibaji Banerjee, under communication, *arXiv:2304.06680*
3. “**Constraining the parameters of an isolated neutron star using the lensed HI signal at uGMRT**”, [Rupa Basu](#), Siddhartha Bhattacharyya, Anjan Kumar Sarkar, Shibaji Banerjee and Debasish Majumdar, under communication, *arXiv:2406.17896* or *arXiv:2406.17896v2*
4. “**Bound on dark matter-baryon scattering cross-section in the light of 21-cm HI signal**”, [Rupa Basu](#), Debasish Majumdar and Shibaji Banerjee, under communication.

Publications not included in the Thesis:

“Exploring multimessenger signals from heavy dark matter decay with EDGES 21-cm result and IceCube”, Ashadul Halder, Madhurima Pandey, Debasis Majumdar and [Rupa Basu](#), published on *Journal of Cosmology and Astroparticle Physics*, DOI: 10.1088/1475-7516/2021/10/033.